CHARACTERISATION OF THE USQ HYPERSONIC FACILITY FREESTREAM

A Thesis submitted by

Byrenn JC Birch, BEng (Hons)

For the award of

Doctor of Philosophy

2019

Abstract

Hypersonic ground testing can make significant contributions to the design process for hypersonic flight vehicles. However, experimentation in conventional hypersonic ground testing facilities is complicated by the high levels of freestream fluctuations which are typically one-to-two orders of magnitude greater than in flight. This noisy test environment can have a significant impact on flow phenomena, such as boundary layer transition, and this leads directly to uncertainties in the prediction of essential hypersonic vehicle design parameters. To assess the noise level in 'TUSQ', the hypersonic wind tunnel at the University of Southern Queensland, the Mach 6 nozzle exit flow was characterised by measurements which provided: (1) the time-averaged and fluctuating components of Pitot pressure; (2) the time-averaged and fluctuating components of stagnation temperature; and (3) the fluctuating component of density. The Pitot pressure measurements were made using Kulite XTL-190M B-screen pressure transducers which were exposed directly to the flow. The stagnation temperature was determined from the experimental measurement of heat flux using microsecond response time coaxial surface junction thermocouples mounted in a stagnation point heat transfer gauge. A focused laser differential interferometer was designed for TUSQ, and this instrument was used to measure the freestream density fluctuations.

Using the Pitot pressure measurements and the measurements of the stagnation pressure in the nozzle reservoir (the barrel), the Mach number was found to decrease over the flow duration from 5.95 to 5.85. Through the measurement of stagnation temperature, the piston compression and the nozzle expansion of the test gas were found to be approximately isentropic for the first 65 ms of hypersonic flow. Thereafter, the stagnation temperature reduces due to the heat lost to the cold barrel. Thermodynamic modelling based on the measured pressure history in the barrel combined with empirical heat transfer correlations can be used to simulate the stagnation temperature in TUSQ to within 2 % of the actual value for $t = 0 - 150$ ms, increasing to within 5 % at $t = 170$ ms. The heat transfer process in the barrel was found to significantly affect the fluctuations in the hypersonic freestream. For $t < 65$ ms, the freestream fluctuations of Pitot pressure, stagnation temperature and density were found to be broadband in nature, consistent with a disturbance environment dominated by the radiation of acoustic noise from the turbulent boundary layer on the nozzle walls. At $t \approx 65$ ms, a 3 – 4 kHz narrowband disturbance was detected in the barrel and in the freestream flow, and this disturbance remains superimposed on the broadband disturbance environment for the remainder of the test flow. Because the characteristics of the flow changed during the run, it is appropriate to specify two RMS Pitot pressure fluctuation magnitudes in the 300 Hz to 25 kHz bandwidth: 2.52 % for $t = 5 - 65$ ms; and 2.86 % for $t = 65 - 200$ ms for $\mathrm{Re}_u = 6.94 \times 10^6\,\mathrm{m}^{-1}$. The RMS Pitot pressure fluctuations in the TUSQ freestream are similar to comparable Ludwieg and blowdown facilities. RMS stagnation temperature fluctuations were resolved for $f = 4$ Hz – 5 kHz and were found to increase throughout the flow period from approximately 1.5 % at the start of the run to 2.4 % at the termination of the nozzle flow. RMS freestream density fluctuations were determined for $f = 1 - 250$ kHz, increasing from 0.4 % to 0.6 % over the flow period. The bandwidth of the density fluctuation measurement was sufficient to resolve the classic Kolmogorov $-5/3$ rolloff in the inertial subrange.

Preliminary measurements of the boundary layer on a conical nose cylinder were made using the focused laser differential interferometer. These measurements identified the second mode instabilities in the transitional boundary layer, and identified the amplification of the narrowband 3 – 4 kHz freestream fluctuations within the boundary layer. Further opportunities to explore boundary layer transition in the TUSQ facility are expected to arise in the near future, at which time the FLDI instrument can be deployed with improved focusing ability.

Dedicated to my father, Dr. Colin Birch

Certification of Thesis

This Thesis is the work of Byrenn JC Birch except where otherwise acknowledged. The work is original and has not previously been submitted for any other award, except where acknowledged.

Principal Supervisor:	Prof. David Buttsworth
Associate Supervisor:	Dr. Fabian Zander
Associate Supervisor:	Dr. Rishabh Choudhury

Student and supervisors' signatures of endorsement are held at the University.

List of Publications

Birch, B., Buttsworth, D., Choudhury, R. & Stern, N. (2018). Characterization of a Ludwieg Tube with Free Piston Compression Heating in Mach 6 Configuration. In *22nd AIAA International Space Planes and Hypersonics Systems and Technologies Conference*. doi:10.2514/6.2018-5266

James, C. M., Birch, B. J. C., Smith, D. R., Cullen, T. G., Millard, T., Vella, S., . . . Buttsworth, D. R. (2019). Testing of Ultra Fast Response, Durable Co-axial Thermocouples for High Enthalpy Impulse Facilities. In *2019 AIAA Aviation and Aeronautics Forum and Exposition*. doi:10.2514/6.2019-3007

Acknowledgements

This research would not have been possible without the support and encouragement of many people.

I would like to gratefully acknowledge the guidance, advice and encouragement of my supervisory team: Prof. David Buttsworth, Dr. Rishabh Choudhury and Dr. Fabian Zander. Thanks for always making yourselves available for any query I had, no matter how big or small; and for being there to help with data collection, providing guidance on how to improve the experiments, and for your patience in reviewing this thesis.

Thanks to the team at the University of Stuttgart led by Dr.-Ing. Stefan Löhle, in particular to Fabian Hufgard who took time from his own studies to assist me during my two weeks in Stuttgart.

I am thankful for the Australian Government Research Training (RTP) Scholarship which enabled me to conduct this research. My research was also partially funded by the Australian Government through the Australian Research Council, and the work presented in Chapter 8 was supported by USQ under the Australia-Germany Joint Research Cooperation Scheme for the project "Spacecraft re-entry break-up". A portion of this research was undertaken using the University of Southern Queensland (USQ) Fawkes HPC which is co-sponsored by QCIF (Queensland Cyber Infrastructure Foundation) – www.usq.edu.au/eresearch/hpc.

I am very grateful for the contributions made to the development of the thermocouples used in this research by my fellow PhD candidate Nathan Stern, who provided practical advice in the design phase and machined the components. To everyone who has been involved in helping me operate the facility, every little bit of assistance was greatly appreciated– especially when that assistance was opening or closing the butterfly valve.

To everyone from the P7 and P10 group, and to my father's colleagues at USQ, your support through my toughest days is greatly appreciated. I could not have done this without you. Special thanks to David Buttsworth and Ray Malpress who went well beyond their professional roles during this time, and have done so ever since.

Most importantly, to my amazing wife Bec. Thanks for your patience and understanding while I have studied into the night and over many weekends. You are my greatest support and I could not have achieved this without your encouragement.

Table of Contents

List of Figures

List of Tables

Acronyms

ALTP	Atomic layer thermopile
BL	Boundary layer
CFD	Computational fluid dynamics
DNS	Direct numerical simulation
emf	Electromotive force
ESA	European Space Agency
FFT	Fast Fourier transform
FLDI	Focused laser differential interferometry
FSI	Fluid-structure interaction
HP	High-pass filtered
HWA	Hot wire anemometry
IRS	Institut für Raumfahrtsysteme
PSD	Power spectral density
PTFE	Polytetrafluoroethylene
PWK4	Plasmawindkanal 4 at the IRS
RMS	Root mean square
SNR	Signal-to-noise ratio
SWT	Stationary wavelet filter
TC	Thermocouple
TSL	Turbulent shear layer
TUSQ	USQ hypersonic facility
UQ	University of Queensland
USQ	University of Southern Queensland

Nomenclature

Roman Symbols

Symbol	Description	Units
a	Speed of sound	$\mathrm{m\,s^{-1}}$
a	Acceleration	$\mathrm{m\,s^{-2}}$
A	Area	$\mathrm{m^2}$
b	Sanderson prism thickness	m
$B_{1,2,3}$	Sellmeier coefficients	–
c	Constant	–
c_p	Specific heat at constant pressure	$\mathrm{J\,kg^{-1}\,K^{-1}}$
c_v	Specific heat at constant volume	$\mathrm{J\,kg^{-1}\,K^{-1}}$
C_{AB}	Coherence of signals A and B	–
$C_{1,2,3}$	Sellmeier coefficients	$\mathrm{\mu m^2}$
C_j	Junction capacitance	pF
d	Diameter	m
D	Diameter	m
$D_{4\sigma}$	Maximum FLDI beam diameter	m
d_0	Laser output diameter	m
e	Translational energy	$\mathrm{J\,kg^{-1}}$
e	Thermal effusivity, thermal product ($\sqrt{\rho c_p k}$)	$\mathrm{J\,m^{-2}\,K^{-1}s^{-0.5}}$
E	Expansion wave	–
E	Modulus of Elasticity	MPa
$f/$	f-number	–
f	Focal length	m
f	Frequency	Hz
f^*	Frequency of the second mode instabilities	Hz

Continued on next page

Symbol	**Description**	**Units**
f_s	Sample frequency	Hz
$\mathcal{F}$	Fourier transform	–
F_{AB}	Normalised FLDI detector signal	–
g	Scalar property	–
G	Gain	–
h	Distance of FLDI focus above surface	m
h	Enthalpy	$\mathrm{J\,kg^{-1}}$
h	Impulse response for heat flux	$\mathrm{J\,m^{-2}\,K^{-1}\,s^{-1}}$
h_c	Convective heat transfer coefficient	$\mathrm{W\,m^{-2}\,K^{-1}}$
$H_{\Delta x}$	FLDI transfer function, beam separation	–
H_A	Transfer function, amplifier response	–
H_{PD}	Transfer function, photodetector response	–
H_z	FLDI transfer function, path integration	–
I	Berek compensator indicator setting	–
k	Thermal Conductivity	$\mathrm{W\,m^{-1}\,K^{-1}}$
k	Wavenumber	$\mathrm{m^{-1}}$
K	Stagnation point velocity gradient	$\mathrm{s^{-1}}$
K_{GD}	Gladstone-Dale coefficient	$\mathrm{m^3\,kg^{-1}}$
l_0	Dissipative length scale	m
L	Distance between laser and heat flux gauge	m
L	Distance from FLDI focus to extremity of nozzle flow	m
L	Length	m
L	Sanderson prism geometry	m
L_0	Integral length scale	m
$\overline{L}$	Distance from initial position	m
$\dot{m}$	Mass flow rate	$\mathrm{kg\,s^{-1}}$
m	Mass	kg
M	Mach number	–
M_{s1}	Incident shock Mach number	–
n	Refractive index	–
n_p	Number of pressure transducers	–
n_r	Number of runs	–
Nu	Nusselt number	–
P	Pressure	Pa

Continued on next page

Symbol	Description	Units
P	Force	N
P_{XX}	Autocorrelation of signal X	–
P_{XY}	Cross correlation of signals X and Y	–
Pr	Prandtl number	–
$\tilde{q}$	Time invariant heat flux	$\mathrm{Ws^{0.5}m^{-2}}$
q_{11}, q_{12}	Stress optic coefficient	$\mathrm{Pa^{-1}}$
q	Heat flux	$\mathrm{W\,m^{-2}}$
Q	Heat addition per unit volume	$\mathrm{W\,m^{-3}}$
r	Radius	m
r	Distance along R	m
R	Phase retardance	Waves
R	Radius of flat nosed body	m
R	Gas constant	$\mathrm{J\,kg^{-1}\,K^{-1}}$
Re	Reynolds number	–
R_T	Termination resistance	Ω
S	Seebeck coefficient	$\mathrm{\mu V\,{}^{\circ}C^{-1}}$
S	Sensitivity	$\mathrm{kPa\,V^{-1}}$
S	Signal	V
s	Specific entropy	$\mathrm{J\,kg^{-1}\,K^{-1}}$
T	Temperature	K, °C
T_s	Sample period	s
t	Time	s
U	Velocity	$\mathrm{m\,s^{-1}}$
U_c	Convective velocity	$\mathrm{m\,s^{-1}}$
u	Velocity	$\mathrm{m\,s^{-1}}$
V	Voltage	V
V	Volume	$\mathrm{m^3}$
W	Incident shock	–
W_R	Reflected shock	–
w	Shock speed	$\mathrm{m\,s^{-1}}$
w_0	Beam waist radius	m
X	Midspan deflection	m
X_L	Loading bar deflection	m
x	Axial distance	m
Y	Sanderson prism geometry	m

Continued on next page

Symbol	**Description**	**Units**
y	Laminar boundary layer thickness	m
z	Radial location	m
z	Distance along FLDI beam	m

Greek Symbols

Symbol	**Description**	**Units**
α	Thermal diffusivity	$\mathrm{m^2\,s^{-1}}$
α	$\left[1 + ((\gamma - 1)/2)\,M^2\right]^{-1}$	–
β	Berek compensator incident angle	°
β	$\alpha\,(\gamma - 1)\,M^2$	–
γ	Ratio of specific heats	–
δ^*	Displacement thickness	m
δ_M	Meniscus lens traverse distance	m
δ_x	FLDI beam separation	m
δ_{99}	Boundary layer thickness	m
$\Delta\varphi_A - \Delta\varphi_B$	FLDI phase difference signal	rad
θ	Entropy mode	–
θ_R	Berek compensator tilt angle	rad
θ_w	$\frac{T_w}{T_e}$	–
λ	Wavelength	nm
μ	Viscosity	Pa s
ν	Thermal conductivity power law index	–
ρ	Density	$\mathrm{kg\,m^{-3}}$
σ	Sound mode	–
σ	Divergence angle	rad
τ	Dummy integration variable	–
τ	Shear stress	Pa
ω	Vorticity mode	–
ω	Angular Frequency	$\mathrm{rad\,s^{-1}}$

Subscripts, Superscripts and Accents

Script	Description
∞	Freestream
$*$	Cell not fully formed
$*$	Referenced to nozzle throat
0	Stagnation condition
0	Initial value
$1, 2, ...$	Counter for state, material, layer
amb	Ambient condition
atm	Atmospheric condition
B	Barrel
BW	Bandwidth
c	Cutoff value
c	Window centre
cr	Critical
D	Diameter
e	Edge of boundary layer
e	Extra-ordinary ray
F	Field lens
$FLDI$	Focused laser differential interferometry
HP	High-pass filtered pressure data
i	Initial value
$isen$	Isentropic value
low	Low frequency cutoff
max	Maximum value
min	Minimum Value
M	Meniscus lens
o	Ordinary ray
p	Piston
p	Pre-flow data
pt	Pitot
R	Reflected
R	Reservoir
ref	Reference value
$rise$	Rise
RP	Raw pressure data

Continued on next page

Script	**Description**
$s1$	Stage 1
$s2$	Stage 2
T	Transmitted
TC	Thermocouple
u	Unit value
v	Valve
w	Wall value
x	Distance along model
$'$	Fluctuation
$\bar{}$	Average
$\tilde{}$	Time invariant
$\langle\ \rangle$	Root-mean-square

Chapter 1

Introduction

Contents

1.1 Background and Motivation

The University of Southern Queensland's hypersonic Ludwieg tube facility with free piston compression heating, known as TUSQ, produces quasi-steady cold flows of Mach 6 air for durations of approximately 200 ms. These relatively long flow durations facilitate fundamental investigation of: hypersonic mixing, aerodynamics, boundary layer flows, fluid-structure interactions, heat transfer, scramjet inlet starting, and the analysis of flight vehicles and related geometries.

Conventional hypersonic ground testing facilities, such as TUSQ, suffer from high levels of freestream fluctuations which are typically one-to-two orders of magnitude greater than in flight. The elevated freestream fluctuations can have a significant impact on the results of ground test experiments, such as moving the laminar-turbulent transition location forward on a body, and exciting the natural frequencies of structures. Uncertainties in transition prediction lead directly to uncertainties in the estimation of essential hypersonic vehicle design parameters such as viscous drag and the surface heat flux, and these uncertainties have a significant impact on the weight of a flight vehicle (Wendt, 1997). Therefore, the flow quality, including the freestream fluctuations, must be well understood so that experiments in ground testing facilities can be correctly interpreted, as evidenced by the considerable worldwide effort to characterise hypersonic tunnel noise (Wagner et al., 2018).

By improving the understanding of the TUSQ freestream flow environment, the value of the experimental data obtained in the TUSQ facility can be maximised. Accurate measurement of the flow properties enhances the research quality and output of the USQ hypersonics research group, facilitating more accurate and reliable contributions to hypersonics research.

A previous effort was made to quantify the temperature variations in TUSQ (Widodo, 2012), who recommended that additional fast response heat flux data be obtained in TUSQ, and that the relatively low bandwidth stagnation point heat flux probe used in that work be further developed in order to resolve stagnation temperature fluctuations due to turbulent mixing in the barrel.

The freestream acoustic disturbance environment in hypersonic wind tunnel testing has the potential to have a significant impact on boundary layer stability and transition to turbulence, and can influence the results of fluid-structure interaction studies. This acoustic disturbance environment is commonly inferred from the measurement of Pitot pressure fluctuations, and having this data allows the comparison of results obtained in different facilities. However Pitot pressure measurements are an intrusive measurement and the results are sensitive to probe forebody geometry.

An alternative to the intrusive diagnostic methods is focused laser differential interferometry (FLDI), which has been used to measure the freestream density fluctuations in a reflected shock tunnel (Parziale, Shepherd & Hornung, 2012) and intermittent blowdown facilities (Fulghum, 2014). The FLDI technique is free from the complexity of inferring freestream properties from measurements behind a normal shock, and is capable of a very high frequency response ($> 10\,\mathrm{MHz}$).

1.2 Objectives

The characterisation of the freestream flow in TUSQ will significantly improve the value of the experimental data obtained in the facility. The primary objectives of this research are to:

1. measure the time-averaged and fluctuating components of Pitot pressure and use these results to compare the quality of the TUSQ flow to other hypersonic ground testing facilities;
2. determine the time-averaged and fluctuating components of stagnation temperature;
3. measure the freestream density fluctuations using focused laser differential interferometry;
4. relate the results of objectives 1 to 3 to flow features which originate in the barrel and the nozzle; and
5. provide experimental data that can be used for the validation of numerical simulations of the facility, and for the inflow conditions for numerical studies of models tested in TUSQ.

1.3 Thesis Overview

Including this introductory chapter, this thesis contains eleven chapters which are supplemented by seven appendices.

Chapter 2 is a review of the literature which establishes the need for, and challenges of, hypersonic ground testing, and specifically Ludwieg tube facilities. The freestream disturbance environment in conventional hypersonic ground testing facilities is different from that of flight testing, and for complete and reliable experimentation in ground testing facilities the mean and fluctuating components of the hypersonic flow must be well understood. The characteristics of the freestream disturbance environment are reviewed, and the effects of these disturbances on flow phenomena discussed. The flow diagnostics used in this research to quantify the disturbance environment of TUSQ are also reviewed.

Chapter 3 is a description of the Mach 6 free piston compression Ludwieg tube facility (TUSQ) at the University of Southern Queensland. The geometry of the facility and Mach 6 nozzle, and the properties of the data acquisition system used in this research are stated. Facility operation is discussed with reference to the most critical quantitative facility diagnostic, the pressure in the barrel. A previous research effort to measure the stagnation temperature variations in TUSQ is reviewed.

Chapter 4 describes a steady state simulation of the Mach 6 nozzle and an analysis of the piston compression process in TUSQ using a quasi one dimensional solver.

Chapter 5 is an analysis of the barrel pressure, Pitot pressure and Mach number. Mean and fluctuating pressures are presented and analysed. The Pitot pressure fluctuations are analysed using: (1) a traditional root-mean-square method; and (2) a power spectral density (PSD) method to analyse the frequency content of the fluctuations. The identified Pitot pressure fluctuations are compared to other facilities where similar measurements have been published.

Chapter 6 details the design, manufacture and construction of the coaxial surface junction thermocouples which are the measuring elements for the heat flux gauges used in Chapter 7 and Chapter 8. The microsecond response time coaxial surface junction thermocouples are calibrated using a reflected shock technique. The calibration method and the results of the calibration are presented.

In **Chapter 7**, the time-averaged and fluctuating components of total temperature are calculated from heat flux measurements using the surface junction thermocouples. To calculate the total temperature, the convective heat transfer coefficient is required. The convective heat transfer coefficient was identified experimentally and compared to a theoretical heat transfer coefficient value.

Chapter 8 takes a detour away from the cold flow of TUSQ, to the high enthalpy flow of a plasma wind tunnel. Type K thermocouples of similar construction to the type E thermocouples used in Chapters 6 and 7 were the sensing element for a heat flux gauge embedded in a 50 mm diameter ESA (European Space Agency) standard flat faced probe, demonstrating that the instrumentation developed for the measurement of fluctuations in the TUSQ flow can be applied, albeit in a modified form, to the investigation of flow quality in other types of high-speed facilities. This heat flux gauge was used to measure the heat flux distribution for one condition of Plasmawindkanal 4 (PWK4) at the Institut für Raumfahrtsysteme (IRS, Institute of Space Systems) within the University of Stuttgart, Germany. Mean and fluctuating components of heat flux up to 1 kHz were spatially resolved.

Chapter 9 details the design of a focused laser differential interferometer built for the purposes of this research. Custom, adjustable Wollaston-like prisms, hereafter referred to as Sanderson prisms, were designed and manufactured for the interferometer. Using these prisms introduces a phase delay which was compensated for using a Berek compensator. The calibration of the Sanderson prisms and Berek compensator are included in this chapter.

In **Chapter 10**, the focused laser differential interferometer is used to measure the density fluctuations in the TUSQ freestream. A von Kármán spectrum model is used to identify turbulent length scales of the density fluctuations. The boundary layer on a conical-nosed cylinder model is also investigated, with the interferometer resolving 2^{nd} mode instabilities in the transitional boundary layer.

Chapter 11 is the concluding chapter of the thesis, where the findings of the research are summarised and recommendations for future work are made.

The **Appendices** contain important detail that is supplementary to the body of the thesis, such as engineering drawings and calculations.

Chapter 2

Literature Review

Contents

2.1 Hypersonic Ground Testing

Ground testing of materials, structures, components and flight hardware is of critical importance in the development of systems and technology for hypersonic vehicles (Leslie & Marren, 2009). However, no single ground test facility can simultaneously fully simulate the flow duration, flow velocity, gas chemistry effects, Mach number, Reynolds number, surface temperature, ablation effects, nor the quality of the freestream (Leslie & Marren, 2009). Computational techniques, optimised for specific tasks, are used to develop vehicles, however the results of the computations require experimental validation over a representative range of operating parameters (Birch, Prince, Ludlow & Qin, 2001; Hirsch, 2007; Maicke, Barber & Majdalani, 2010). Because of the challenges of replicating a true flight hypersonic flow in ground testing, experimentation is performed in many classes and types of ground test facilities (Lu & Marren, 2002). The flow duration and enthalpy simulation capabilities of a selection of ground testing facilities is illustrated in Fig. 2.1.

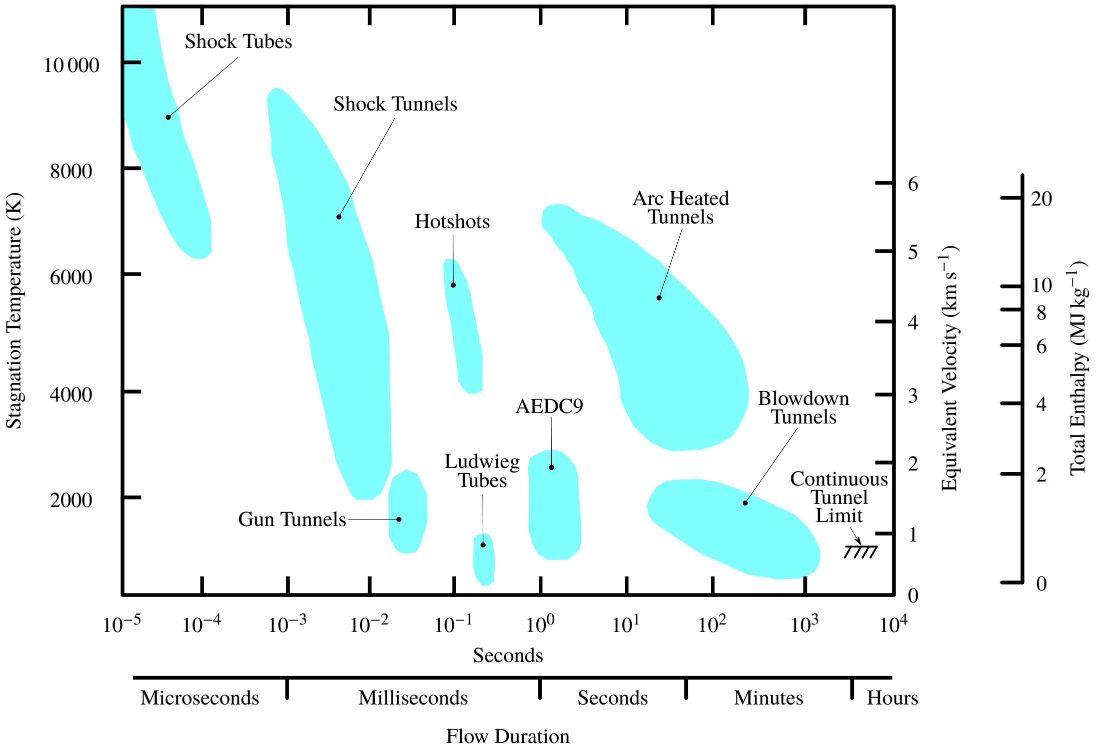

Figure 2.1: Comparison of the capabilities of different test facilities. Adapted from Smith, Felderman, Shope and Balboni (2002).

The USQ hypersonic Ludwieg tunnel facility (TUSQ) with free piston compression heating (Buttsworth, 2010), which is described in detail in Chapter 3, has a nominal test time and stagnation temperature of 200 ms and 550 K respectively. The free piston compression heating process is unlike most Ludwieg tube facilities, such as BAM6QT[*] , AFRL[†], HLB[‡] and GALCIT[§] which electrically heat the test gas prior to a run. Despite the different methods for heating the test gas, the performance of TUSQ is consistent with the Ludwieg tube class of facility shown in Fig. 2.1. Ludwieg tubes, including TUSQ, have been used for the study of hypersonic mixing, aerodynamics (Currao, Neely, Buttsworth & Choudhury, 2016; Kennell, Neely, Buttsworth, Choudhury & Tahtali, 2016; Stern, Buttsworth, Birch & Choudhury, 2018), boundary layers (Casper et al., 2016), heat transfer (Kraetzig, Buttsworth, Zander & Löhle, 2015; Vennik, Neely, Tuttle, Choudhury & Buttsworth, 2017) and scramjet inlet starting (Buttsworth & Smart, 2010).

---

[*] Boeing/AFOSR Mach 6 Quiet Tunnel at Purdue University (Schneider, 2008)

[†] Air Force Research Laboratory Ludwieg Tube (Kimmel et al., 2017)

[‡] Hypersonic Ludwieg Tube at the Technische Universität Braunschweig (Estorf, Wolf & Radespiel, 2005)

[§] California Institute of Technology Ludwieg Tube (Eremenko, Mouton & Hornung, 2003)

2.2 Freestream Disturbances in Hypersonic Ground Test Facilities

Conventional hypersonic ground testing facilities suffer from high levels of freestream fluctuations, and these fluctuations are typically one-to-two orders of magnitude greater than flight levels (Schneider, 2008).

Kovásznay (1953) used first order small perturbation theory to manipulate the Navier-Stokes equations and show that compressible turbulence can be decomposed into three quasi-independent fluctuating modes:

1. vorticity (ω), the turbulent velocity fluctuations arising from the variation of the rotational component of the velocity field;
2. entropy (θ), the isobaric variation of entropy, density and temperature, which is also referred to in literature as the entropy spottiness or temperature spottiness mode; and
3. sound (σ), the isentropic variation of pressure, density, temperature and the coupled irrotational field, which is also known as the acoustic mode.

In supersonic and hypersonic wind tunnels the vorticity and entropy modes are convected along streamlines (Laufer, 1954) and may be related to the conditions in the settling chamber (Masutti, Spinosa, Chazot & Carbonaro, 2012), while the acoustic mode can propagate across the streamlines (Weiss, 2002) along a path close to the Mach angle. In conventional supersonic facilities, vorticity and entropy modes can be minimised through careful design of the settling chamber (Morkovin, 1959). Laufer (1961) showed that the acoustic mode fluctuations from the turbulent boundary layer on the nozzle wall are largely dominant, and the magnitude of the acoustic noise increases with the fourth power of Mach number.

The modal analysis using a hot wire anemometer (Kovásznay, 1953) was further developed by Logan (1988) to include measurements from a Pitot probe and this is known as combined modal decomposition. The combined modal decomposition has been used to determine the contributions of each mode to the freestream disturbance environment of hypersonic Ludwieg tubes (Ali, Wu, Radespiel, Schilden & Schroeder, 2014; Schilden et al., 2016) and blowdown facilities (Masutti et al., 2012). For the combined modal analysis, the logarithmic derivative of the mass flow, total temperature and the equation of state are (Schilden et al., 2016):

$$\frac{m'}{m} = \frac{\rho'}{\rho} + \frac{u'}{u} \tag{2.1}$$

$$\frac{T_0'}{T_0} = \alpha\frac{T'}{T} + \beta\frac{u'}{u} \tag{2.2}$$

$$\frac{P'}{P} = \frac{\rho'}{\rho} + \frac{T'}{T} \tag{2.3}$$

where m, ρ, u, T and P are mass, density, velocity, temperature and pressure respectively, and primes refer to the fluctuating component and subscript 0 indicates the stagnation condition. The coefficients α and β in Eq. 2.1–2.3 are given by $\alpha = \left[1 + \left(\left(\gamma - 1\right)/2\right) M^2\right]^{-1}$ and $\beta = \alpha\left(\gamma - 1\right) M^2$, where M is the Mach number and γ is the ratio of specific heats. Logan (1988) reformulates Eq. 2.1 – 2.3 to determine the relations for the three modes of fluctuation as:

$$\omega' = \frac{u'}{\overline{u}} + \frac{1}{\gamma M^2}\frac{P'}{\overline{P}} \tag{2.4}$$

$$\theta' = \frac{T'}{\overline{T}_0} - \frac{\gamma - 1}{\gamma}\frac{\overline{T}}{\overline{T}_0}\frac{P'}{\overline{P}} \tag{2.5}$$

$$\sigma' = \left(1 - \frac{1}{M^2}\right)\frac{P'}{\gamma\overline{P}} \tag{2.6}$$

Each mode of disturbance has multiple sources as illustrated in Fig. 2.2, but it must be noted that this graphic is not exhaustive; other disturbance sources are known to exist, such as imperfections of a surface at joints (Schneider, 2008).

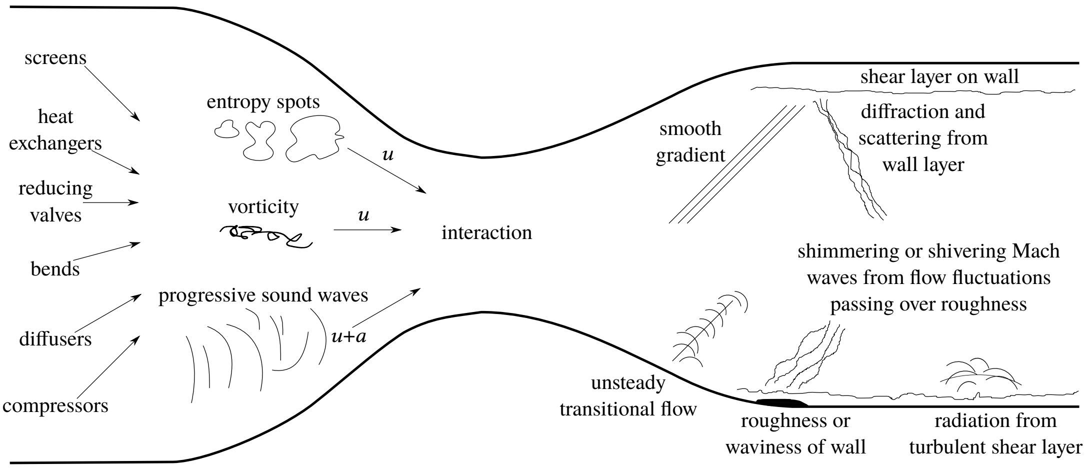

Figure 2.2: Freestream disturbances in supersonic wind tunnels. Adapted from Schneider (2008).

In hypersonic ground testing facilities, the turbulent boundary layer that grows on the nozzle wall is widely acknowledged as the dominant source of acoustic mode disturbances (Blanchard, Lachowicz & Wilkinson, 1997; Casper et al., 2016; Schneider, 2008). The acoustic disturbances can be split into two distinct types; eddy Mach waves and shivering Mach waves. Eddy Mach waves are radiated across the freestream and are generated by the turbulent boundary layer of the nozzle wall. Examining the top surface of the cone in Fig. 2.3 where the boundary layer is intermittently turbulent, it is visible that acoustic noise is not present above the laminar regions (Schneider, 2008). Shivering Mach waves are caused by diffraction, scattering and reflection of steady pressure gradients by the wall boundary layer (Weiss, Knauss & Wagner, 2003) and are also illustrated on Fig. 2.2. These pressure gradients are caused by nozzle imperfections or surface irregularities and can be minimised by careful manufacture and maintenance.

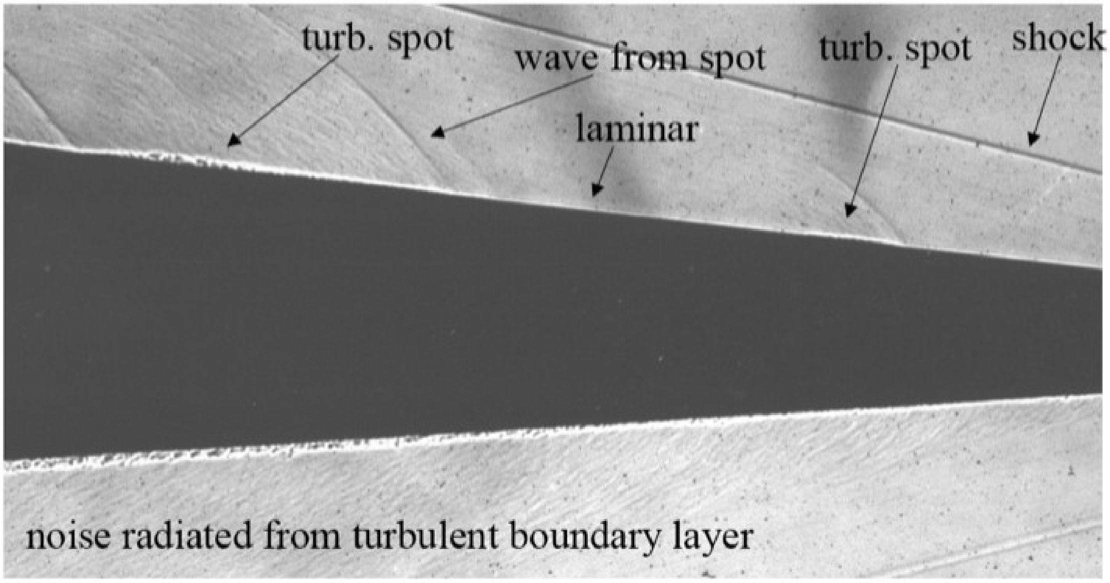

Figure 2.3: Shadowgraph of transition on a sharp cone at Mach 4.31 (Reda, 1979).

The effects of tunnel noise are most evident in laminar-turbulent transition studies (Laufer, 1954; Morkovin, 1957), where transition occurs earlier than in flight (Schneider, 2001). Quiet tunnels for transition research have been developed (Beckwith, 1975; Schneider, 2008), however they are uncommon. These quiet facilities can be costly to maintain because they must operate with a laminar boundary layer on the nozzle wall. Consequently, most laminar to turbulent transition research is still conducted in conventional tunnels (Casper et al., 2009) where the boundary layer on the nozzle wall is turbulent, and therefore an understanding of the noise environment is required to assess the impact of tunnel noise on the experimental results.

During boundary layer transition, the pressure fluctuations are higher than for a fully turbulent boundary layer (Casper et al., 2018), and the rate of heat transfer towards the end of transition can exceed the fully turbulent case (Casper et al., 2018; Grossir, Masutti & Chazot, 2015; Pate, 1978). Because transition occurs earlier in ground testing than in flight due to the increased noise environment, the results of conventional tunnel testing represent a worse-case Reynolds number from a skin friction and vehicle heating perspective as the tunnel noise appears to only move the transition point forward (Schneider, 2001).

Ito, Randall and Schneider (2001) investigated the effect of tunnel noise on roughness induced boundary layer transition for a scramjet inlet and found that freestream noise affected the onset of transition on rough and smooth models. The boundary layer was fully turbulent under noisy flow conditions earlier than under quiet inflow conditions. This early onset transition led Ito et al. (2001) to state that conventional tunnel tests for boundary layer transition should be interpreted with care. However, natural transition may not occur at the Reynolds numbers achievable in quiet facilities (Ito et al., 2001), and therefore tripping elements have been used to study effects such as scramjet inlet unstart. This tripping emulates the inflow from a conventional noisy wind tunnel (Ito et al., 2001).

Broadband fluctuations from freestream noise in wind tunnels are known to excite the natural frequencies of structures and generate much higher amplitude responses than experimentation in quiet flow conditions, such as BAM6QT, where only high frequency second mode waves at around 200 kHz are observed (Casper et al., 2018). By using a flow perturber to simulate turbulent spots, a structure can be strongly excited when the perturbation frequency matches a structural mode (Casper et al., 2018). Relative to the unperturbed values, the panel structure response magnitude was amplified by one order of magnitude for noisy flows but it was amplified by two orders of magnitude under quiet freestream conditions. Therefore, it is important to characterise both the magnitude and frequency content of tunnel noise for fluid-structure interaction studies.

Total temperature fluctuations are entropy mode disturbances (Heitmann et al., 2008; Masutti et al., 2012), and these disturbances were theoretically shown to generate intense acoustic waves behind an oblique shock (McKenzie & Westphal, 1968). A numerical study of the receptivity of supersonic boundary layers on flat plates by Ma and Zhong (2005) showed that the interaction of the oblique shock and freestream entropy waves play an important role in boundary layer receptivity. When the entropy mode disturbances interact with an oblique shock, fast acoustic waves are generated behind the shock, and this led to Ma and Zhong (2005) stating that the mechanisms of receptivity to freestream entropy waves are very similar to those of the receptivity to freestream acoustic waves.

2.3 Measurement of Hypersonic Flows and Instabilities

2.3.1 Pitot Pressure

The flow quality produced from a converging-diverging nozzle is traditionally inferred from Pitot pressure surveys (Panda & Seasholtz, 2002; Paull & Stalker, 1992), and Pitot pressure surveys are also a popular diagnostic for quantification of tunnel noise in supersonic and hypersonic test facilities (Ali et al., 2014; Beckwith, 1975; Casper et al., 2009; Grossir et al., 2015; Lafferty & Norris, 2007; Wagner et al., 2018). A pressure transducer flush mounted to the tip of a Pitot probe is the most direct measurement of freestream acoustic fluctuations in a hypersonic flow field (Lafferty & Norris, 2007). The noise level in conventional hypersonic test facilities is defined as the root-mean-square (RMS) Pitot pressure divided by the mean Pitot pressure, and is typically about 1 % but can sometimes be as high as 2 – 5 % (Casper et al., 2009).

To identify the root-mean-square fluctuation, the fluctuating component of a signal must be identified, and this is often done by a Reynolds decomposition. A scalar property g, such as Pitot pressure or stagnation temperature, can be decomposed as

$$g = \overline{g} + g' \tag{2.7}$$

where the time-averaged component is

$$\overline{g} = \frac{1}{\tau} \int_0^{\tau} g(t)\, \mathrm{d}t \tag{2.8}$$

and the time-average of the fluctuating component is

$$\overline{g'} = \frac{1}{\tau} \int_0^{\tau} g'(t)\, \mathrm{d}t = 0 \tag{2.9}$$

The Reynolds decomposition is illustrated in Fig. 2.4 assuming (a) steady and (b) unsteady mean motion. For a steady flow $\overline{g}$ is simply the average of all samples, but for an unsteady flow $\overline{g}$ can be found by low-pass filtering g at an appropriate cutoff frequency.

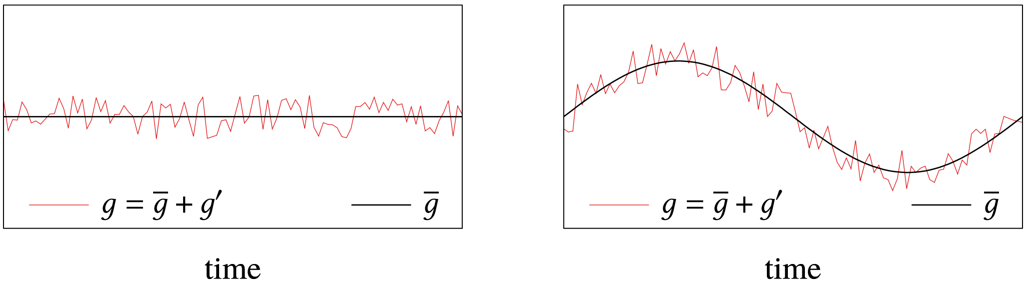

(a) Steady (b) Unsteady

Figure 2.4: Reynolds decomposition of steady and unsteady mean signals.

Lafferty and Norris (2007) isolated the time-averaged and fluctuating components of Pitot pressure measurements in a blowdown facility (AEDC9) using a 6th order Butterworth digital low-pass filter with a 120 Hz cutoff frequency (f_c). Because the time-averaged flow is different across facilities and run conditions, $f_c = 120$ Hz may not be appropriate for post-processing of data in other facilities.

Expressing the tunnel noise as a RMS Pitot pressure fluctuation provides a result that is independent of the signal length and sampling frequency, assuming the signal RMS is invariant and sufficiently oversampled with respect to the Nyquist criterion (Wagner et al., 2018). However, for results to be valid, the method needs to be applied only in frequency bands that avoid transducer or amplification resonances.

Welch's power spectral density (PSD) estimate is an alternative method that can provide information about the amplitude of measured fluctuations at individual frequencies which has been widely used for the analysis of Pitot pressure fluctuations (Ali et al., 2014; Bounitch, Lewis & Lafferty, 2011; Casper et al., 2016; Greenwood, 2014; Mai, 2014; Wagner et al., 2018). Window functions are used to modify the level of a PSD computed using Welch's method to alleviate the effects of spectral leakage. The suitability of different window functions and sizes is known to be a function of the frequency content of the signal (Harris, 1978). The parameters used to compute a PSD using Welch's method are summarised in Table 2.1 for six of the literature items identified. Wagner et al. (2018) did not state the parameters used, so this work is not included in Table 2.1.

The root-mean-square for a PSD is calculated for a bandwidth of interest, where the lower frequency bound is analogous to the low-pass filter cutoff frequency used for the traditional type RMS analysis, and the high frequency cutoff is often dictated by the maximum

Reference	Window type	Frequency resolution (Hz)	Overlap	DFT points
Ali et al. (2014)	Blackman-Harris	488	75 %	–
Bounitch et al. (2011)	Hamming	1000	1 point	2^{11}
Casper et al. (2009)	Blackman	2440	25 %	–
Greenwood (2014)	Blackman	1250	50 %	2^{15}
Mai (2014)	Hamming	977	50 %	–
Masutti et al. (2012)	–	–	25 %	2^{16}

Table 2.1: Examples of parameters used for calculation of a PSD of Pitot pressure data using Welch's method.

bandwidth of the pressure transducer used. The definition of the lower frequency cutoff (f_{low}) varies significantly. Lafferty and Norris (2007) used f_{low} = 120 Hz for consistency with their traditional RMS analysis. Other researchers set f_{low} by making assumptions about the flow. Wagner et al. (2018) used f_{low} = 1 kHz, justifying this by assuming disturbances of less than 1 kHz were not of relevance to the boundary layer transition process; Ali et al. (2014) justified f_{low} = 3 kHz by considering the maximum scale of structures carrying flow distortions. For one of the sensors used by Ali et al. (2014), the minimum resolvable frequency fluctuations were 11 kHz, and therefore this limitation set f_{low}. Because the low frequency content dominates the RMS of a signal (Wagner et al., 2018), increasing f_{low} can result in a significant reduction of the amplitude of the calculated RMS fluctuation.

If the bandwidth of the Pitot pressure fluctuations is sufficiently high, the $-7/3$ roll-off for the decay of pressure fluctuations predicted by Kolmogorov's 1941 theory of small-scale turbulence can be identified. Masutti et al. (2012) attempted to identify the inertial subrange and to determine turbulence length scales, and found a nominally flat spectra up to about 30 kHz. For $f = 30-42$ kHz, the pressure spectra roll-off was $-15/3$ and for $f > 42$ kHz the roll-off was $-25/3$, and these rates of pressure fluctuation decay are significantly more rapid than predicted by Kolmogorov's theory. This may have been because the Pitot pressure transducers used by Masutti et al. (2012) were a Kulite B-screen variant which have a dynamic frequency up to 25 kHz (Bounitch et al., 2011). Bounitch et al. (2011) improved the Pitot pressure fluctuation measurements at AEDC9 using pressure sensors with improved frequency response ($f \approx 1$ MHz). The roll-off of this Pitot pressure data was later reported to be approximately -3.5 (Duan et al., 2019).

Despite the popularity of Pitot probe pressure measurements for flow characterisation, the probe geometry is not standardised in shape, nor in size (Wagner et al., 2018). Pitot probes must be flush mounted facing into the flow which leaves the transducer vulnerable to excessive thermal loading and particulate impact. Protective cavities and screens have been used to protect the sensing element of the pressure transducer (Casper et al., 2016; Masutti et al., 2012), but these can introduce damping and resonance effects (Wagner et al., 2018) which limits the useful bandwidth of the measurements. Chaudhry and Candler (2016) used a direct numerical simulation (DNS) method to investigate the flow around a variety of Pitot probe geometries that appear in literature (Bounitch et al., 2011; Masutti et al., 2012; Steen, 2010), and the cone probe design of Ali et al. (2014). The investigation compared the pressure spectrum behind the shock which would be measured by the pressure transducer to the forced entropy and acoustic freestream disturbances, and the ratio of these results was used to define the transfer function. The transfer function was found to be a strong function of the probe geometry and shock standoff distance, and this probe geometry dependence can make direct comparison of results obtained using different probes difficult.

Conical probes (Ali et al., 2014) and wedge probes (Wagner et al., 2018) have been developed for the measurement of the freestream disturbance environment. These probes avoid the complexities associated with the subsonic flow field and complex amplification and attenuation of tunnel disturbances which can occur behind strong shocks ahead of blunt bodies. Wagner et al. (2018) developed a wedge probe design to measure the static pressure fluctuations in flow fields which cannot be accessed by means of Pitot probes or hot wire techniques, and converted the static pressure fluctuations to effective Pitot pressure fluctuations using the unsteady analysis of Stainback and Wagner (1972). The unsteady approach of Stainback and Wagner (1972) effectively produces a transfer function that is independent of frequency and Pitot probe geometry (Duan et al., 2019), however Wagner et al. (2018) found good agreement between the wedge probe and complementary Pitot probe measurements. An increase of unit Reynolds number has a stabilising effect on the flow (Masutti et al., 2012) and this stabilising effect has the effect of reducing the normalised Pitot pressure fluctuations. The Reynolds number stabilising effect was found to be more significant for the Pitot pressure measurements of Wagner et al. (2018) than the wedge probe measurements, but this was probably caused by damping mechanisms, such as cavities, inherent in the Pitot pressure measurements.

2.3.2 Stagnation Temperature

Stagnation temperature is a crucial parameter in most hypersonic flow experiments (Widodo & Buttsworth, 2013), but due to the impulsive loading and short test times it can be a difficult parameter to measure (Widodo, 2012). Isentropic flow relations have been used to estimate the flow static temperature from the measured barrel pressure in TUSQ. This approximation was made by Currao et al. (2016) for the purposes of numerically investigating experimental data obtained in TUSQ for an oscillating plate fluid-structure interaction experiment. However, Widodo and Buttsworth (2013) have previously identified a reduction of the time-averaged stagnation temperature from $T_0 \approx 560\,\mathrm{K}$ to $T_0 \approx 520\,\mathrm{K}$ over the first 150 ms of nozzle flow for a condition similar to that used by Currao et al. (2016). Although Currao et al. (2016) found good agreement between the experimental and numerical data, the reduction of total temperature over the flow time in TUSQ may be non-negligible for other experiments, such as studies of heat transfer.

Mack (1986, 1987) found that, at the same Mach and Reynolds numbers, increasing T_0 from 512 K to 728 K resulted in a marked stabilisation of the boundary layer on sharp adiabatic cones. This stagnation temperature stabilisation effect was also observed by Kimmel and Poggie (2000) for $T_0 = 472\,\mathrm{K}$ and $T_0 = 583\,\mathrm{K}$ who investigated the growth of the second mode instability. This was in opposition to earlier work by Ross (1973) who reported that at $T_0 = 295\,\mathrm{K}$ and $T_0 = 434\,\mathrm{K}$, the stagnation temperature did not seem to be important for boundary layer transition. However, the results of Ross (1973) are somewhat difficult to interpret since the unit Reynolds number was not held constant as the stagnation temperature was changed (Kimmel & Poggie, 2000).

Fluctuations of stagnation temperature have been sparsely determined for the quantification of test section flows in supersonic and hypersonic ground test facilities (Heitmann et al., 2008), and there have been few studies of stagnation temperature fluctuations in the decade since. Hot wire anemometry (HWA) is the most common technique for the identification of total temperature fluctuations, however the wire is also sensitive to mass flux fluctuations. Early work by Stainback and Wagner (1972) recognised the difficulty of separating the desired flow variables with the quasi-steady approach of HWA data reduction, and this difficulty was alleviated using different wire-heating strategies (Smith & Smits, 1993; Smits, Hayakawa & Muck, 1983). Hot wire anemometers are prone to wire breakage (Casper et al., 2009; Parziale, Shepherd & Hornung, 2014; Settles & Fulghum, 2016), and this is especially true for flows with high dynamic pressures and/or impulsive starting/terminating properties. Consequently, much of the literature for freestream flow characterisation using HWA are limited to continuous or intermittent flows in blowdown type facilities (Ali et al., 2014; Blanchard et al., 1997; Kovásznay, 1953; Laufer, 1961; Masutti et al., 2012) where the loading of the hot wire is not impulsive. Since hot wire anemometry is unsuitable for impulsive flows, experimental determination of the three disturbance modes via modal analysis cannot be performed in these flow fields (Weiss et al., 2003). More rugged intrusive, or non-intrusive, diagnostics techniques are required for measurements of temperature fluctuations in tunnels with impulsive loading and/or high dynamic pressure. In place of a full modal analysis, measurements of the fluctuations of fundamental flow properties such as stagnation temperature and Pitot pressure are used to characterise the flow quality.

Atomic layer thermopile (ALTP) sensors have a time constant 2 – 3 orders smaller than hot wires which enables their use for up to 1 MHz (Heitmann et al., 2008). ALTPs have been used to measure boundary layer fluctuations of heat flux on sharp cones (Ali et al., 2014; Heitmann et al., 2008; Roediger, Knauss, Smorodsky, Estorf & Schneider, 2009). ALTP sensors were integrated in the wedge probe of Wagner et al. (2018) who report a good SNR, but did not present the data obtained because the sensitivity of the ALTP is subject to strong uncertainties. Wagner et al. (2018) also tested thin film and coaxial surface junction thermocouples in the wedge probe without success, claiming that thin film gauges and thermocouples provide a very low SNR in cold flows making application in Ludwieg tube facilities "pointless". However, Widodo (2012) measured fluctuations of stagnation heat flux on a 3 mm diameter hemisphere probe using a platinum thin film gauge in TUSQ. The same geometry probe head was used by Buttsworth and Jones (2003) to measure the fluctuations of heat flux in a gun tunnel facility. The low SNR issues encountered by Wagner et al. (2018) were possibly a function of the reduced heat flux that would be measured for a thin film gauge on a wedge probe when compared to measurements at the stagnation region of a small probe.

The hemispherical probe heads used by Buttsworth and Jones (2003) and Widodo (2012) introduce a complexity in that the heat flux distribution over a hemisphere cylinder is non-uniform (Kemp, Rose & Detra, 1959). Using a flat nosed cylinder probe would have allowed the thin film to be exposed to a uniformly distributed heat flux (Clutter & Smith, 1965), provided that the thin film gauge was not positioned in the corner region. Widodo (2012) noted that stagnation temperature measurements made using thin film and coaxial thermocouple methods require the assumption of a convective heat transfer coefficient, and this assumption can lead to uncertainties. The convective heat transfer coefficient is a property of the stagnation point boundary layer, and therefore a function of the probe geometry and upstream flow conditions. By repeatedly measuring the heat flux for a nominally identical flow field at a range of thin film gauge temperatures, the flow total temperature can be determined without assuming the upstream flow properties or probe geometry (Buttsworth & Jones, 1998). The same methodology can be applied to coaxial surface junction thermocouples to determine the stagnation temperature in a shock tunnel (Buttsworth & Jacobs, 1998).

Coaxial surface junction thermocouples have been used to measure the heat flux in a range of facilities with harsh flow conditions, including impulsive loading and high specific stagnation enthalpy (h_0) flows with diaphragm particles (James et al., 2019). Heat flux measurements using coaxial surface junction thermocouples have been obtained in a wide variety of wind tunnels. For example, heat flux measurements have been obtained in a blowdown facility (Marineau et al., 2013) ($h_{0,max} \approx 1\,\mathrm{MJ\,kg^{-1}}$), in shock tunnels by Agarwal, Sahoo, Irimpan, Menezes and Desai (2017) at $h_{0,max} \approx 1.4\,\mathrm{MJ\,kg^{-1}}$ and Sanderson and Sturtevant (2002) at $h_{0,max} \approx 20\,\mathrm{MJ\,kg^{-1}}$, and in an expansion tunnel at up to $h_{0,max} \approx 63\,\mathrm{MJ\,kg^{-1}}$ by James et al. (2019). The successful measurements of heat flux in such harsh flow conditions shows the rugged and versatile nature of the coaxial surface junction thermocouple design, with James et al. (2019) reporting the lifetime for a single thermocouple being hundreds of shots.

A coaxial surface junction thermocouple consists of an annular component and a pin, separated by an electrically insulating layer such as an epoxy (Agarwal et al., 2017; Marineau et al., 2013; Mohammed, Salleh & Yusoff, 2009; Sanderson & Sturtevant, 2002) or an oxide coating (James et al., 2019). The surface of the thermocouple is scratched to form junctions using different methods, commonly using abrasive paper of different grit size or a scalpel blade. The thinner the surface junction, the faster the response time of the thermocouple (Sanderson & Sturtevant, 2002). The method of creating the surface junction is known to influence the effective thermophysical properties of the gauge (Buttsworth, 2001; Mohammed et al., 2009), and therefore individual thermocouple calibration is preferred.

When an epoxy layer is used to bond and electrically insulate the two thermocouple materials, the epoxy layer limits the maximum operating temperature of the thermocouple. For example, Mohammed et al. (2009) used Araldite which has a maximum operating temperature of 80 °C. Agarwal et al. (2017), Marineau et al. (2013), Sanderson and Sturtevant (2002) did not report the type of epoxy used, nor the operating temperature range of the epoxy.

If the heat transfer coefficient is known for a stagnation point heat transfer gauge, the flow total temperature can be determined (Buttsworth & Jones, 2003). The stagnation point heat transfer coefficient can be estimated analytically, or determined experimentally by operating the heat transfer gauge over a range of surface temperatures (Buttsworth & Jones, 2003). For the experimental determination of the heat transfer coefficient, operating temperatures as close as possible to the flow total temperature should be used. The stagnation temperature of TUSQ (nominally 560 K) is well above the maximum operating temperature of epoxies such as Araldite (80 °C), and therefore this method of bonding and insulation is unsuitable for the level of preheating required for experimentation in TUSQ.

2.3.3 Focused Laser Differential Interferometry

Focused laser differential interferometry (FLDI) is an optical diagnostic used to analyse density fluctuations. This diagnostic is classified as non-intrusive as it does not interfere with the flow. The non-imaging, common path interferometer was first developed by Smeets (1972) to measure density fluctuations in wind tunnel flows and turbulent jets in desktop-type experiments. The technique was further developed during the 1970's (Smeets, 1977; Smeets & George, 1973) with numerous iterations of two beam laser differential interferometers proposed. Unfortunately these designs were discussed in terms of their function and applicability without any detailed optical analysis due to the limitations of photodetectors, data acquisition systems and the unavailability of suitable lasers at the time (Schmidt & Shepherd, 2015). Discussion of FLDI is apparently absent from literature from 1977 until 2012 when Parziale et al. (2012) successfully implemented the technique to measure the disturbance levels in the freestream of T5 at the California Institute of Technology.

Despite the limited application of FLDI in literature, Schmidt and Shepherd (2015) describe FLDI as a very attractive instrument for measuring second mode (Mack) waves in hypersonic boundary layers. FLDI is suitable because of its high frequency response (>10 MHz) which is limited only by the photodetector (Kegerise & Rufer, 2016), streamwise spatial resolution of the order of hundreds of microns and its high SNR. FLDI has a wavenumber dependent spatial resolution in the order of tens of millimetres in the spanwise direction (Fulghum, 2014; Parziale, Shepherd & Hornung, 2013; Schmidt & Shepherd, 2015).

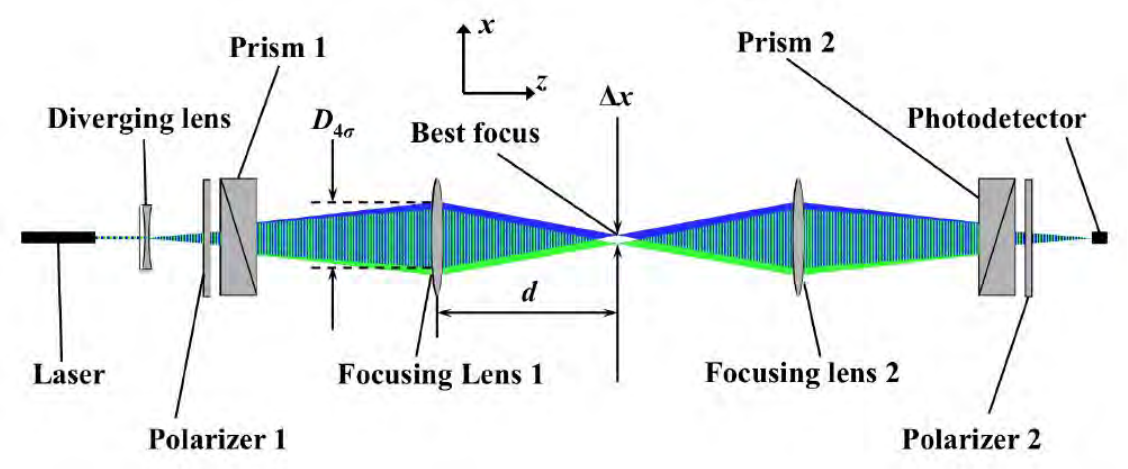

Figure 2.5: FLDI Schematic (Schmidt & Shepherd, 2015)

A general schematic of a modern FLDI layout, as presented by Schmidt and Shepherd (2015), is shown in Fig. 2.5. A linearly polarised laser beam is expanded, then passed through a prism placed at the focus of a converging lens. This prism has the effect of splitting the beam into two orthogonally polarised beams (shown in green and blue in Fig. 2.5) separated by a small angle (σ). The converging lens fixes the beam separation to a finite distance (Δx) and focuses the beams to a point in the test section. The system is symmetric about the focus so the beams can be recombined by means of a second polariser and the interference signal measured by a change in intensity on a photodetector (Schmidt & Shepherd, 2015). The focusing technique causes a spatial filtering effect allowing the FLDI instrument to measure low intensity density fluctuations at the focus of the instrument, even when passing through a turbulent boundary layer of higher intensity. FLDI is sensitive to phase differences between the two beams of the instrument. The phase changes are caused by fluctuations in refractive index (n) which can then be related to density (ρ) perturbations by the Gladstone-Dale relation:

$$n = K_{GD}\,\rho + 1 \tag{2.10}$$

Parziale et al. (2012) used FLDI to investigate the relationship between reservoir enthalpy and freestream density perturbations in the T5 facility. Their FLDI instrument had a beam separation of 350 µm with a minimum beam diameter less than 100 µm and was found to have a temporal resolution of 25 MHz, and spatial resolutions of 700 µm (streamwise) and 30 mm (spanwise). Later, the spanwise spatial resolution was revised down to 20 mm (Parziale et al., 2013; Parziale, 2013). Parziale et al. (2013) made quantitative measurements of the acoustic instability in a hypervelocity slender-body boundary layer on a five degree half-angle cone. It was also concluded that the noise floor is sufficiently low so that the FLDI technique can resolve the acoustic instability. Parziale et al. (2013) added to the earlier papers by describing the fundamental equations and theory. Later, Parziale et al. (2014) investigated the freestream density perturbations in the T5 reflected shock tunnel. At reservoir enthalpies of $5-18$ MJ kg^{-1} and flows of approximately Mach 5.5, no correlation was found between RMS density perturbations (5 kHz to 20 MHz) and tunnel run parameters. Spectrograms were produced to show that the intensity and spectral content of the freestream density fluctuations level are constant throughout the test time. FLDI was successfully used by Parziale, Shepherd and Hornung (2015) to measure the incipient instability waves prior to transition to turbulent flow at hypervelocity conditions on a right-circular 5 deg half angle cone at zero angle of attack in the T5 reflected-shock tunnel. The experimental frequency content was compared to linear stability computations and reasonable agreement was found between the peaks on the frequency spectrum of FLDI data and the calculated most amplified frequencies.

Schmidt and Shepherd (2015) state that the most thorough description of FLDI to date was completed by Fulghum (2014), containing derivation of system transfer functions for simple flow geometries and an analysis of the optical components. Fulghum (2014) successfully replaced Wollaston prisms with stress birefringent Sanderson prisms and implemented the use of two photodetectors. The two detectors simultaneously measure the polarisation shift due to refractive index differences between the two laser beam paths of the instrument; the S-detector measuring the polarisation component perpendicular to the laser polarisation vector, while the P-detector measures the parallel component. This method allows direct measurement of the interferometer phase and largely rejects electronic noise and stray light (Fulghum, 2014).

Fulghum (2014) demonstrated that FLDI measures turbulence spectra that are convolved with transfer functions related to the separation of the beams and their convergence angle; a relationship confirmed computationally by Schmidt and Shepherd (2015). The measured signal ($\Delta\varphi_A - \Delta\varphi_B$) is related to the density fluctuations ($\rho'(t)$) by

$$\rho'(t) = \frac{\lambda}{2\pi K_{GD}\Delta x}\mathcal{F}^{-1}\left\{\frac{\mathcal{F}\{\Delta\varphi_A - \Delta\varphi_B\}}{H_{\Delta x}(k)H_z(k)}\right\} \tag{2.11}$$

where λ is the wavelength of the laser, K_{GD} the Gladstone-Dale coefficient, Δx the beam separation, $H_{\Delta x}(k)$ the transfer function due to finite beam separation and $H_z(k)$ the transfer function due to beam width along the beam path.

Fulghum (2014) demonstrated the validity of using FLDI to measure the core flow turbulence of high speed wind tunnels, but recommended increasing the focusing ability of the instrument used.

2.4 Conclusions

The freestream disturbances present in conventional hypersonic ground test facilities can have a significant impact on the results of experiments conducted in these facilities. The elevated disturbance level in ground based facilities relative to true flight conditions results in uncertainty in the prediction of essential vehicle design parameters such as boundary layer transition, viscous drag and surface heat flux.

Significant global efforts have been made, and are continuing to be made, to characterise the freestream flow and the freestream disturbances in hypersonic flows to improve the understanding and applicability of ground based experiments, and to facilitate comparison of results obtained in different facilities. The most widely used flow diagnostic for hypersonic flow characterisation is the measurement of Pitot pressure. Where total temperature fluctuations have been reported, the measurements were commonly made using hot wire anemometry. However, because hot wires are fragile and susceptible to damage in impulsive flows, much of the data is limited to continuous and intermittent flows in blowdown type facilities. Coaxial surface junction thermocouples offer a rugged alternative to hot wire anemometry, and have been used successfully for the measurement of heat flux in high enthalpy facilities. Focused laser differential interferometry is a non-intrusive flow diagnostic that is used to measure density fluctuations for bandwidths in the order of 1 MHz, and can be used to identify length scales of turbulence.

Chapter 3

TUSQ Facility

Contents

3.1 Facility Description

The University of Southern Queensland's Ludwieg tube with free piston compression heating (TUSQ) is used to generate quasi-steady cold flows of Mach 6 hypersonic air for approximately 200 ms (Buttsworth, 2010). The facility can also be configured for other Mach numbers and in an atmospheric blowdown mode of operation, and these configurations are described by Buttsworth (2010).

An annotated schematic of the TUSQ facility is presented as Fig. 3.1a, and photographs from the high pressure reservoir (Fig. 3.1b) and test section (Fig. 3.1c) ends are also provided. The properties of the major components of the TUSQ facility are listed in Table 3.1.

Prior to firing, the facility is comprised of three discrete volumes of gas: (1) the 350

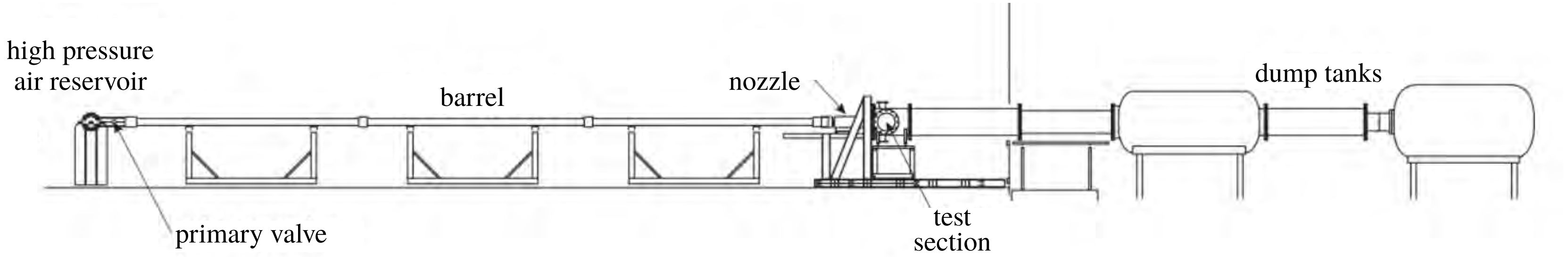

(a) Schematic of the main components of TUSQ

(b) View from high pressure air reservoir end

(c) View from the (open) test section end

Figure 3.1: Schematic arrangement and photographs of the TUSQ facility.

Component	Characteristics
HP air reservoir	$V = 350\,\mathrm{L}$
Primary valve	$\varnothing 27.6\,\mathrm{mm}$ (ball valve)
Piston	$m = 340\,\mathrm{g}$, Nylatron
Barrel	$\varnothing = 130\,\mathrm{mm}$, $L = 16\,\mathrm{m}$
Test section	$\varnothing = 600\,\mathrm{mm}$, $L = 830\,\mathrm{mm}$, $V = 0.235\,\mathrm{m}^3$
Dump tanks	$V = 12.5\,\mathrm{m}^3$

Table 3.1: Properties of the main components of the TUSQ facility.

litre high pressure air reservoir; (2) the air in the Ludwieg tube or barrel; and (3) the low pressure (<1 kPa) region within the nozzle, test section and dump tanks. A 340 g piston is positioned in the barrel immediately downstream of the primary valve and a light Mylar diaphragm separates the barrel and nozzle inlet.

For the condition analysed herein (Table 3.2) and used extensively in other recent experiments (Buttsworth, Stern & Choudhury, 2017; Currao et al., 2016; Kennell et al., 2016; Vennik et al., 2017), the test gas initially residing in the barrel is at atmospheric pressure (P_{atm}) and ambient temperature (T_{amb}). A run is initiated by opening the pneumatically actuated primary valve. This valve opening is relatively slow (>500 ms) to limit the magnitude of the piston oscillations which cause oscillations of the barrel pressure during the compression process (Jones, Schultz & Hendley, 1973). The high pressure air in the reservoir is expelled through the primary valve, and this gas forces the piston along the barrel, compressing the test gas. Compression continues until the pressure ruptures the diaphragm which is clamped at the downstream end of the barrel, 67 mm upstream of the nozzle throat. After the diaphragm rupture, the test gas is accelerated through the nozzle and into the test section. The geometry of the Mach 6 nozzle and the relative position of the barrel pressure transducer is shown schematically in Fig. 3.2.

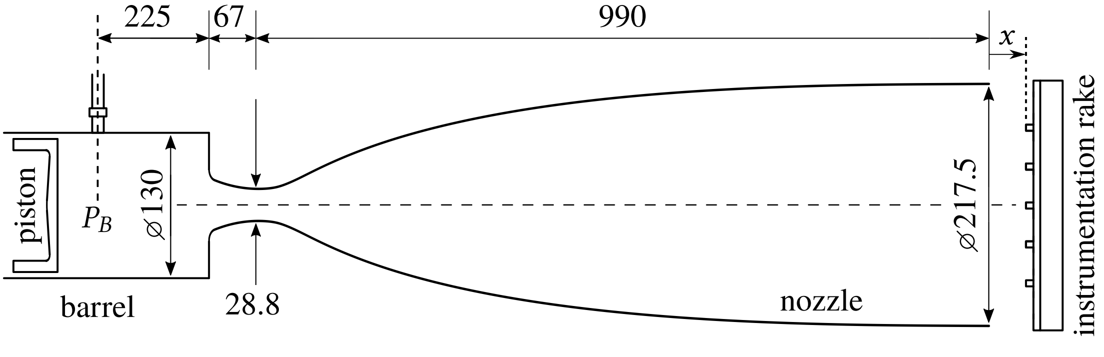

Figure 3.2: Schematic of Mach 6 nozzle and instrumentation rake position.

A test condition is primarily arranged by the selection of a suitable diaphragm. For this condition a 100 µm Mylar diaphragm was used which, when used with the Mach 6 nozzle, nominally ruptures at 1 MPa. The nominal test condition is shown in Table 3.2, where the stagnation temperature T_0 was calculated assuming isentropic compression from the initial state (P_{atm} = 94 kPa, T_{amb} = 293 K) to the nozzle reservoir pressure (P_0 = 1 MPa). In this research the Mach number of the flow was found to be M = 5.9 ± 0.05, and therefore the nozzle exit flow conditions in Table 3.2 were populated using this Mach number on the assumption of isentropic flow. All testing was conducted at the same nominal unit Reynolds number Re_u, which when referenced to the nozzle exit diameter is denoted as Re_D. Velocity is designated as u, and the subscripts ∞, 0 and pt refer to the freestream, stagnation and Pitot pressure conditions respectively.

P_0 (MPa)	T_0 (K)	P_∞ (Pa)	T_∞ (K)	M –	u_∞ ($\mathrm{m\,s^{-1}}$)	P_{pt} (kPa)	Re_u ($\mathrm{m^{-1}}$)	Re_D –
1.0	576	702	72	5.9	1006	31.8	6.94×10^6	1.51×10^6

Table 3.2: Nominal Test Conditions.

Test models and probes such as Pitot rakes are mounted on the model support block (Fig. 3.1c) at different positions relative to the nozzle exit. The instrumentation amplifiers can be mounted underneath the test block and the amplified output passed through the main flange via instrumentation flanges. Should the signal be sufficiently high such that it does not require amplification, or if the amplifiers are too large or unsuitable for operation in a vacuum, the unamplified signals are passed through the instrumentation flanges.

3.2 Barrel Pressure

The pressure in the barrel was measured using a PCB 11A03 piezoelectric pressure transducer with a manufacturer supplied sensitivity of $-65.48\,\mathrm{pC\,MPa^{-1}}$. The charge from this sensor was amplified and converted to a voltage using a Kistler Type 5015 charge amplifier with a nominal amplification of either $400\,\mathrm{kPa\,V^{-1}}$ or $800\,\mathrm{kPa\,V^{-1}}$. The gauge and amplifier pairing was calibrated using a DH-Bundenberg 580 Series hydraulic dead weight tester, and for the charge amplifier setting of $800\,\mathrm{kPa\,V^{-1}}$, the true sensitivity ($S$) was found to be $833\,\mathrm{kPa\,V^{-1}}$. A recalibration was conducted during the test campaign where the sensitivity was found to be $S = 825\,\mathrm{kPa\,V^{-1}}$, which is less than a 1 % change of sensitivity over all of the experiments. The amplified pressure signal is converted from a voltage (V) to absolute pressure in the barrel (P_B) using

$$P_B = S \cdot V + P_{atm} \tag{3.1}$$

where P_{atm} is the atmospheric pressure in the laboratory, measured using a Fortin barometer. The barrel pressure transducer was mounted slightly recessed ($<$ 1 mm) from the inner wall of the barrel, and stationed at 225 mm upstream of the nozzle entrance as shown in Fig. 3.2. The measured barrel pressure is used for triggering of data acquisition systems and other diagnostics, and measuring the pressure history of the piston compression flow discharge process. The pressure history of the piston compression process can be used to estimate flow conditions in the hypersonic freestream using isentropic flow relations.

A typical barrel pressure trace for the tunnel operating condition used in this research is displayed in Fig. 3.3, arranged such that diaphragm rupture is at $t = 0$ s. The slow opening of the primary valve begins at $t \approx -1100$ ms which accelerates the piston, compressing the test gas. The gradual valve opening has been tuned to largely eliminate the strong compression waves that are induced during the compression process if a more rapid valve opening time is used. Once the primary valve is fully open, the rate of pressure rise in the barrel is nominally constant ≈ 1.41 MPa s^{-1} until diaphragm rupture.

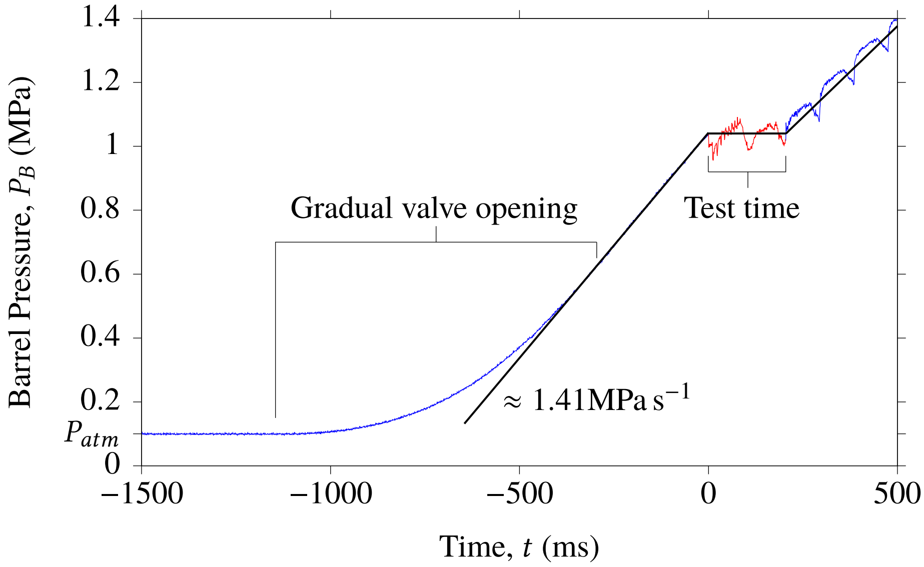

Figure 3.3: Typical barrel pressure history. Time data is offset such that the beginning of test time is $t = 0$ ms.

If the pressure in the reservoir is chosen so the volumetric flow rate into the barrel is approximately equal to the volumetric flow rate through the nozzle, the barrel pressure during a run is nominally constant (Jones et al., 1973). This is known as a matched condition. If the reservoir pressure is not arranged correctly, the barrel pressure and subsequently the static pressure of the hypersonic flow, can decrease (below matched) or increase (over matched). Over matched conditions have been previously observed in TUSQ (Widodo & Buttsworth, 2013).

Once the piston reaches the end of the barrel there is no longer any gas to expel through the nozzle and the test flow is terminated. At this time the barrel pressure transducer is measuring the pressure behind the piston which increases until the primary valve is closed.

3.3 Data Acquisition System

The main data acquisition system at TUSQ is comprised of two PXI-6123 and two PXIe-6124 multifunction I/O modules, and these modules are mounted in a National Instruments PXIe-1082 chassis. The properties of the two modules are shown in Table 3.3, and this system was used for all data acquisition in TUSQ.

	PXI-6123	PXIe-6124
Number of channels	8	4
Resolution	16 bit	16 bit
Maximum sample rate	$500\,\mathrm{kS\,s^{-1}}$	$4\,\mathrm{MS\,s^{-1}}$
Input coupling	DC	DC
Maximum voltage input	±11 V	±11 V

Table 3.3: Properties of the TUSQ data acquisition system.

3.4 Previous Characterisation of the TUSQ Freestream

3.4.1 Pitot Pressure Measurements

The Pitot pressure measurements reported by Widodo (2012) were made using Sensor-Technics BSDX2000A2R piezoresistive pressure transducers which were connected to a stagnation probe via a short length of tube. The bandwidth of the Pitot pressure measurements was not reported, however, based on the graphical data presented by Widodo (2012) the maximum frequency that could be resolved has been estimated to be in the order of 1 kHz. Widodo (2012) reported that the core flow radius decreased with run time, and that the spatial variation of Pitot pressure increased with run time. Widodo (2012) found that the Pitot pressure increased with run time, however this was probably due to the above matching condition investigated.

3.4.2 Variations of Stagnation Temperature

Widodo (2012)* measured the time-resolved stagnation temperature at the exit of the Mach 6 nozzle at TUSQ using an aspirating tube device, and investigated the stagnation temperature fluctuations at 20 mm downstream of the nozzle exit using a platinum thin film painted on the end of a 3 mm diameter fused quartz rod. A condition investigated by Widodo (2012) was similar to the condition analysed in this research, however for the Widodo (2012) work the condition was over matched.

The aspirating tube device with a 0.075 mm diameter type K butt welded thermocouple junction positioned at its inlet gave a signal that responded to the initiation of flow within approximately 1 ms (Widodo & Buttsworth, 2013). This response time was sufficient to find that the flow which is initially discharged from the hypersonic nozzle is very close to the isentropic compression value, and that over the first 150 ms of flow the stagnation temperature decreases by approximately 40 K†. A sudden decrease of stagnation temperature of about 100 K occurs at approximately 160 ms after diaphragm rupture, and this was attributed to the cold vortical flow in the vicinity of the piston being discharged through the nozzle. This vortical structure is known to significantly cool the flow in similar facilities (East & Qasrawi, 1978; Jones et al., 1973).

For facilities with comparable barrel aspect ratios (L/d) to TUSQ, an unstable vortical structure propagates well ahead of the piston during the compression process (East & Qasrawi, 1978). This structure is a turbulent mixing zone and results in a reduction of the flow total temperature to below the isentropic value. Widodo (2012) extrapolated the results of East and Qasrawi (1978) for the TUSQ facility and condition, and determined that at diaphragm rupture this turbulence zone would extend approximately 2 m ahead of the piston. The piston is approximately 3 m from the diaphragm at rupture, and therefore the initial test flow is unaffected by this vortical structure. Widodo (2012) does not discuss the detection of this vortical structure which, given its position and the position of the piston, can be expected to reduce the stagnation temperature after approximately $1/3$ of the test time has elapsed. Widodo (2012) also concluded that significant mixing across the diameter of the barrel occurs prior to the discharge of test flow through the nozzle, and that no discrete large scale thermal disturbances were detected.

---

[*] Partial results of this PhD were published as a journal article by Widodo and Buttsworth (2013).

[†] Widodo (2012) occasionally reports this to be 20 K, however graphical data indicates this to be an error.

A platinum thin film gauge on a 3 mm diameter hemispherical head fused quartz probe was used to measure the fluctuations of heat flux. Initially, the time-resolved stagnation heat flux determined using the thin film gauges were compared to the aspirating tube device. The results obtained using the thin film gauge were found to exceed that of the aspirating tube device, and the isentropic temperature value. This was attributed to the uncertainty of the heat transfer coefficient used, and when the results of the thin film gauge were scaled by 0.85, results more closely matched the results of the aspirating tube device. For the period of data presented graphically by Widodo (2012) (t = 30 – 50 ms), the time-resolved heat flux was 36 – 28 kW m^{-2} and the pre-run noise level was ± 5 kW m^{-2}. Because of the significant pre-run noise level, the heat flux was processed by a centred, moving average filter of 0.2 ms width which limited the bandwidth of the measurements. The filtered heat flux data were then used to determine that the largest fluctuations of heat flux were approximately 3.95 kW m^{-2}.

3.4.3 Summary

The flow conditions produced in TUSQ are often inferred using isentropic flow relations based on the measured pressure in the barrel, and the conditions in the barrel prior to the run which require the knowledge of at least the ambient pressure and temperature. Experimental flow characterisation data is sparse for the Mach 6 flow, with one previous study at an above-matching condition performed by Widodo (2012) whose work was focused on investigating the total temperature variations and fluctuations. The measurements of total temperature were complemented by a brief Pitot pressure survey in that work, but did not include any frequency domain analysis of the experimental data. The measurement of density fluctuations has not been attempted in TUSQ previously, and non-intrusive quantitative flow diagnostics have not been used for flow characterisation. Therefore ample opportunities exist to make contributions to the characterisation of the TUSQ facility through Pitot pressure, stagnation temperature and non-intrusive density fluctuation measurements.

Chapter 4

Computational Fluid Dynamics and Simulation Methods

Contents

4.1 Introduction

A steady flow simulation of the Mach 6 nozzle at the nominal test condition was performed using the finite volume flow solver `Eilmer4`, as presented in Section 4.2. The simulation results provide visibility on flow properties that cannot or have not been measured directly. However, the accuracy of the definition of the inflow conditions directly impacts the reliability of the simulated nozzle exit flow conditions, and unless some of the simulated nozzle exit flow properties are assessed through experimental measurements, the overall reliability of the simulation cannot be gauged.

The piston compression process and nozzle discharge processes were partially modelled using the quasi one dimensional flow solver L1d3, and this analysis is presented in Section 4.3. The L1d3 code was not able to be used to model the full piston compression process, however a method to initialise a simulation at the instant of diaphragm rupture was proposed. To achieve this starting process the properties of the gas ahead of and behind the piston were determined from an experimentally measured barrel pressure. The L1d3 simulation was used to identify unsteady waves that propagate in the barrel, and was later used as a validation of the experimentally identified stagnation temperature in Chapter 7.

4.2 `Eilmer4`

`Eilmer4` is a program for the numerical simulation of transient, viscous, reacting, compressible gas flows in two and three dimensional domains, in fixed or rotating frames of reference (Gollan & Jacobs, 2013; Jacobs & Gollan, 2016). `Eilmer4` was developed at the University of Queensland for time accurate simulations of hypersonic flows, and is second-order accurate in time and space. Flow simulations are based on a finite-volume formulation of the gas dynamics.

The results of any numerical simulation are limited by the ability to properly simulate the true flow conditions, which for simulation of models in TUSQ are the freestream flow conditions. In the absence of freestream flow conditions obtained experimentally, steady flow simulations of the nozzle flow can be used to approximate the inflow. `Eilmer4` was used to simulate the nozzle flow based on the stagnation flow conditions listed in Table 3.2 ($P_0 = 1\,\mathrm{MPa}$, $T_0 = 576\,\mathrm{K}$).

The nozzle was simulated as a 2D axisymmetric flow problem, and the geometry included a short inlet region of almost stagnated gas and a larger volume of cells representing the test section volume as illustrated in Fig. 4.1. At $t = 0$ two regions of gas were defined: (1) upstream of the diaphragm station with ideal air at the stagnation conditions, and (2) a low pressure ($P = 500\,\mathrm{Pa}$, $T_{amb} = 293\,\mathrm{K}$) volume downstream of the diaphragm station. The inlet was maintained at $P_0 = 1\,\mathrm{MPa}$, $T_0 = 576\,\mathrm{K}$, and the outlet a simple outflow boundary without a specified back pressure. All walls of the simulation were fixed as $T_{wall} = 293\,\mathrm{K}$ with viscous effects to impose a no-slip velocity condition. The simulation was run until $t = 10\,\mathrm{ms}$ to ensure a steady flow was developed which was free from nozzle starting effects.

The nominal condition was evaluated using isentropic flow relations at Mach 5.85 and Mach 5.95 with the results compared to the CFD results at $x = 0\,(x^* = 1), r = 0$ in

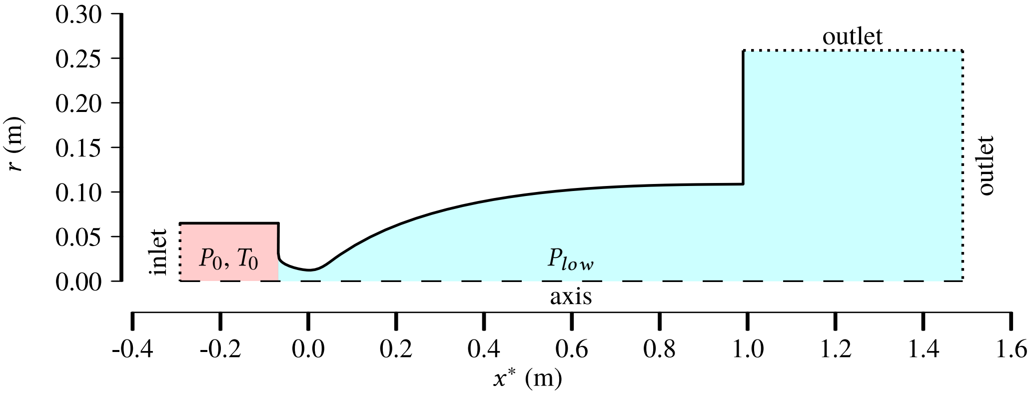

Figure 4.1: Simulation geometry and initial flow state for the simulation of the steady nozzle flow using `Eilmer4`.

Table 4.1. The CFD results for all flow properties are in reasonable agreement with the nominal flow conditions, however the Mach number of the `Eilmer4` simulation is slightly above the nominal condition. This increase of Mach number results in a lower freestream pressure, freestream temperature and freestream density than the nominal flow condition. The higher simulated Mach number flow is the result of a laminar flow simulation. The inclusion of appropriate turbulence modelling would likely increase the boundary layer thickness on the nozzle wall, which in turn will reduce the Mach number. However, inclusion of the turbulence models and the required mesh improvement comes at a significant computational cost.

Property	Unit	Nominal		`Eilmer4`
M_∞	–	**5.85**	**5.95**	5.98
P_∞	Pa	740	666	648
T_∞	K	73.4	71.3	70.6
ρ_∞	$\mathrm{g\,m^{-3}}$	35.1	32.6	31.8
$U_{x,\infty}$	$\mathrm{m\,s^{-1}}$	1005	1007	1007
$U_{r,\infty}$	$\mathrm{m\,s^{-1}}$	0	0	0

Table 4.1: Comparison of the CFD results at the centre of the nozzle exit plane and the nominal flow condition.

The radial distribution of the flow as calculated by the `Eilmer4` simulation are presented in Fig. 4.2 at nine axial locations referenced to the nozzle exit plane at $x = 0$ mm. The CFD identified a long core flow region, with highly uniform flow distribution at the nozzle exit plane for $r < 100$ mm. These CFD results provide a baseline facility performance, however the static CFD results lack any transient effects, including flow quality in terms of fluctuating values. Therefore, for a more complete understanding of the flow and improved application of CFD methods, an experimental study of the nozzle flow is required.

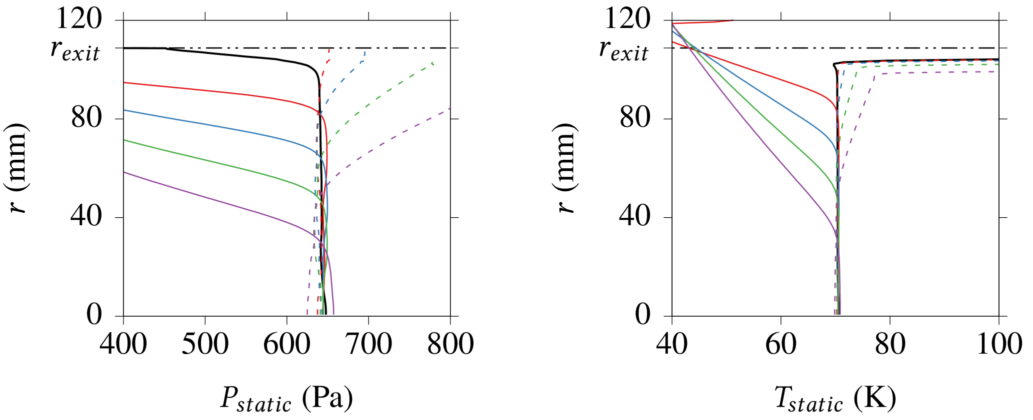

(a) Static pressure

(b) Static temperature

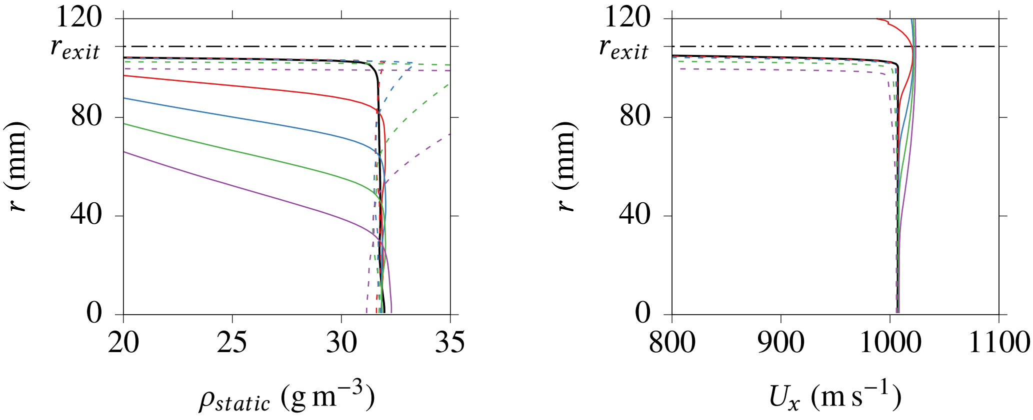

(c) Static density

(d) Axial velocity

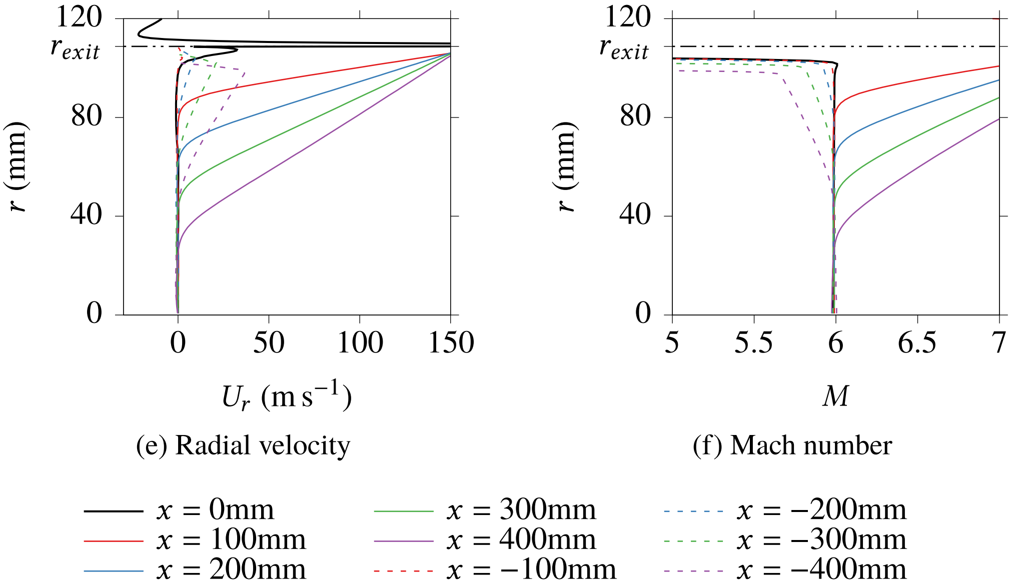

(e) Radial velocity

(f) Mach number

Figure 4.2: Results of the `Eilmer4` simulation.

4.3 Quasi One Dimensional Solver- L1d3

4.3.1 Introduction

A Lagrangian quasi one dimensional flow solver, L1d3, was used to simulate the piston compression process and the transient effects in the barrel during a run. L1d3 has been commonly applied to the simulation of entire shock tube and expansion tube facilities (Jacobs, 1998). Simulations are set up by writing a Python script that defines the geometry of the facility, including features such as pistons and diaphragms (Jacobs, 2005), with a valve model being recently added by Doolabh (2016). The Python script also requires the gas properties to be defined, separated into slugs of uniform properties.

The simulation was intended to analyse the full compression process, from primary valve opening through diaphragm rupture to the termination of test flow. However, for a facility with a valve opening time of hundreds of milliseconds and a compression stroke time in the order of seconds, the valve model implemented by Doolabh (2016) was found to be prohibitively computationally slow. Therefore the valve model had to be bypassed and a method where the properties of a gas slug could be defined as non-uniform was developed. Because of the valve model limitation, a simulation had to be initialised after the valve was fully open, but prior to, or at the instant of, diaphragm rupture such that the upstream propagating expansion wave is created at diaphragm rupture.

An in-house MATLAB simulation tool to determine the stagnation temperature of TUSQ based on the measured pressure in the barrel was developed by Widodo and Buttsworth (2013), and this routine formed the foundation for determining the spatial distribution of the test gas with non-uniform properties. The existing simulation of Widodo and Buttsworth (2013) did not include any model for the properties of the gas driving the piston which is needed for initialisation of the L1d3 simulations.

4.3.2 Simulation Geometry

For the purposes of simulation using L1d3, the gases within the TUSQ facility were treated as three discrete gas slugs as shown in Fig. 4.3. Slug 1 contains all the gas upstream of the piston in the barrel, in the reservoir and in the interconnecting pipework between the two.

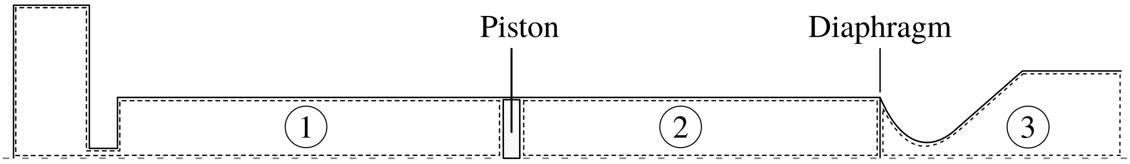

Figure 4.3: Facility geometry for L1d3 simulation. Slug 1 is the gas initially residing upstream of the piston. Slug 2 is the test gas that is initially bound between the piston and diaphragm. Slug 3 represents the stationary gas initially in the nozzle and the slug is expelled from the simulation shortly after diaphragm rupture.

Slug 2 contains the test gas that is bounded by the piston and diaphragm during the compression process. Slug 3 is a low pressure gas volume representing the nozzle, test section and dump tanks, and this slug is expelled from the simulation domain shortly after diaphragm rupture.

The hypersonic nozzle is approximated by a Bezier curve passing through the three points of Table 4.2. All walls are a constant temperature boundary at 293 K.

Point	x (mm)	D (mm)	Description
1	0	63.8	Nozzle Entrance
2	67	28.4	Nozzle Throat
3	1057	217.5	Nozzle Exit

Table 4.2: Points for constructing the Bezier curve approximation of the Mach 6 nozzle.

4.3.3 Determining Gas Properties from Measured Barrel Pressure

Widodo and Buttsworth (2013) developed a simulation tool for modelling stagnation temperature during the free piston compression process based on the measured pressure in the barrel and models for heat loss from the test gas to the barrel. A flat plate model based on incompressible flat-plate boundary layer correlations with the Reynolds number calculated on local flow conditions and the distance the element has travelled from its initial location was found to closely match observed values until the arrival of the cold vortical flow ahead of the piston. Transition was assumed to occur over $200\times10^3 < Re < 2\times10^6$. The same model can be applied to the condition studied in this research as a theoretical comparison to experimental results.

Considering the pressure through the test gas to be uniform at any point in time, the unsteady energy equation can be expressed as:

$$\frac{\mathrm{d}T_i}{\mathrm{d}t} = \frac{1}{m_i c_v}\left(Q_i - P\frac{\mathrm{d}V_i}{\mathrm{d}t}\right) \tag{4.1}$$

where c_v is the specific heat at constant volume, Q_i the heat addition of element i, and V_i the volume of element i as illustrated in Fig. 4.4. The temperature of each element of the test gas and the position of the downstream piston face can be found using the ideal gas law and engineering correlations for the heat lost to the barrel, and this procedure is described elsewhere (Widodo & Buttsworth, 2013).

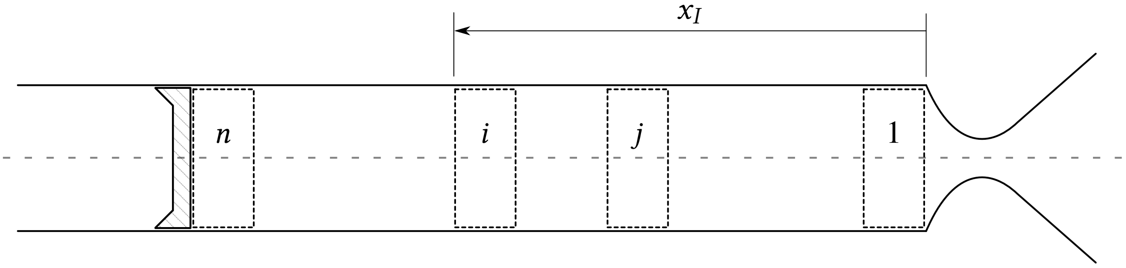

Figure 4.4: Arrangement used for thermodynamic simulation of the free piston compression process.

The code did not have the capability to determine the properties upstream of the piston, and these are required for the L1d3 simulation, therefore this capability had to be developed. Each cell within each gas slug is defined by the thirteen properties listed in Table 4.3. Normally only pressure, temperature, velocity and mass fraction are defined by the user with the other properties determined from the grid or derived from the defined properties. The position and volume of each cell are determined from the predefined mesh and do not require any modification, while the initial values of shear stress and heat flux are specified to be zero arbitrarily because these values are actually calculated from the other cell properties using engineering calculations.

The temperature, pressure and velocity distribution of the test gas within the barrel, and the position of the downstream face of the piston, can be determined using experimentally measured barrel pressure data for any instant of the piston compression process up to diaphragm rupture. $\overline{L}$ is the displacement of each cell from its initial position, and is required for calculating the Reynolds number. To be valid, $\overline{L}$ must be referenced to the cell position prior to the valve being actuated, and therefore had to be determined using the Widodo and Buttsworth (2013) simulation and interpolated to suit the L1d3 meshing. Combined with the cell position and cell volume defined by the L1d3 mesh, the derived

Column	Property	Symbol	Units
1	Position	x	m
2	Volume	V	$\mathrm{m^3}$
3	Velocity	u	$\mathrm{m\,s^{-1}}$
4	Cell displacement	$\overline{L}$	m
5	Density	ρ	$\mathrm{kg\,m^{-3}}$
6	Pressure	P	Pa
7	Sound Speed	a	$\mathrm{m\,s^{-1}}$
8	Shear Stress	τ	Pa
9	Heat Flux	q	$\mathrm{W\,m^{-2}}$
10	Specific Entropy	s	$\mathrm{J\,kg^{-1}\,K^{-1}}$
11	Mass fraction - air	–	–
12	Translational energy	e	$\mathrm{J\,kg^{-1}}$
13	Temperature	T	K

Table 4.3: Cell properties required for a L1d3 simulation.

values can be determined using Eq. 4.2 to Eq. 4.5.

$$\rho = \frac{P}{RT} \tag{4.2}$$

$$a = \sqrt{\gamma RT} \tag{4.3}$$

$$s = c_v \ln\left(\left[\frac{T}{300}\right]^{\gamma}\left[\frac{P}{101300}\right]^{1-\gamma}\right) \tag{4.4}$$

$$e = 717.66T \tag{4.5}$$

Slug 1 was split into three volumes as shown in Fig. 4.5 and the properties of each cell determined. Slug 1a contains the cells within the reservoir and connecting pipework, and Slug 1b is a slug of gas within the barrel, and these slugs are defined using discrete cells of fixed mass m_i. A fixed time step is used for the simulation, and since the mass flow rate into the barrel is not constant, a single cell of gas of mass $m^* < m_i$ exists at the entrance of the barrel. This single cell is designated as Slug 1^*. When $m^* = m_i$, the cell that defines Slug 1^* becomes a part of Slug 1b, and and a new Slug 1^* is formed.

The distribution of gas properties in Slug 1 was determined assuming:

1. Zone 1a undergoes only isentropic processes,
2. Slug 1a is at zero velocity and uniform thermodynamic properties,
3. Isentropic expansion from 1a to 1b,
4. Ideal gas with constant specific heats,

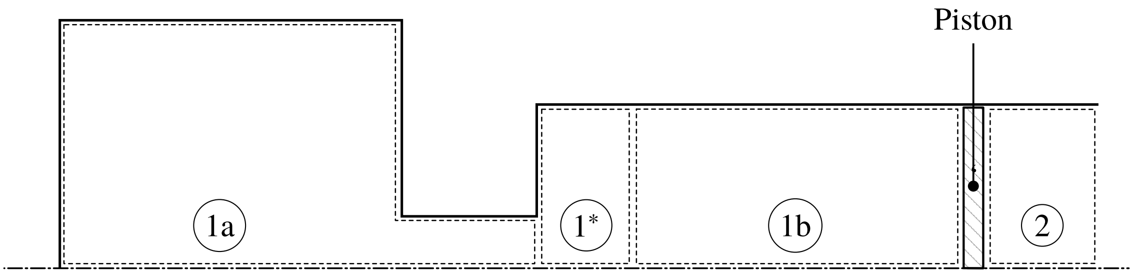

Figure 4.5: Zones of Slug 1 for determining the spatial distribution of gas properties.

5. Uniform state uniform flow process,
6. Negligible kinetic and potential energy,
7. The piston forms a perfect seal.

The calculated position of the piston during the compression process is shown in Fig. 4.6, and the knowledge of the piston trajectory can be used to determine the pressure of Slug 1b and 1^* using:

$$P_{1b,1^*} = P_2 + \frac{m_p a_p}{A_p} \tag{4.6}$$

where m_p, a_p and A_p are the piston mass, acceleration and area respectively.

Since the expansion from the reservoir to the barrel has been assumed isentropic,

$$\frac{P_{1b}}{P_{1a}} = \left(\frac{\rho_{1b}}{\rho_{1a}}\right)^{\gamma} \tag{4.7}$$

$$= \left(\frac{m_{1b}/V_{1b}}{m_{1a}/V_{1a}}\right)^{\gamma} \tag{4.8}$$

$$= \left(\frac{m_{1b}}{m_R} \times \frac{V_R}{x_p\,A_p}\right)^{\gamma} \tag{4.9}$$

$$= \left(\frac{\int_0^t \dot{m}_v\,\mathrm{d}t}{m_{R,0} - \int_0^t \dot{m}_v\,\mathrm{d}t} \times \frac{V_R}{x_p\,A_p}\right)^{\gamma} \tag{4.10}$$

where V_R is the reservoir volume, A_p the area of the piston, $m_{R,0}$ the mass of the gas contained within the reservoir prior to valve actuation, and $\dot{m}_v$ the mass flow rate through the valve into the barrel. Since the pressure loss in the reservoir (Slug 1a) can be assumed to be isentropic,

$$P_{1a} = c\,\rho_{1a}^{\gamma} \tag{4.11}$$

$$= c\left(\frac{m_{R,0} - \int_0^t \dot{m}_v\,\mathrm{d}t}{V_R}\right)^{\gamma} \tag{4.12}$$

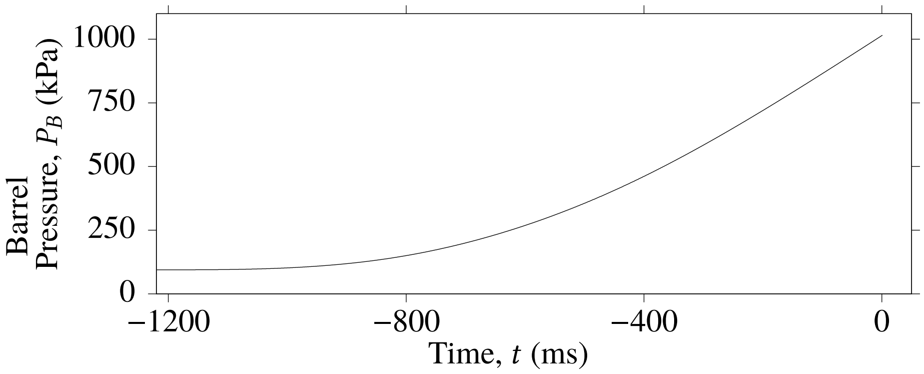

(a) Barrel pressure

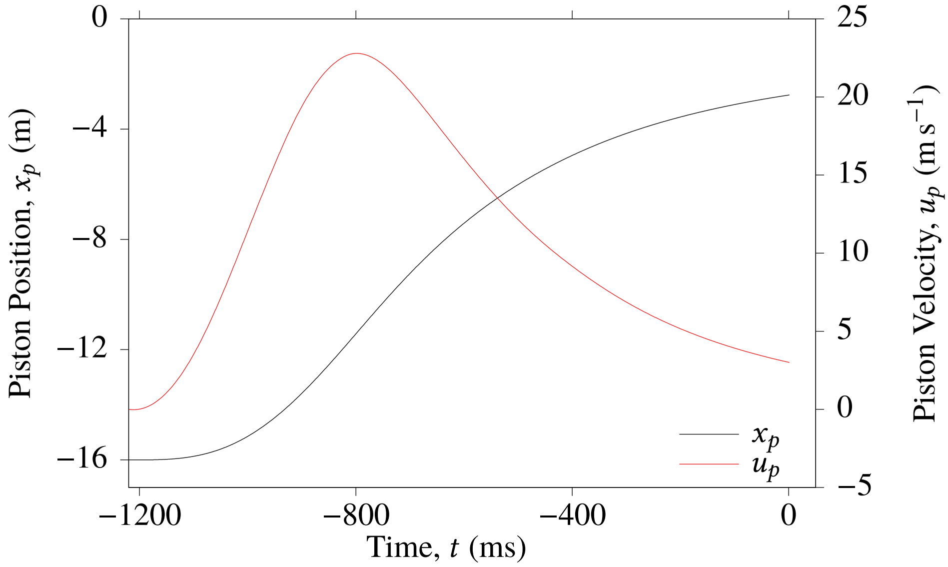

(b) Piston position and velocity

Figure 4.6: Calculated piston trajectory using measured barrel pressure. Diaphragm rupture is at $t = 0$ ms, the upstream end of the barrel at $x = 16$ m, and the downstream end of the barrel at $x = 0$ m.

where c is a constant defined as

$$c = \frac{P_{R,0}}{\rho_{R,0}} \tag{4.13}$$

Substituting Eq. 4.12 and Eq. 4.13 into Eq. 4.10, the mass flow rate from the reservoir into the barrel can be expressed as a function of known and calculated values by:

$$\frac{P_{1b}}{c\left(\frac{m_{R,0}-\int_0^t \dot{m}_v\,\mathrm{d}t}{V_R}\right)^{\gamma}} = \left(\frac{V_R}{m_{R,0}-\int_0^t \dot{m}_v\,\mathrm{d}t}\right)^{\gamma} \times \left(\frac{\int_0^t \dot{m}_v\,\mathrm{d}t}{x_p\,A_p}\right)^{\gamma} \tag{4.14}$$

$$\frac{P_{1b}}{c} = \left(\frac{\int_0^t \dot{m}_v\,\mathrm{d}t}{x_p\,A_p}\right)^{\gamma} \tag{4.15}$$

$$\dot{m}_v = A_p \frac{\mathrm{d}}{\mathrm{d}t}\left(x_p \left[\frac{P_{1b}\,\rho_{R,0}}{P_{R,0}} \right]^{\frac{1}{\gamma}} \right) \tag{4.16}$$

The properties of Zone 1a were assumed to be uniform, and since it is a constant volume its density is easily calculated. The pressure of Zone 1a is then found using Eq. 4.12, and the temperature using the ideal gas law; and this is sufficient to define all properties required for Zone 1a.

The properties of Zone 1^* and Zone 1b were calculated using a finite mass method where each cell is of mass m_i. When $m^* = m_i$, the cell is considered part of Zone 1b and a new Zone 1^* is developed. The process is continued until the desired point in time, between the valve being fully open and diaphragm rupture is reached.

The temperature and pressure distribution when $x_p = -9.6$ m is shown in Fig. 4.7. To model the geometry of the barrel entrance, a small section of connecting pipework between the reservoir and barrel entrance has been modelled, and this section assumed to have the same properties as the gas in the barrel upstream of the piston. All thirteen properties required for the L1d3 simulation can be determined along the entire facility.

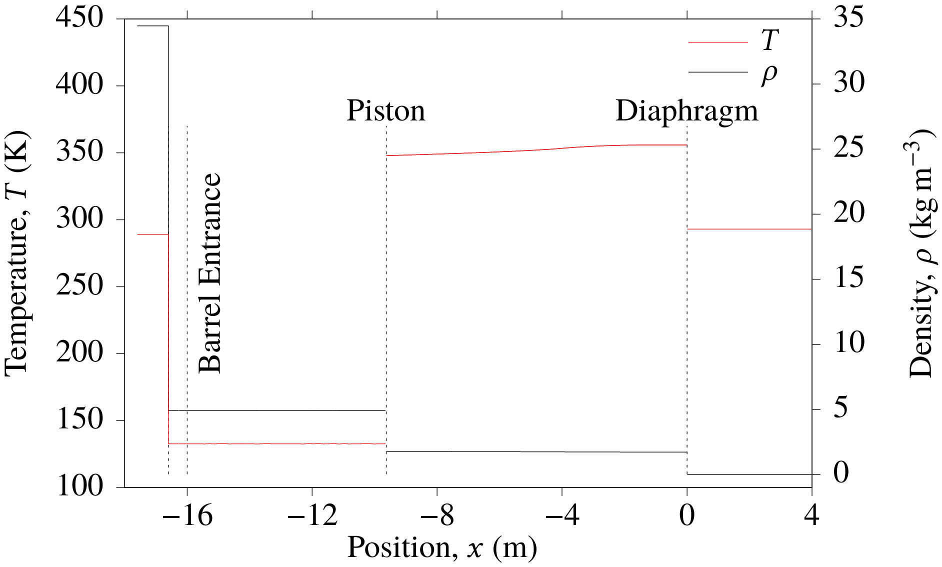

Figure 4.7: Distribution of temperature and density along the facility when $x_p = -9.6$ m. A small connection between the reservoir volume and barrel entrance was included so the barrel entrance sizing was correct.

4.3.4 Simulation Refinement

A technique for defining gas slugs of variable thermodynamic properties was developed such that the prohibitively slow valve model of L1d3 was not required, and the implementation of this technique is described in Appendix A. This technique could be implemented as long as the valve separating the reservoir and driver gas could be considered fully open, and the diaphragm not yet ruptured.

However, because of the large pressure differential of the reservoir and driver section, strong expansion waves were generated when the simulation initialised. These expansion waves cause the piston to accelerate to speeds much greater than the real case. This caused the test gas to be compressed faster in the simulation than in an experiment.

To remove or mitigate the effects of the expansion wave that propagates from the reservoir-barrel interface, three alternatives were considered: (1) a simulation of just the barrel, initialised at diaphragm rupture; (2) a simulation initialised at diaphragm rupture where the gas in the reservoir has the same thermodynamic properties as the driver gas in the barrel; and (3) a configuration similar to (2), but with a larger reservoir volume such that the pressure decrease over the run is small.

Option (1) would result in significant pressure reduction during nozzle flow discharge, and this would cause a significant reduction of stagnation temperature over the run duration and therefore be of little use for validation of the experimental total temperature data presented in Chapter 7. The piston trajectory and strength of the transient waves would also be questionable.

Option (2), using a 350 L reservoir volume results in a nearly 7 % pressure reduction in the barrel over the run duration. Like (1), this pressure reduction would limit the applicability of the simulation to validation of total temperature measurements. Modelling the actual thermodynamic properties of the reservoir volume was not considered beneficial, and (2) discarded.

Option (3), while still unable to model the thermodynamic properties of the gas upstream of the piston in the barrel, was considered the most likely to model the real conditions in the barrel. The reservoir volume was arranged such that there was less than 1 %

pressure reduction over the run and a nominally matched condition achieved. To model the reflections of the transient waves off the upstream end of the barrel, the region of smaller cross sectional area representing interconnecting pipework was preserved. When the diaphragm ruptures the piston accelerates, and this acceleration, despite there being no pressure differential across the interconnecting pipework region, causes an expansion wave to form at the barrel entrance. However this expansion wave was much weaker than the expansion wave created when the reservoir is considered a separate volume and, while the effects of the expansion wave were significant, the simulations provided insightful data.

4.3.5 Results

An L1d3 simulation based on the experimentally measured barrel pressure for Run 496 (up to the instant of diaphragm rupture at $t = 0\,\mathrm{s}$) was used to identify large scale events in the barrel.

The pressure at the barrel pressure transducer location is determined by the L1d3 simulation with non-uniform initial conditions. An x–t diagram for the barrel compression process is shown in Fig. 4.8, and the numerically simulated barrel pressure is compared to the experimentally measured barrel pressure for Run 496 in Fig. 4.9. There was good agreement for three periods of experimental and simulated data: (1) for $0 \leq t \lesssim 50\,\mathrm{ms}$; (2) for $100 \lesssim t \lesssim 130\,\mathrm{ms}$ which has been annotated A; and (3) for $180 \lesssim t \lesssim 195\,\mathrm{ms}$ which has been annotated B.

However, there are two periods of flow where the simulation is in poor agreement with the experimental data: (1) for $50 \lesssim t \lesssim 100\,\mathrm{ms}$; and (2) for $130 \lesssim t \lesssim 180\,\mathrm{ms}$. These periods of poor agreement are the result of a limitation in the simulation that could not be overcome. To model the transient waves that propagate along the barrel in the upstream and downstream directions, the upstream end of the barrel had to have a contraction to a smaller diameter such that the transient waves are properly reflected. As the simulation is started, an expansion wave, E_v (Fig. 4.8), forms at the change of cross sectional area at the barrel entrance and propagates towards the piston. This expansion wave is transmitted through the piston at (i) and again at (ii) on Fig. 4.9, and these are the beginning of the periods of poor agreement with experimental data.

For $0 \leq t \lesssim 40\,\mathrm{ms}$ the expansion wave E_v has not interacted with the piston, and con-

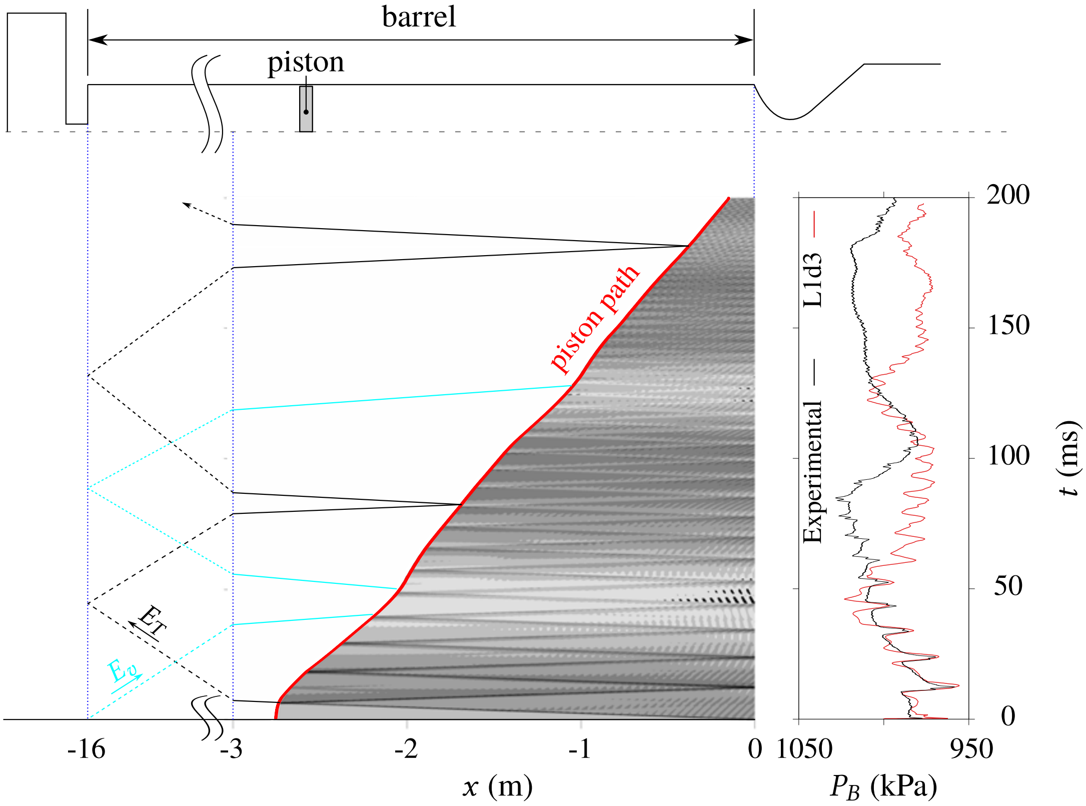

Figure 4.8: x-t diagram of pressure (logarithmic scale) in the barrel for $0 \leq t \lesssim 200$ ms.

sequently there was good agreement between the simulation and experimental data. This region is best discussed with reference to the x-t diagram of Fig. 4.10 where the pressure changes in the test gas and immediately behind the piston are shown for $0 \leq t \lesssim 40$ ms. Upon diaphragm rupture at $t = 0$ s, the pressure in the barrel suddenly drops, shown in Fig. 4.9, and an expansion wave (E) forms which propagates upstream in the barrel. E propagates upstream until it reaches the piston, at which point it is partially transmitted (E_T) and partially reflected (E_R). The reflected expansion wave continues to oscillate between the piston and nozzle inlet. The transmitted expansion wave E_T propagates upstream until it reaches the barrel inlet and is reflected back downstream towards the piston. E_T returns to the piston, and the effects of this event are first detected at (I) on Fig. 4.9. E_T completes a second transit up and down the barrel and is detected for a second time at (II) on Fig. 4.9. The L1d3 simulation was unable to identify (I) directly, but the pressure recovery in region (A) is ultimately the result of the reflection of E_T interacting with the piston (East & Qasrawi, 1978).

Figure 4.10 is annotated with the location of the barrel pressure transducer, and every pass of the reflected expansion waves in the time period shown. Because the barrel pressure

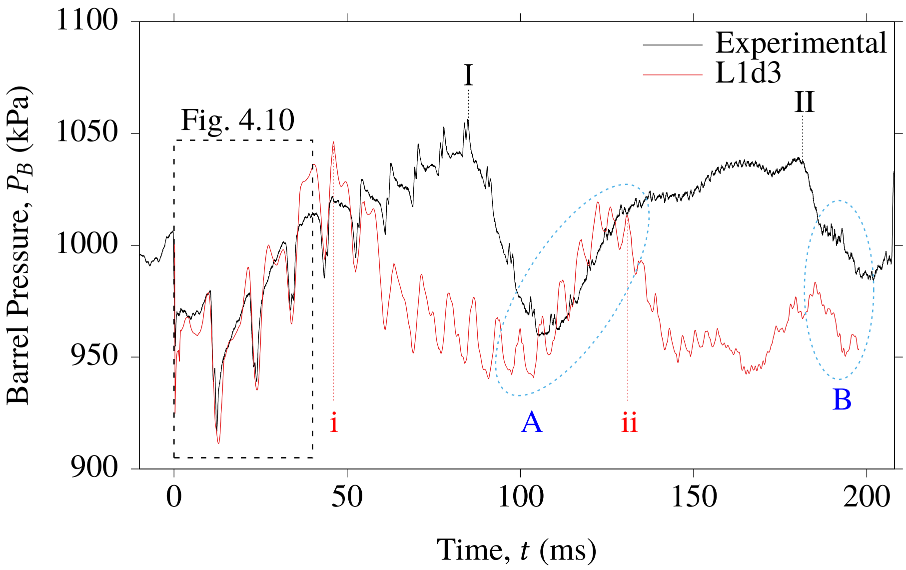

Figure 4.9: Comparison of simulated barrel pressure to experimental data (Run 496).

transducer is not mounted flush with the barrel end wall, every transit of E_R is detected twice, and this is discussed in more detail in Section 5.2.

The total temperature history determined from this L1d3 simulation is compared to the experimentally determined total temperature in Section 7.6.

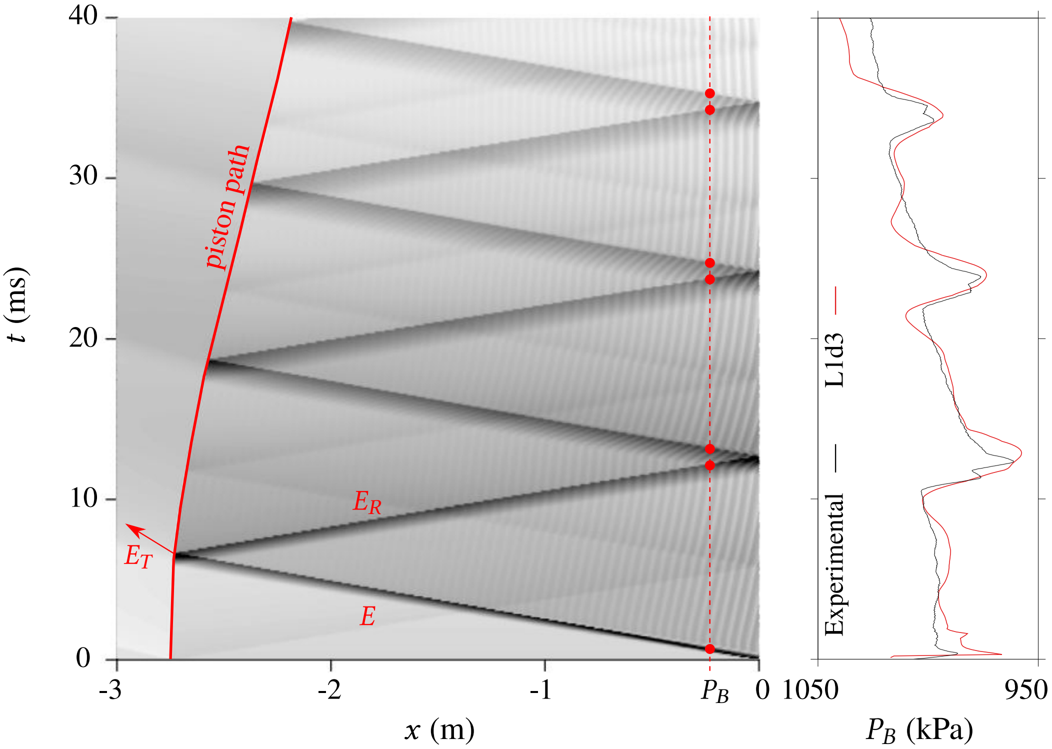

Figure 4.10: x-t diagram of pressure (logarithmic scale) in the barrel for $0 \leq t \lesssim 40$ ms near the nozzle entrance at $x = 0$ m. Red dots indicate the times when expansion waves are detected by the barrel pressure transducer.

Chapter 5

Stagnation and Pitot Pressures in TUSQ

Contents

5.1 Introduction and Overview

In TUSQ, the barrel pressure measurement is the primary quantitative flow diagnostic, and the measurement of the barrel pressure can be used to determine the nominal flow conditions in the hypersonic freestream. Therefore, it is important to have a complete understanding and description of the barrel pressure signal over a run. The measurement of the barrel pressure can also be used to identify sources of disturbances that propagate into the test section and affect the flow quality.

Pitot pressure measurements have been used extensively to infer the test flow quality of supersonic and hypersonic test facilities, and this method was discussed in Chapter 2. Often Pitot pressure measurements are limited to a statement of the root-mean-square (RMS) level, however by investigating the amplitude of freestream disturbances for specific frequency ranges a more complete description of the disturbance environment is possible.

5.2 Barrel Pressure

A typical trace of barrel pressure in the region of the run time is presented in Fig. 5.1. Prior to diaphragm rupture at point (i) in Fig. 5.1, unsteady waves resulting from primary valve actuation and finite piston mass effects are observed. The mean barrel pressure over the run duration closely matches the burst pressure, demonstrating a matched condition. However large deviations from the mean pressure $\overline{P}_B$ are evident, bound in the range $\overline{P_B}^{+6\%}_{-10\%}$. The large variance is caused by the near-instantaneous opening of the nozzle at diaphragm rupture, which generates an expansion wave which propagates upstream towards the piston.

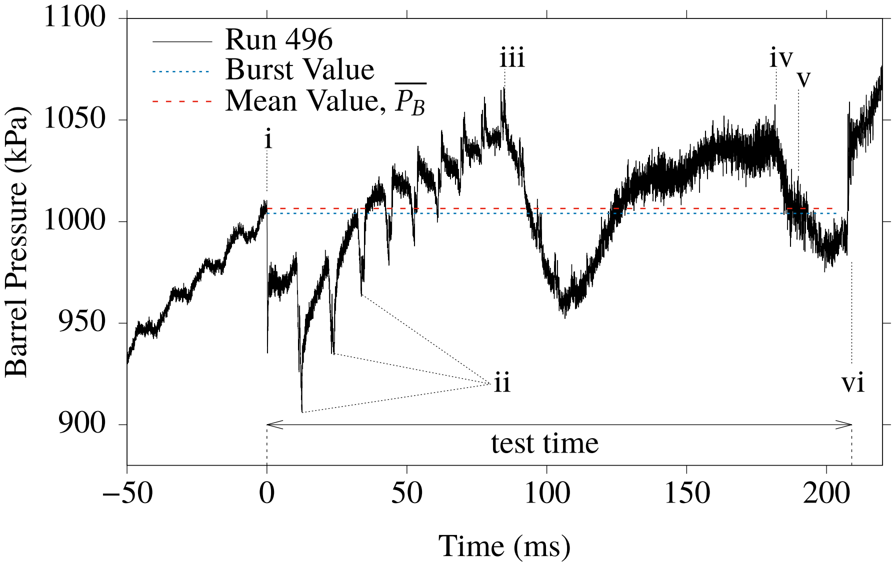

Figure 5.1: Identification of barrel pressure (nozzle inlet) events. i- Expansion wave generated by diaphragm rupture; ii- the first three reflected expansion waves; iii- reflected expansion wave returns to the nozzle inlet end of the barrel; iv- reflected expansion wave returns to the nozzle inlet end of the barrel for the second time; v- piston passes over the transducer; vi- termination of nozzle flow.

When the expansion wave reaches the piston, the interaction results in a transmitted expansion wave which continues towards the primary valve, and a reflected expansion wave which propagates towards the nozzle inlet (see Fig. 4.8 and Fig. 4.10). The reflected expansion wave-trains continue to transit between the piston and nozzle inlet, and the first three of these wave-trains are denoted as features (ii) on Fig. 5.1. Over time, the strength of this wave decays and the period of oscillation reduces as the piston moves closer to the nozzle inlet. The first expansion wave (feature i in Fig. 5.1), when transmitted through the piston, continues to propagate towards the upstream end of the barrel until it reaches the valve region. Here the dispersed form of the expansion wave is partially transmitted into the reservoir, but, of more consequence to the run conditions, the dispersed expansion wave is also reflected back towards the nozzle. Since the primary valve open area is a small fraction of the barrel area, the strength of the dispersed expansion wave virtually doubles. The arrival of the expansion wave at the barrel pressure transducer is detected at point (iii) in Fig. 5.1. This wave continues to oscillate between the nozzle inlet and the primary valve and is detected again at (iv) at a reduced amplitude. The piston passes the pressure transducer at point (v) and reaches the end of the barrel at (vi). Barrel pressure data between (v) and (vi) is not of significant value as it is the pressure behind the piston.

Finite piston mass effects are observed in the barrel pressure history because the piston is unable to accelerate instantaneously with the arrival of the expansion waves generated at diaphragm rupture, so the expansion waves partially reflect from the piston which contributes to the pressure drop immediately following diaphragm opening. The discussion of large scale barrel transients is important for isolating low frequency piston oscillation effects from broadband noise. Additionally, barrel pressure is often the most important flow diagnostic recorded during routine operation and therefore needs to be well characterised and understood. The barrel pressure trace can be better understood by considering the location of the barrel transducer which is 225 mm from the nozzle inlet, and a further 67 mm from the nozzle throat (Fig. 3.2). Figure 5.2 presents a detailed analysis of one feature in the barrel pressure.

In Fig. 5.2, feature (i) is the drop in pressure as the expansion wave that is reflected from the piston is travelling in the downstream direction and is passing over the transducer. When the initial expansion wave generated at diaphragm rupture reaches the piston, it causes a change in pressure differential either side of the piston, causing an acceleration of the piston. But because of its finite mass, the piston cannot accelerate instantaneously. The pressure increase from the piston acceleration is detected as feature (ii). These features are detected again as features (iii) and (iv) when the expansion wave is reflected off the nozzle inlet and throat, and travels in the upstream direction.

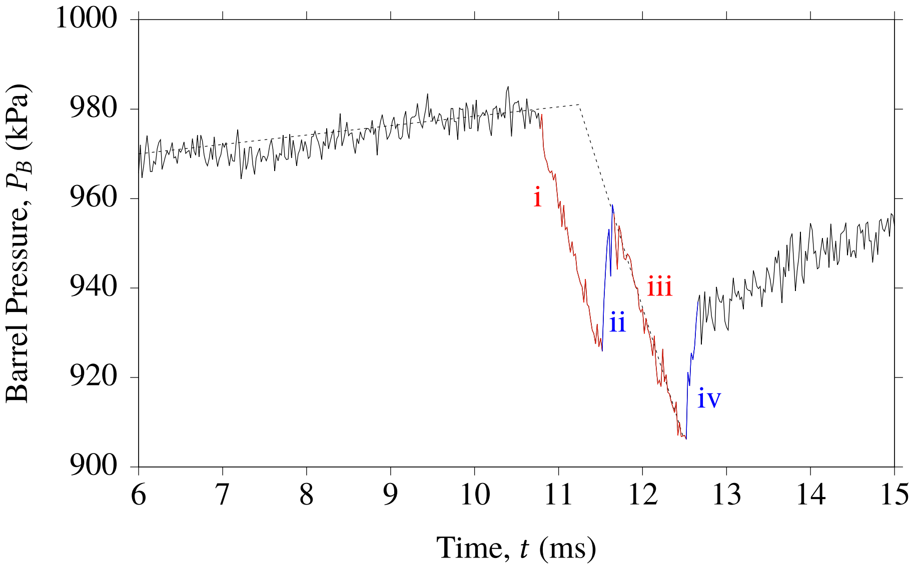

Figure 5.2: Repeated detection of reflected expansion waves and piston mass effects.

If the barrel pressure transducer was moved closer to the nozzle inlet, the time between (i) and (iii) would reduce and approach a limit where the features become collinear and feature (ii) would not be evident. The limit is illustrated by the dashed lines on Fig. 5.2 and resembles the reflected expansion waves that are present in the hypersonic test flow. Understanding that these features would not be detected twice in the nozzle exit flow is critical to interpreting the results of the nozzle exit diagnostics, and especially important for correct temporal alignment of the barrel pressure history and nozzle exit flow data.

5.3 Pitot Pressure Survey

Mean and fluctuating Pitot pressure measurements were made using 0.7, 1.7 and 3.5 bar variants of Kulite XTL-190M miniature ruggedised pressure transducers. The transducers were fitted with B-screens to prevent damage from particulate impact, however this limited the maximum resolvable frequency to 25 kHz as per manufacturer specifications. Pitot pressure transducers were exposed directly to the flow, offering the most direct measurement of the hypersonic flow field (Lafferty & Norris, 2007). The transducer faces protruded approximately 10 mm ahead of a 45° half angle probe rake (Fig. 5.3). Pitot pressure surveys were conducted at three locations: $x = 0$ mm, 50 mm and 100 mm downstream of the nozzle exit plane. Radial positions extending from the nozzle centreline, through the core flow and into the turbulent shear layer and expansion region, were examined. The rake was designed so that the rake centreline was coaxial with the nozzle centreline. Internal cavities and cable channels protected the transducer wiring from the flow, and vacant ports in the rake were terminated with grub screws to prevent test flow entering the rake cavities.


(a) (b)

Figure 5.3: Pitot rake geometry. (a) Kulite pressure transducers are shown protruding approximately 10 mm from the 45° half angle rake leading edge. (b) Configuration where the rake is instrumented with eight Kulite pressure transducers.

The geometry of the Kulite pressure transducers and Pitot rake limited the minimum distance between two pressure transducers to 20 mm, and schlieren imaging confirmed that 20 mm spacing was sufficient to ensure there was no interference of the shock front for adjacent transducers which is demonstrated later in Fig. 5.9.

As the nozzle stagnation pressure (the barrel pressure) and the Pitot pressures were spatially separated by approximately 1 m, post-processing required a small time shift to be added to the stagnation pressure to temporally align the stagnation pressure and Pitot pressure signals for direct comparison. This time shift corresponded to the transit time for disturbances recorded at the barrel transducer to propagate to the position of the Pitot transducers. Barrel stagnation pressure can be used to identify features originating from the compression process, such as piston oscillations and expansion waves from valve opening and diaphragm rupture.

Three different amplifier types were used with the Kulite transducers: (1) in-house amplifiers; (2) Alligator USBPIA-S1 instrument amplifiers; and (3) an AMETEK Model 5113 pre-amplifier. At a gain of 100, the in-house amplifiers were limited to the 0 – 5 kHz bandwidth while the Alligator and AMETEK amplifiers provided a flat response up to 100 kHz, and the AMETEK amplifier provided a 6 dB/octave roll-off for $f > 100$ kHz. The in-house amplifiers were therefore unsuitable for analysis of fluctuations over the full dynamic range of the Kulite pressure transducers. However, as more pressure transducers than high speed amplifiers were available, the 5 kHz amplifiers assisted in the definition of the spatial uniformity of the core flow. Data was recorded at 200 kS s^{-1} using LabView and the National Instruments PXIe-6123 and PXIe-6124 modules, well above the useful maximum frequency of the Kulite pressure transducers. The amplified signals were converted to absolute pressure via in-situ calibration of each gauge for each run.

Conventionally, tunnel noise levels inferred from Pitot pressure measurements are presented as a RMS percentage relative to mean values. The power spectral density (PSD) analysis offers information beyond the standard RMS value, however, as identified in Chapter 2, the way in which the PSD is used is not always well justified.

5.4 Temporal Alignment of Spatially Separated Signals

The total pressure and Pitot pressure cannot be measured in the same location, and therefore, there is a time delay between the signals that needs to be accommodated if the data is to be combined for identification of the flow conditions, including the flow Mach number. Simple temporal alignment of the diaphragm rupture event identified on the barrel pressure record and the sudden pressure rise measured by the Pitot pressure transducers are inadequate as the time delay associated with the nozzle starting process is different from the delay associated with pressure wave transmission through the nozzle, once the quasi-steady flow has been established. Instead, the pressure increase associated with the acceleration of the piston in response to the first reflected expansion wave was used, as this feature is clearly visible in both the Pitot and barrel pressure traces. Detection of these features can be automated for fast and consistent temporal alignment. Recall from Fig. 5.2 that this wave is detected twice by the barrel pressure transducer. Identification of the minima where feature (iii) changed to (iv) was used as the reference point for the barrel pressure signal, not features (i) and (ii).

The result of the alignment procedure is shown in Fig. 5.4 for the centreline Pitot pressure transducer of Run 500. The signal lag was 470 µs, 520 µs and 580 µs for transducer locations at $x = 0$ mm, 50 mm and 100 mm downstream of the exit respectively. Stagnation and freestream temperatures reduce gradually over time (Widodo, 2012) causing the transit time of acoustic features between the barrel transducer and Pitot probes to increase over time. The final, clearly identifiable feature on both the barrel and Pitot transducers was the reflection expansion wave at approximately 120 ms, and using this feature as a gauge, the increase in acoustic transit time was less than 60 µs at this time in the run.

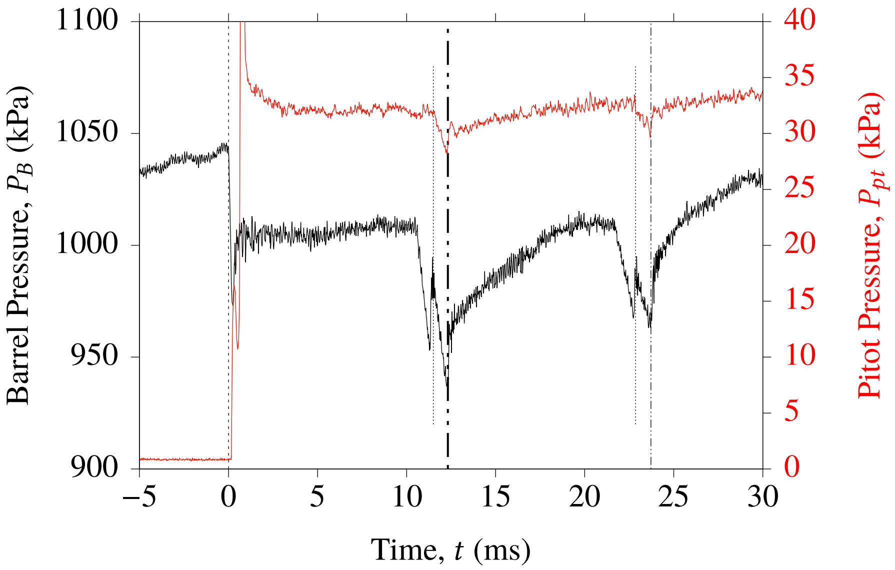

Figure 5.4: Temporal alignment of barrel and centreline Pitot pressure measurements. The reflected expansion wave at 12.32 ms was used as the reference for the temporal alignment of the barrel and Pitot pressure signals.

Referring to Fig. 5.4, the Pitot pressure was aligned with the barrel pressure history at 12.32 ms using the first reflected expansion wave alignment technique. This resulted in excellent temporal alignment of all reflections and piston responses and an illustration of this is shown for the features at 23 ms. The vertical line at $t = 0$ s indicates the diaphragm rupture as registered at the barrel transducer, not the beginning of the test flow. Nozzle starting effects are observed in the Pitot pressure history from 0.2 – 1.5 ms.

5.5 Time-Averaged Pitot Pressure

The time-averaged Pitot pressure can be used to assess the core flow uniformity and repeatability of flow conditions between shots. A variety of amplifiers were used in the experimentation, and these amplifiers had different maximum frequency resolutions and were recorded at different sample rates. Data recorded at 50 kHz has ten times more data for a particular time period than data recorded at 5 kHz and therefore, so not to bias the data towards particular measurements, all data were decimated to 5 kHz. The data were then low-pass filtered at 1 kHz using a 6th order Butterworth filter to extract a time-averaged level for each run and position.

The time-averaged Pitot pressure at $x = 0$ mm and $x = 50$ mm are presented as Fig. 5.5a and Fig. 5.5b respectively. At $x = 0$ mm the Pitot pressure transducers are flush with

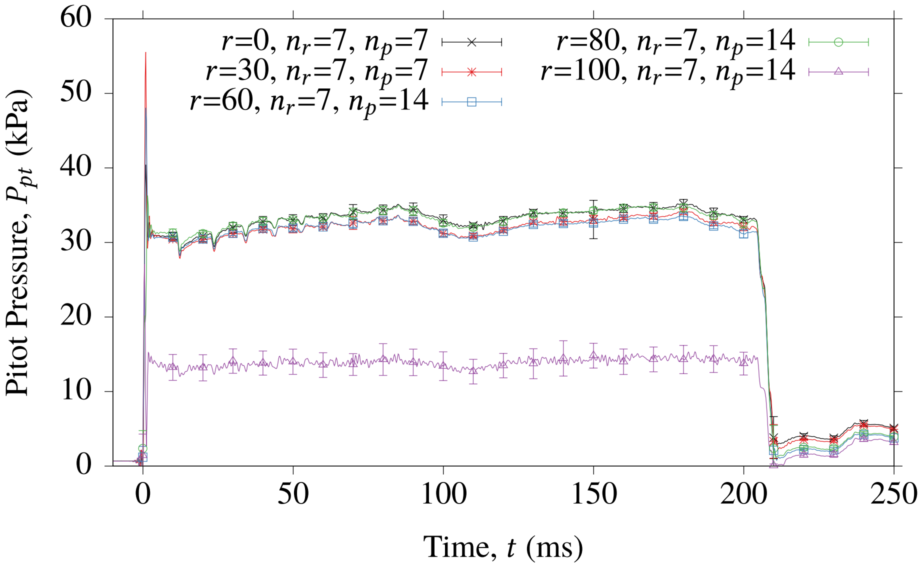

(a) $x = 0\,\text{mm}$

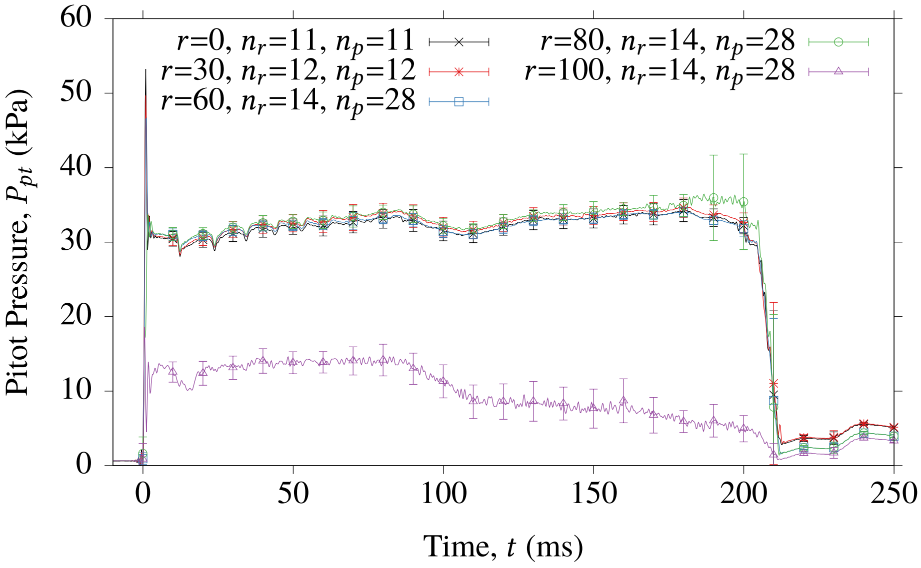

(b) $x = 50\,\text{mm}$

Figure 5.5: Time-averaged Pitot pressure at two Pitot rake locations downstream of the nozzle exit. Axisymmetric flow was demonstrated and therefore data from opposing radial locations combined. n_r indicates the number of runs analysed to obtain the data, and n_p the total number of Pitot pressure transducer signals used to determine the mean level. Error bars indicate two standard deviations from the mean value at time t.

the nozzle exit plane, and at this location the core flow radius is in excess of 80 mm for the full hypersonic flow duration of approximately 200 ms. At $x = 50$ mm, the core flow size reduces towards the end of the flow, and this is indicated by the increase of the time-averaged and standard deviation of the Pitot pressure from $t = 180$ ms onwards for $r = 80$ mm. For $r < 80$ mm the time-averaged Pitot pressure is consistent for both locations, and the run-to run variations are small; the standard deviation at the nozzle exit plane is less than 2 % for the full run duration, and at $x = 50$ mm the run-to-run changes are less than 3.5 % while the probe is measuring the core flow.

5.6 Time-Averaged Mach Number Flow

The Pitot pressure signals that were conditioned using the in-house amplifiers and that were limited to 5 kHz bandwidth, and the signals which were amplified using higher bandwidth amplifiers, were to calculate Mach number of the flow over the run duration. Pitot and total pressure (barrel pressure) data were temporally aligned using the method described in Section 5.4 and all data were low-pass filtered at 5 kHz using a 6th order Butterworth filter prior to calculation of Mach number (M_∞) using:

$$\frac{P_{pt}}{P_B} = \left(\frac{\frac{\gamma+1}{2}M_\infty^2}{1+\frac{\gamma-1}{2}M_\infty^2}\right)^{\frac{\gamma}{\gamma-1}} \left(\frac{1}{\frac{2\gamma}{\gamma+1}M_\infty^2 - \frac{\gamma-1}{\gamma+1}}\right)^{\frac{1}{\gamma-1}} \tag{5.1}$$

Mach number variations over the run duration are shown in Fig. 5.6. Mach number at the nozzle exit plane (Fig. 5.6a) indicates that the centreline result ($r = 0$ mm) matches well with $r = 80$ mm data. At $x = 50$ mm (Fig. 5.6b) the centreline Mach number is higher than at the nozzle exit plane and matches well with the $r = 30$ and $r = 60$ mm traces. The Mach number decreases slightly over the run duration and this is possibly due to the known decrease in flow stagnation temperature (Widodo, 2012) which causes an increase in the Reynolds numbers, thickening the nozzle boundary layer and thus reducing the effective nozzle area ratio. At $t \approx 170$ ms the cooler vortical flow ahead of the piston arrives at the nozzle inlet causing a reduction in core flow size and Mach number. Figure 5.6 suggests large and sudden changes in Mach number occur within the first 100 ms, but this is an artefact of the duplicate detection of the reflected expansion waves by the barrel transducer (Fig. 5.2), not a true flow effect. The average core flow Mach number over the entire run is 5.9 ± 1 % with a minimum core flow diameter of 160 mm at the nozzle exit. The boundary layer displacement thickness (δ^*) increases over the run duration as the Mach number decreases and, considering the nozzle area ratio, can be calculated as

$\delta^* = 7.43$ mm when $M = 5.9$.

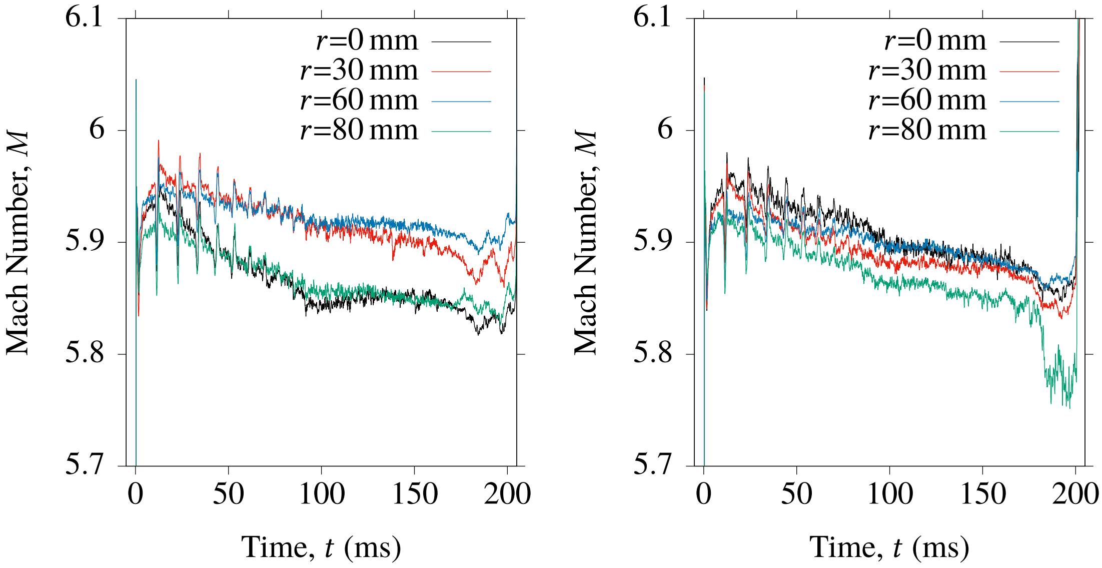

(a) Mach number at $x = 0$ mm. (b) Mach number at $x = 50$ mm.

Figure 5.6: Time-averaged Mach number flow.

5.7 Pitot Pressure Fluctuations

To determine the fluctuations of Pitot pressure two analysis methods were used: (1) a high-pass filtering technique; and (2) a power spectral density (PSD) method. While both methods can be used to calculate root-mean-square (RMS) values, the high-pass filter method can identify changes in fluctuation amplitude over the run time while the PSD technique reveals spectral power and can be interpreted to identify noise sources.

5.7.1 Signal Conditioning for Analysis of Pitot Pressure Fluctuations

The centreline Pitot pressure from Run 500 is displayed in Fig. 5.7. The average Pitot pressure value was identified from data between 5 – 200 ms to avoid any nozzle starting and flow termination effects. Like the barrel pressure history, there are moderately large, relatively low frequency deviations from the average Pitot pressure. As the relatively low frequency components of the Pitot pressure change during the run, it was necessary to isolate the fluctuating component of Pitot pressure measurements from the mean pressure level. Determination of the fluctuating component using the low-pass filtering method proposed by Lafferty and Norris (2007) was investigated. However, due to the impulsive starting of TUSQ, the low-pass filter response was unsatisfactory for cutoff frequencies up to the order of kilohertz. Instead, the data was high-pass filtered to attenuate the low frequency components caused by reflected expansion waves which are responsible for the large deviations from the mean pressure level.

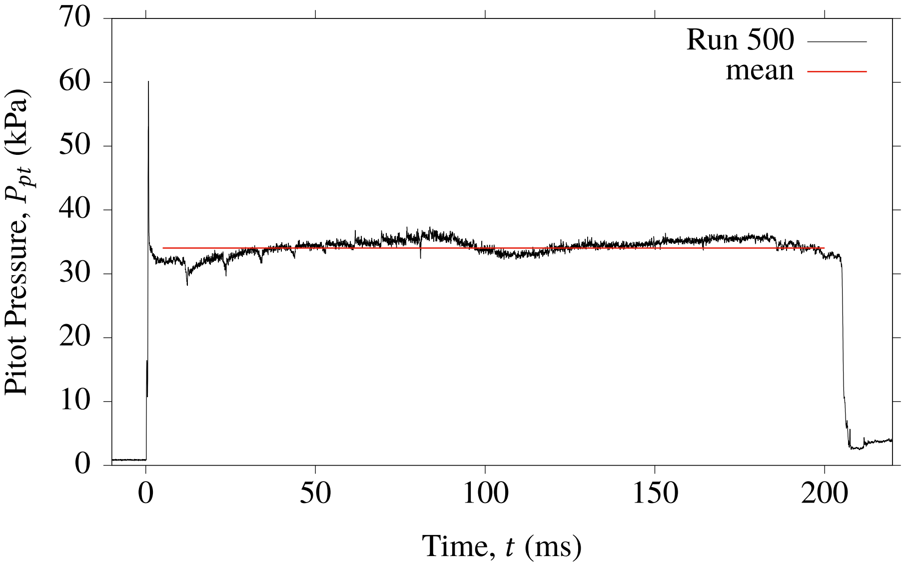

Figure 5.7: Centreline Pitot pressure for Run 500. Mean Pitot pressure from 5 – 200 ms is illustrated as the horizontal line.

A 6th order digital Butterworth high-pass filter with a cutoff frequency greater than the piston oscillation frequencies was desired. The cutoff frequency was set by calculating RMS Pitot pressure fluctuations $\langle P'_{pt} \rangle$ at multiple frequencies and plotting the results as shown in Fig. 5.8. As expected, the fluctuation amplitude is dependent on the high-pass filter cutoff frequency. At less than 200 Hz there is significant contribution from the piston oscillations which result in an increased RMS pressure level. By 300 Hz the contribution to the RMS fluctuations of the low frequency piston oscillations is negligible. Therefore, a 300 Hz cutoff frequency was used for isolation of the Pitot acoustic fluctuations.

An important consideration for data interpretation is that the centreline Pitot data contained spikes that were not repeatable in time or amplitude which had a significant impact on the resultant RMS fluctuation values. The spikes in Pitot pressure were occasionally detected using high speed schlieren imaging, recorded at 2000 frames per second with a 250 μs exposure time. An example of disturbance detection is displayed in Fig. 5.9. The high speed camera trigger was recorded using the data acquisition system and this information allowed the exposure start timing for each frame to be calculated. Figure 5.9d displays the fluctuating Pitot pressure in the region of one of these randomly appearing spikes, with the beginning of frame 404 exposure and end of frame 407 exposure annotated.

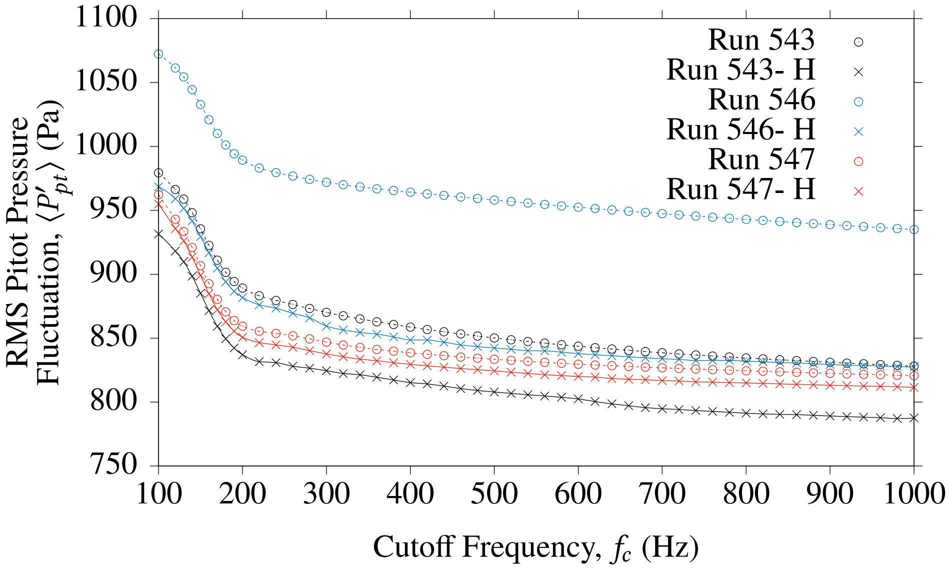

Figure 5.8: Effect of the high-pass filter cutoff frequency on RMS Pitot pressure on the nozzle centreline. A suffix H indicates that the RMS data was Hampel filtered to remove outliers likely caused by particulates.

As these spikes were unpredictable and did not occur in all runs, they were eliminated using a Hampel filtering technique for the purposes of RMS calculation. It is likely that these unpredictable and randomly occurring spikes of Pitot pressure are caused by particulates interacting with bow shock ahead of the pressure transducer. For the data displayed in Fig. 5.8, the result of this filtering is most pronounced for Run 546, while Run 547 had fewer spikes which were of lower amplitude so the effects of the filtering were minimal. Hampel filtering was set to replace data outside 5 standard deviations of the mean of a 1001 sample window centred on the point of interrogation with the median value of the window. As shown in Fig. 5.10, this predominantly removed only the non-repeatable data spikes from the fluctuation signal. Even at a filter setting of five standard deviations there were some falsely identified outliers, however, the impact of this on the overall RMS calculation was negligible.

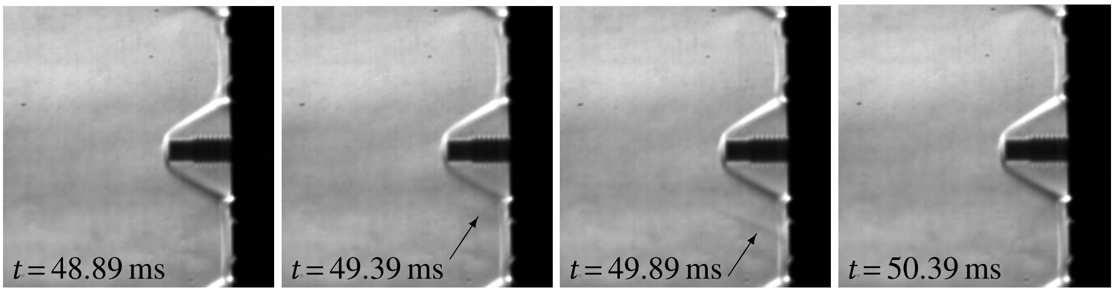

(a) Frame 404 (b) Frame 405 (c) Frame 406 (d) Frame 407

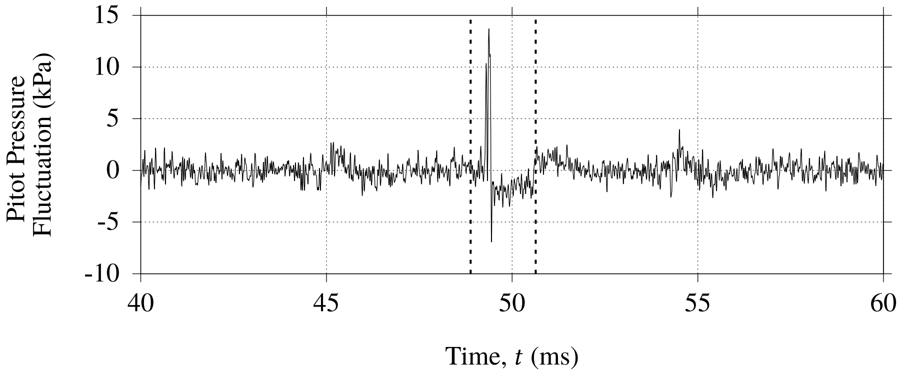

(e) Fluctuations of Pitot pressure

Figure 5.9: Schlieren image sequence of centreline pressure transducer for Run 543. (a) No disturbance evident, (b) disturbance first visualised below bow shock, (c) disturbance propagates perpendicular to bow shock in a downwards direction, (d) disturbance no longer evident, (e) P'_{pt} variation with time with the beginning of frame 404 exposure and the end of frame 407 exposure shown as the broken vertical lines. Figure 5.9d contains an embedded video of frames 404-407 that can be played using Adobe Acrobat Reader, initiated by clicking the subfigure. This video aids in identifying the disturbance propagation, especially for frame 405.

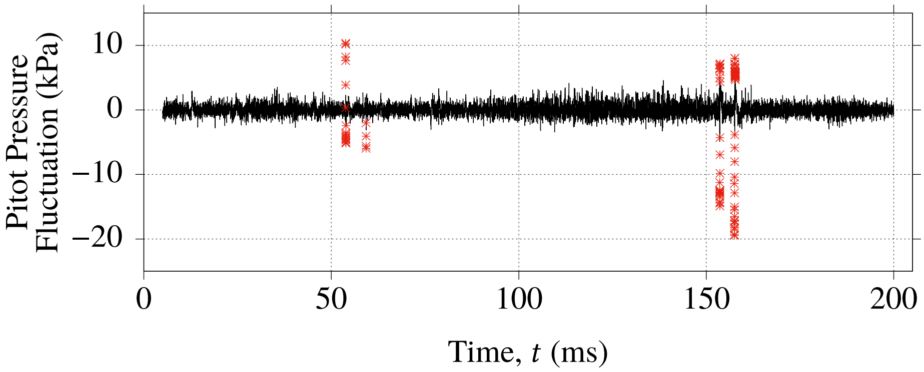

(a) Run 546

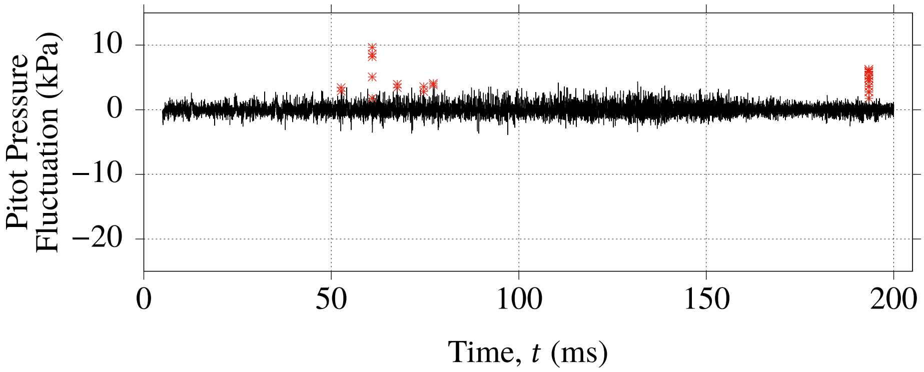

(b) Run 547

Figure 5.10: Removal of outliers (∗) from Pitot pressure fluctuation signals.

5.7.2 Traditional Type Root-Mean-Square Analysis

In the 300 Hz–25 kHz range at $x = 50$ mm, the percentage Pitot pressure fluctuations from $t = 5$ ms to $t = 200$ ms are presented in Fig. 5.11 for six runs and four different transducer locations. Traditionally, the fluctuations in Pitot pressure are presented using a survey of centreline Pitot pressure, but in Fig. 5.11 off axis data is also presented to demonstrate the level of uniformity in fluctuation amplitude across the core flow. The variance in results across runs appears smallest at the nozzle centreline. The appearance of multiple data points at the same radius or $r = 30$ mm for Runs 545, 546 and 547 arises because two transducers, located at the same distance either side of the nozzle centreline, were used in the Pitot rake. Mean centreline Pitot pressure fluctuation across five runs using the high-pass filtering technique in the 300 Hz–25 kHz frequency band was 2.76 %.

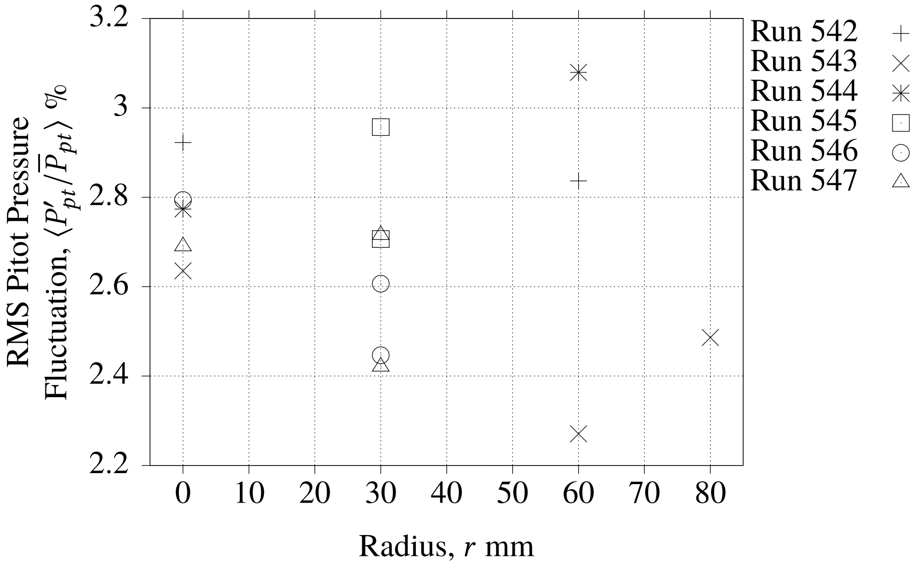

Figure 5.11: Percentage Pitot pressure fluctuations from $t = 5 - 200$ ms for Runs 542 – 547.

5.7.3 RMS Pitot Pressure Fluctuations Using Welch's Method

The pitot pressure fluctuations were analysed using the power spectral density technique for t = 5–200 ms for f = 300 Hz–25 kHz. The spectra of the centreline pitot pressure fluctuations, calculated using Blackman windows of 2^{12} points width and 50 % are shown in Fig. 5.12. There are two distinct disturbance bands on a broadband noise background: 1) the low frequency content associated with piston oscillation; and 2) a noise band between 3 – 4 kHz.

Three 100 kHz amplifiers were available for use: one AMETEK Model 5113 low noise pre-amplifier (LN) and two Alligator USBPIA-S1 instrument amplifiers (A1 and A2).

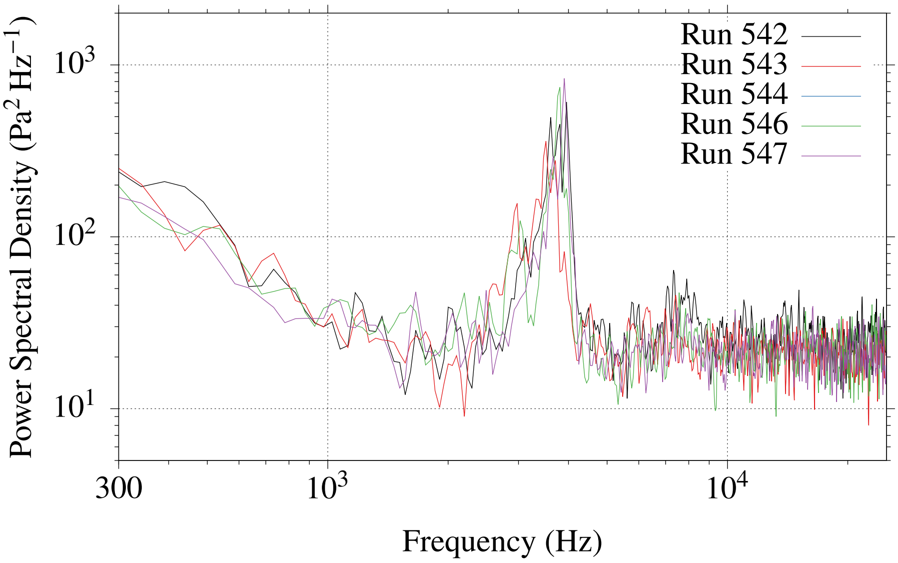

Figure 5.12: Power spectral density of the Pitot pressure fluctuations for five runs at the nozzle centreline.

Therefore, in any given run, a maximum of three Kulite pressure transducers could be amplified to examine the frequency content up to 25 kHz. The baseline (pre-flow) noise was found by analysing a 195 ms section of data ending 5 ms before flow onset. The baseline amplifier noise as illustrated by the broken lines in Fig. 5.13 was found to be significantly lower than the signal, shown as the solid lines in Fig. 5.13. Spikes at 6.5 and 10 kHz from the LN amplifier were not evident in the test data. The content in the 3–4 kHz bandwidth was consistent across all transducers and amplifier combinations as shown in Fig. 5.13.

The root-mean-square pressure fluctuations within the frequency band f_1–f_2 is:

$$\langle P' \rangle = \sqrt{\int_{f_1}^{f_2} \mathrm{PSD}(f)\,\mathrm{d}f} \tag{5.2}$$

As predicted by Parseval's theorem, the root-mean-square of the pitot pressure fluctuations calculated from the PSD is equal to the RMS pitot pressure fluctuations calculated by the traditional type analysis which were presented in Fig. 5.11.

5.7.4 Analysis in the Time and Frequency Domain

The evolution of the frequency content of the Pitot pressure fluctuations throughout flow test time was examined through the use of a spectrogram as shown in Fig. 5.14. Similar windowing to the PSD fluctuations was used, however the Blackman window was reduced to 2^{11} points wide with 90 % overlap to improve the graphical presentation of the spectrogram. Prior to the flow onset, two peaks appear at 6.5 and 10 kHz identified as amplifier noise in Fig. 5.13. At $t = 0$ s, the impulsive flow starting is shown as a high amplitude broadband signal, and this is annotated as feature (i) in Fig. 5.14.

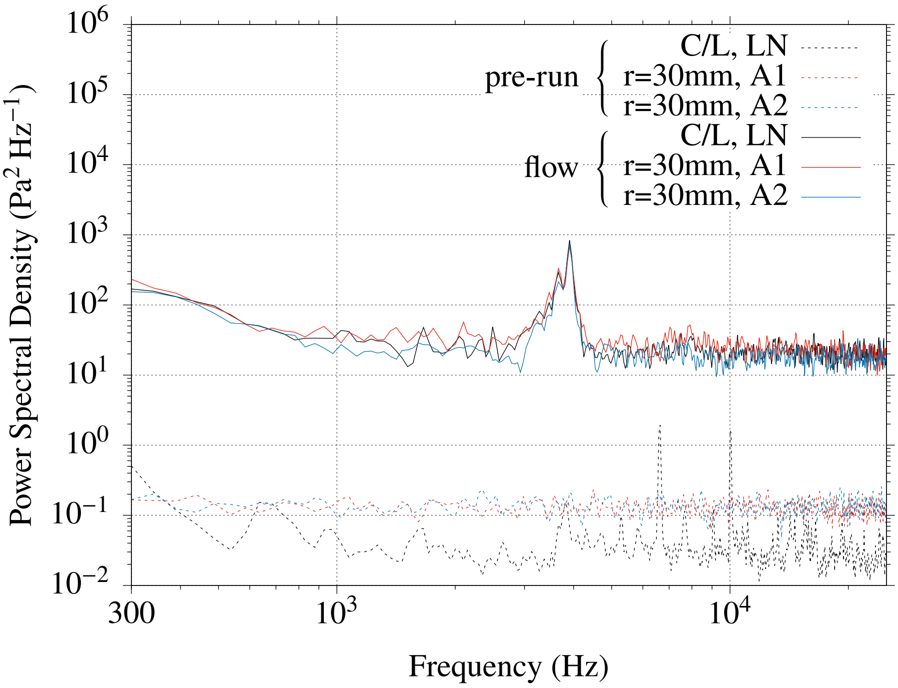

Figure 5.13: Power spectral density of the Run 547 Pitot pressure fluctuations for three transducer and amplifier combinations.

Acoustic pressure fluctuations from the turbulent boundary layer of the supersonic nozzle walls are known to dominate the fluctuations and are recognizable as broadband noise, while other sources such as flow path geometry and valves can exhibit dominant frequencies (Lafferty & Norris, 2007). For the duration of the flow, terminating at feature (vi), there is an approximately uniform level of broadband frequency content which is typical of the acoustic disturbances radiated from the turbulent boundary layer on the nozzle wall. Most evident in the 0 – 100 ms period are the periodically occurring, high amplitude disturbances at frequencies lower than 300 Hz. These are caused by the interaction of the piston and reflected expansion waves initiated by diaphragm rupture: the first three of which are annotated (ii) on Fig. 5.14, and these events were also identified as (ii) on the time-resolved barrel pressure signal shown in Fig. 5.1. Flow termination (vi) is shown as a region of a high amplitude, low frequency energy and a sudden decrease in broadband energy levels. Of most interest is the high amplitude disturbance at 3 – 4 kHz starting at approximately 65 ms (feature (iii)) and continuing for the remainder of the flow. Feature (iii) is initiated approximately 20 ms before the reflected expansion wave returns to the nozzle inlet (iv), and therefore feature (iii) is not a function of the reflected expansion wave. When the reflected expansion wave returns for a second time (v) there is a small period of flow where (iii) is not detected.

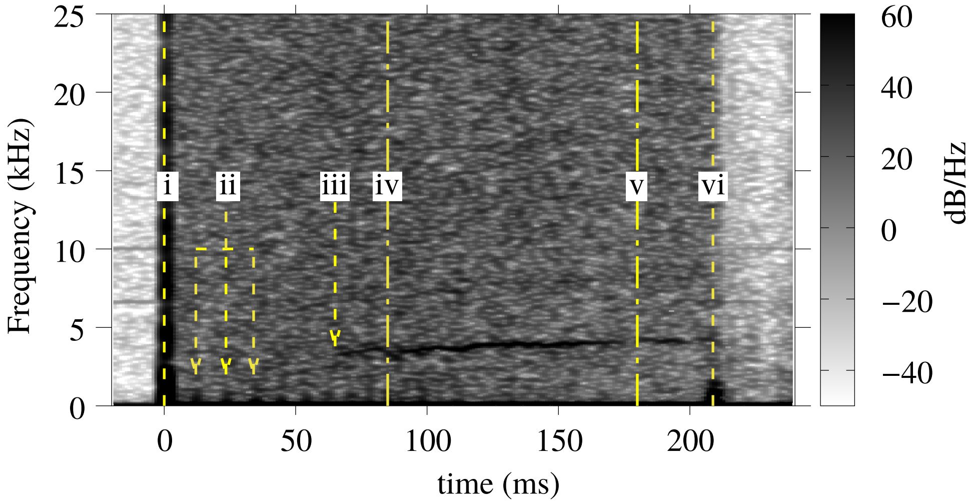

Figure 5.14: Spectrogram of Run 547 centreline Pitot pressure transducer created using Blackman windows of width 2^{11} points with 90 % overlap. Features: (i) Test flow first reaches the Pitot pressure transducer; (ii) the effects of the first three reflected expansion waves in the barrel; (iii) the start of the 3 – 4 kHz disturbance; (iv) the reflection of the expansion wave initiated by the diaphragm rupture arrives at the nozzle inlet end of the barrel; (v) the reflected expansion wave (iv) returns to the nozzle inlet a second time; (vi) termination of flow.

Since initiation of feature (iii) preceded event (iv) by 20 ms, a spectrogram of the barrel pressure signal (Fig. 5.15) with the same windowing method was generated to investigate if there was a similar disturbance event in the barrel. The barrel pressure transducer is located in a noisier background environment, however distinct features were still identifiable, and features (i) – (vi) are consistent with the annotations on Fig. 5.14. Two additional features are annotated on Fig. 5.15: (vii) is the 3 – 4 kHz disturbance the period $t = 65 – 85$ ms; and (viii) is the piston passing over the barrel pressure transducer.

The interaction of the piston and reflected expansion waves (feature (ii)) is evident in Fig. 5.15 supporting the discussion of Fig. 5.14. Unlike Fig. 5.14, there are high energy levels above 300 Hz in the events recorded by the barrel transducer. This may arise in part due to the dual detection of waves as shown in Fig. 5.2. At approximately 190 ms, a sudden termination of high energy content features and a general decrease in the broadband noise were observed. This arises from the piston passing the barrel pressure transducer (viii), and any spectral data between this event and the flow termination at approximately 210 ms is not representative of the nozzle inlet conditions.

Like Fig. 5.14, Fig. 5.15 contains a region of high amplitude spectral content at 3 – 4 kHz beginning at $t = 65$ ms, and this energy remains until the test gas entering the nozzle is no longer measured by the barrel pressure transducer. In the barrel, the narrowband disturbance is repeatedly observed at positive integer multiples of 3 – 4 kHz at a decaying amplitude. Therefore, the narrowband 3 – 4 kHz energy originates in the barrel.

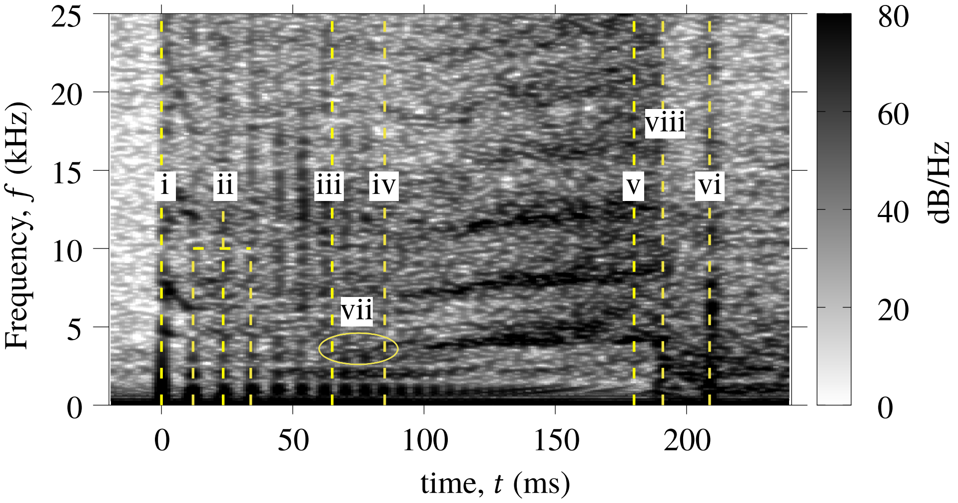

Figure 5.15: Spectrogram of Run 547 barrel transducer created using Blackman windows of width 2^{11} points with 90 % overlap. Features (i) – (vi) are the same as allocated in Fig. 5.14. The 3 – 4 kHz disturbance at the barrel pressure transducer from $t = 65$ ms to $t = 190$ ms, and the region from 65 – 85 ms have been annotated as (vii). At $t = 190$ ms the piston passes over the barrel pressure transducer and no narrowband frequency content is detected behind the piston.

5.7.5 Amplitude of Pitot Pressure Fluctuations

Due to the change in tunnel noise characteristics, both in amplitude and frequency content, it is appropriate to divide the tunnel noise result into two periods. Period 1 is from the establishment of hypersonic flow through to the arrival of the 3 – 4 kHz disturbance at $t = 65$ ms (Fig. 5.1, feature iii) and this period is dominated by broadband acoustic noise radiated from the turbulent boundary layer on the nozzle wall. Period 2 is the time bounded by the arrival of the 3 – 4 kHz disturbance at $t = 65$ ms and termination of the nozzle flow, and this period contains the high level 3 – 4 kHz energy content superimposed on the broadband acoustic environment. Table 5.1 shows the centreline root-mean-square Pitot pressure fluctuations calculated using the high-pass filter technique. From 5 – 65 ms the RMS Pitot pressure fluctuations measured at the nozzle centreline were consistently 2.52 % with Run 542 having a higher noise level at 2.78 %. The increased background noise level was the result of less than optimal facility operation – for Run 542 the test section pressure immediately before diaphragm rupture was 1 kPa, while for the other runs the test section pressure was 590 – 630 Pa. Since operation at test section pressures as high as 1 kPa are not routine and the results were outside what can be expected for a representative test, Run 542 was excluded from the calculation of the average Pitot pressure and the average Pitot pressure fluctuations. No centreline Pitot pressure measurements were made in Run 545. A significant increase of centreline Pitot pressure fluctuations from 2.52 % for $t = 5-65$ ms to 2.86 % for $t = 65-200$ ms can be observed.

	$t = 0-65$ ms		$t = 65-200$ ms	
Run	RMS (%)	$\overline{P}_{pt}$ (kPa)	RMS (%)	$\overline{P}_{pt}$ (kPa)
541	2.52	30.8	–	–
542	2.78	30.4	3.12	32.1
543	2.50	31.2	2.67	31.8
544	2.52	30.5	3.12	31.8
546	2.52	29.7	2.87	31.2
547	2.52	29.9	2.78	31.7
Mean	2.52	30.4	2.86	31.6

Table 5.1: Centreline Pitot pressure fluctuations.

5.8 Comparison to Other Facilities

A method for comparison of root-mean-square pressure fluctuations in different supersonic and hypersonic test facilities independent of Mach number, facility size and working fluid was proposed by Laderman (1977). RMS pressure fluctuations are normalised by dynamic pressure:

$$\text{Normalised Noise} = \frac{\langle P'_{pt} \rangle / \overline{P}_{pt}}{\gamma M^2/2} \tag{5.3}$$

and plotted as a function of the Reynolds number based on nozzle exit diameter. Using this method the TUSQ Mach 6 noise level for the 1 MPa total pressure condition is compared to four facilities, two blowdown (AEDC9 and VKI) and two Ludwieg tubes (BAM6QT and HLB), in Fig. 5.16. Resolved bandwidths for each facility differ significantly, however the TUSQ normalised noise level compares well with published data from other facilities.

Consistent with the theory of the stabilisation effect with increasing Reynolds number, normalised RMS noise for published data decreases as Reynolds number increases. This theory allows qualitative comparison with facilities of higher Reynolds number.

Since two distinct acoustic environment periods were identified, the TUSQ noise levels in the 0.3 – 25 kHz bandwidth are shown for the periods 5 – 65 ms and 65 – 200 ms on Fig. 5.16. Because of the different frequency bands presented in Fig. 5.16, direct comparison of the normalised noise levels is difficult, however qualitative comparisons can be made.

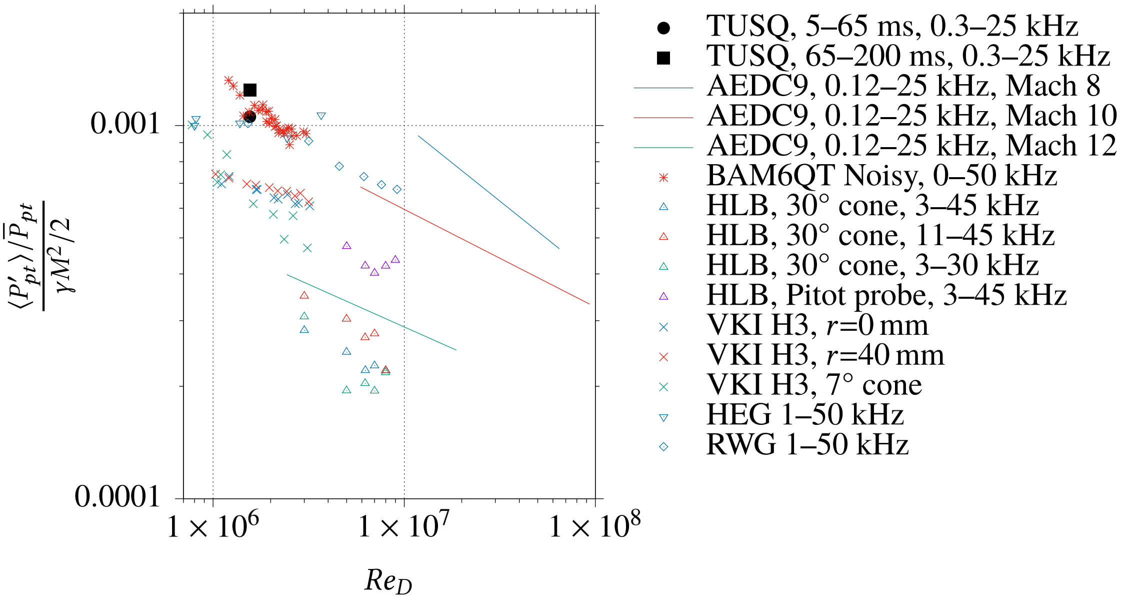

Figure 5.16: Comparison of centreline TUSQ RMS Pitot pressure fluctuations to selected facilities and conditions - AEDC9 (Lafferty & Norris, 2007), BAM6QT noisy (Steen, 2010), HLB (Ali, Wu, Radespiel, Schilden & Schroeder, 2014), VKI (Masutti, Spinosa, Chazot & Carbonaro, 2012), HLB (Wagner et al., 2018) and RWG (Wagner et al., 2018).

Normalised Pitot pressure fluctuations for the noisy operation of BAM6QT (Purdue University Boeing/AFOSR Mach 6 Ludwieg tube) from nominally 0 Hz to 50 kHz (Steen, 2010) are similar to the levels identified in TUSQ. Normalised noise levels in TUSQ appear higher than in VKI (von Kárman Institute Mach 6 blowdown to vacuum) (Masutti et al., 2012), however the frequency range analysed is unclear. Similar instrumentation to this research was used by Masutti et al. (2012) (Kulite XCA-093-50A, B-screen exposed directly to the flow) where a frequency roll-off of $f^{-15/3}$ from 30 – 45 kHz was attributed to the energy decay of pressure fluctuations. This was recognised as higher than the Kolmogorov $k^{-7/3}$ law for pressure fluctuations decay, but the change in dynamic response of the sensor when fitted with the B screen was not considered and is likely to have affected the roll-off. However, due to the small amplitude of frequency content above 30 kHz, the RMS fluctuation values presented by Masutti et al. (2012) are likely to be dominated by the 30 kHz content. Experimental results in HLB (Technische Universität Braunschweig Mach 6 blowdown facility) (Ali et al., 2014) exhibit a high level of spread across methods due to the different frequency bands analysed. Because of the minimum 3 kHz considered, the HLB data is of limited value for direct comparison to TUSQ. By analysing the TUSQ data in the 3–25 kHz bandwidth, noise levels reduce to 88 % of the 0.3–25 kHz value. It is likely that there is also significant content at frequencies less than 3 kHz present in HLB. Normalised noise level data for AEDC9 (Arnold Engineering Development Center Hypervelocity Wind Tunnel 9 blowdown facility) (Lafferty & Norris, 2007) is at a significantly higher Reynolds number than TUSQ, however the lines shown agree well with the other normalised pressure fluctuation data. Wagner et al. (2018) used a 20° half angle wedge probe and a classic blunt-body Pitot probe to measure the fluctuations of Pitot pressure in the free piston driven reflected shock tunnel HEG (High Enthalpy Shock Tunnel Göttingen) and the Ludwieg tube facility at DLR Göttingen (RWG) and found strong agreement between the two probes used for $Re_u \lesssim 10 \times 10^6\,\mathrm{m}^{-1}$ for $f = 1-50$ kHz. The normalised Pitot pressure fluctuations in HEG are similar level to those in TUSQ at a similar Re_D, and the trend for RWG follows the trend for BAM6QT Noisy which was found to have similar noise levels to TUSQ. Overall, the normalised RMS Pitot pressure fluctuations of the Mach 6 TUSQ flow compare well with the other hypersonic facilities shown.

5.9 Conclusions

The acoustic noise level of the TUSQ Mach 6 environment from 300 Hz to 25 kHz was measured by a centreline Pitot survey of the hypersonic flow, supplemented by analysis of Pitot pressure data within the core flow at $r = 30$, 60 and 80 mm. Analysis of the Pitot pressure fluctuations was performed using two methods: (1) a high-pass filtering technique; and (2) a power spectral density (PSD).

Spectrogram analysis of the Pitot pressure and barrel pressure data identified that there is a $3-4$ kHz disturbance originating in the barrel section ahead of the piston which propagates into the hypersonic flow from approximately 65 ms after the hypersonic flow is established. Consequently, it was appropriate to quote two centreline tunnel noise levels in the 300 Hz to 25 kHz bandwidth:

1. 2.52 % from $t = 5-65$ ms, prior to the arrival of the narrowband $3-4$ kHz content;

and

2. 2.86 % from $t = 65 - 200$ ms, after the arrival of the narrowband $3 - 4$ kHz content.

Chapter 6

Heat Flux Probes

Contents

6.1 Introduction

To obtain the fastest possible transient heat transfer measurements, it is advantageous to base the heat transfer measurements on temperature data obtained directly at the surface of the body under study (Sanderson & Sturtevant, 2002). This can be achieved using surface junction thermocouples, provided that the junction is sufficiently thin. By using fine grit abrasive papers, thin junctions are more likely to be formed than with coarse abrasive papers or scratching techniques using scalpels and similar implements.

The measured temperature of the surface junction thermocouple can be converted to a surface heat flux via an impulse response filter, and the surface heat flux used to calculate the total temperature of the flow. The design and application of impulse response filters is described in Section 6.3. For a semi-infinite surface junction thermocouple, the impulse response can be created using a pair of analytical basis functions for heat flux and surface temperature, and the thermal effusivity of the thermocouple. The thermal effusivity is known to be highly uncertain for surface junction thermocouples, but can be determined using experimental calibration techniques.

The heat flux (q) identified using the surface junction thermocouple measurements is

$$q = h_c \left(T_0 - T_w\right) \tag{6.1}$$

where h_c is the heat transfer coefficient, T_0 the stagnation temperature, and T_w the temperature of the thermocouple surface. The heat transfer coefficient can be experimentally determined by measuring the stagnation point heat flux in a nominally identical flow at a range of thermocouple operating temperatures.

6.2 Design and Manufacture of Heat Flux Gauges

6.2.1 Thermocouple Design and Construction

Type E (Chromel-Constantan) coaxial surface junction thermocouples were manufactured at USQ. The design is presented in Appendix B and features a 3 mm long, 3.2 mm diameter chromel annulus with a 6/0 tapered hole, and a matching 4.5 mm long constantan pin. The constantan pin was oxidised in a temperature controlled furnace at 850 °C for 2 h prior to assembly, while the chromel annulus was not heat treated. The oxide layer on the constantan pin forms a thin electrically insulating layer between the positive (chromel) and negative (constantan) legs when assembled.

To assemble the thermocouple, the pin is pressed into the annulus with approximately 10 kg force. However, during assembly the oxide layer is prone to damage, and such damage can result in electrical shorting in the assembled gauge and subsequent rejection of the thermocouple. The success rate was improved by adding one to two drops of Resbond 907TS Green to the tapered hole of the annulus immediately prior to pressing the pin into the hole. Resbond 907TS Green is an electrically insulating high temperature thread sealant with 2 Pa s viscosity, designed for fine openings up to 76 μm thick. When the assembly is pressed together the thread sealant is dispersed ahead of, around and behind the pin. The increased success rate was attributed to a combination of the thread sealant lubricating the components and the thread sealant immediately penetrating and filling any small scratches of the oxide layer.

Post assembly, the oxide coating was removed from the rear surface of the pin in preparation for spot welding of the thermocouple extension wires. Once the two extension wires were attached to the corresponding thermocouple legs, the resistance through the thermocouple circuit was measured. If the resistance was in the order of 100 kΩ or greater the two thermocouple materials were well electrically insulated. Thermocouple assemblies that were well electrically insulated were accepted and ready for the formation of the surface junctions.

To form the surface junctions, the thermocouple was held in a small benchtop vice with soft rubber jaws (Fig. 6.1), and the thermocouple extension wires connected to a benchtop multimeter to measure the junction resistance. Using a flat solid surface, such as polycarbonate, as a backing material for the abrasive paper, the thermocouple face was scratched using paper of increasing grit size until the resistance was in the order of 10 Ω or less, which indicated at least one junction had been formed. Junctions formed with smaller grit sizes were likely to result in faster response thermocouples, however when it was clear a junction was unable to be created at a particular grit size, the next larger grit size was used. Should large particle sizes be required to form the junctions, the thermocouple response time could be improved by carefully polishing the surface with fine grit abrasive paper to reduce the depth of the junctions.

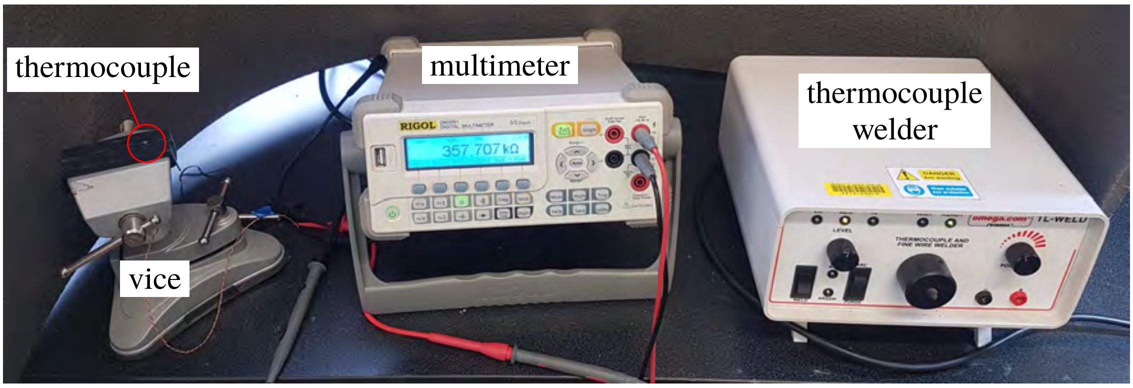

Figure 6.1: Equipment for thermocouple assembly.

6.2.2 Thermocouple Housing

For use in the hypersonic flow of TUSQ, the thermocouples had to be mounted in a housing that could be used to interface with a probe support, chosen to be the same rake as implemented in the Pitot pressure survey. To avoid the complexities of a non-uniform heat flux distribution on a hemisphere cylinder, a flat faced geometry was selected where a uniform heat flux distribution is found from the centreline of the body up to about 0.6 R

where R is the radius of the flat nosed body (Kemp et al., 1959). For a thermocouple of $r = 1.6$ mm, the minimum body radius of the flat nosed body was therefore 2.7 mm. However, for interfacing with the M5×0.8 rake geometry, R was set to 5 mm. A flat-nosed body was also advantageous for the identification of the thermal effusivity (also known as thermal product) of the thermocouple using the reflected shock calibration technique where a flat end wall is required.

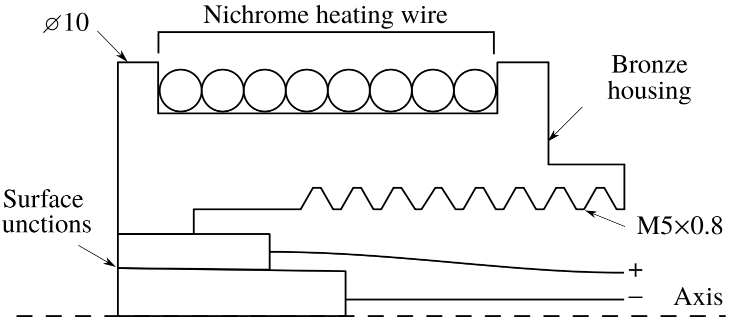

Figure 6.2: Heat flux gauge design for experimentation in TUSQ.

Illustrated in Fig. 6.2, the 10 mm flat faced probe is fitted with an enamelled nichrome resistance heating wire coil to preheat the thermocouple so that it can be operated at different initial temperatures which facilitates the experimental identification of the convective heat transfer coefficient h_c. A second probe head geometry of 10 mm diameter without the provision for heating wire was also used. All probe heads were machined from bronze C65500 silicone bronze bar stock. Bronze C65500 was selected because of its similar thermal properties to the thermocouple materials. A mismatch of material properties between a sensor body and the material in which the sensor is mounted can result in significant errors in transient heat flux measurements (Gatowski, Smith & Alkidas, 1989). The nichrome heating wire was 32AWG (0.2109 mm diameter) with a resistance of $36.19\,\Omega\,\mathrm{m}^{-1}$. A 0.4 mm pitch thread of depth 0.3 mm was machined on the bronze probe head, enabling the heating wire to be tightly coiled for twelve revolutions of the probe (Fig. 6.3a).

The heating wire was secured to the probe head using Resbond 907TS Green (Fig. 6.3b) and allowed to cure at room temperature for a minimum of 4 h prior to being post cured at 150 °C for another 2 h. Once fully cured, the Resbond was sanded so the probe geometry was a smooth 10 mm diameter cylinder. This process was completed before the thermocouple was installed in the bronze housing component (Fig. 6.2).

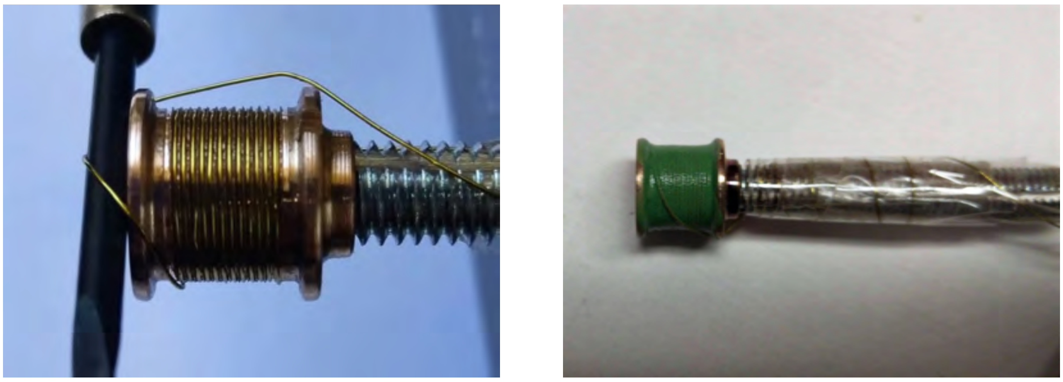

(a) Fitting of heating wire (b) First Resbond coating

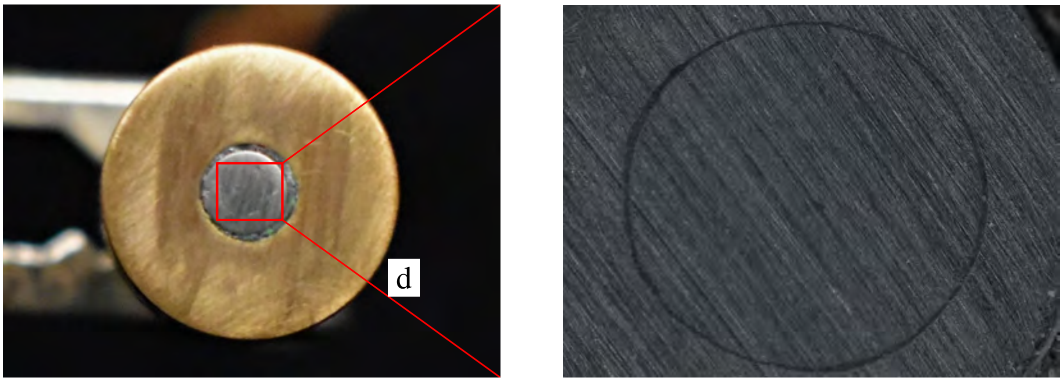

(c) Heat flux gauge assembly (d) Surface of thermocouple

Figure 6.3: Assembly of the heat flux gauges.

Following the sanding of the cylindrical housing body, the thermocouple had to be installed into the housing. Because the thermocouple annulus was not oxidised, a thin layer of PTFE was used as an electrical insulating layer between the thermocouple and housing body. The PTFE layer also acted to seal the gap between the thermocouple and the housing body. With the probe held such that the thermocouple axis was vertical and the sensing surface of the thermocouple face up, two drops of Resbond 907TS were applied to the face of the thermocouple and housing. The Resbond was allowed to penetrate any openings and cure for 24 h to secure the thermocouple in the housing. When the Resbond was set, and therefore the thermocouple permanently fixed to the housing body, the assembly formed a heat transfer gauge.

Once cured the surface layer of Resbond was removed from the face of the heat transfer gauge by a combination of peeling, chipping and sanding. This process identified the difficulty of accurately aligning the surfaces of the thermocouple and housing as a thin layer of Resbond occasionally remained on the thermocouple. Where this occurred the heat flux gauge was sanded to remove the Resbond from the surface and ensure a flush mounting of the thermocouple in the housing.

All thermocouples required resurfacing after mounting in the housing. A microscope image of the surface of a thermocouple is shown in Fig. 6.3d, and the oxide layer visible as the black circle.

Type E thermocouple wire was unable to be sourced; instead chromel (yellow) wire was taken from the positive lead of a spool of type K thermocouple wire and constantan (red) from the negative leg of a spool of type T thermocouple wire. Therefore, although appearing as type K, the thermocouple wires are type E and consistent with the thermocouple materials.

6.3 Impulse Response Analysis

The unsteady conduction of heat within a solid body is described by a linear partial differential equation when the temperature gradients remain small such that thermal properties can be treated as constants. The unsteady conduction of heat in a one-dimensional semi-infinite solid is described by

$$\frac{\partial^2 T(x,t)}{\partial x^2} = \frac{1}{\alpha}\frac{\partial T(x,t)}{\partial t} \tag{6.2}$$

where T is the temperature, x is the spatial coordinate normal to the surface, t is time, and α is the thermal diffusivity of the material.

The heat flux gauge results were analysed using the impulse response method described by Oldfield (2008) which uses analytical models for one dimensional heat conduction within the gauge substrate to define suitable impulse response filters. The response of a linear, time invariant (LTI) system can be calculated from the impulse response $h(t)$ of the system by the convolution ($*$)

$$q(t) = h(t) * T(t) = \int_{-\infty}^{\infty} h(\tau)T(t-\tau)\mathrm{d}\tau \tag{6.3}$$

where τ is the dummy time variable for the convolution integral. In the continuous time domain, $h(t)$ often has singularities at the origin (Oldfield, 2008), but can be replaced by the discrete time domain expression

$$q[n] = h[n] * T[n] = \sum_{k=-\infty}^{\infty} h[n-k]\, T[k] \tag{6.4}$$

when signals $q(t)$ and $T(t)$ are sampled at sampling period T_s, or sampling frequency $f_s = 1/T_s$ to give discrete sequences $T[n] = T(nT_s)$, k is the summation variable, and $n = \ldots, -3, -2, -1, 0, 1, 2, 3, \ldots$. The signals are assumed to be zero for $n < 0$ and of finite length N. Therefore Eq. 6.4 becomes

$$q[n] = h[n] * T[n] = \sum_{k=0}^{N-1} h[n-k]\, T[k] \tag{6.5}$$

for $k = 0, 1, 2, \ldots, N-1$. Assuming a unit step input of $q(t)$, this discrete convolution can be solved using the MATLAB command `h = filter(q, T, delta)` where `q` is a vector of ones of length N, `T` is the thermocouple temperature signal, and `delta` is the Dirac delta function.

For a surface junction thermocouple that can be treated as semi-infinite, the impulse response filter can be created using the function created by Oldfield (2008)

```
[h,shift] = desT2qsiimp1(fs, np, rrck, test)
```

where `fs` is the sample frequency, `np` equal to or greater than the length of the signal, `rrck` the thermal effusivity of the thermocouple and `test` a Boolean flag for testing of the impulse response.

Once $h[n]$ has been determined, it can be used to calculate the transient heat flux from an experimentally measured surface temperature signal using the MATLAB command `q = fftfilt(h, T)` which solves the convolution of Eq. 6.5.

6.4 Calibration of the Heat Flux Gauges

6.4.1 Introduction

The impulse response filter $h[n]$ can be created analytically if a pair of basis functions $T_1(t)$ and $q_1(t)$ can be defined. A surface junction thermocouple measures the temperature at its surface $T_1(t)$ which is the result of a surface heat flux $q_1(t)$. Treating the surface junction thermocouple as a semi-infinite solid, the most convenient basis functions for generating $h[n]$ are the response $T_1(t)$ for a step in $q_1(t)$ (Oldfield, 2008).

The solution of the heat conduction equation for a semi-infinite substrate in Laplace transformed form is (Oldfield, 2008)

$$\overline{T_1}(s) = \frac{1}{e_1}\frac{1}{\sqrt{s}}\overline{q_1}(s) \tag{6.6}$$

where $e_1 = \sqrt{\rho_1 c_1 k_1}$ is the thermal effusivity of the substrate. For a step in $q_1(t) = u(t)$, $\overline{q_1}(s) = 1/s$, and therefore

$$\overline{T_1}(s) = \frac{1}{\sqrt{e_1}} s^{-3/2} \tag{6.7}$$

Taking the inverse Laplace transform,

$$T_1(t) = \frac{2}{e_1}\sqrt{\frac{t}{\pi}} \tag{6.8}$$

which shows that an impulse response $h[n]$ can be created for the surface junction thermocouple if its thermal effusivity is known. For the surface junction thermocouples used in this research, the thermal effusivity of the thermocouple must be determined experimentally. The thermal effusivity of a surface junction thermocouple can be identified by experimental calibration where a known heat flux is applied to the surface of the thermocouple.

The reflected shock technique has previously been applied to the calibration of microsecond response heat flux gauges (Buttsworth, 2001; Marineau & Hornung, 2009) and is suitable because the heat flux in a reflected shock tube is well defined for tens of microseconds. Instead it is used to determine thermophysical properties of a heat flux gauge for use in analytical impulse response filters. To use the reflected shock calibration technique, the heat flux to the end wall (containing the thermocouple) must be determined analytically.

Fluid bath plunging techniques have been used for determining the thermal capacitance of calorimeter gauges (Sprinks, 1963). However, for the calibration of surface junction thermocouples on microsecond timescales, it is difficult to ensure a sufficiently rapid plunging of the thermocouple into the fluid bath (Buttsworth, 2001).

Radiative techniques can apply a well defined input heat flux to a heat flux gauge for longer durations than the reflected shock and fluid bath plunging techniques. These techniques use a light source of calibrated intensity (Gatowski et al., 1989) and require the knowledge of the absorptivity of the surface of the heat flux gauge. For an unknown absorptivity, the heat flux gauge may be coated with another well defined material for calibration, however this may introduce uncertainty to the model due to the introduction of another material in the vicinity of the thermocouple junctions. A radiative technique allows a short or long duration heat flux to be applied, however the exposure time should be chosen to be of the same time scale as the heat flux gauge (Buttsworth, 2001). In addition to identifying the thermophysical properties of a heat flux gauge for use in analytical models, the increased calibration duration possible with radiative techniques facilitates identification of an experimental impulse response independent of an analytical model. However, the equipment required to implement a radiative calibration technique is not currently available at USQ.

The reflected shock calibration technique was selected for identifying the thermophysical properties of the thermocouples, with analytical heat flux models required for determining heat flux from a measured temperature history. The radiative technique was used for the calibration of heat flux gauges for the collaborative research campaign at the Institute for Space Systems (IRS) within the University of Stuttgart. The radiative calibration technique is discussed in more detail in Section 8.5.1.

6.4.2 Reflected Shock Tube Method

Illustrated in Fig. 6.4, the shock tube was initially filled with ambient air from the surrounding laboratory environment. A light Mylar diaphragm separated the driver and driven sections and the thermocouple was mounted on the centreline of the shock tube, flush with the end wall. Two pressure transducers were mounted flush with the inside wall of the shock tube to identify the shock wave propagation along the shock tube. PT1 is located approximately 45 tube diameters downstream of the diaphragm station which is normally sufficient (5-40 tube diameters) for full shockwave formation at a constant velocity (Davis & Curchack, 1969). The pressure of the driver gas was increased until the pressure differential at the diaphragm was great enough that the diaphragm ruptures.

The instant immediately prior to rupture is shown as $t = 0$ on Fig 6.5. Immediately following the diaphragm rupture, a shock wave is generated which propagates in the positive x direction towards the end wall where the thermocouple is mounted. The

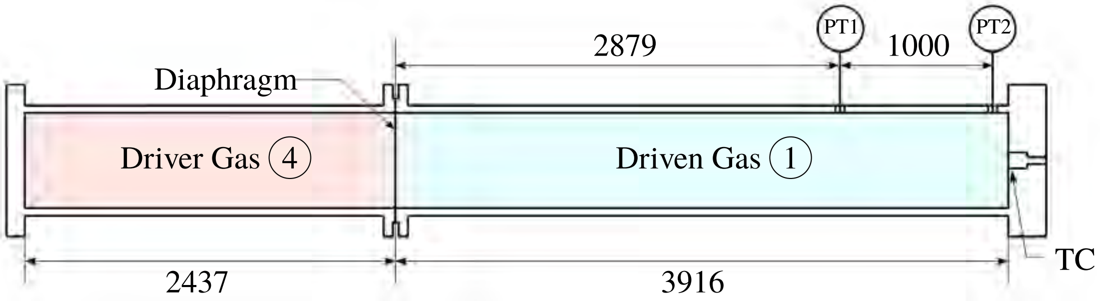

Figure 6.4: Shock tube geometry and instrumentation positions. Inside diameter of shock tube is 63 mm.

incident shock continues to propagate downstream until it reaches the end wall where it is reflected. This reflection is seen by the thermocouple as an instantaneous increase in gas temperature from T_1 to T_5, which provides the step input required for calculation of the thermal effusivity of the thermocouple.

The thermocouple acts as a heat sink and, in theory, the surface of the thermocouple experiences an instantaneous change of temperature which, together with the properties of the gas which was processed by the reflected shock, is used to determine the thermal effusivity of the thermocouple e_{TC}.

The thermal effusivity of the gas at state 5 is determined through normal shock relations for a calorically imperfect ideal gas from initial conditions and the measured shock speed, w. A sudden pressure increase measured by PT1 and PT2 indicates the arrival of the shock wave. The pressure transducers are separated by a known distance (1000 mm) and the detection of the shock wave passing over the pressure transducers (indicated on Fig. 6.6) is used to determine the shock speed. The fast response of the thermocouple enabled an additional two measurements of shock speed to be obtained by measuring the time taken for the shock to travel the 1037 mm from PT1 to the thermocouple, and to pass from PT2 to the thermocouple. The three shock speed measurements determined from the pressure and temperature signals were within 2 % of the mean value for each run, indicating a fully developed shock wave propagating at constant velocity. The constant velocity between the three measurement stations confirms a fully developed shock by the time it reaches PT1.

The temperature and pressure of state 1 are known a priori, as is the temperature of state 4. Using the known properties and the measured shock speed, the shock tube can then

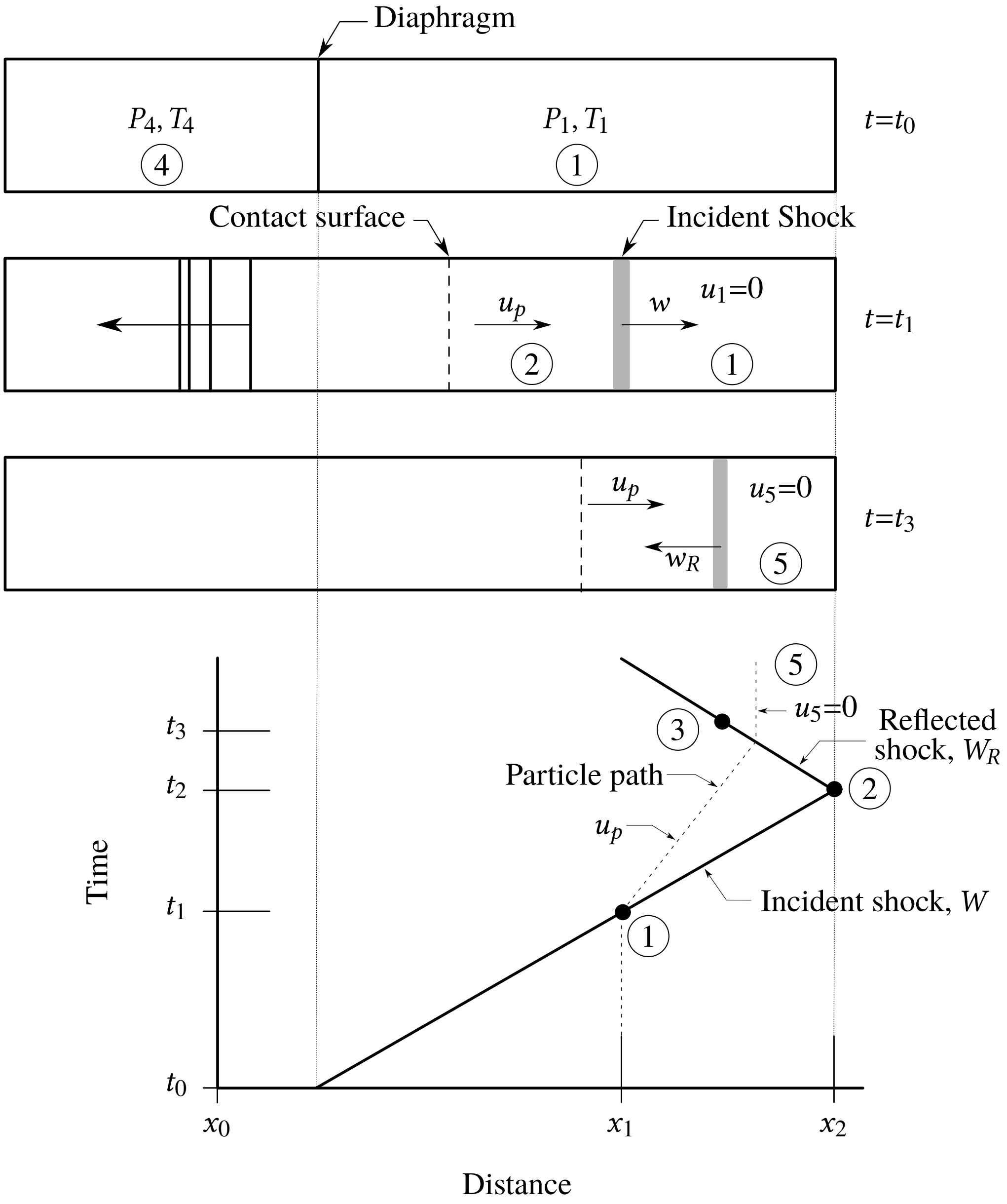

Figure 6.5: Reflected shock tube wave diagram.

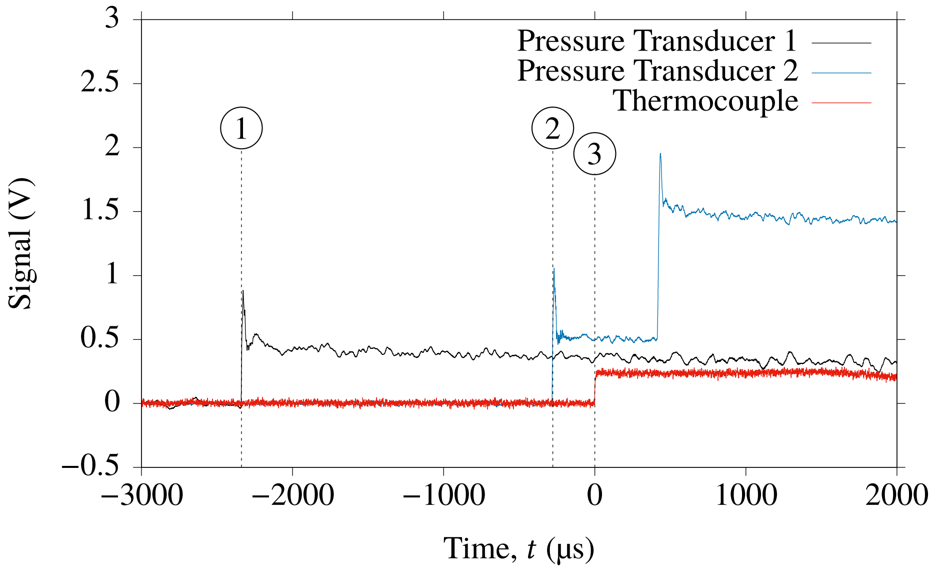

Figure 6.6: Raw data from a shock tube calibration. The shock wave is detected by PT1 at ①, PT2 at ②, and by the thermocouple at ③.

be fully characterised. The shock tube conditions achieved for a sample calibration are shown in Table 6.1, and the procedure for populating Table 6.1 is presented in Appendix C.

	State 1	State 2	State 4	State 5
P (kPa)	94.0	203.9	491.4	408.2
T (K)	296.7	375.2	296.7	462.1
ρ (kg m^{-3})	1.104	1.893	5.770	3.078
a (m s^{-1})	345.4	387.5	345.4	428.8
u (m s^{-1})	0	203.8	0	0

Table 6.1: Sample reflected shock tube calibration conditions for Run 26.

6.4.3 Heat Flux Behind a Reflected Shock

Two analytical models for determining the heat flux to the wall from the gas behind a reflected shock were identified: (1) a method for weak shocks where the contraction of the gas in the thermal boundary layer is neglected (Buttsworth, 2001)

$$q_{w,B} = \frac{\sqrt{\rho_e c_{p,e} k_e}}{\sqrt{\pi}\sqrt{t}} \left(T_5 - T_{wall,i}\right) = \frac{\tilde{q}_{w,B}}{\sqrt{t}} \tag{6.9}$$

and (2), where the contraction of the gas in the thermal boundary layer is considered and ionisation of the gas neglected (Fay & Kemp, 1965)

$$q_{w,F} = 1.13\sqrt{\frac{\rho_e k_e c_{p,e}}{2t}} T_e \left[\frac{1-\theta_w^{\nu}}{\nu} - \frac{1-\theta_w^{\nu+1}}{\nu+1}\right]^{\frac{1}{2}} = \frac{\tilde{q}_{w,F}}{\sqrt{t}} \tag{6.10}$$

where $\theta_w = T_w/T_e$ and ν is the index of the thermal conductivity power law, the subscripts e and i are the values at the edge of the boundary layer and initial state respectively, and $\tilde{q}$ is the time invariant heat flux and depends only on the flow properties behind the reflected shock.

The properties of the gas at the edge of the boundary layer (subscript e) are the properties of the gas at state 5, and therefore

$$\sqrt{\rho_e c_{p,e} k_e} = \sqrt{\rho_5 c_{p,5} k_5} = e_5 \tag{6.11}$$

where k_5 is estimated using Sutherland's law and $c_{p,5}$ estimated using the cubic correlation presented by Cengel and Boles (2007).

For both Eq. 6.9 and Eq. 6.10 the heat flux varies as $1/\sqrt{t}$. In the shock tube case, the wall impulsively reaches a constant temperature, and this temperature is determined using (Marineau & Hornung, 2009)

$$T_{TC} = \frac{\tilde{q}\sqrt{\pi}}{e_{TC}} + T_{TC,i} \tag{6.12}$$

where e_{TC} is the effective thermal effusivity of the thermocouple, T_{TC} is the surface temperature of the thermocouple and subscript i indicates the initial value. Since the thermocouple temperature is measured, and $\tilde{q}$ can be calculated from measured flow properties, the thermal effusivity of the thermocouple can be identified.

Inspecting Eq. 6.12, it is clear that any uncertainty in the calculation of $\tilde{q}$ will lead directly to uncertainty in e_{TC}. The two methodologies for determining the wall heat flux (Eq. 6.9 and Eq. 6.10) are compared graphically in Fig. 6.7 for the shock tube conditions used in this research, including an extension to higher shock strengths to illustrate the difference between the two models. Figure 6.7 shows that the wall heat flux is underestimated when the thermal boundary layer contraction is neglected.

For shocks in air, neglecting the contraction of the gas in the thermal boundary layer

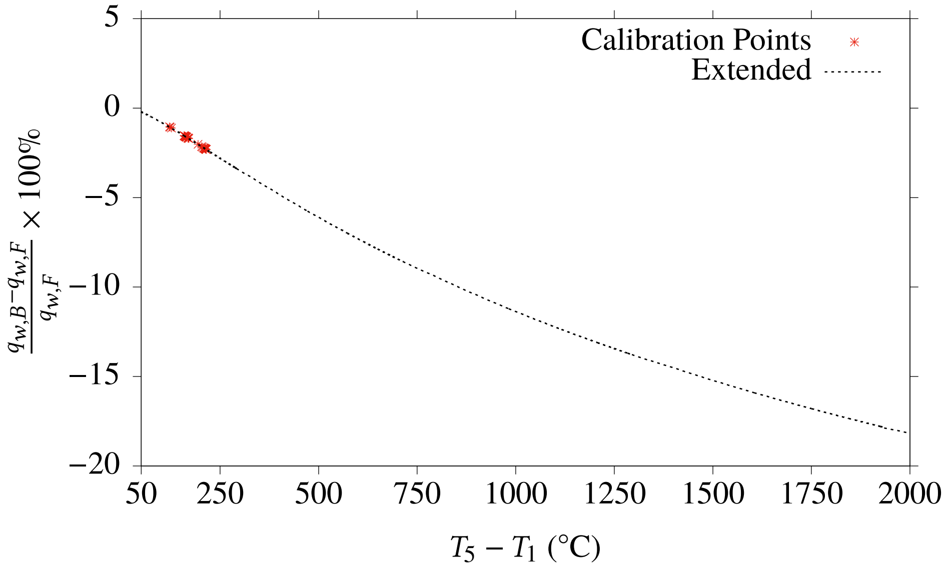

Figure 6.7: Underestimation of wall heat flux as a function of reflected shock step temperature increase for shocks in air when $T_1 = 295$ K.

results in a heat flux result within 2.5 % of the more complete analysis (Eq. 6.10) for the conditions in this research. As $T_5 - T_1$ increases, the error introduced by neglecting the thermal boundary layer becomes significant, and it is clear that for strong shocks that using Eq. 6.9 is inappropriate. In an effort to reduce the experimental uncertainty of this research, the effect of contraction of the gas in the thermal boundary layer was considered.

6.4.4 Conversion of Thermocouple Output Voltage to Temperature

The temperature of a thermocouple can be determined from its voltage output using the Seebeck coefficient. For E type thermocouples, the Seebeck coefficient is often quoted as 68 µV $°\mathrm{C}^{-1}$, however the relationship between output voltage and the junction temperature is non-linear. Using a constant Seebeck coefficient for the range of operating temperatures used in this research would result in significant error. For operating temperatures of −100 to 1000°C, the output voltage from an E type thermocouple can be used to find the junction temperature using the ninth order polynomial (*Practical Temperature Measurements*, n.d)

$$T = a_0 + a_1 x + a_2 x^2 + \cdots + a_n x^n \tag{6.13}$$

where the coefficients are presented in Table 6.2.

By differentiating Eq. 6.13 and plotting the results as function of junction temperature, the sensitivity of an E type thermocouple can be determined as shown in Fig. 6.8, where

Coefficient	Value	Coefficient	Value
a_0	0.104 967 248	a_5	$1.108\,66 \times 10^{10}$
a_1	17 189.452 82	a_6	$-1.768\,07 \times 10^{11}$
a_2	−282 639.0850	a_7	$1.718\,42 \times 10^{12}$
a_3	12 695 339.5	a_8	$-9.192\,78 \times 10^{12}$
a_4	−448 703 084.6	a_9	$2.061\,32 \times 10^{13}$

Table 6.2: Coefficients of Eq. 6.13 (*Practical Temperature Measurements*, n.d).

the temperature range is windowed to the region of interest for this research.

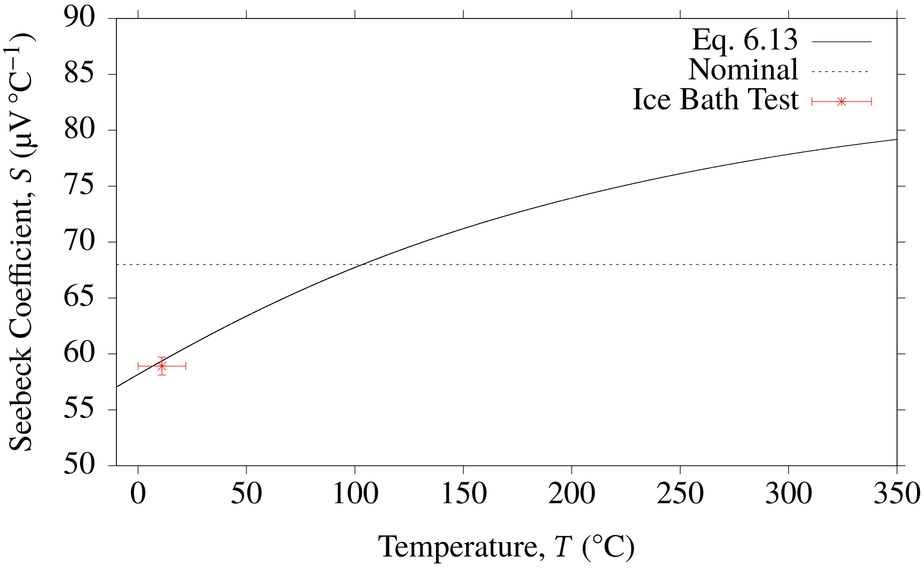

Figure 6.8: Sensitivity of a type E thermocouple as a function of the thermocouple operating temperature. An ice bath calibration demonstrated agreement with the sensitivity provided by Eq. 6.13 and demonstrated that using a nominal 68 μV °C^{-1} can introduce significant error. Horizontal error bars show the extents of the maximum and minimum thermocouple temperature for the calibration.

For experiments at room temperature with small temperature rises, such as the shock tube calibration, using the nominal $S = 68$ μV °C^{-1} will result in measured temperature changes approximately 12.5 % below the actual value. Similarly, experiments using thermocouples pre-heated to the approximate stagnation temperature (300 °C) of the TUSQ Mach 6 flow will result in an over-calculation of the temperature change by approximately 12 %.

The sensitivity of the thermocouples was tested using an ice bath calibration where the voltage from the thermocouple was recorded at room temperature (22 °C) and at 0 °C when immersed in the ice bath. The signal was amplified using the same amplifier as used for the shock tube calibrations so not to introduce any additional uncertainty. At a gain of 2500, the voltage change over 22 °C was 3.24 V, corresponding to an average sensitivity of 58.9 µV °C^{-1} which is within 0.8 % of the average type E sensitivity in the range 0 – 22 °C.

6.4.5 Calibration Results

Five thermocouples created using various junction forming techniques were calibrated using shock speeds of 458 m s^{-1} to 530 m s^{-1}. Operating conditions and the results of these calibrations are summarised in Table 6.3. The thermocouple output was amplified using an AMETEK model 5113 pre-amplifier at gains of 5000, 8000, 10 000, and 25 000. At high gains, the amplified signal exceeded the maximum rated output of the amplifier. By using the selectable 300 kHz lowpass filter in the Model 5113 amplifier, the resulting output signal fell to within the amplifier parameters.

The measured thermocouple signal was converted to temperature using the polynomial model for type E thermocouple sensitivity presented in Eq. 6.13. The step change of temperature measured by the thermocouple that resulted from the impulsively applied heat flux was evaluated over the first 50 µs of data after the thermocouple face was first exposed to the shock. The finite rise time of the thermocouple resulted in a number of data points in the 0 – 50 µs that are not representative of the magnitude of the step temperature change. These points were isolated from the mean level calculation by an iterative process whereby values outside two standard deviations of the mean were removed until the change in standard deviation between iterations was less than 10 %. The result of this process is shown in Fig. 6.9 where the 63 % rise level is also shown. The 300 kHz lowpass filter was implemented for this run, and since a perfect step signal has frequency components extending to infinity, the rise time of the thermocouple identified from Fig. 6.9 may be an overestimate of the native value for the thermocouple gauge itself.

Using the measured step change in temperature (ΔT) and the time invariant wall heat flux ($\tilde{q}$) calculated from the reflected shock conditions, the thermal effusivity of the thermocouple (e_{TC}) is calculated by

$$e_{TC} = \frac{\tilde{q}\sqrt{\pi}}{\Delta T} \tag{6.14}$$

The thermal effusivity calculated from each calibration run is presented in Fig. 6.10 with run-specific properties and numerical results shown in Table 6.4. The average theoretical reference value of thermal effusivity of the two base metals that form a type E thermo-

Run	TC	Junction	ΔT °C	w $\mathrm{m\,s^{-1}}$	T_5 K	$\tilde{q}$ $\mathrm{Ws^{0.5}m^{-2}}$	e_{TC} $\mathrm{J\,m^{-2}\,K^{-1}s^{-0.5}}$	σ %	t_{rise} µs
1	2	1200	0.521	498.8	474.7	1154	3930	9.40	< 1
2	2	1200	0.513	495.7	470.9	1117	3857	9.54	< 1
3	2	1200	0.559	494.4	469.0	1103	3499	4.13	1 – 2
4	2	1200	0.740	531.5	515.2	1616	3870	6.70	1
5	2	1200	0.533	516.9	496.7	1403	4668	10.0	2 – 3
6	4	scalpel*	0.471	489.6	462.9	1050	3954	9.91	< 1
7	4	scalpel*	0.469	489.2	462.4	1046	3948	9.39	< 1
8	4	scalpel*	0.502	497.9	473.1	1152	4064	4.89	1 – 2
9	4	scalpel*	0.617	524.9	507.1	1511	4337	8.35	< 1
10	4	scalpel*	0.625	526.7	509.4	1537	4358	7.68	1
11	4	scalpel*	0.661	532.9	517.3	1630	4370	8.59	< 1
12	6	1200	0.423	495.5	472.0	1099	4608	11.5	< 1
13	6	1200	0.385	491.4	467.1	1051	4835	5.97	2 – 3
14	6	1200	0.410	493.2	469.8	1077	4651	6.51	4 – 5
15	6	1200	0.269	469.1	441.0	793	5227	6.87	9 – 10
16	6	1200	0.282	464.6	435.7	748	4693	6.08	4
17	6	1200	0.306	468.0	439.8	782	4533	23.2	2
18	6	1200	0.670	532.6	520.1	1580	4182	9.27	2
19	6	1200	0.593	532.3	519.6	1575	4704	4.99	1 – 2
20	6	1200	0.567	529.4	516.0	1533	4791	8.03	2 – 3
21	10	2000	0.629	531.4	515.4	1610	4535	7.02	2 – 3
22	10	2000	0.617	528.9	512.4	1568	4506	3.08	3
23	10	2000	0.635	530.9	515.1	1599	4463	9.07	2 – 3
24	10	2000	0.407	494.4	469.0	1107	4813	12.1	3
25	10	2000	0.401	492.0	466.1	1078	4766	14.6	1 – 2
26	10	2000	0.396	489.0	462.4	1041	4662	5.42	3 – 4
27	10	2000	0.568	529.2	512.6	1578	4922	9.11	2
28	13	800	0.518	497.3	472.4	1146	3919	10.7	< 1
29	13	800	0.507	497.3	472.3	1145	4006	5.83	2
30	13	800	0.503	493.6	467.7	1100	3874	6.55	1 – 2
31	13	800	0.730	530.6	514.1	1602	3891	11.7	< 1
32	13	800	0.654	528.8	512.1	1568	4247	10.3	1 – 2
33	13	800	0.707	533.4	518.2	1632	4094	8.26	7

Table 6.3: Summary of the results of the shock tube calibration experiments. *scalpel junctions were formed and polished to reduce the junction depth for gauge 4 for which abrasive paper junctions were difficult to form.

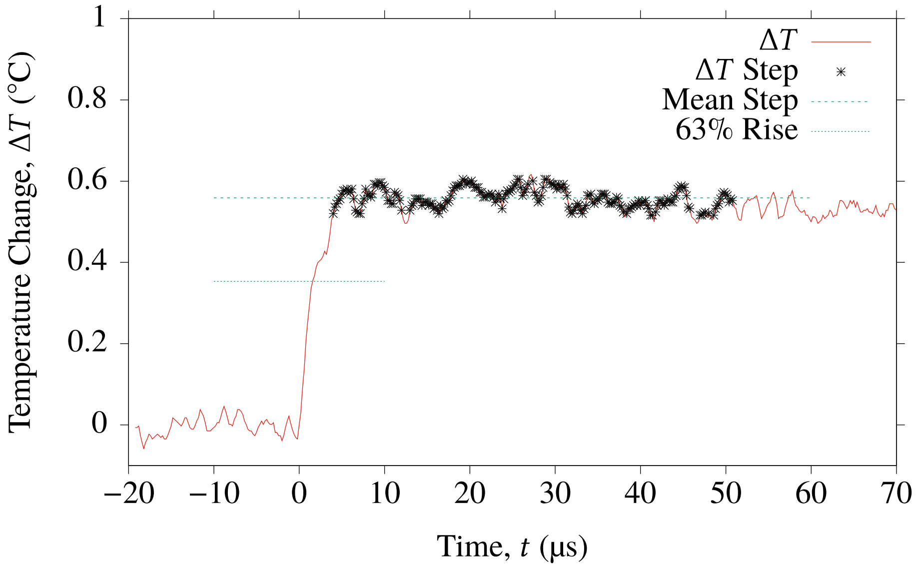

Figure 6.9: Example of the thermocouple temperature measured in the shock tube calibration experiments where a 300 kHz, −12 dB lowpass filter was applied to the amplified temperature signal. Run 3, thermocouple 2.

couple is $e_{ref} = 8645\,\mathrm{J\,m^{-2}\,K^{-1}s^{-0.5}}$ (*Physical Properties of Thermoelement Materials*, n.d.). The values of thermal effusivity found in the calibration are significantly lower than the mean value of the chromel and constantan. This result was not unexpected; for type E microsecond response time thermocouples of similar construction Marineau and Hornung (2009) reported the thermal effusivity to be approximately 30 % lower than the average value of chromel and constantan. Buttsworth (2001) tabulated thermal effusivity values for microsecond response time type K coaxial thermocouples with junctions formed using abrasive paper, with results ranging between 45 % and 150 % of the average value of chromel and alumel. Buttsworth (2001) reported that the thermal effusivity was related to the substrate on which the junction was formed. The thermal effusivity of the base metals that form a type K thermocouple differ by 33 %, compared to a 2 % difference for the type E thermocouple base metals. This difference in base metal thermal effusivity may have contributed to the increased variability for type K thermocouples when compared to the present results using type E thermocouples as illustrated in Fig. 6.10.

Across all calibrations, the thermal effusivity was bound within $4357\,\mathrm{J\,m^{-2}\,K^{-1}s^{-0.5}} \pm 20\,\%$. Each individual gauge exhibited less variation between calibrations, with the standard deviation of thermal effusivity for thermocouples TC4, TC10 and TC13 less than 5 %.

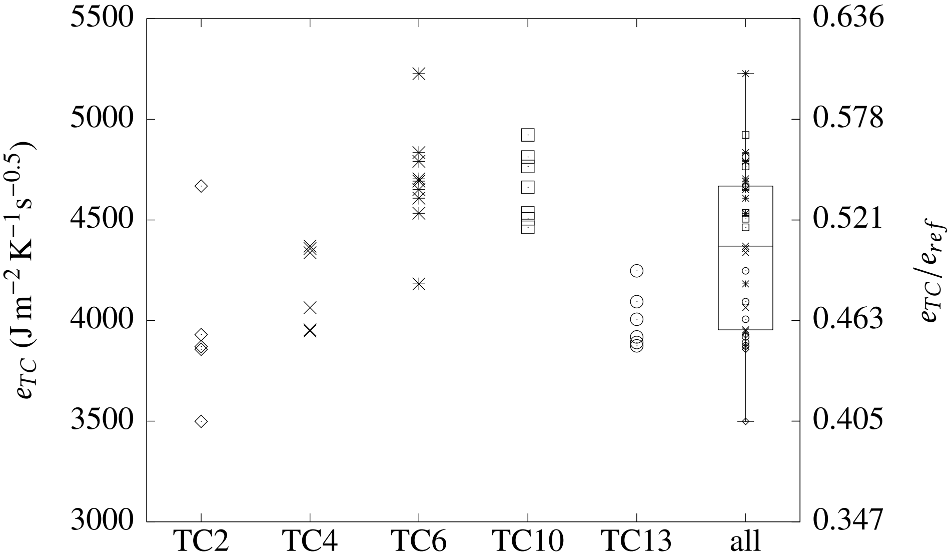

Figure 6.10: Thermal effusivity of the thermocouples determined using the reflected shock calibration technique.

The uncertainty of the thermocouple thermal effusivity is related to the uncertainty of the calibration technique used. For the reflected shock calibration, the analytical model used to determine the wall heat flux (Eq. 6.10) is a source of systematic uncertainty. Engineering models are required to calculate the thermal conductivity and specific heat of the gas at state 5, and for the reflected shock temperatures used, these engineering models are accurate to ± 2 % for $160 \leq T \leq 2000$ K (White, 2005) and ± 0.72 % for $273 \leq T \leq 1800$ K (Cengel & Boles, 2007). The three signals used to identify the shock speed were in agreement to within ± 1.5 %, and the uncertainty in the measured shock speed error results in a reflected shock temperature uncertainty of up to ± 2.0 %, while assuming ± 1 K tolerance for the atmospheric temperature introduces another ± 0.4 % error. The thermocouple materials have a manufacturer specified standard limit of error of 1.7 °C at the thermocouple temperatures used for calibration. Combining the error sources, the uncertainty of the identified thermal effusivity is ± 5.7 %.

Thermocouple TC2 had the most variation in deduced thermal effusivity, however three of the five results were 3800 – 3900 J m^{-2} K^{-1}s$^{-0.5}$. The highest thermal effusivity for TC2 was found for Run 5 which had a rise time of 2 – 3 µs while the other tests exhibited a rise time of approximately 1 µs. Similarly, for TC6 the highest thermal effusivity was found when the rise time was larger than other calibrations of the same thermocouple. The mean values of thermal effusivity for each thermocouple are presented in Table 6.4, and these values are used for post-processing of data obtained in the TUSQ facility. No trend of e_{TC} increasing or decreasing with the method of creating the junction was evident, nor was there a relationship between junction creating technique and rise time.

Gauge	Junction	e_{TC} ($\mathrm{J\,m^{-2}\,K^{-1}s^{-0.5}}$)	σ (%)
TC2	1200	3965	10.8
TC4	scalpel*	4172	4.92
TC6	1200	4692	5.89
TC10	2000	4667	3.73
TC13	800	4005	3.60
Mean	-	4357	9.28

Table 6.4: Thermal effusivity of the thermocouples.

Chapter 7

Total Temperature of TUSQ Flow

Contents

7.1 Introduction

The mean and fluctuating components of stagnation temperature were identified using the measurements of heat flux made using the five type E coaxial surface junction thermocouples described in Section 6.2, which were mounted in a 10 mm diameter bronze housing. Thermocouples were operated at temperatures between ambient laboratory temperature and slightly above the total temperature of the facility. This chapter presents analysis of the mean and fluctuating components of stagnation temperature and heat flux, and compares the experimental results to the results of simulations using L1d3 and an in-house analytical tool based on the experimental measurements of the pressure in the barrel (Widodo & Buttsworth, 2013).

The five heat flux gauges were fitted to a smaller version of the Pitot probe rake at radial locations $r = \{0, \pm 20, \pm 40\}$ mm where the face of each thermocouple was positioned 50 mm downstream of the nozzle exit, as shown in Fig. 7.1.

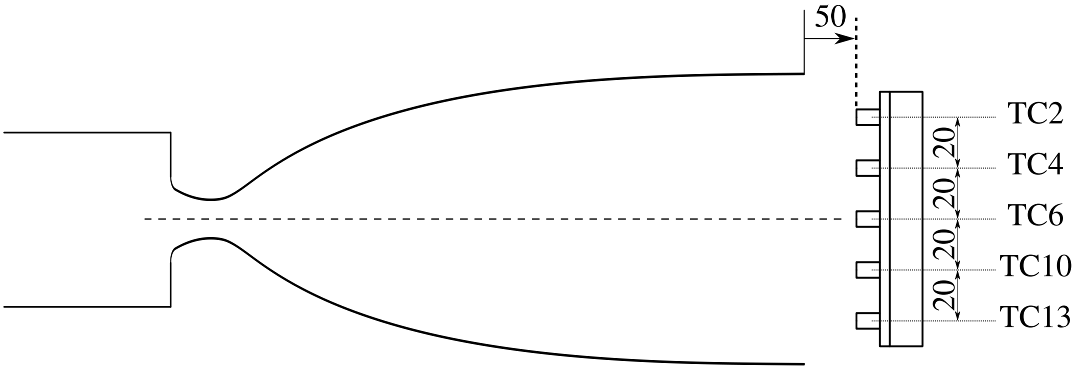

Figure 7.1: Schematic of thermocouple positions relative to the nozzle exit.

7.2 Temperature Signal Conditioning

The thermocouple voltage signal was amplified using an in-house two stage thermocouple amplifier with a bandwidth of 500 kHz. Stage 1 is a fixed DC gain of 100 and stage 2 a capacitively coupled (AC) stage with selectable gain and optional low-pass filter. The amplifier was operated using a battery source so as not to introduce noise from the mains power. The negative lead of the twisted pair thermocouple extension wire was connected to the thermocouple amplifier shield.

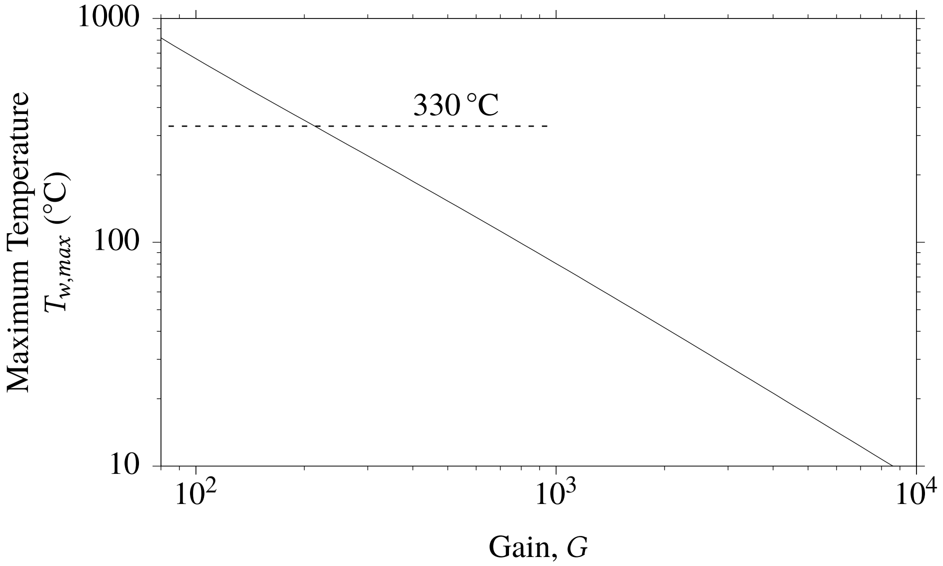

Figure 7.2: Maximum resolvable thermocouple temperature at different amplifier gain settings.

The maximum voltage signal that could be recorded by the data acquisition system is 5 V, which for a type E thermocouple limits the maximum allowable amplifier gain (G) as shown in Fig. 7.2. For a thermocouple preheated to the isentropic stagnation temperature for the condition of interest (around 330 °C) the maximum amplifier gain is $G = 200$. This gain may not be sufficiently high to resolve the small thermocouple surface temperature changes caused by fluctuations in the surface heat flux. Additionally the signal from the thermocouples was found to contain a large amount of electrical noise, and this noise could be attenuated somewhat using low-pass filters on the AC channel output.

The signal resolution can be improved by using a capacitively coupled (AC) high gain amplifier which acts as a high-pass filter to attenuate the low frequency DC signal components. However the low frequency heat transfer effects dominate the voltage output from the thermocouple. By recording both a relatively low gain DC signal and a higher gain AC coupled signal it is possible to reconstruct the thermocouple signal with appropriately amplified higher frequency components.

The two stage amplifier used for this research is illustrated in Fig. 7.3. Output S_1 is from a DC-coupled amplifier with a gain fixed at $G_1 = 100$. The output S_1 is the input of Stage 2 and is AC filtered prior to being amplified. The AC filter stage is a 1st order high-pass filter with the −3 dB point at 3 Hz. G_2 is a switchable gain stage where $G_2 \in \{1, 2, 5, 10, 20, 50, 100\}$ resulting in a total selectable gain for the output S_2 of $G_{total} \in \{100, 200, 500, 1000, 2000, 5000, 10\,000\}$.

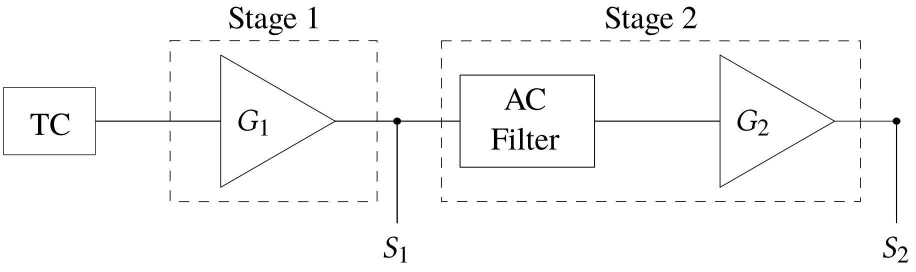

Figure 7.3: Two stage thermocouple amplifier schematic.

The amplified thermocouple signal was found to contain a large amount of electromagnetic interference from a variety of sources, and this interference was spread over a large number of narrow frequency bands. The selectable first order 40 kHz low-pass filter on the second stage output of the amplifier was used which attenuated the interference for $f > 40$ kHz. However significant baseline noise was still present and had to be removed digitally.

Simple Butterworth filters were found to be inadequate, and a stationary wavelet transform (SWT) filtering technique was implemented. The electromagnetic interference and the SWT filtering technique used to attenuate this interference are described in Appendix D. The amplified thermocouple signal for stage 1 and stage 2 outputs were filtered using a second order level 6 symlet wavelet, and an example of this filtering is shown in Fig. 7.4.

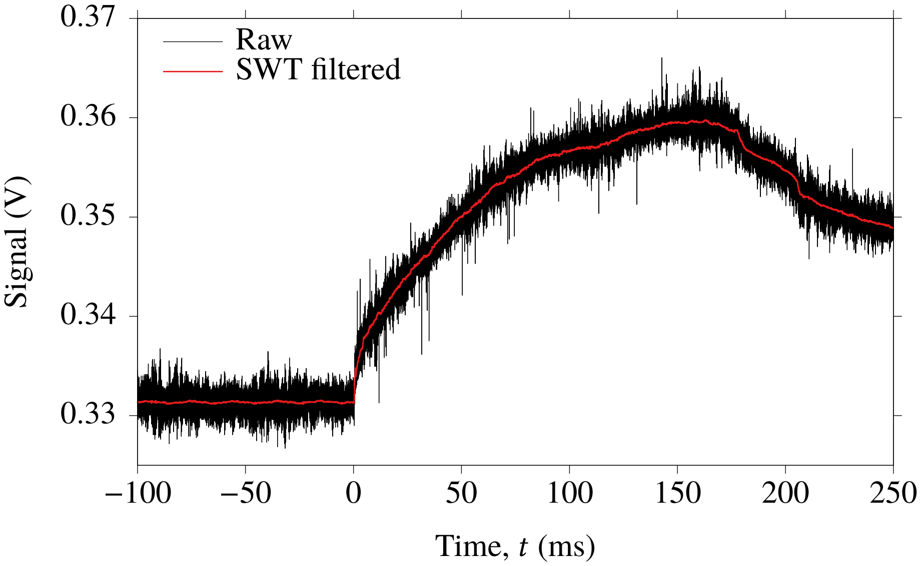

Figure 7.4: Conditioning of an amplified thermocouple signal (TC6, Run 817) using SWT filtering.

A DC offset existed in the amplifier circuit, and therefore to correctly determine the electromotive force (emf) generated by the thermocouple, the DC offset introduced during the amplification stage had to be removed. The DC offset for S_1 was identified by performing a cold calibration at a known temperature prior to the preheating of the thermocouple. The emf of the thermocouple as measured from S_1 was found using

$$\mathrm{emf}_{S_1} = \frac{S_1}{G_1} - \frac{S_{1,cold}}{G_1} + \mathrm{emf}_{\mathrm{E}}(T_{cold}) \tag{7.1}$$

where $S_{1,cold}$ is the signal from the cold reference and $\mathrm{emf}_{\mathrm{E}}(T_{cold})$ is the known emf of a type E thermocouple at $T = T_{cold}$.

The emf as measured from S_2 is

$$\mathrm{emf}_{S_2} = \frac{S_2}{G_1 + G_2} - \frac{\overline{S_{2,p}}}{G_1 + G_2} \tag{7.2}$$

where subscript p indicates pre-flow data and overline a mean value.

The results of Eq. 7.1 and Eq. 7.2 are shown in Fig. 7.5 for a representative experiment illustrating the process for transformation of the AC coupled signal to a true DC level. The effect of attenuating the low frequency content by using the AC filter on the signal emf_{S_2} is clear when comparing it to the DC filtered signal emf_{S_1}.

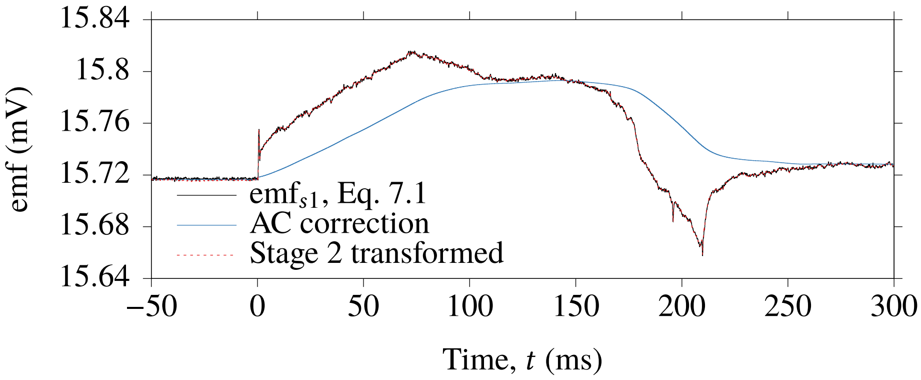

(a) DC coupled signals

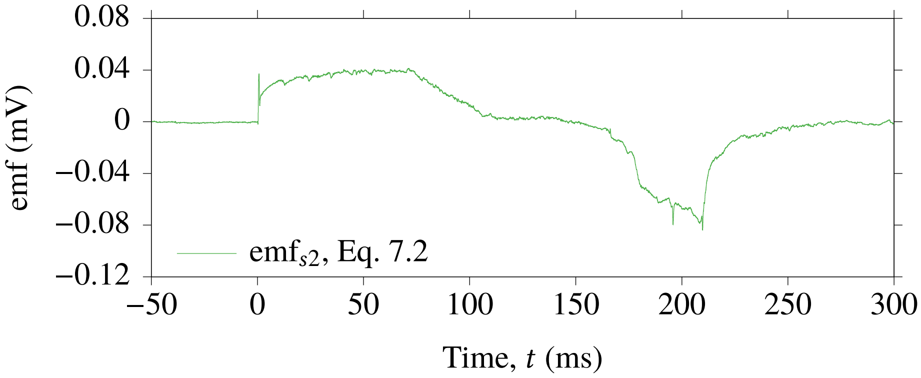

(b) AC coupled signal

Figure 7.5: Transformation of an AC coupled signal to a DC signal level. Data of TC4 obtained from Run 818.

A correction signal, analogous to the portion of the signal attenuated by the AC filter, can be identified by first calculating $\mathrm{emf}_{S_1} - \mathrm{emf}_{S_2}$, and then low-pass filtering to remove the high frequency difference signal. A 50 Hz cutoff frequency was found to be appropriate, high enough to reconstruct the mean shape and level of emf_{S_1} but low enough that the transformation process does not lose significant low frequency fluctuation content.

An interesting feature to note from Fig. 7.5 is that, for about the first 60 ms of flow, the raw thermocouple data has identified the reflected expansion waves that reflect off the piston and propagate into the test flow. This demonstrates that the SWT filtering technique preserved the sharp changes of the raw thermocouple voltage and therefore retained a large amount of physical flow data. This preservation allowed an accurate mean level stagnation temperature to be determined.

7.3 Thermocouple Temperature and Heat Flux

Following the reconstruction of the thermocouple signal, the thermocouple emf was used to determine the temperature of the thermocouple junctions using Eq. 6.13. Three thermocouples were mounted in housings that were wrapped with nichrome heating wire and two were not fitted with any heating wire. Despite there being no heating control for two of the thermocouples, thermal conduction through the rake resulted in a moderate temperature rise when neighbouring thermocouples were heated. The temperature of each thermocouple immediately prior to flow onset for the test runs are presented in Table 7.1.

Run	Initial Thermocouple Temperature, $T_{w,i}$ (K)					$\overline{T}_{0,isen.}$ (K)
	TC2	TC4	TC6	TC10	TC13	
811	297.5	297.6	297.5	297.6	297.6	574.1
812	299.1	299.1	299.1	299.1	299.1	578.3
813	609.0	478.3	342.3	462.6	338.1	577.1
814	644.9	551.3	322.1	501.6	312.0	574.6
815	523.5	570.5	329.2	511.9	318.8	579.4
816	297.0	297.5	297.6	298.0	297.5	579.0
817	344.5	642.9	368.8	629.3	362.0	577.1
818	311.6	503.9	325.2	523.7	320.5	576.1
819	323.9	564.8	341.5	556.2	335.1	575.6
820	321.3	624.4	338.1	570.6	329.7	570.8

Table 7.1: Temperature of thermocouples before flow onset and the mean flow total temperature calculated assuming isentropic compression based on measured barrel pressures for $t = 2-8$ ms after diaphragm rupture.

Thermocouple TC2 was found to regularly electrically short to the rake during heating and was operated in a cold mode for Runs 816 – 820. The mean flow total temperature from 2 – 8 ms that was calculated based on the isentropic pressure ratio achieved in the barrel compression process is included for reference. The time period from 2 – 8 ms was selected as it corresponds to the period between diaphragm rupture and the arrival of the first expansion wave reflected by the piston.

To determine the heat flux from the measured thermocouple temperature history, the impulse response analysis method (Section 6.3) was used. The identification of h can be a time consuming process for long signals (Oldfield, 2008), so a unit impulse response `h_div_rrck` was identified by

```
[h_div_rrck,shift] = desT2qsiimp1(fs, np, 1, test)
```

and `h_div_rrck` saved. The unit impulse response (Fig. 7.6) was then multiplied by the thermal effusivity for each individual thermocouple to determine h.

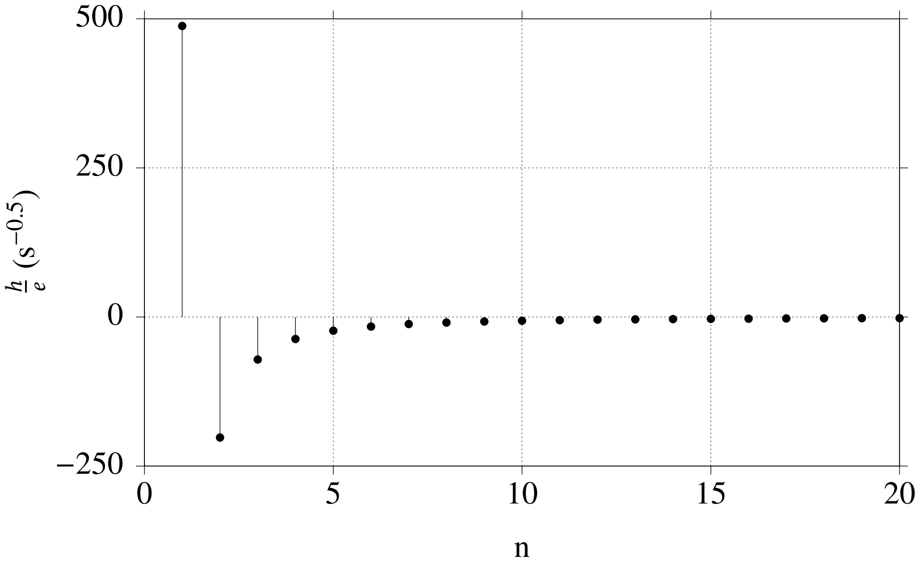

Figure 7.6: First 20 points of the normalised impulse response.

The thermal effusivity for each thermocouple was defined as the mean value for each thermocouple identified during the calibration process (Table 6.4). Using the measured temperature signal of the thermocouple and the impulse response of the system, the time-resolved heat flux was determined using

```
q = fftfilt(h, dT)
```

.

where $dT = T - T_{initial}$ which is the change of thermocouple temperature as a result of the nozzle flow. Sample temperature data collected using TC10 at different initial temperatures from five runs are shown in Fig. 7.7a and the calculated heat flux for these data in Fig. 7.7b.

At this point it is important to discuss the validity of the semi-infinite conduction assumption used to calculate the heat flux shown in Fig. 7.7b. The semi-infinite heat conduction assumption is valid when the thermal penetration depth is less than the thickness of the substrate (Gatowski et al., 1989). Sanderson and Sturtevant (2002) proposed that the length of a heat flux gauge (x) must satisfy the condition

$$\frac{x}{\sqrt{\alpha t}} \gg 1 \tag{7.3}$$

to be analysed as semi-infinite. The length of the thermocouple is nominally 3 mm, and

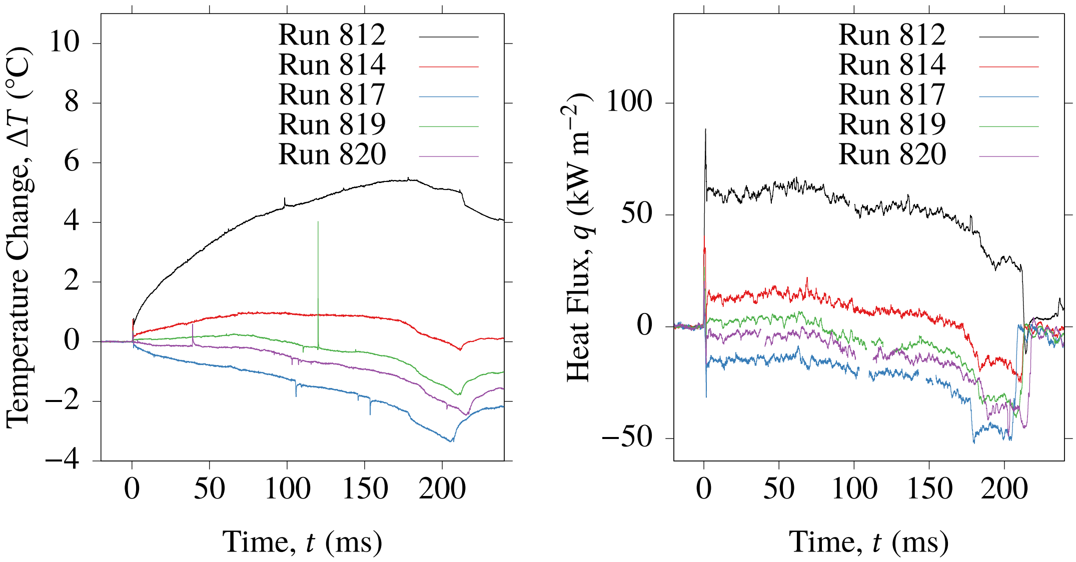

(a) Change of thermocouple temperature

(b) Heat flux

Figure 7.7: Comparison of thermocouple temperature changes when TC10 was operated at different initial temperatures for five runs, and the resulting change in measured heat flux.

for a test duration of $t = 200\,\text{ms}$, $\frac{x}{\sqrt{\alpha t}} = 3$ for the chromel substrate and $\frac{x}{\sqrt{\alpha t}} = 2.7$ for the constantan substrate. These values satisfy the inequality of Eq. 7.3, but when they are sufficiently large is not clear from this analysis alone. However, the semi-infinite solid assumption is validated by the experimental data presented in Fig. 7.7b for test times in excess of the flow duration by the return of the heat flux to approximately zero upon flow termination.

Large non-repeatable spikes in the temperature data are evident in three of the five runs shown. This behaviour was observed in the Pitot pressure survey and was attributed to the effects of small particulates contaminating the measurement of the flow. The spikes in temperature data resulted in large non-physical changes in heat flux, so these regions were omitted from Fig. 7.7b. The thermocouples exhibited the expected short response times as shown by the sudden impulse at $t = 0\,\text{ms}$ when the flow arrives at the probe which is clear in the heat flux data.

The heat flux for the first several tens of milliseconds for Run 819 was slightly positive while for this time period the heat flux was slightly negative for Run 820. This indicates that, if the flow conditions in the two runs were identical, the stagnation temperature for the first 60 ms was bound between 556.2 – 570.6 K. The heat flux at $t \approx 80\,\text{ms}$ and

$t \approx 160\,\mathrm{ms}$ was approximately zero for Runs 819 and 814 respectively. At these points the flow stagnation temperature is approximately the temperature of the thermocouple.

7.4 Determining the Probe Heat Transfer Coefficient

7.4.1 Analytical Model

The transient heat flux (q) identified by the surface junction thermocouples can be described by

$$q = h_c \left(T_0 - T_w\right) \tag{7.4}$$

where h_c is the heat transfer coefficient, T_0 the stagnation temperature, and T_w the temperature of the thermocouple face.

If the heat transfer coefficient of the thermocouple probe is known or can be approximated with reasonable accuracy, the flow total temperature can be estimated using single measurements of thermocouple temperature and transient heat flux.

An analytical model exists for estimating the heat transfer coefficient which requires knowledge of flow parameters. In the stagnation region of an axisymmetric body in high speed flow, the heat flux can be expressed as

$$q_w = 0.763\,\mathrm{Pr}_e^{-0.6}\,\sqrt{\rho_e \mu_e K}\left(\frac{\rho_w\,\mu_w}{\rho_e\,\mu_e}\right)^{0.1}\left(h_e - h_w\right) \tag{7.5}$$

where Pr is the Prandtl number, ρ is density, k thermal conductivity, K the stagnation point velocity gradient, h is enthalpy and the subscripts e and w denote the conditions at the edge of the boundary layer and wall respectively (White, 2005). Approximating

$$h_e - h_w = \overline{c_p}\,\left(T_e - T_w\right) \tag{7.6}$$

where $\overline{c_p}$ is the average of the specific heat at the wall and edge of the boundary layer allows Eq. 7.5 to be expressed in the form of Eq. 7.4. For a flat nosed body in hypersonic flow, White (2005) presents

$$\frac{K\,D}{u_\infty} \approx 0.3 \tag{7.7}$$

where D is the diameter of the face and u_∞ the velocity of the freestream.

Using Eq. 7.4–7.7 the analytical heat transfer coefficient can then be expressed as

$$h_c = 0.763\,\mathrm{Pr}_e^{-0.6}\,\sqrt{\rho_e\,\mu_e}\sqrt{\frac{0.3\,u_\infty}{D}}\left(\frac{\rho_w\,\mu_w}{\rho_e\,\mu_e}\right)^{0.1}\overline{c_p} \tag{7.8}$$

Equation 7.8 can be used to calculate a convective heat transfer coefficient on the assumption of isentropic compression and expansion within the facility. If air initially at 94 kPa and 300 K is isentropically compressed to 1 MPa and then accelerated isentropically to Mach 5.95, the heat transfer coefficient is approximately 206 W m^{-2} K^{-1} for a 10 mm diameter flat faced axisymmetric probe operated at 300 K. However, the compression process is known to not be isentropic and the stagnation point velocity gradient of 0.3 is an approximation so there is a high degree of uncertainty in the analytical value of h_c. Therefore a more reliable method for determining the heat transfer coefficient is desirable, although $h_c \approx 206$ W m^{-2} K^{-1} gives a good first order estimate.

7.4.2 Linear Regression Analysis

By operating gauges at different temperatures for nominally identical runs, different transient heat fluxes are measured. The convective heat transfer coefficient was identified, as shown later in Eq. 7.18, as a weak function of the surface temperature and flow total temperature ($T_e^{0.2028}$), and therefore h_c can be assumed constant to within the accuracy of the heat flux measurements as:

$$h_c = \frac{q_n}{T_0 - T_{wn}} \tag{7.9}$$

where n is the n$^{\text{th}}$ run. Equation 7.9 can be expressed as

$$T_{wn} = -\frac{q_n}{h_c} + T_0 \tag{7.10}$$

and since T_{wn} and q_n are known and h_c assumed constant, with data from thermocouples at different initial temperatures, a linear regression analysis can be performed to determine h_c.

By analysing windows of temporally aligned thermocouple temperature and heat flux, changes in the heat transfer coefficient over the flow time can be investigated. Where $q_n = 0$, the mean flow total temperature over the window is equal to the mean thermocouple temperature during this window.

Three window lengths were used for the linear regression: 1 ms; 5 ms; and 10 ms. The windowing process is shown in Fig. 7.8 for a 10 ms window width centred at t_c using data from Run 818, thermocouple TC10. Longer window widths have the effect of smoothing the data for consecutive windows, but do not fully capture changes in the heat transfer coefficient at sharp changes in heat flux. However, temporal alignment of strong changes in heat flux is not possible due to the varying run-to-run conditions in the barrel and variance in diaphragm rupture pressures which result in varied transit time for reflections of the expansion wave initiated at diaphragm rupture. Therefore the longer duration windows were less affected by temporal misalignment.

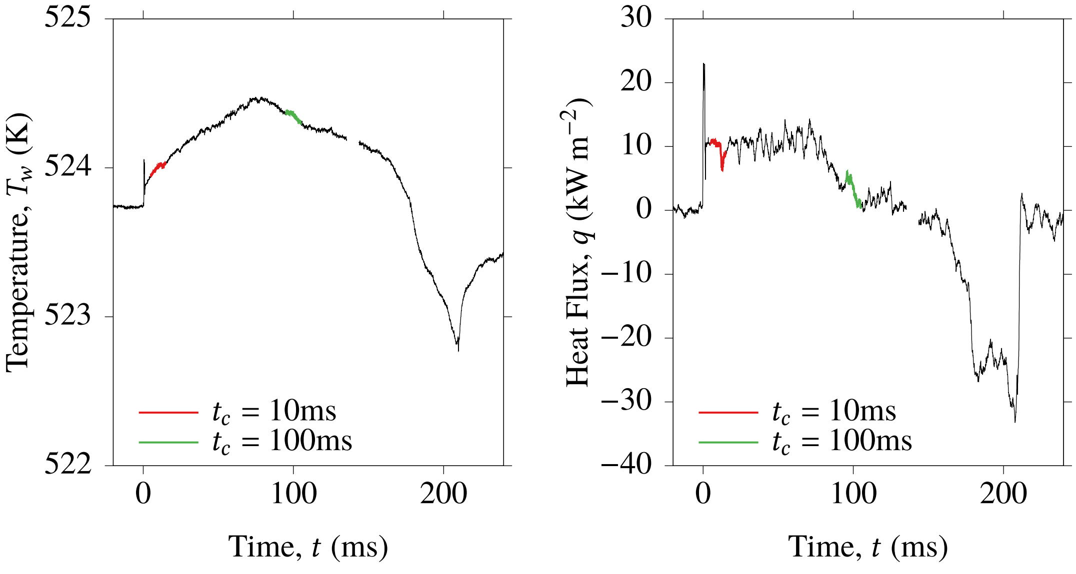

(a) Temperature of the thermocouple (T_w)

(b) Heat flux

Figure 7.8: Thermocouple temperature and heat flux for Run 818 TC10 identifying two of the windows of data used for determining the convective heat transfer coefficient using 10 ms windows centred at t_c.

The results of linear regression analysis for 10 ms windows centred at $t_c = 10$ ms and 100 ms are shown in Fig. 7.9a and 7.9b respectively. Valid data were only available for two of the three preheated thermocouples at elevated temperatures, so here TC2 is treated as a cold thermocouple. For cold operation there was significant spread in the data which resulted in a poor linear regression, but the data does show a trend similar to the regression for TC10. This apparent co-linearity indicates that any changes in thermal effusivity at elevated operating temperatures was not significant. The cold operation of TC10 was removed from the regression as it was assessed as an outlier. The average flow stagnation temperature measured by TC4 and TC10 for $5 \leq t \leq 15$ ms was 561.8 K and 559.9 K respectively. Assuming an isentropic facility operation, the mean stagnation temperature across the runs used to identify the linear regression was 573.4 K.

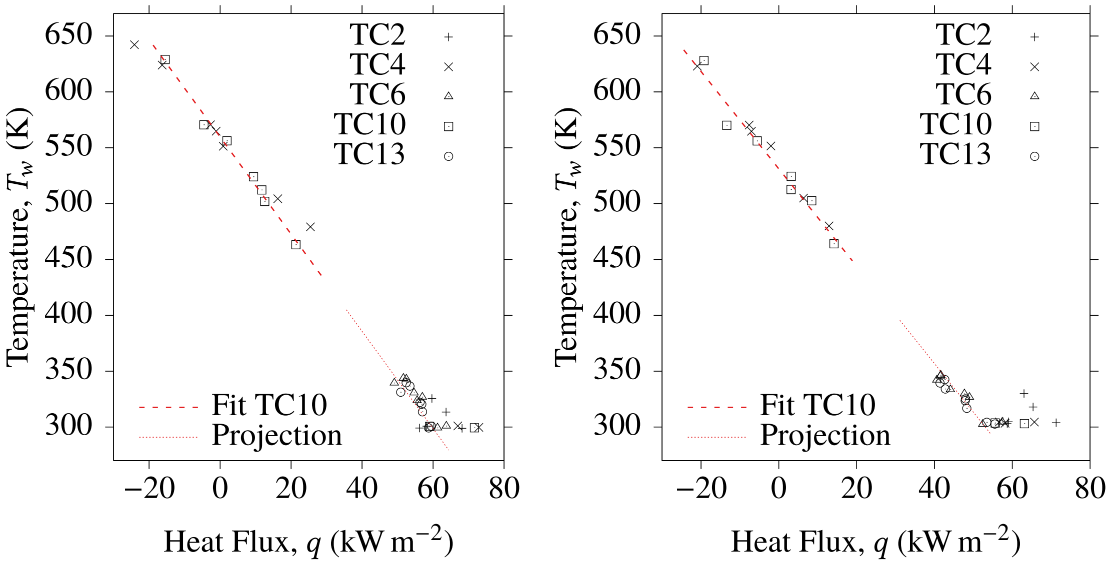

(a) 10 ms of data centred at $t = 10$ ms

(b) 10 ms of data centred at $t = 100$ ms

Figure 7.9: Linear regression analysis to determine the convective heat transfer coefficient using the probe surface temperature (T_w) and heat flux (q).

The heat transfer coefficient determined for TC10 using the regressions shown on Fig. 7.9a and Fig. 7.9b were in strong agreement, 229.8 W m^{-2} K^{-1} and 229.5 W m^{-2} K^{-1} respectively. Over the full run duration, with 10 ms windows analysed every 1 ms, more variance in the mean heat transfer coefficient was exhibited as shown by Fig. 7.10. There were regions of data affected by non-physical impulses of temperature and heat flux, and these were omitted from the analysis. Over the run duration h_c tended to increase slightly, and this is predicted by the analytical model as the flow Mach number decreases. These changes were small and well within the uncertainty of heat transfer measurements, therefore the mean heat transfer coefficient was deduced as $h_c = 229$ W m^{-2} K^{-1} for thermocouple TC10 and $h_c = 232$ W m^{-2} K^{-1} for thermocouple TC4.

The analytical model was found to underestimate the heat transfer coefficient by approximately 12.5 %. Given the limitations of the analytical model, such as the stagnation point velocity gradient K being described as the "author’s educated guess" (White, 2005), and the assumption of nominally identical runs that is required for use of the linear regression method, the 12.5 % difference in the measured and the theoretical h_c values is relatively small.

The assumption of nominally identical runs can be simply examined by calculating the flow stagnation temperature if the facility operation was isentropic. In this case the

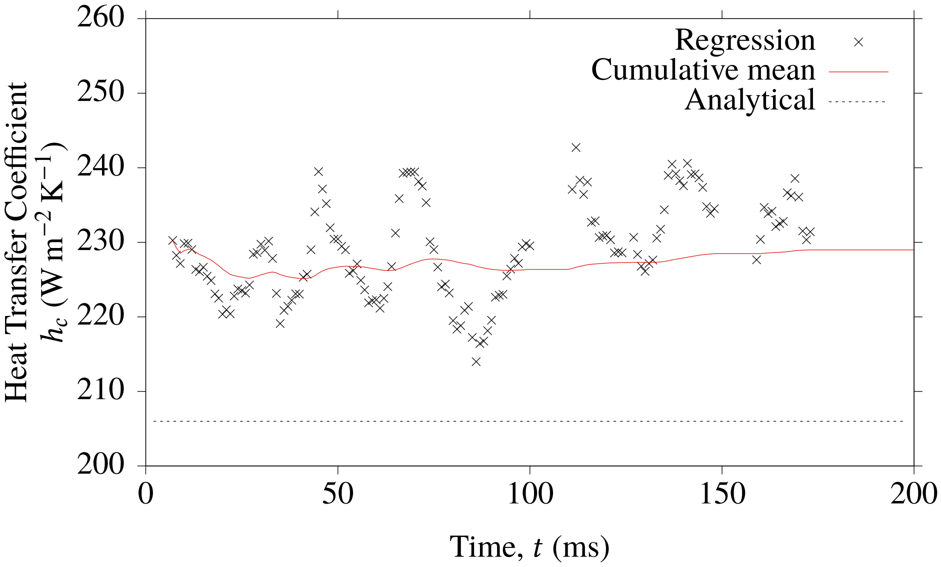

Figure 7.10: Changes of mean heat transfer coefficient for TC10 using 10 ms windows and evaluated every 1 ms, centred at t_c.

stagnation temperature can be calculated by

$$T_0 = T_{atm} \times \left(\frac{P_0}{P_{atm}}\right)^{\frac{\gamma-1}{\gamma}} \tag{7.11}$$

Figure 7.11 shows the stagnation temperatures for the runs with the maximum and minimum stagnation temperatures, assuming an isentropic process as per Eq. 7.11. It is clear that there is approximately 10 K difference between the maximum and minimum values immediately following diaphragm rupture, and this difference is approximately maintained for the period shown. The sharp changes associated with reflected expansion waves are reasonably well aligned for the first two reflections, but as time increases the timing differences become more significant.

Since the probe face shape and dimensions for heated and unheated thermocouples were identical, the convective heat transfer coefficient was assumed to be $h_c = 230\,\mathrm{W\,m^{-2}\,K^{-1}}$ for thermocouples 2, 6 and 13; and the identified $h_c = 229\,\mathrm{W\,m^{-2}\,K^{-1}}$ for thermocouple TC10 and $h_c = 232\,\mathrm{W\,m^{-2}\,K^{-1}}$ for TC4. With these heat transfer coefficients, and the identified thermal effusivity for each gauge, a consistent stagnation temperature across the core flow for each individual run was measured using TC4, TC6, TC10 and TC13.

It was difficult to assess the validity of $h_c = 230\,\mathrm{W\,m^{-2}\,K^{-1}}$ for data obtained using TC2 because the thermocouple failed for the majority of runs. For two of the four runs where

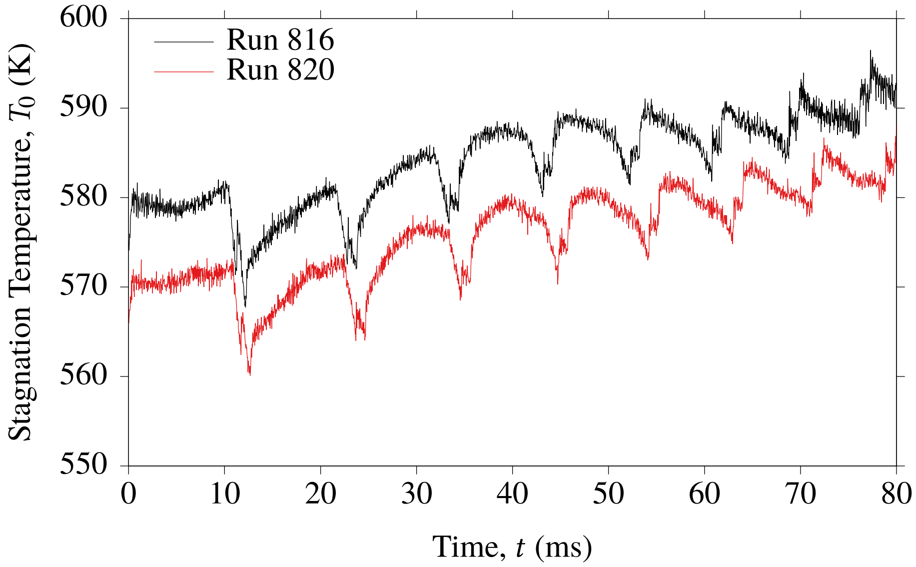

Figure 7.11: Stagnation temperature assuming isentropic facility operation as per Eq. 7.11 for the maximum (Run 816) and minimum (Run 818) stagnation temperatures identified for the runs where the thermocouple rake was used.

data was successfully obtained, the flow stagnation temperature exceeded the isentropic temperature by approximately 10 K for the period $5 \leq t \leq 15$ ms. Although the physical probe geometry was not changed, there was an apparent change in heat transfer coefficient. This cannot be the case, and is the result of changes of the effective thermal effusivity of the thermocouple. Thermocouple 2 was found to have the most variable thermal effusivity (3965 $\mathrm{J\,m^{-2}\,K^{-1}s^{-0.5}}$ ± 10.8 %). Since any uncertainty in e_{TC} propagates into the measured heat flux q, the apparent change of h_c was traced to a change of thermal effusivity for the thermocouple from the mean calibrated value. For TC2, considering the period $5 \leq t \leq 15$ ms, the calculated stagnation temperatures across the four runs where data were obtained differed by approximately 40 K, with T_0 exceeding the ideal isentropic value for two of these runs. Because of the limited data and high uncertainty for TC2, results from it were not analysed further.

It was common for the heated thermocouples to require resurfacing after runs, while occasional resurfacing was also required for the cold thermocouples. The junction resistance was found to increase or decrease as a result of a run indicating that junctions were created and destroyed, and a sample of the pre and post flow resistance data is shown in Table 7.2. The generation of this new junction then had the potential to change the effective thermal effusivity of the thermocouple.

TC	Run 818		Run 819		Run 820	
	pre-run	post-run	pre-run	post-run	pre-run	post-run
2	4.3 Ω	1.1 Ω	1.1 Ω	1.0 Ω	1.0 Ω	1.1 Ω
4	10.0 Ω	33.1 Ω	8.0 Ω	59.9 Ω	4.5 Ω	140 kΩ
6	8.6 Ω	6.9 Ω	6.9 Ω	9.0 Ω	9.0 Ω	12.9 Ω
10	2.6 Ω	57.1 Ω	0.4 Ω	121.3 Ω	1.5 Ω	44.9 Ω
13	7.3 Ω	7.2 Ω	7.2 Ω	9.5 Ω	9.5 Ω	9.0 Ω

Table 7.2: Thermocouple junction resistance before and after a run.

Changes in thermal effusivity between runs were observed for the other thermocouples, but because of the large amount of data available, the runs where the thermal effusivity for any thermocouple differed significantly from the mean calibrated value could be easily identified by comparing the determined stagnation temperature to the isentropic value for $5 \leq t \leq 15$ ms, and to the other measured data. In this time period the flow stagnation temperature is known to be close to the temperature calculated assuming an isentropic compression and expansion process. If the measured stagnation temperature exceeded the isentropic value, the data was removed, and similarly if the stagnation temperature was significantly lower than the other measured values this data was also removed. The results of this data reduction are shown in Table 7.3.

Run	TC4	TC6	TC10	TC13
811	$> T_{isen}$	✓	$> T_{isen}$	$<< T_{isen}$
812	$> T_{isen}$	✓	✓	✓
813	$> T_{isen}$	✓	✓	✓
814	✓	✓	✓	✓
815	✓	✓	✓	✓
816	$> T_{isen}$	$> T_{isen}$	$> T_{isen}$	✓
817	✓	✓	✓	✓
818	✓	✓	✓	✓
819	✓	✓	✓	✓
820	✓	✓	✓	✓

Table 7.3: Summary of thermocouple data used for determining the temporally resolved flow stagnation temperature for $f < 1$ kHz.

7.5 Temporally Resolved Stagnation Temperature

The temporally resolved stagnation temperature T_0 was calculated using

$$T_0 = \frac{q}{h_c} + T_w \tag{7.12}$$

where T_w is the measured thermocouple temperature, q was identified using the procedure described in Section 7.3 and the calibrated thermal effusivity, and h_c the convective heat transfer coefficient which was identified using the regression analysis presented in Section 7.4.

The stagnation temperature which was identified for each run was low-pass filtered at 1 kHz using a 256 point Blackman-Harris window. The windowing technique was found to significantly reduce high-frequency artefacts that were present when using a Butterworth low-pass filter, and in using the Blackman-Harris window there was little difference in the results when the stagnation temperature was determined using SWT filtered and raw temperature data. The effect of this filter is shown in Fig. 7.12 which compares stagnation temperatures determined using SWT filtered data with and without the filter. Despite the relatively low cutoff frequency, the 1 kHz bandwidth remained sufficient to resolve relatively high frequency events, such as those associated with reflections of the expansion wave off the piston propagating into the test flow.

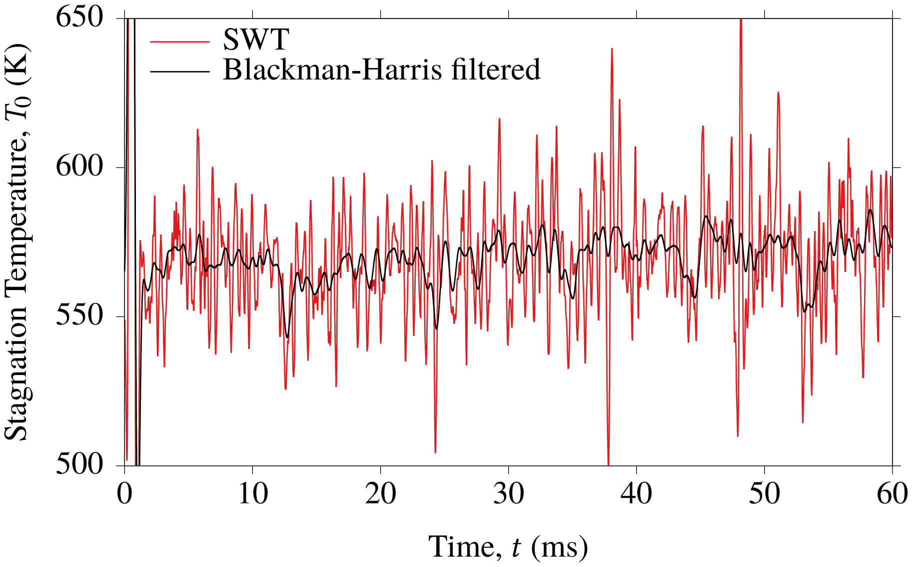

Figure 7.12: Blackman-Harris filtering of the SWT filtered data to determine the temporally resolved stagnation temperature.

The stagnation temperature data at each position for every run were temporally aligned such that flow onset occurred at $t = 0$ ms. This signal alignment facilitated the mean stagnation temperature to be determined across all TUSQ runs at every time step and each thermocouple. The mean level comparison is shown in Fig. 7.13 for $0 \leq 30$ ms, and this flow period represents the region of best temporal run-to-run signal alignment. For $t > 30$ ms the quality of the signal alignment is reduced because the change of timing of run-to-run events becomes significant, such as the reflections of the expansion wave off the piston. This timing difference was shown in Fig. 7.11.

For $t < 10$ ms, the preheated thermocouples (Fig. 7.13a) were found to resolve the flow stagnation temperature better than the cold thermocouples (Fig. 7.13b). For $t < 10$ ms, the stagnation temperature calculated using data from thermocouples operated without preheating tended to exceed the value of the stagnation temperature calculated by isentropic expansion of the test gas. This behaviour was not observed when using preheated thermocouples, and for $t > 10$ ms the heated and preheated thermocouples produce similar results.

The initial overshoot behaviour of the cold thermocouples is the period of greatest variance between runs, but the standard deviation of stagnation temperature from 8 – 30 ms is consistent for cold and heated thermocouples. For this period of flow, the average standard deviation was 1.58 % for both TC4 and TC10, while the average standard deviation of the cold thermocouples, TC6 and TC13, was 1.96 % and 1.97 % respectively. The lower run-to-run variance of stagnation temperature registered by the heated thermocouples is likely a result of the thermocouple operating temperature being more closely matched to the flow stagnation temperature.

The stagnation temperature of the hypersonic flow as identified using $f_c = 1$ kHz and the data from TC10 is shown in Fig. 7.14, illustrating good run-to-run repeatability. The mean flow line terminates at the end of the run with the shortest flow duration (approximately 206 ms). The pre-flow data ($t < 0$ ms) represent the initial temperature of the thermocouple and also shows the baseline noise level of the measurements, which varied between runs. The highest noise level was for Run 813, and for this run, the DC offset of the AC stage of the amplifier was set incorrectly and the signal saturated, and therefore only stage 1 of the amplifier was used.

Using TC10, the average stagnation temperature for each run in the first 10 ms of flow is between the preheat temperatures for Run 819 (556.2 K) and Run 820 (570.6 K). This is consistent with the results presented in Fig. 7.7a where the thermocouple temperature increased by a small amount for Run 819 and dropped slightly during Run 820 for $0 < t < 10$ ms which corresponded to a slightly positive and slightly negative heat flux for Runs 819 and 820 respectively (Fig. 7.7b). Therefore, the flow stagnation temperature immediately following diaphragm rupture can be confidently stated as being in the range

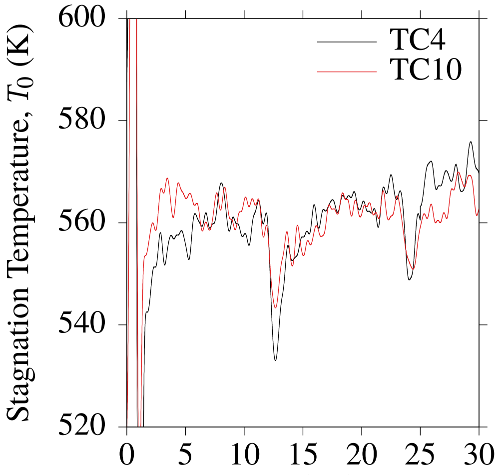

(a) Preheated thermocouples

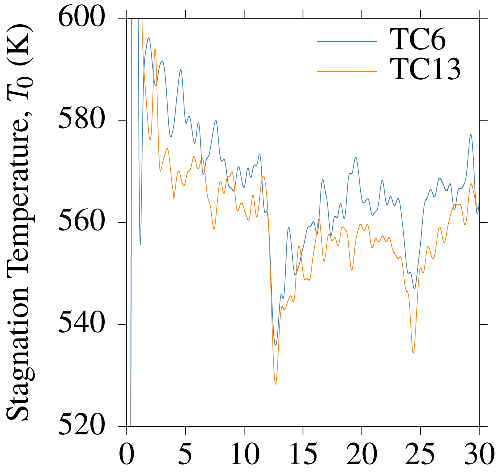

(b) Cold thermocouples

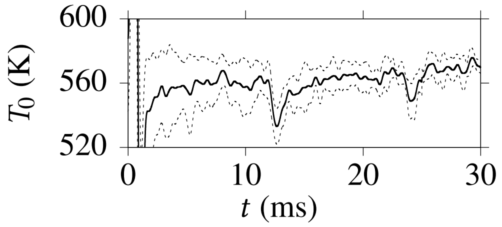

(c) Thermocouple TC4

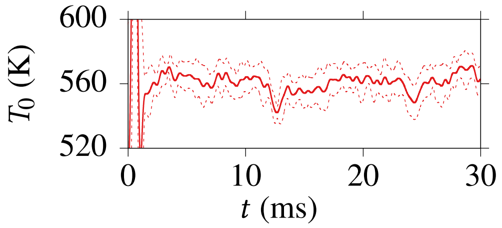

(d) Thermocouple TC10

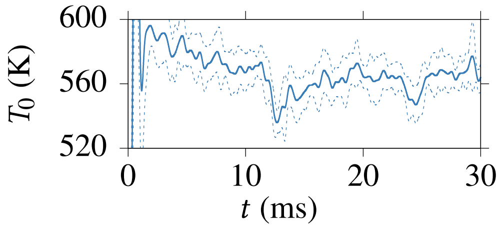

(e) Thermocouple TC6

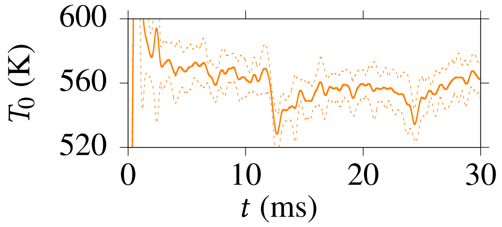

(f) Thermocouple TC13

Figure 7.13: Comparison of flow stagnation temperature for $0 \leq t \leq 30$ ms measured by four thermocouples. Dashed lines indicate one standard deviation from the mean.

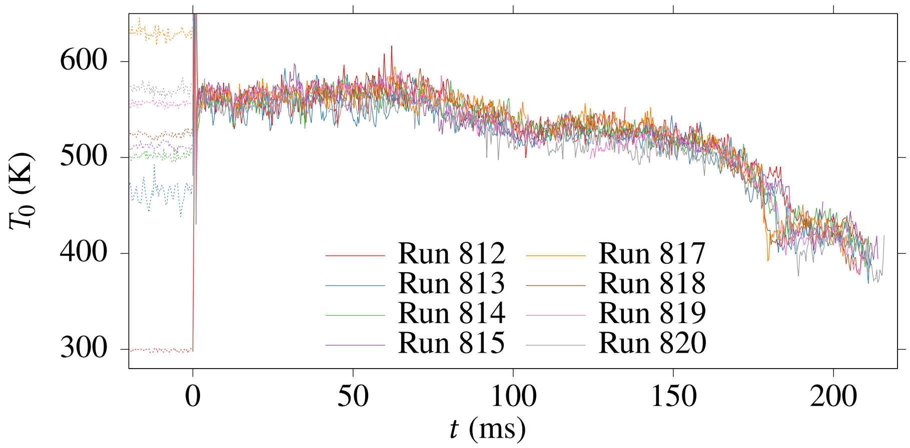

(a) Stagnation temperature for eight runs

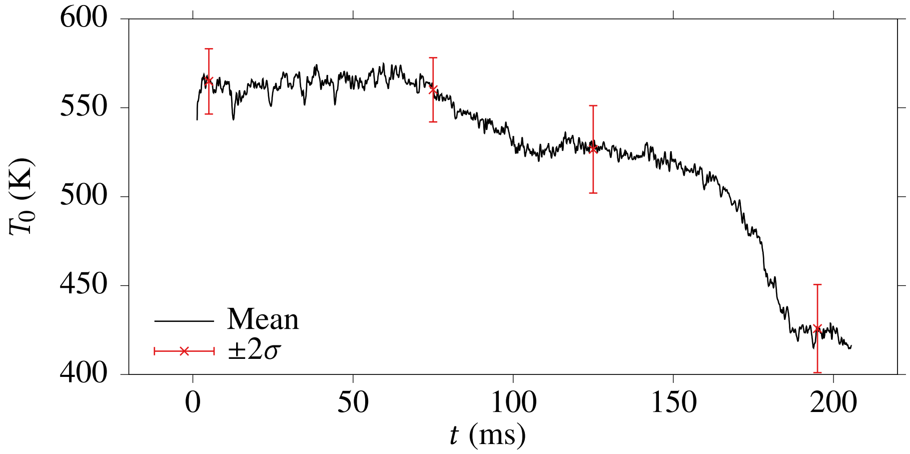

(b) Time-averaged stagnation temperature

Figure 7.14: Stagnation temperature traces identified using TC10 over the full duration of the flow for $f < 1$ kHz. The time-averaged line terminates at the end of the run with the shortest flow duration. Dashed lines indicate pre-flow data and represent the initial temperature of the thermocouple.

556.2 – 570.6 K, which is just below the isentropic values shown in Fig. 7.11 (570 – 580 K).

An approximately constant stagnation temperature between diaphragm rupture and the arrival of the first wave reflected off the piston at approximately 12.5 ms was expected from isentropic flow relations (Fig. 7.11), and a constant stagnation temperature during this period of flow was confirmed experimentally. The constant stagnation temperature was better resolved using the thermocouples preheated to near the flow stagnation temperature than those operated at, or near, ambient temperature (Fig. 7.13). The thermocouples that were not preheated tended to overshoot the flow stagnation temperature for $t < 5$ ms. Table 7.4 shows the stagnation temperature identified using the preheated thermocouples for $5 < t < 10$ ms, and demonstrates that the stagnation temperature is approximately

98 % of the isentropic value during this period.

Run	$\overline{T}_0$ (K)		σ (K)		$\overline{T}_0/\overline{T}_{isen}$	
	TC4	TC10	TC4	TC10	TC4	TC10
812*	–	562.1	–	8.5	–	0.975
813	–	558.8	–	12.1	–	0.973
814	561.9	558.7	3.6	4.5	0.979	0.973
815	560.8	564.3	10.6	8.9	0.972	0.978
817	540.5	564.0	11.6	4.3	0.940	0.981
818	580.0	570.0	2.3	2.2	1.011	0.994
819	564.3	569.1	3.6	2.9	0.984	0.992
820	564.3	551.6	7.3	4.5	0.972	0.967
Mean	560.3	562.3	3.2	2.5	0.975	0.979

Table 7.4: Mean stagnation temperature data for $5 < t < 10$ ms. * indicates a run without preheating.

Figure 7.14 shows that for TC10 there were six runs where $T_w \approx T_0$ for different periods of flow, and the regions where this is true are the periods of flow where stagnation temperature fluctuations can be analysed. Additionally, the stagnation temperature identified when $T_w \approx T_0$ are the periods of smallest measurement uncertainty as the effects of changes of effective thermocouple effusivity, and the uncertainty of the heat transfer coefficient, are minimised.

As shown on Fig. 7.14, the stagnation temperature is approximately constant for the first 70 ms of flow, followed by a period of cooling by about 50 K over the next 40 ms. For $110 \lesssim t \lesssim 150$ ms the stagnation temperature is again approximately constant. When $t > 150$ ms the rate of cooling increases until a sudden drop in stagnation temperature down to approximately 420 K. This sudden drop in stagnation temperature takes less than 2 ms and begins between $177 < t < 187$ ms depending on the run. Because of the variation in the time of occurrence of this sudden drop in stagnation temperature, its gradient is not well resolved by the mean flow line. The stagnation temperature remains approximately 420 K until the end of nozzle flow.

To investigate if any of these changes in stagnation temperature can be attributed to events identified from the analysis of the stagnation pressure, the mean stagnation temperature identified using each of the thermocouples is shown in Fig. 7.15. The annotations (i), (ii) and (iii) were identified from the barrel pressure measurement, and these features were presented in Fig. 5.1 in Chapter 5. The stagnation temperature is uniform, at least to the accuracy of transient heat flux measurements, across the core flow. The stagnation temperature in the vicinity of TC13 appears to be slightly cooler than that of the other probes for $40 < t < 80$ ms, however it is observed to agree well with the remaining test time.

Stagnation temperature measurements were able to resolve the effects associated with the interaction of expansion waves and the piston propagating into the core flow (feature i, Fig. 7.15), with the first four wave reflections clearly visible on all of the mean traces. Later reflections are less evident on the mean traces because the temporal misalignment of these events becomes more significant as time increases.

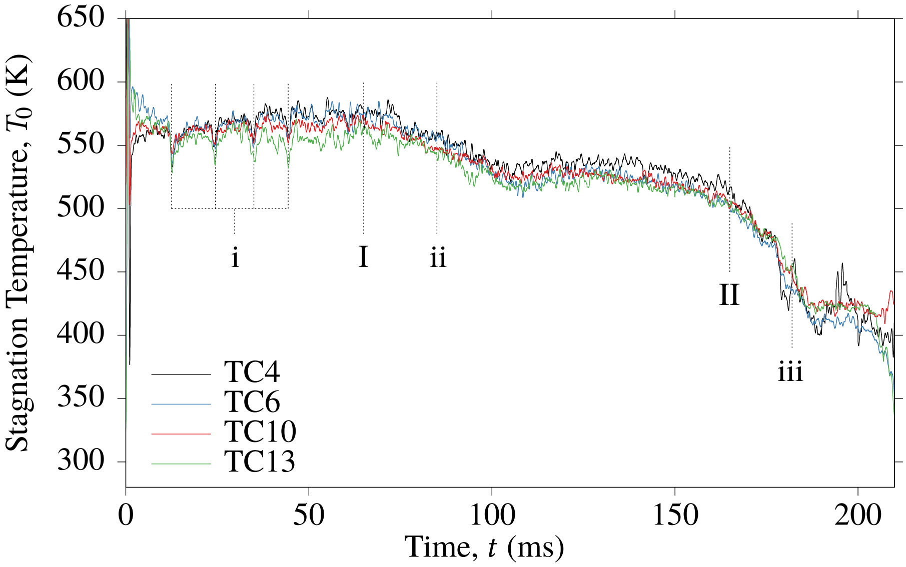

Figure 7.15: Mean stagnation temperature at four locations, annotated with pressure events originating in the barrel. (i)- the first four reflected expansion waves off the piston; (ii)- the reflected expansion wave that has travelled to the barrel inlet returns to the nozzle inlet; (iii)- reflected expansion wave (ii) returns to the nozzle inlet end of the barrel for the second time. Two changes in the stagnation temperature have been annotated; (I) the start of the first cooling event, and (II) the start of a second cooling event.

Feature (ii), the reflected expansion wave that has travelled to the barrel inlet returning to the nozzle inlet, occurs during a period of reducing stagnation temperature. However the start of cooling event (I) leads the arrival of (ii) by approximately 18 ms, and the rate of cooling after its arrival does not change. Therefore the cooling from 70 – 110 ms is not attributed to feature (ii). The actual source of this event will be discussed further in Section 7.6.

Feature (iii), the reflected expansion wave (ii) returning to the nozzle inlet end of the barrel for the second time, occurs after the sudden reduction in stagnation temperature that begins at $t = 162$ ms, annotated (II) on Fig. 7.15. Therefore the sudden cooling event towards the end of hypersonic flow is not driven by the second reflected expansion wave (feature (iii)). Instead, the source of this sudden cooling and the lower stagnation temperature flow that occurs after this cooling are the results of the cold vortical flow propagating ahead of the piston. Similar results were measured in TUSQ in an earlier study (Widodo & Buttsworth, 2013) and an unstable vortical structure is known to propagate ahead of the piston in similar piston driven facilities (East & Qasrawi, 1978; Jones et al., 1973).

Such vortical structures are known to adversely affect flow stagnation temperatures for the final 15 – 20% of the flow duration for barrels of large l/d ($\gtrsim 100$). This vortex contains the tube boundary layer gas which has been scraped from the wall and therefore has a lower thermal energy content due to heat lost to the cold barrel walls.

7.6 Comparison to Simulation

A simulation tool to calculate the stagnation temperature in TUSQ based on the measured pressure in the barrel was developed by Widodo and Buttsworth (2013). The simulation uses thermodynamic models for the heat loss from the test gas to the cold barrel walls during the compression and nozzle discharge processes. This simulation is fully described in Widodo and Buttsworth (2013), and was summarised in Section 4.3.3.

The experimentally measured barrel pressure from Run 819, up until the instant of diaphragm rupture, was used to determine the stagnation temperature of the facility over time using the flat plate and pipe flow heat loss models of Widodo and Buttsworth (2013). Flat plate laminar to turbulent transition was assumed to start at a Reynolds number of $Re_{cr} = 0.2 \times 10^6$ and to be completed by a Reynolds number of 2×10^6 as identified by Widodo and Buttsworth (2013), however, as shown in Fig. 7.16, the knee in the flat plate model associated with the transition process occurred earlier than in the experimental measurements of stagnation temperature. Setting the critical Reynolds number $Re_{cr} = 1 \times 10^6$ resulted in a better match between the flat plate model and the experimentally identified stagnation temperature. Similar to the work of Widodo and Buttsworth (2013), the pipe flow model was a poor fit for the experimental measurements, and the barrel heat transfer process is better simulated using the flat plate model.

The stagnation temperature of the test flow was simulated in L1d3 using the procedure

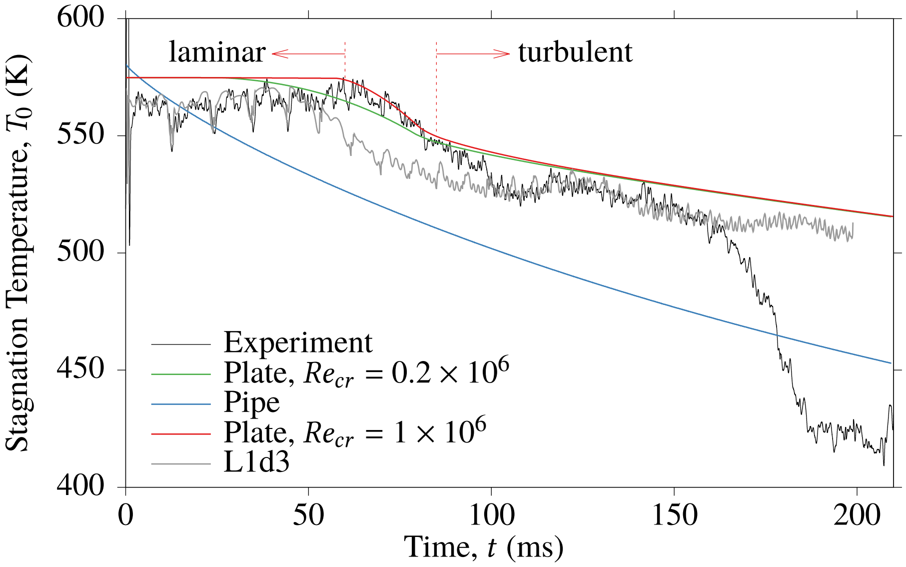

Figure 7.16: Comparison of the mean stagnation temperature to the results of the stagnation temperature simulation using two different critical Reynolds numbers.

described in Section 4.3 and results from this simulation are also shown in Fig. 7.16. There was excellent agreement between the L1d3 simulation and the experimental data in the amplitude of the temperature changes resulting from the reflected expansion waves off the piston. The amplitude of the stagnation temperature was well simulated using L1d3 except for two regions: (1) in the laminar-turbulent transition region; and (2) the final portion of flow time where the cold vortices propagating ahead of the piston are expelled through the nozzle. The second region of disagreement was expected, as such features are not modelled in L1d3. In the L1d3 simulation, the onset of laminar-turbulent transition appears to lead the onset of laminar-turbulent transition predicted by the Widodo and Buttsworth (2013) flat plate simulation. For the L1d3 simulation, the friction and heat flux were calculated using a flat plate model where transition was set to occur for $0.5 \times 10^6 < Re < 10 \times 10^6$, and because the critical Reynolds number here ($Re_{cr} = 0.5 \times 10^6$) is greater than the critical Reynolds number of the Widodo and Buttsworth (2013) simulation ($Re_{cr} = 0.2 \times 10^6$), it should result in the L1d3 transition onset being later than the Widodo and Buttsworth (2013) simulation. The unexpected behaviour of the L1d3 simulation was traced to a limitation in the simulation definition. In Section 4.3, the L1d3 valve model was found to be prohibitively slow for application to the TUSQ facility, and a method for configuring gas slugs of non-uniform thermodynamic properties described. This method caused an expansion wave to propagate from the upstream end of the barrel when the simulation was started, and the interaction of this expansion wave with the piston caused the Reynolds number to exceed Re_{cr} prematurely.

The Widodo and Buttsworth (2013) simulation tool is limited in that the pressure is assumed constant throughout the flow duration. This limitation was overcome by a convolution of the isentropic stagnation temperature and the stagnation temperature models of Widodo and Buttsworth (2013), with the results shown in Fig. 7.17. For this convolution, the Widodo and Buttsworth (2013) models were normalised by their maximum stagnation temperature value which occurs at $t = 0$ s. The normalised pipe and flat plate models were multiplied by 0.98 to account for the small amount of heat lost during compression up until diaphragm rupture, consistent with the values of Table 7.4.

With the time-varying pressure conditions now included in the results of the simulation, the level of agreement between the flat plate model and experimental data is exceptional for the first 150 ms, remaining within 2 % of the experimental value. This error remains less than 5 % at $t = 170$ ms, and increases to approximately 20 % when the cold vortices ahead of the piston are discharged through the nozzle.

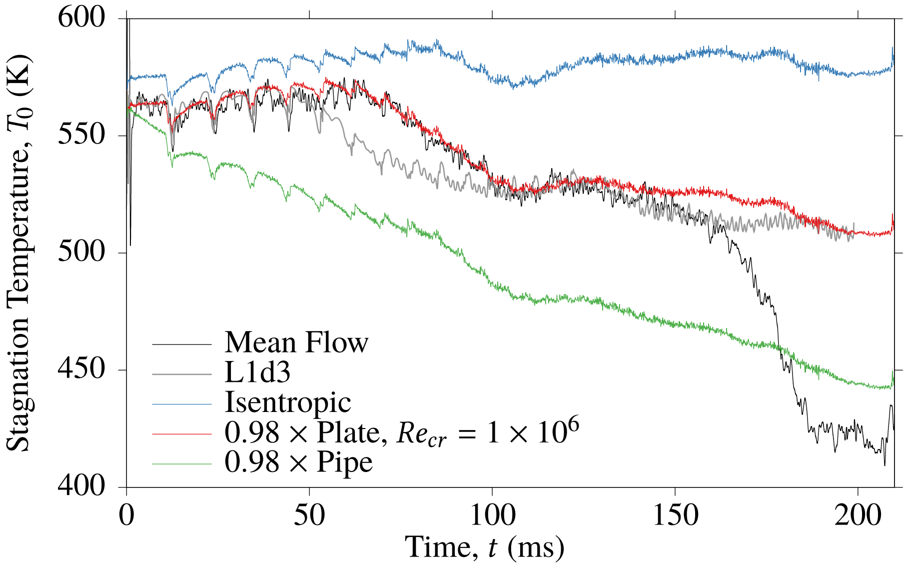

Figure 7.17: Transformation of the simulated models for comparison to the mean stagnation temperature.

7.7 Fluctuations of Stagnation Temperature

The heat transfer coefficient for convective heat transfer to the stagnation point of an axisymmetric body in a high speed flow was presented as Eq. 7.8 and can be alternatively expressed in a non-dimensional form as:

$$\mathrm{Nu} = 0.763\,\mathrm{Pr}^{0.4}\,\mathrm{Re}^{0.5}\,C^{0.1}\left(\frac{KD}{u_\infty}\right)^{0.5} \tag{7.13}$$

where Nu and Re are the Nusselt number and Reynolds number respectively, and both are referenced to the probe diameter, Pr the Prandtl number at the edge of the boundary layer, $C{=}\frac{\rho_w \mu_w}{\rho_e \mu_e}$ and $K{=}\frac{\mathrm{d}u_e}{\mathrm{d}x}$ is the local velocity gradient at the stagnation point.

In cases where Pitot pressure measurements are available, the heat transfer coefficient can be expressed as a function of Pitot pressure as:

$$h_c \propto \sqrt{P_{pt}} \quad \underbrace{\left[\frac{k_e^{0.6}\, C^{0.1}}{\mu_e^{0.1}\, T_e^{0.25}}\right]}_{\substack{\text{Probe surface}\\ \text{temperature and}\\ \text{freestream total}\\ \text{temperature effects}}} \quad \underbrace{\left[M_\infty^{0.5} \left(\frac{T_\infty}{T_e}\right)^{0.25} \left(\frac{KD}{u_\infty}\right)^{0.5}\right]}_{\text{Mach number effects}} \tag{7.14}$$

where the term $\frac{KD}{u_\infty} = 0.3$ for $M > 5$ (White, 2005) in the case of a flat faced cylindrical probe. The sensitivity of h_c to the freestream Mach number in the present work can be determined by analysing Mach number dependent terms in Eq. 7.14 for the range $5.85 \leq M \leq 5.95$. In the Mach number range 5.85 – 5.95, and using T_e calculated from isentropic flow and normal shock relations, the freestream Mach number term changes the heat transfer coefficient by $\lesssim$0.1 %. Therefore, the convective heat transfer coefficient is largely independent from the Mach number so the changes of the heat transfer coefficient resulting from the Mach number effect term can be neglected.

The relationship between the convective heat transfer coefficient and the probe surface and total temperature effects can be investigated by using the power law approximations for thermal conductivity and viscosity,

$$\frac{k}{k_0} = \left(\frac{T}{T_0}\right)^{n_k} \tag{7.15}$$

$$\frac{\mu}{\mu_0} = \left(\frac{T}{T_0}\right)^{n_\mu} \tag{7.16}$$

where n, k_0, T_0 and μ_0 are constants for each gas. By substituting n_k=0.81 and n_μ=0.666 for air,

$$\left[\frac{k_e^{0.6}\, C^{0.1}}{\mu_e^{0.1}\, T_e^{0.25}}\right] \propto \frac{T_e^{0.2028}}{T_w^{0.0334}} \tag{7.17}$$

and if the probe is operated at an essentially constant surface temperature, the heat transfer coefficient can be then expressed as (Buttsworth & Jacobs, 2000)

$$h_c = c\sqrt{P_{pt}}\, T_e^{0.2028} \tag{7.18}$$

where c is the constant of proportionality. Expressing the convective heat transfer coefficient in terms of time-averaged ($e.g.$ $\overline{h}_c$) and fluctuating components ($e.g.$ h'_c)

$$h_c = c\left(\overline{P}_{pt} + P'_{pt}\right)^{0.5}\left(\overline{T}_e + T'_e\right)^{0.2028} \tag{7.19}$$

Dividing both sides of Eq. 7.19 by $\overline{h}_c$,

$$\frac{\overline{h}_c + h'_c}{\overline{h}_c} = \frac{\left(\overline{P}_{pt} + P'_{pt}\right)^{0.5}\left(\overline{T}_e + T'_e\right)^{0.2028}}{\overline{P}_{pt}^{0.5}\,\overline{T}_e^{0.2028}} \tag{7.20}$$

and collecting like terms,

$$1 + \frac{h'_c}{\overline{h}_c} = \left(1 + \frac{P'_{pt}}{\overline{P}_{pt}}\right)^{0.5}\left(1 + \frac{T'_e}{\overline{T}_e}\right)^{0.2028} \tag{7.21}$$

Eq. 7.21 can be simplified using the series expansion and neglecting second order and higher terms since $P'_{pt}/\overline{P}_{pt}$ and $T'_e/\overline{T}_e$ are much less than one as

$$1 + \frac{h'_c}{\overline{h}_c} = \left(1 + 0.5\frac{P'_{pt}}{\overline{P}_{pt}}\right)\left(1 + 0.2028\frac{T'_e}{\overline{T}_e}\right). \tag{7.22}$$

By neglecting the product of $P'_{pt}/\overline{P}_{pt}$ and $T'_e/\overline{T}_e$ since this is a small contributor to the equation,

$$\frac{h'_c}{\overline{h}_c} = 0.5\frac{P'_{pt}}{\overline{P}_{pt}} + 0.2028\frac{T'_e}{\overline{T}_e} \tag{7.23}$$

the heat flux can be expressed as time-averaged and fluctuating components as

$$q = \underbrace{\overline{h_c}\left(\overline{T_e} - \overline{T_w}\right)}_{\overline{q}} + \underbrace{h'_c\left(\overline{T_e} - \overline{T_w}\right) + \overline{h}_c\left(T'_e - T'_w\right)}_{q'} \tag{7.24}$$

and therefore,

$$\frac{q'}{\overline{q}} = \frac{h'_c}{\overline{h}_c} + \frac{T'_e - T'_w}{\overline{T_e} - \overline{T_w}}. \tag{7.25}$$

Substituting Eq. 7.23 into Eq. 7.25, and considering that for a gauge operated at essentially constant temperature $T'_w \ll T'_e$,

$$\frac{q'}{\overline{q}} = \left(\frac{\overline{T_e}}{\overline{T_e} - \overline{T_w}} + 0.2028 \right) \frac{T'_e}{\overline{T_e}} + 0.5 \frac{P'_{pt}}{\overline{P_{pt}}} \tag{7.26}$$

The ratio $\frac{\overline{T_e}}{\overline{T_e - T_w}}$ is at a minimum when evaluated for the case of an unheated thermocouple at the beginning of the run, where the stagnation temperature is at its maximum. In this case, $\frac{\overline{T_e}}{\overline{T_e - T_w}} + 0.2028 \approx 2.25$, meaning the fluctuations in the measured heat flux are at least 4.5 times more sensitive to relative fluctuations in total temperature than to relative fluctuations in Pitot pressure. The heat flux is measured at the stagnation point, and since the stagnation temperature across a normal shock does not change, the flow temperature at the edge of the boundary layer T_e is therefore the flow stagnation temperature T_0. In a case where $T_w = 510\,\mathrm{K}$ and $T_0 = 560\,\mathrm{K}$, the relative fluctuations of heat flux are 22 times more sensitive to fluctuations in total temperature than to relative fluctuations in Pitot pressure. Therefore, it is desirable to operate a thermocouple as close to the flow stagnation temperature as possible to accurately determine stagnation temperature fluctuations. However when a thermocouple is operated at $T_w \approx T_0$, Eq. 7.26 is undefined since $\frac{q'}{\overline{q}} \to \infty$ and $\frac{\overline{T_0}}{\overline{T_0 - T_w}} \to \infty$. Therefore, Eq. 7.26 is only suitable for specifying thermocouple operation when $T_w \neq T_0$.

Instead, for the case of $T_w = T_0$, the fluctuating component of heat flux is

$$\frac{q'}{\overline{q}} = \overline{h}_c \left(T'_0 - T'_w \right) \tag{7.27}$$

from Eq. 7.24. The magnitude of fluctuations of surface temperature for a surface junction thermocouple is related to the magnitude of heat flux fluctuation in the frequency domain by

$$\frac{|T'_w|}{|q'|} = \left(\sqrt{\omega} \sqrt{\rho c k} \right)^{-1} \tag{7.28}$$

where ω is the angular frequency, $\omega = 2\pi f$, and $\sqrt{\rho c k}$ is the thermal effusivity of the thermocouple. Equation 7.28 can be written as

$$\frac{|T'_0|}{|T'_w|} = \overline{h}_c^{-1} \sqrt{\omega} \sqrt{\rho c k} + 1 \tag{7.29}$$

by using Eq. 7.27. Substituting $\overline{h}_c = 230\,\mathrm{W\,m^{-2}}$ and $\sqrt{\rho c k} = 4350\,\mathrm{J\,m^{-2}\,K^{-1}s^{-0.5}}$, Eq. 7.29 indicates the fluctuations in stagnation temperature are more significant than those of wall temperature by a factor of 100 at 4 Hz, and this ratio increases with frequency. Thus, when T_w' is neglected relative to T_0', from Eq. 7.27

$$T_0' = \frac{q'}{\bar{h}_c} \tag{7.30}$$

which is in a form that can be used to identify fluctuations of stagnation temperature when $T_w \approx T_0$.

Numerous regions of data were identified where the thermocouples were operated at approximately the stagnation temperature of the flow. To get the best estimates of stagnation temperature fluctuations, only regions where the time-averaged stagnation temperature data was within 15 K of the thermocouple temperature were investigated. For $t \leq 160$ ms, the $|T_0 - T_w| \leq 15$ K threshold represents flow temperature data that is within 3 % of the thermocouple operating temperature. Due to the high baseline noise level in the stagnation temperature fluctuations, the data were filtered using a Blackman-Harris window function with an effective low-pass filter cutoff frequency of 3 kHz. The data was then high-pass filtered at 4 Hz to isolate the fluctuations of stagnation temperature.

Four regions of stagnation temperature fluctuations are shown in Fig. 7.18, and these were selected so the fluctuations of stagnation temperature in four distinct flow periods could be analysed. Figure 7.18a shows the stagnation temperature fluctuations in the period of nominally constant stagnation temperature, where the heat transfer to the wall of the barrel is best described by the laminar flat plate model. The first two reflected expansion waves off the piston are visible at $t \approx 12.5$ ms and $t \approx 24.5$ ms.

The region of flow cooling where the heat transfer to the walls of the barrel is represented by a laminar-turbulent flat plate transition is shown in Fig. 7.18b. No reflected expansion waves are immediately evident, but the fluctuations of stagnation temperature show a strong degree of periodicity with a period of approximately 250 µs.

Figure 7.18c shows a segment of flow from the region where the mean stagnation temperature is nominally constant and the heat transfer to the walls of the barrel is in agreement with the turbulent flat plate model. There appears to be some strong fluctuations with a period of approximately 500 µs.

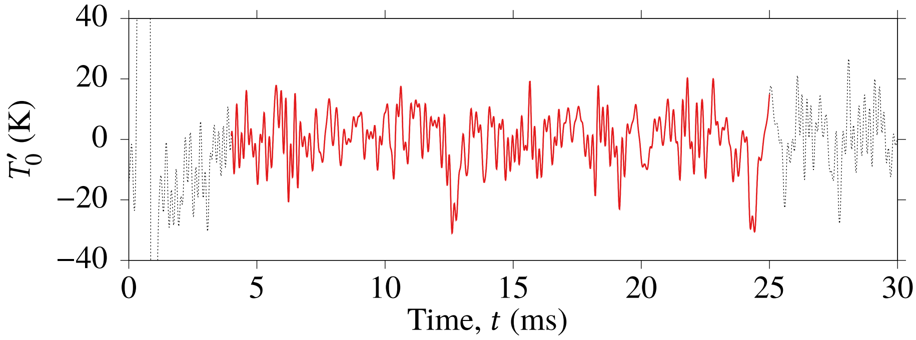

(a) Run 819 TC10

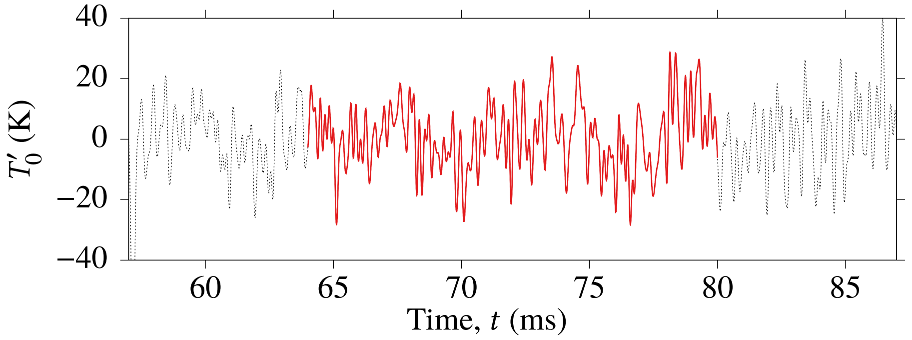

(b) Run 819 TC4

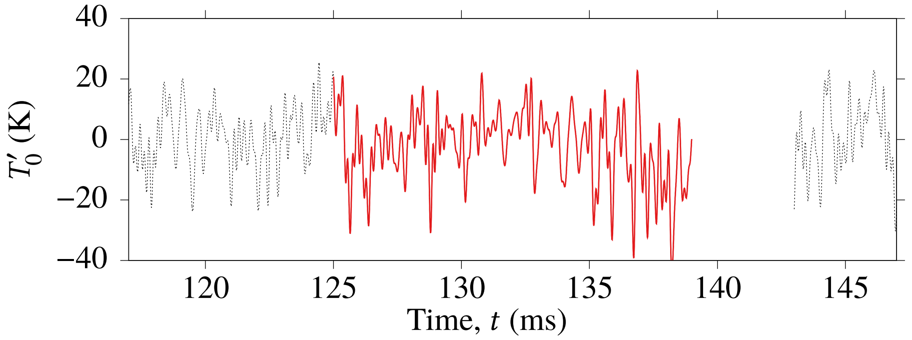

(c) Run 818 TC10

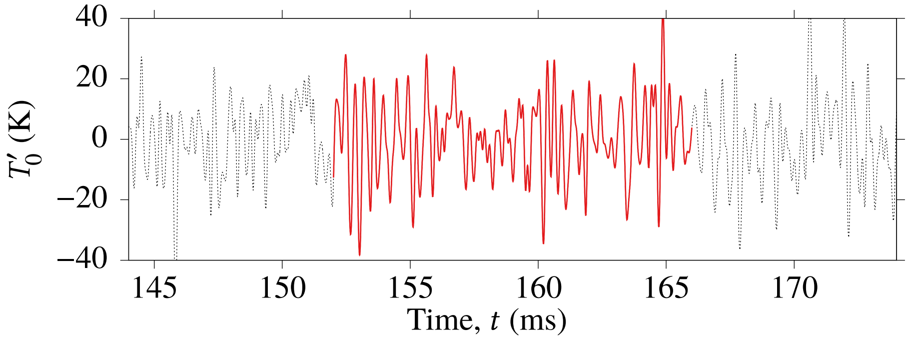

(d) Run 815 TC10

Figure 7.18: Stagnation temperature fluctuations during four segments of flow where $T_w = T_0 \pm$ 15 K and 4 Hz $\leq f \leq$ 3 kHz. Dashed lines indicate data outside this window.

Strong periodicity is again evident in Fig. 7.18d. For this period, the heat transfer in the barrel from the test gas to the barrel walls is best described as a combination of the turbulent flat plate and pipe flow models developed by Widodo and Buttsworth (2013), and this period is before the arrival of the cold flow resulting from the cold vortices propagating ahead of the piston.

The root-mean-square stagnation temperature fluctuations were 8.5 K, 10.7 K, 11.9 K, and 12.6 K for Fig. 7.18a to Fig. 7.18d respectively. However the baseline RMS noise level was in the order of 5 K with the signal-to-noise ratio (SNR) ranging from 1.3 – 2.4 depending on the run. Therefore, the amplitude of the stagnation temperature fluctuations identified must be viewed with some caution.

Despite the limitations resulting from high baseline noise levels, trends in the data can be identified. By plotting the percentage stagnation temperature fluctuations where $\overline{T}_0 = T_w \pm 15\,\mathrm{K}$ for each data segment where SNR > 1.2, the percentage stagnation temperature fluctuations are observed to increase with run time as shown in Fig. 7.19. When the raw thermocouple data was processed using the SWT filtering technique the same trend was evident, but at 80 – 90 % of the levels when the data were filtered using only the Blackman-Harris windows.

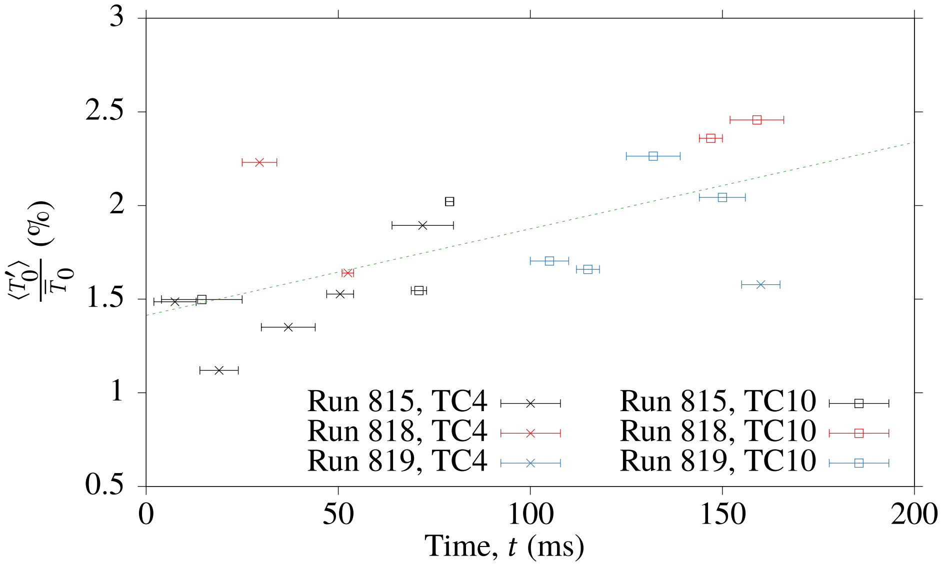

Figure 7.19: Percentage RMS stagnation temperature fluctuations where $\overline{T}_0 = T_w \pm 15\,\mathrm{K}$ exhibit a trend of increasing throughout the run. Error bars indicate the times where data was used to determine the fluctuations.

Periodicity was identified in Fig. 7.18, and these fluctuations can be investigated using the power spectral density method. For this analysis only the relative magnitude of stagnation temperature fluctuations was of interest, and therefore to achieve the highest frequency resolution the low-pass filter was not implemented. The spectrum of fluctuations was determined using Welch's power spectral density estimate using Blackman-Harris windows of width 2^{12} points and 50% overlap.

The baseline noise level was identified using a representative segment of data from prior to the flow onset. For frequencies above 5 kHz, the magnitude of stagnation temperature fluctuations was not sufficiently above the baseline noise level, and therefore the PSD estimates shown in Fig. 7.20 only present the $0-5$ kHz frequency band.

No strong narrowband spectral content was identified in Fig. 7.20a, which is consistent with the pitot pressure fluctuations for the same time period (Fig. 7.20a). Figure 7.20b exhibits a very strong spectral feature at 3.5 – 4 kHz. The Pitot pressure survey identified significant energy in a similar 3.6 – 4 kHz band. This feature, when first detected by the Pitot survey, was speculated to be approximately consistent with the return of the reflected expansion wave formed at diaphragm rupture that is transmitted through the piston and reflects off the barrel end wall back towards the nozzle to the nozzle entrance (Birch et al., 2018). However, in both the Pitot pressure and stagnation point heat flux measurements, the start of this content led the arrival of this reflected expansion wave, and in the case of Run 819 this expansion wave arrived at the barrel pressure transducer at $t \approx 85$ ms. The high 3.5 – 4 kHz spectral content is not evident in Fig. 7.20c, but is visible again in Fig. 7.20d.

The onset of the 3.5 – 4 kHz spectral content was analysed using PSD estimates of 20 ms periods of flow using the same Blackman-Harris windows as used for Fig. 7.20. Using the data from TC4 measured during Run 819, the content was not present before $t = 70$ ms as shown in Fig. 7.21, however when windowed to the 60 – 80 ms period of flow, the 3.5 – 4 kHz peak is clearly visible. This suggests the onset of the 3.5 – 4 kHz spectral content occurs at 70 – 80 ms. It is at about this time the heat transfer of the test gas in the barrel to the cold barrel walls was found to agree with flat plate transition from laminar to turbulent flow.

The maximum amplitude of this peak was for the period of 80 – 100 ms, and this is fully within the flow period identified as transitional in the barrel. The 70 – 90 ms and 90 – 110 ms periods contain data within this transitional zone and because of this, higher

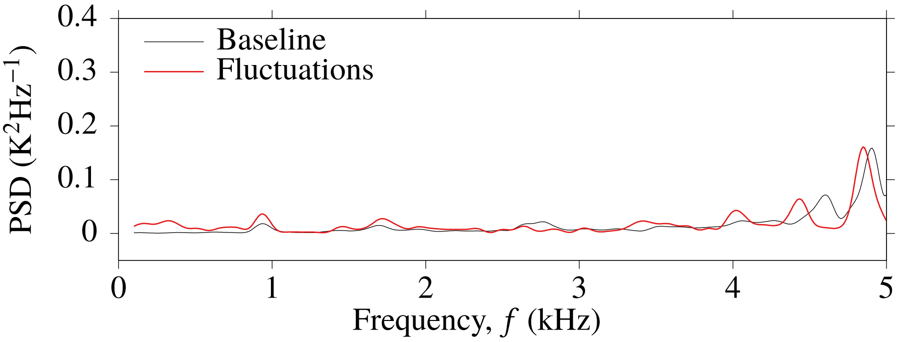

(a) Run 819 TC10, 4 ≤ t ≤ 25 ms.

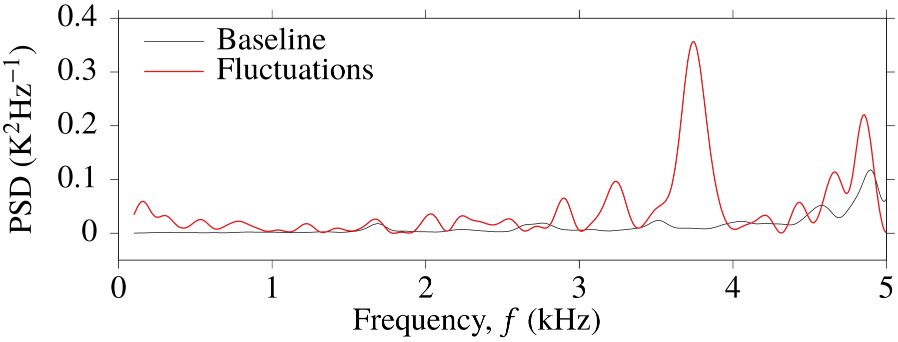

(b) Run 819 TC4, 64 ≤ t ≤ 80 ms.

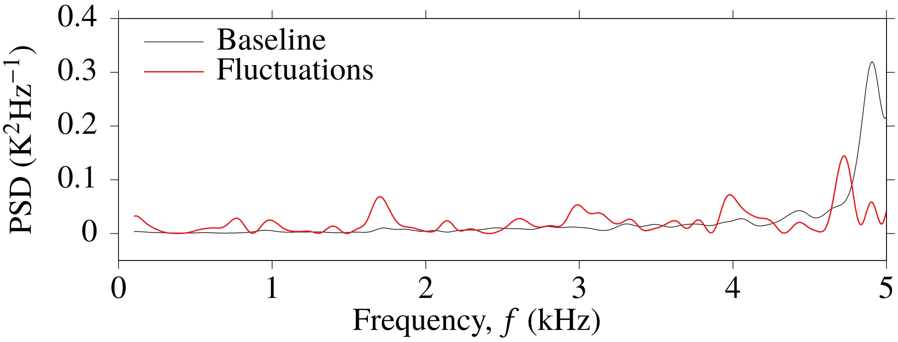

(c) Run 818 TC10, 125 ≤ t ≤ 139 ms.

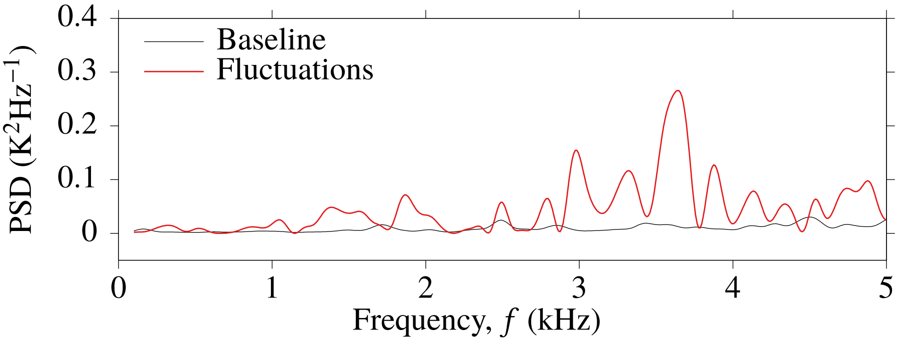

(d) Run 815 TC10, 152 ≤ t ≤ 166 ms.

Figure 7.20: Power spectral density estimates of the stagnation temperature fluctuations for the data presented in Fig. 7.18.

stagnation temperature fluctuations are registered.

When the test gas in the barrel to the barrel walls can be modelled analytically by the turbulent flat pate model (for $100 \lesssim t \lesssim 120\,\mathrm{ms}$) the spectral content at 3.5 – 4 kHz was found to be present, but at a much reduced amplitude. After $t \approx 120\,\mathrm{ms}$ the 3.5 – 4 kHz spectral content was observed to increase in amplitude to about half that of the peak observed from 80 – 100 ms. Consistent with the Pitot survey results, the 3.5 – 4 kHz spectral content remained present in the flow until the end of the run.

The onset of the 3.5 – 4 kHz spectral content was consistent with the transition of the boundary layer of the test gas in the barrel from laminar to turbulent, and remained whilst the boundary layer was turbulent. This correlation indicates that the 3.5 – 4 kHz frequency content is caused by the boundary layer on the walls of the barrel.

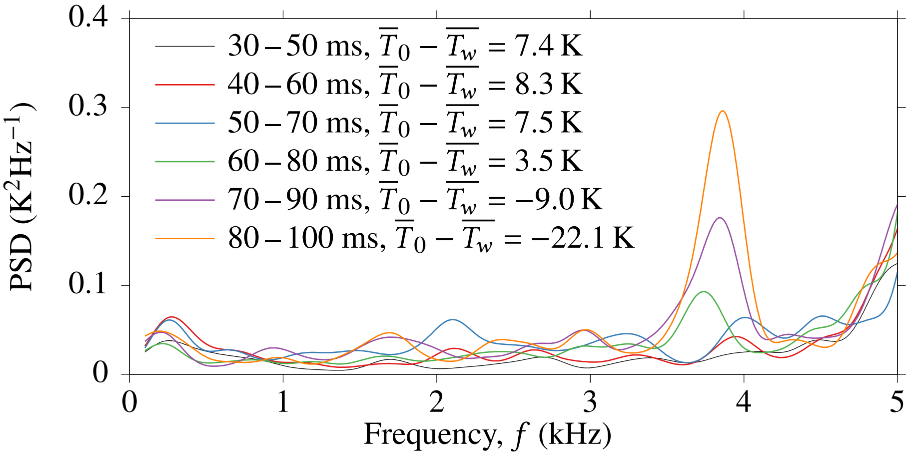

(a) $30 \le t \le 100$ ms

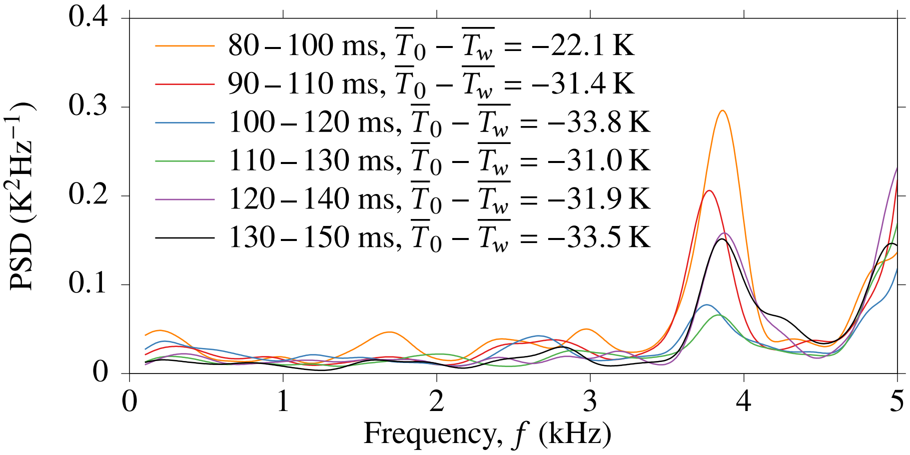

(b) $80 \le t \le 150$ ms

Figure 7.21: Power spectral density (PSD) estimates of stagnation temperature fluctuations from Run 819 using 20 ms windows of data to identify the onset of the 3.5 – 4 kHz peak, and its relative magnitude as the flow time increases.

Chapter 8

Fast Response Heat Flux Measurements in a Plasma Wind Tunnel

Contents

8.1 Overview and Background

During the course of the primary research at TUSQ, an opportunity arose for a collaboration with the Institut für Raumfahrtsysteme (IRS, Institute of Space Systems) at the University of Stuttgart, Germany. The goal of this collaboration was to measure the heat flux distribution and the fluctuations of heat flux in a plasma wind tunnel. To measure the heat flux, type K coaxial surface junction thermocouples similar to the thermocouples described in Chapter 6 and Chapter 7 were mounted in a heat flux probe that was the standard ESA 50 mm diameter flat faced geometry. The experimental measurements of heat flux in a plasma wind tunnel described herein demonstrate that the fast response thermocouples developed for TUSQ can be successfully applied in a modified arrangement to investigate the flow quality of other high speed flow facilities.

8.2 Introduction

Plasmawindkanal 4 (PWK4) (Auweter-Kurtz, Kurtz & Laure, 1996), located at the Institute of Space Systems (IRS) within the University of Stuttgart, is a plasma wind tunnel equipped with a thermal arcjet generator that provides continuous high enthalpy, supersonic air plasma flows for the investigation of Earth entries from low Earth orbits at altitudes between 50 km and 30 km (Löhle et al., 2016). Pitot pressure and heat flux measurements are undertaken to characterise the flow. Past centreline heat flux measurements in PWK4 (Löhle et al., 2016) using a variety of heat flux gauge types and geometries have identified significant uncertainty in the surface heat flux measurements. Because of the long run time of plasma wind tunnels, fast response heat flux gauge development has not been a priority (Penty Geraets, McGilvray, Loehle & Hufgard, 2019), however high-speed spectral imaging of the PWK1 facility (Zander, Hermann & Loehle, 2016) has identified significant spatial variations in oxygen and nitrogen concentrations, and short high intensity events on sub-millisecond time scales. Recent efforts have been made to measure a transient surface heat flux in PWK4 using a diamond heat transfer gauge with a response time less than 50 µs (Penty Geraets et al., 2019). To convert the measured temperature to a heat flux, Penty Geraets et al. (2019) used the non-integer system identification (NISI) model, however for stability the measured temperature data had to be down-sampled to 200 Hz.

8.3 Plasma Wind Tunnel 4

Figure 8.1 shows the PWK4 facility at the Institute of Space Systems, Stuttgart. PWK4 is driven by a coaxial thermal plasma generator called RB3 (Fig. 8.1c) which is attached to a movable front flange of the vacuum chamber (Fig. 8.1a).

The operation of PWK4, and other IRS facilities, is described by Herdrich, Löhle, Petkow and Fasoulas (2010). The test gas is heated in the discharge chamber by an electric arc and accelerated in the nozzle. The cathode is 2 % thoriated tungsten and the anode is a water-cooled copper cylinder and the nozzle is electrically insulated. To avoid oxidation of the cathode, it is only exposed to a nitrogen gas flow. Oxygen is injected at the downstream

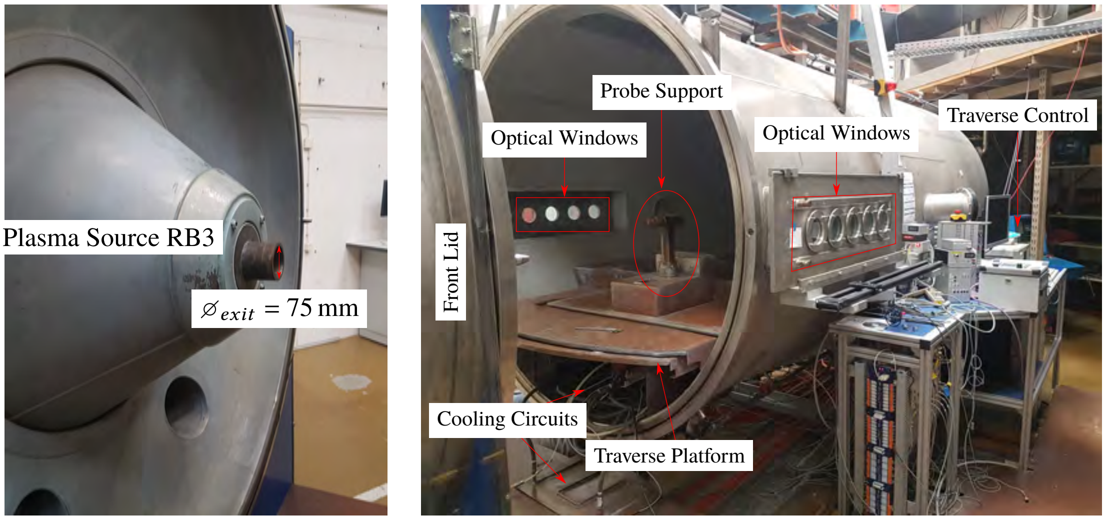

(a) Front flange

(b) Test section

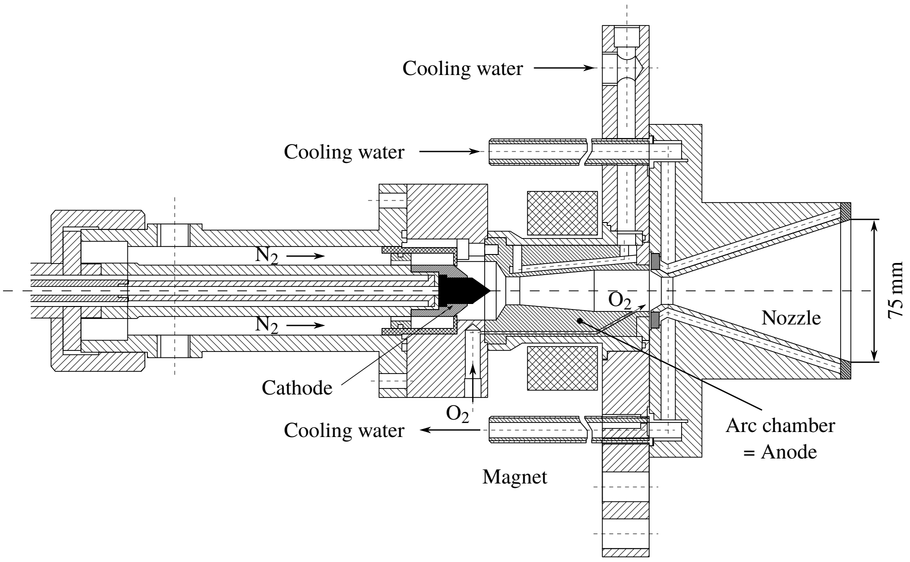

(c) Plasma Source RB3. Adapted from Herdrich, Löhle, Petkow and Fasoulas (2010)

Figure 8.1: Photographs and schematic of major PWK4 facility components.

end of the anode in a subsonic region, near the nozzle throat. A flow condition is achieved by adjusting the arc current, mass flow rate of the nitrogen and oxygen, ambient pressure in the vacuum chamber and the distance of the probe or test sample from the exit of the RB3 nozzle.

Probes are mounted on a movable and rotatable table which allows positioning and traversing of probe heads in and out of the plasma jet during testing. The parameters of the flow condition investigated are summarised in Table 8.1. This condition was selected as it is a well-established operating condition that has been used in several previous experiments in the PWK4 facility (Hufgard et al., 2019; Lein, 2016; Löhle, 2006; Löhle et al., 2016; Penty Geraets et al., 2019). However, there was a period of testing in PWK4 where an incorrect conversion calculation resulted in an oxygen mass flow rate less than the well-established operating condition. The experiments described herein were performed during this period. As a result of the reduced oxygen mass flow the plasma was not a simulated air-plasma. Because of the changed condition, the results obtained are not expected to be directly comparable to previous heat flux measurements by Hufgard et al. (2019), Lein (2016), Löhle (2006), Löhle et al. (2016), Penty Geraets et al. (2019).

Parameter	**Unit**	**Value**
	Facility	
Current	A	600
Voltage	V	87
Electric input power	kW	52.2
Nitrogen mass flow	$\mathrm{g\,s^{-1}}$	5
Oxygen mass flow	$\mathrm{g\,s^{-1}}$	0.76*
Ambient Pressure	Pa	24
	Nozzle	
Exit diameter	mm	75
	Probe	
Axial position	mm	90
Pitot pressure	Pa	1250
Reference heat flux	$\mathrm{kW\,m^{-2}}$	929†

Table 8.1: PWK4 facility and probe operating conditions.

---

*The oxygen mass flow rate should have been 1.52 $\mathrm{g\,s^{-1}}$

†Referenced to the ESA standard 50 mm diameter flat faced geometry

8.4 Heat Flux Gauges

8.4.1 Water Cooled Calorimeter

The reference heat flux listed in Table 8.1 was determined using a 50 mm diameter hemispherical head calorimetric heat flux probe of IRS (Laure, 1998; Nawaz, Loehle, Herdrich & Martinez, 2013). A sketch of the calorimeter probe in the IRS probe stand is depicted in Fig. 8.2. With this probe, the steady state heat flux q is determined using the correlation

$$q = \frac{\dot{m}_w}{A_{SH}} c_{p,w} \Delta T \tag{8.1}$$

where $A_{SH} = 181.5\,\mathrm{mm}^2$ and is the area of the sensor head facing the plasma flow, and $c_{p,w}$ is the specific heat capacity of water. The calorimeter water mass flow $\dot{m}_w$ is measured using a flow meter, and this water flow is separate from the probe head cooling water. Two resistance thermometers (Pt100) are used for the determination of the temperature difference ΔT between in-flowing and out-flowing calorimeter water.

By rotating the probe by 180° such that the opposing end of the probe faces towards the plasma jet, the Pitot pressure can be measured by the same probe. For the transient heat flux measurement in this research, the fast response heat flux gauge was fitted in place of the Pitot pressure probe head.

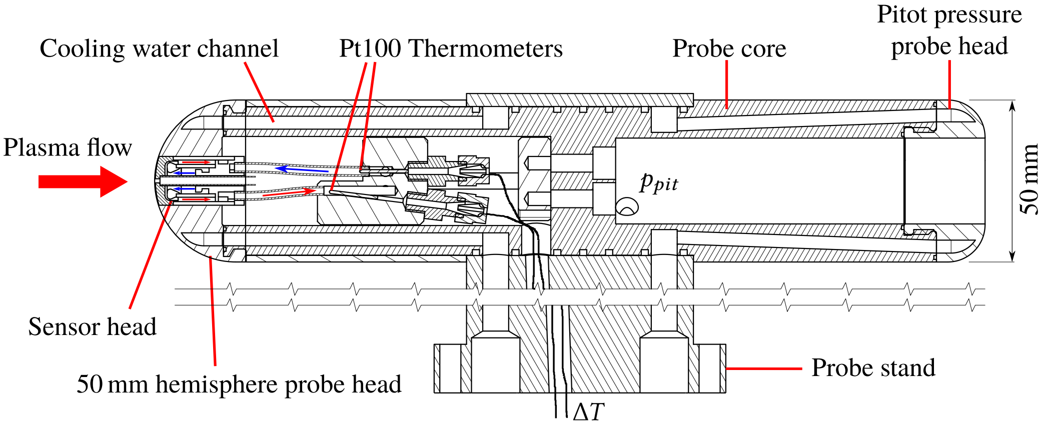

Figure 8.2: Illustration of the calorimetric heat flux probe and an ESA standard 50 mm diameter flat faced Pitot probe head.

8.4.2 Fast Response Heat Flux Gauge

The fast response heat flux gauge consisted of a type K coaxial surface junction thermocouple behind a thin (<100 µm) layer of polytetrafluoroethylene (PTFE) which was mounted in a copper ESA standard 50 mm flat faced probe (Fig. 8.3a). The geometry of the 50 mm diameter flat faced probe is included as Appendix E. The type K thermocouple was of identical geometry to the type E thermocouples described in Section 6.2.1 and presented in Appendix B. However, to form a type K thermocouple, the pin was made from alumel. The alumel pin was heat treated in a temperature controlled furnace at 850 °C for 2 h to form a thin oxide layer, and the pin allowed to cool prior to assembly. The chromel annulus was not heat treated.

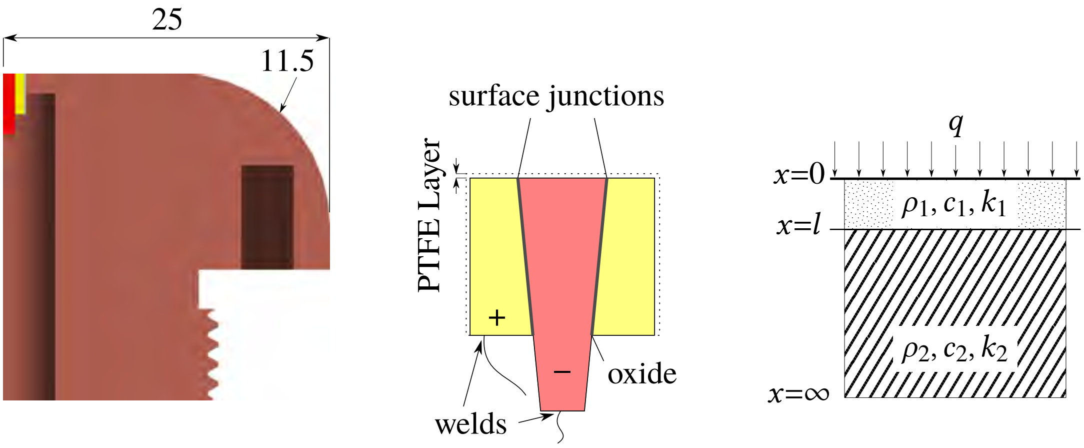

(a) Gauge in probe head (b) Thermocouple gauge (c) Schematic of substrates

Figure 8.3: Fast response heat flux gauge arrangement.

The surface junctions were formed by scratching the surface of the coaxial thermocouple with 800 grit abrasive paper. PTFE tape was stretched over the surface of the thermocouple to form a thin electrically insulating layer to protect the measuring surface from the plasma environment. The thermocouple (Fig. 8.3b) was then inserted into an ESA standard 50 mm flat faced probe, with the PTFE surface flush with the copper probe face to complete the assembly process.

The heat flux gauge is shown schematically in Fig. 8.3c where the PTFE layer (substrate 1) is of thickness l and the thermocouple (substrate 2) is considered one homogeneous material which extends from $x = l$ to $x = \infty$ under the semi-infinite heat conduction assumption. The temperature measured by the thermocouple is at $x = l$ which is the interface of the two substrates. The PTFE tape was initially 100 µm thick, however the stretching process will reduce the thickness and the stretched thickness was not measured directly.

8.5 Calibration of the Fast Response Heat Flux Gauge

8.5.1 Laser-based Calibration

To determine the heat flux at the fast response heat flux gauge from the measured temperature, the heat flux gauge must be calibrated and an impulse response which describes the system identified. In Section 6, a pair of analytical basis functions was used to create an impulse response filter using an experimentally identified effective thermal effusivity. The heat conduction is more complex for the fast response heat flux gauge designed for PWK4 (Fig. 8.3) than the heat conduction for the gauge used in TUSQ because of the additional layer of PTFE insulation and the longer flow duration experienced in PWK4.

For a two layer heat flux gauge (Fig. 8.3c) exposed to a uniform input of heat flux at its surface ($x = 0$), the temperature at $x = l$ is given by Doorly and Oldfield (1987) as

$$\begin{aligned} T(x{=}l, t) = \frac{q\,[1 + A]}{k_1} \Bigg[& \sqrt{\frac{4\alpha_1 t}{\pi}} \exp\left(\frac{-l^2}{4\alpha_1 t}\right) - l \operatorname{erfc}\left(\frac{l}{2\sqrt{\alpha_1 t}}\right) \\ & + \sum_{n=1}^{\infty} A^n \left\{ \sqrt{\frac{4\alpha_1 t}{\pi}} \exp\left(\frac{-l^2 (2n+1)^2}{4\alpha_1 t}\right) \right. \\ & \left. - l(2n+1) \operatorname{erfc}\left(\frac{l\,(2n+1)}{2\sqrt{\alpha_1 t}}\right) \right\} \Bigg] \end{aligned} \tag{8.2}$$

where

$$A = \frac{e_1 - e_2}{e_1 + e_2} \tag{8.3}$$

To create an analytical impulse response filter using Eq. 8.2, the thickness, thermal diffusivity (α), thermal effusivity (e) and thermal conductivity (k) of the PTFE layer and the effective thermal effusivity of the thermocouple must be defined. Material properties for PTFE can be obtained from literature, but the thickness of the PTFE layer was unknown because of the stretching process during assembly. In Chapter 6, the effective thermal effusivity of a coaxial surface junction thermocouple was shown to be different to the mean thermal effusivity of the two thermocouple materials, and therefore e_2 cannot be reliably defined without calibration. Because l and e_2 cannot be estimated with any certainty, an analytical impulse response filter cannot be created.

Instead, with a well defined input surface heat flux and measured thermocouple temperature, the impulse response filter can be determined experimentally without requiring the definition of the heat flux gauge geometry or materials. The fast response heat flux probe was calibrated by exposing the sensor head to a known radiative heat flux using the setup illustrated in Fig. 8.4. This system identification was actually performed after experimental data was taken in the plasma wind tunnel. The radiative heat flux was supplied by a Laserline LDM 500-100 diode laser system with a peak power of 500 W at $\lambda = 980\,\mathrm{nm}$, reported to have a power rise time of <0.1 ms (Löhle & Fuchs, 2012). A function generator was programmed to output a time dependent voltage profile in the range of 0 – 10 V. The output power of the laser module (P) is a function of the voltage supplied by the function generator to the laser control module. A 500 mm focal length lens at the laser head is used to focus the laser beam. The calibrated irradiance (I_{cal}) can be controlled by setting the distance between the lens and probe head (L) and can be calculated by

$$I_{cal} = \frac{P}{A} = \frac{4 \cdot g(V)}{\pi |d_0 \frac{f-L}{f}|^2} \tag{8.4}$$

where A is the cross-sectional area of the laser beam at L, $P = g(V)$ is determined from a prior calibration of the laser and is a function of the input voltage to the system and d_0 is the output diameter of the laser (48 mm). Along the length of the laser beam, the cross section of the beam has a circular shape with a uniform energy density (Löhle & Fuchs, 2012).

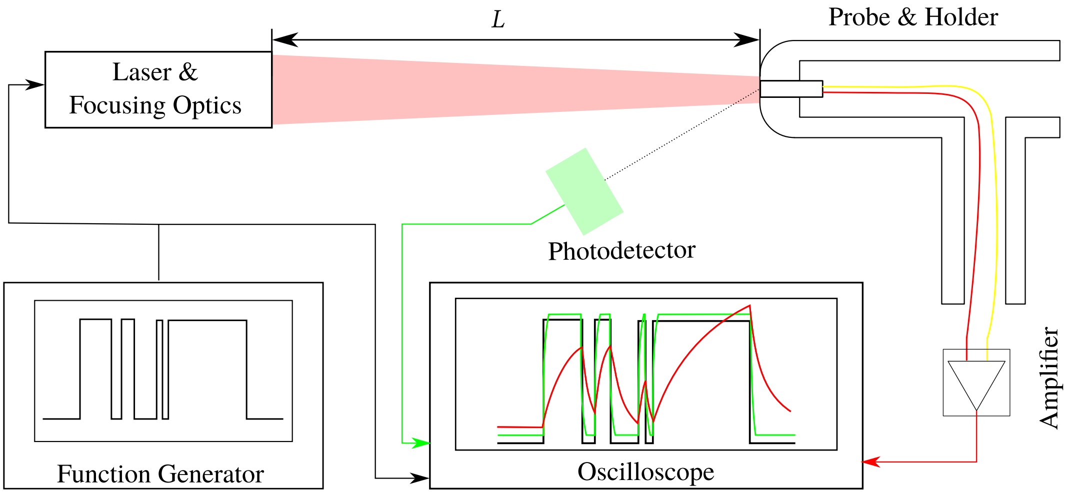

Figure 8.4: Schematic of heat flux gauge laser calibration system.

Three time-varying heat flux profiles for the laser pulses were used: (1) a single square pulse; (2) several square pulses of different randomly chosen lengths; and (3) a Gaussian-like pulse to simulate elements of the heat flux temporal profile the sensor is exposed to in a single traverse of the PWK4 flow. Case (1) was used to provide the basis functions for the experimental derivation of the impulse response filter, whereas (2) and (3) were used to demonstrate the applicability of the derived filter and associated analysis methods. A photodetector was used to measure the intensity of the light that was reflected from the surface of the probe, and this intensity is related to the output power of the laser. The amplifier, when paired with a type K thermocouple, has a sensitivity of 10 mV °C^{-1}. The function generator output, photodetector output and thermocouple signal were recorded using a LeCroy WaveSurfer 24Xs-A. Such results are presented in Fig. 8.5 on a normalised scale, with the photodetector signal suggesting that the input heat flux was time-varying. When appropriately scaled, the photodetector output was used to specify the heat flux input for the gauge calibration.

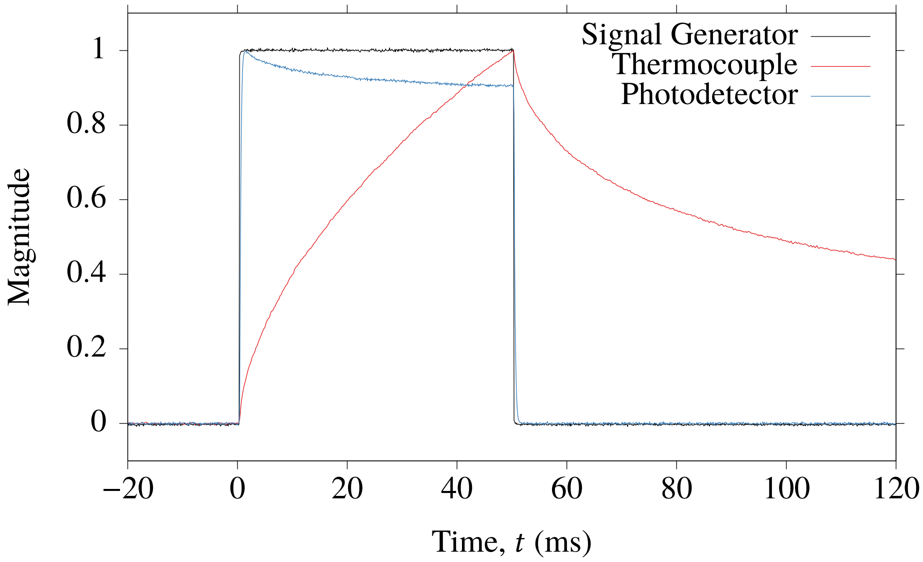

Figure 8.5: Normalised signals from a laser pulse calibration of the heat flux gauge.

8.5.2 Heat Flux Input

The signal from the photodetector during all nominally square pulse laser calibrations exhibited a time-varying magnitude, as illustrated in Fig. 8.5 and Fig 8.6. Because of the time-varying input heat flux, the photodetector signal was fitted with a line of the form $y = A\exp(-Bt) + C$ where C is the limit of the function as $t \longrightarrow \infty$, as shown in Fig. 8.6. Therefore, for the present work, the time-varying irradiance (I) is

$$I = I_{cal}\frac{S_{PD}}{C} \tag{8.5}$$

where S_{PD} is the signal from the photodetector. For all 10 V amplitude square pulses supplied to the laser for durations of 10 – 50ms, C was found to be 4.349 – 4.35 V.

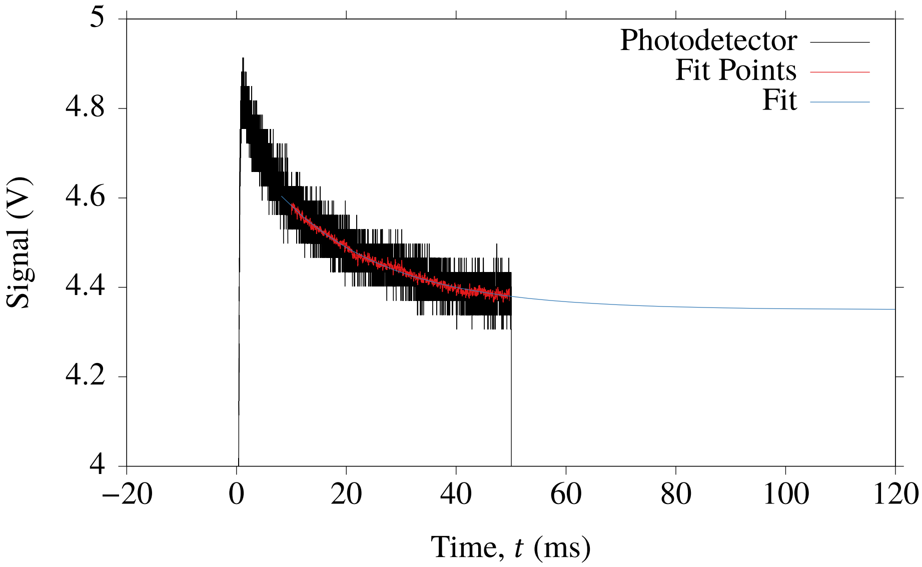

Figure 8.6: A time-varying irradiance was identified from the photodetector signal.

Calibration of heat flux gauges using an applied irradiance (I) requires the absorptivity (a) of the surface to be known since the heat flux delivered into the gauge (q) is given by

$$q = a \cdot I \tag{8.6}$$

The absorptivity of the PTFE layer at 980 nm was not known a priori. The bidirectional reflectance distribution function (BRDF) of HD PTFE has been reported as approximately 0.295 at 1000 nm for viewing angles less than 20° by Tsai, Hanssen, Wilthan and Boris Zeng (2008) for a 19.05 mm thick sample. These optical properties suggest $a \approx 0.7$ at 1000 nm, however since the BRDF is a function of the surface finish, and absorptivity is a function of sample thickness (Mahrle & Beyer, 2009), the applicability of this value for the PTFE layer used in our gauge is somewhat uncertain.

In order to provide greater reliability for the absorptivity during the gauge calibration, a thin layer of soot was deposited on the gauge by passing it through a candle flame several times. At 980 nm, the absorptivity of soot deposited by a candle flame is approximately 0.98 (Liebert & Hibbard, 1970). Through a comparison of the thermal response of the gauge with and without the soot layer, the absorptivity of the PTFE layer without the soot coating was found to be $a = 0.65 \pm 0.01$, for the laser calibrations.

8.5.3 Temperature Response

The temperature response from the thermocouple gauge is illustrated in Fig. 8.7 using a square root of time ($\sqrt{t}$) axis. The heat flux input to the gauge was applied for 50 ms, but traverses across the PWK4 jet flow took an order of magnitude longer. In an effort to reduce the noise associated with the relatively short-length laser pulse of 50 ms, extrapolation of the temperature and heat flux rise basis function were trialled. Because of the slight time-varying input heat flux and the in-depth position of the temperature sensing element, the temperature history during laser calibration was assumed follow the equation

$$T(x{=}l, t) - T_i = C_1 \sqrt{t} \exp\left(\frac{C_2}{t}\right) - C_3 \operatorname{erfc}\left(\frac{C_4}{t}\right) \tag{8.7}$$

where C_1, C_2, and C_3 are fitting constants. The form of equation corresponds to the temperature variation expected at a certain depth beneath the surface of a uniform substrate when a constant heat flux is imposed at its surface.

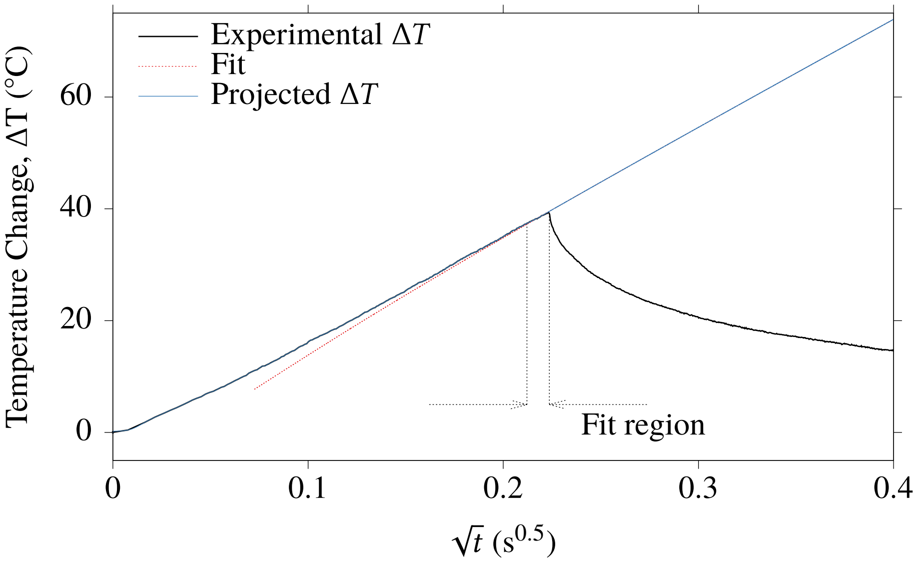

Figure 8.7: Extrapolation of the temperature signal from a 50 ms square pulse calibration to approximate the response of the thermocouple to a longer pulse duration to facilitate analysis of longer test times.

Temperature data from 48 – 50 ms were selected for the fitting process, and so as not to introduce a discontinuity between the actual and the extrapolated temperature rise data, a weighted linear transition from $t = 48$ ms to $t = 50$ ms was used. The projected temperature and fitting process is shown in Fig. 8.7 for $0 \leq t \leq 160$ ms.

8.5.4 Basis Functions

The two basis functions $q(t)$ and $T(t)$ were then completely defined for an arbitrarily long period of time using a combination of measured and extrapolated experimental data. The corrected heat flux $q_{corr.}$ and the uncorrected heat flux $q_{uncorr.}$ basis functions are illustrated with the temperature basis function in Fig. 8.8.

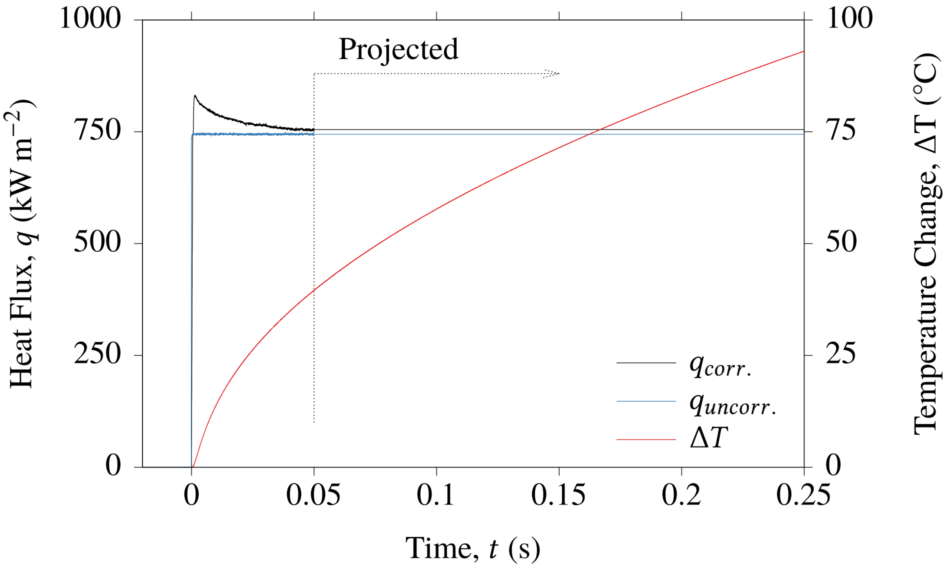

Figure 8.8: Heat flux and temperature basis functions with experimental data for $t \leq 0.05$ s and projected data for $t > 0.05$ s.

8.5.5 Experimental Impulse Response Filter

The impulse response processing method was described in Section 6.3, and this process was used to identify an experimental impulse response filter from the heat flux and temperature basis functions shown in Fig. 8.8. The impulse response filter h was created using the MATLAB command

```
h = filter(q, dT, delta)
```

Two different impulse response functions were created to assess the impact of the identified time-varying laser power: (1) h_E which uses the corrected input heat flux; and (2) h_U which uses the uncorrected input heat flux. Both h_E and h_U use the same temperature basis function.

8.5.6 Impulse Response Filter Testing

The impulse response filters h_U and h_E were first tested using the measured temperature for the 50 ms pulse to assess the reconstruction of the applied heat flux used in the calibration.

This reconstruction of the heat flux input is shown in Fig. 8.9a and Fig. 8.9b for h_U and h_E respectively. For $t < 50\,\mathrm{ms}$ there is excellent agreement between the calibration (q_{cal}) and measured ($q_{uncorr.}$, $q_{meas.}$) heat flux for both Fig. 8.9a and Fig. 8.9b. This cannot physically be the case, but the agreement is the result of the data in this range being used as the basis functions.

A major difference between Fig. 8.9a and Fig. 8.9b is observed when the heat flux is removed at $t = 50\,\mathrm{ms}$. In Fig. 8.9a, where a perfect step input heat flux was assumed to create the impulse response filter, the measured heat flux quickly reduced to 20 % of its step value, but then requires another 150 ms to decay to zero. However, when the photodetector signal was used to correct for the time-varying laser output power (Fig. 8.9b), the measured heat flux reduces to zero within 2 ms of the heat flux load being removed. Therefore, because of the agreement of q_{cal} and $q_{meas.}$ when the heat flux load is removed, the time-varying heat flux defined with the aid of the photodetector is demonstrated to be a real effect which cannot be neglected.

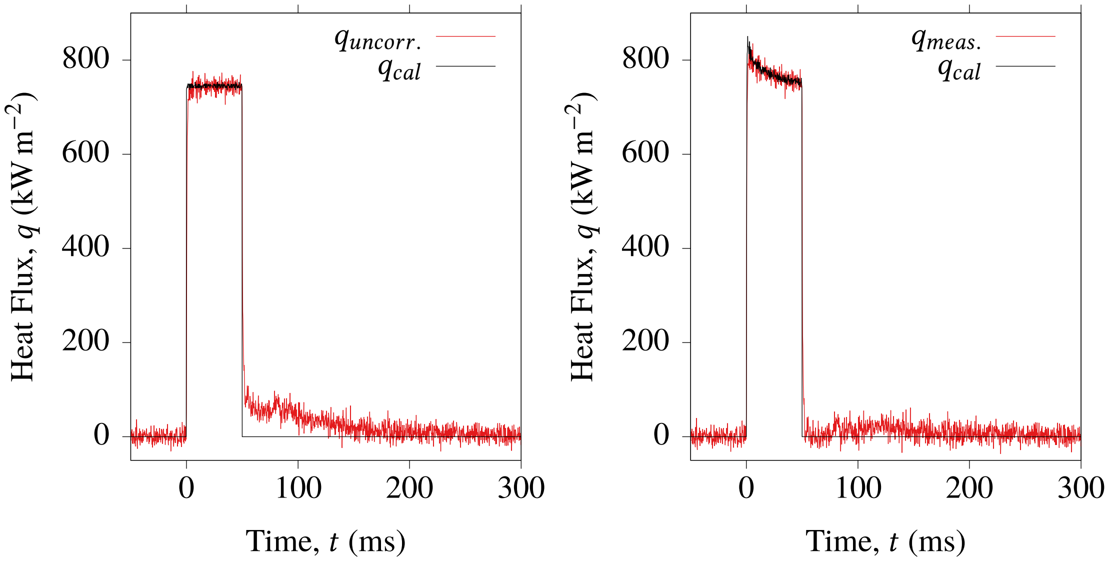

(a) Perfect step input heat flux, h_U

(b) Time-varying input heat flux, h_E

Figure 8.9: Testing of the impulse response filters by reconstructing the applied heat flux for the 50 ms laser pulse calibration assuming (a) a perfect step input of heat flux, and (b) a time-varying step input of heat flux.

The suitability of the experimentally determined impulse response filter h_E was further demonstrated by reconstructing a series of Gaussian-like heat flux pulses from a measured temperature history. The reconstructed heat flux results presented in Fig. 8.10 are compared to the input heat flux history deduced from the voltage signal provided to the laser unit (q_{cal}). The measured heat flux $q_{meas.}$ is in good agreement with q_{cal} for tests approaching 1.5 s duration.

Insight into the uncertainty of the measured heat flux can be determined by comparing the peak value of measured heat flux to the calibrated heat flux. In Fig. 8.10a, the peak measured heat flux was 84 kW m^{-2} greater than the peak calibrated heat flux applied (916 kW m^{-2}). When the heat flux is removed, there is a small "bounce" of the measured heat flux which is a result of the impulse response filter, but the peak of this region is 25 kW m^{-2}.

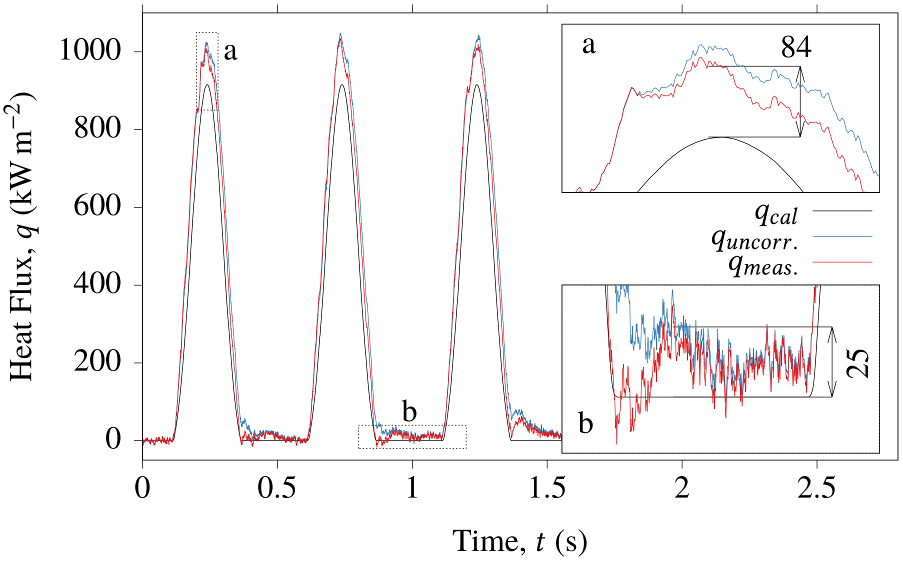

Figure 8.10: Testing of the impulse response filters by reconstructing the applied heat flux for a sequence of three Gaussian-like pulses.

The heat flux $q_{uncorr.}$, calculated using h_U, was included to further demonstrate the effects of neglecting the time-varying calibration heat flux pulse. Compared to the step-like heat flux input of Fig. 8.9, the rate of heat flux application is gradual. Because of the gradual application and removal of the heat flux the error introduced by neglecting the time-varying calibration step is reduced, and the peak values for $q_{meas.}$ and $q_{uncorr.}$ are in reasonable agreement.

8.6 Plasma Wind Tunnel Experiments

Two heat flux gauges – (1) the 50 mm diameter hemispherical calorimeter, and (2) the fast response 50 mm flat faced heat flux gauge – were installed in opposing ends of the IRS 50 mm model support which was illustrated in Fig. 8.2. This support is mounted on a four axis computer controlled platform, allowing the probes to be translated along three axes and rotated about the vertical (y) axis, as illustrated in Fig. 8.11.

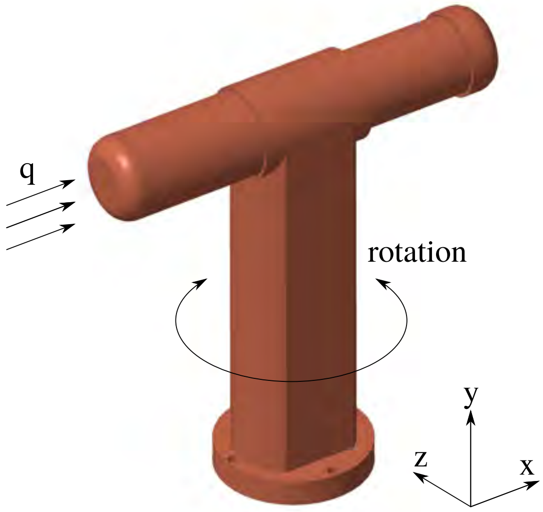

Figure 8.11: Schematic of the PWK4 model support and traverse capabilities showing the 50 mm probe geometry exposed to the heat flux (q) generated by the plasma flow.

The model support was initially arranged so the calorimeter faced the nozzle exit, and in this orientation the probe was repeatedly traversed across the flow until the desired test flow condition was achieved by varying the ambient pressure in the vacuum chamber, probe axial position and generator power input. A series of three images of the 50 mm diameter hemispherical head calorimeter at different positions in PWK4 during the condition establishment process are shown in Fig. 8.12. Once the desired condition was achieved, and with the probes well clear of the flow, the model support was rotated 180° so that the fast response heat flux gauge was facing the nozzle. The probe was then traversed across the plasma flow in the z direction at a constant velocity and the temperature signal recorded. The position where $z = 0$ mm corresponds to alignment between the centrelines of the probe and the nozzle.

The temperature did not rise for any traverse until approximately $z = \pm\, 80$ mm, and therefore the traverse time (t_{tr}) was conservatively defined as the time taken to cross from ± 85 mm to ∓ 85 mm. After each traverse the probe was held outside of the plasma jet for a period of time (t_{cool}) to allow for the thermocouple to reach an almost-isothermal state and the model support to cool before being traversed in the other direction. Eight traverses of the plasma jet were performed over a period of approximately 13 min, summarised in Table 8.2. Temperature data was amplified using an in-house IRS amplifier with a bandwidth of 15 kHz and a nominal sensitivity of 10 mV $°C^{-1}$ for a type K thermocouple. The same amplifier that was used for laser calibration was also used for the tests in PWK4 to remove

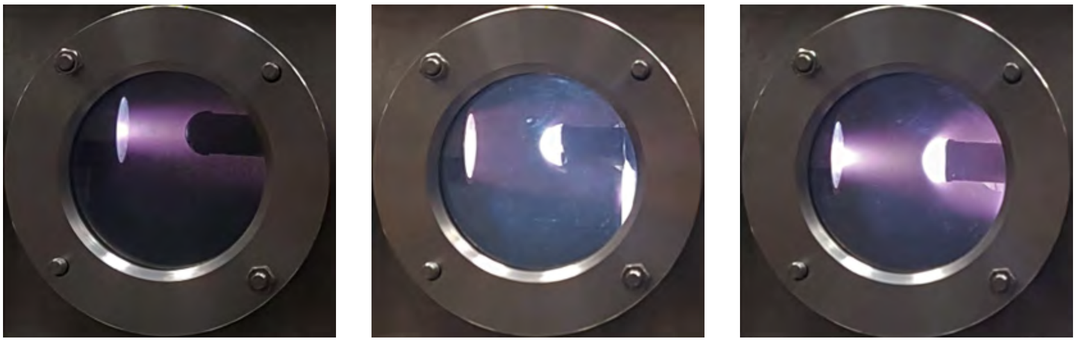

(a) Outside jet (b) Flow adjustments (c) Fully in plasma jet

Figure 8.12: Images of the 50 mm diameter calorimeter at different positions in the plasma jet while establishing the test condition.

Traverse	u_z ($\mathrm{m\,s^{-1}}$)	T_i (°C)	T_{max} (°C)	$T_{max} - T_i$ (°C)	t_{cool} (s)	t_{tr} (s)
1	+165	24.8	70.8	46.0	-	1.16
2	−165	31.8	79.2	47.4	63	1.16
3	+115	28.2	84.5	56.3	116	1.49
4	−115	34.7	92.4	57.7	63	1.49
5	+165	25.1	75.1	50.0	338	1.16
6	−165	36.0	86.4	50.4	32	1.16
7	+115	34.5	73.9	39.4	58	1.49
8	−115	42.8	103.1	60.3	44	1.49

Table 8.2: Summary of traverse properties from the eight traverses of PWK4.

the potential of increased uncertainty that could be introduced by using two different amplifiers. The voltage signals from the heat flux gauge and the z-position measuring potentiometer were recorded at 50 kHz using a LeCroy WaveSurfer 24x oscilloscope.

The z-position of the fast response heat flux probe and its temperature signal are displayed in Fig. 8.13 for traverse 5 (Table 8.2), with the nozzle exit radius of 37.5 mm included for a size reference. The probe traversed at nominally constant velocity (u_z) between the positions $-60 \leq z \leq 60$ mm, but the signal from the potentiometer had noise levels equivalent to ± 1 mm. Therefore, the potentiometer signal was smoothed to reduce the noise effects when plotting the heat flux results as a function of position.

For traverse 1 the oscilloscope vertical divisions were set to 500 mV per division which, for the 16 bit oscilloscope, resulted in the signal being quantised to 62.5 µV intervals. For traverses 2 – 8 the vertical divisions were 200 mV per division and therefore the amplified temperature signal was digitised to 25 µV intervals.

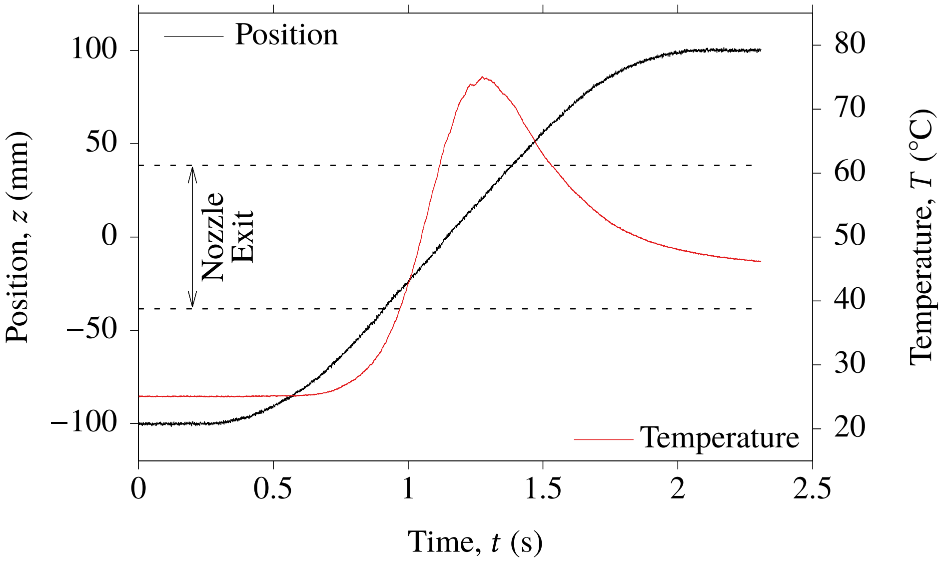

Figure 8.13: Position of the fast response heat flux gauge and temperature signal for a single traverse (trv 5) of the PWK4 flow.

8.7 Results

8.7.1 Average Heat Flux

The heat flux measured by the 50 mm diameter calorimeter (q_{50H}) was scaled to an equivalent heat flux on the ESA 50 mm diameter flat faced gauge (q_{50FF}) using the relation of Zoby and Sullivan (1966) by

$$q_{50FF} = q_{50H}\sqrt{\frac{r_{50H}}{r_{50FF}}} = 929\,\mathrm{kW\,m^{-2}} \tag{8.8}$$

where $r_{50H} = 25$ mm and $r_{50FF} = 57.5$ mm which are the effective nose radii of the hemispherical and flat faced gauges respectively.

The heat flux applied to the fast response heat flux gauge was determined by processing the temperature signal for each traverse using the experimentally identified impulse response filter h_E. To illustrate the spatial distribution of heat flux, the heat flux from the impulse response filtering was low-pass filtered at 100 Hz, with the results for traverses 3 and 7 displayed in Fig. 8.14. Traverses 3 and 7 are in the same direction (positive going) at the slower of the two traverse speeds; these have been used to determine if the impulse response models remain valid for the test duration.

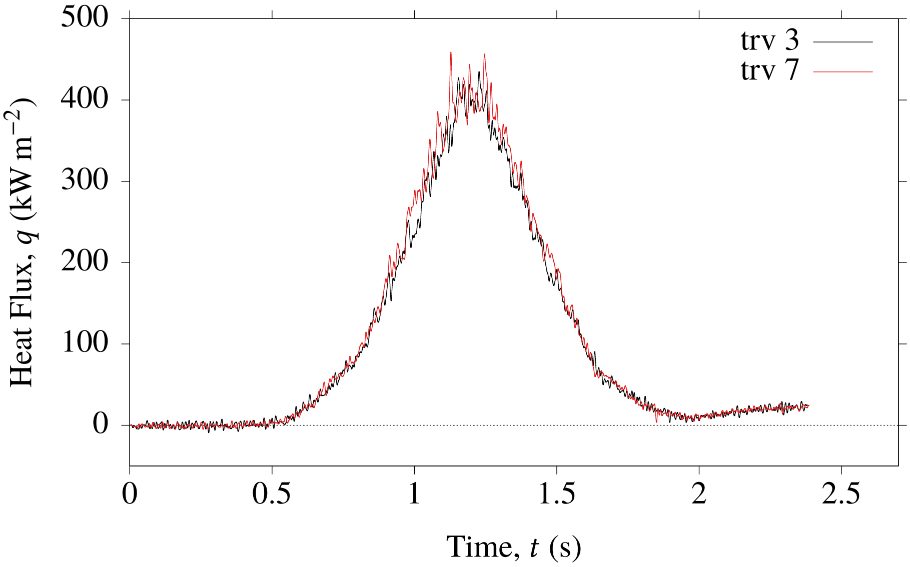

Figure 8.14: Temporally resolved heat flux measurements for the two slowest positive going traverses of the plasma jet.

At $t \approx 0.5$ s the first appreciable increase in heat flux is observed. The heat flux increases until $t \approx 1.3$ s and then decreases to almost zero at $t \approx 1.9$ s. When $t > 1.9$ s, when the probe is out of the plasma jet, the heat flux apparently increases again. This is not a real flow heat transfer effect but is a consequence of applying the impulse response filter that was developed from experimental data obtained for a shorter period of time. A similar apparent rise in temperature is observed on removal of the heat flux in testing the impulse response filter with Gaussian-like pulses (Fig. 8.10).

To determine the spatial distribution of heat flux for each traverse of the PWK4 flow, the signal from the potentiometer was used to transform the temporally resolved data to spatially resolved data. The heat flux distribution for all eight traverses of the PWK4 jet flow is presented in Fig. 8.15, and for clarity these data were low-pass filtered at 100 Hz prior to transformation to spatial coordinates.

The heat flux distribution is consistent and repeatable for all eight traverses, irrespective of the traverse speed and direction, further supporting the use of the impulse response filter which was created by extrapolating data from a 50 ms laser pulse calibration. This consistency of heat flux profile also indicates that the PTFE layer did not degrade during testing in PWK4. The heat flux profile across the plasma jet is seen to be Gaussian-like, and the centreline heat flux for the eight traverses was 404 kW m^{-2} ± 6 %. This is significantly below the reference heat flux of 929 kW m^{-2} for a 50 mm diameter ESA standard flat faced probe geometry. Since there was an error in the establishment of the flow condition in which the oxygen mass flaw was insufficient for correct physical simulation of an air-plasma, the results of this research cannot be directly compared to previously published data which were at the desired air-plasma condition. Because no similar data exists, it is not possible to independently verify the heat flux which was measured using the fast response heat flux gauge or the calorimeter.

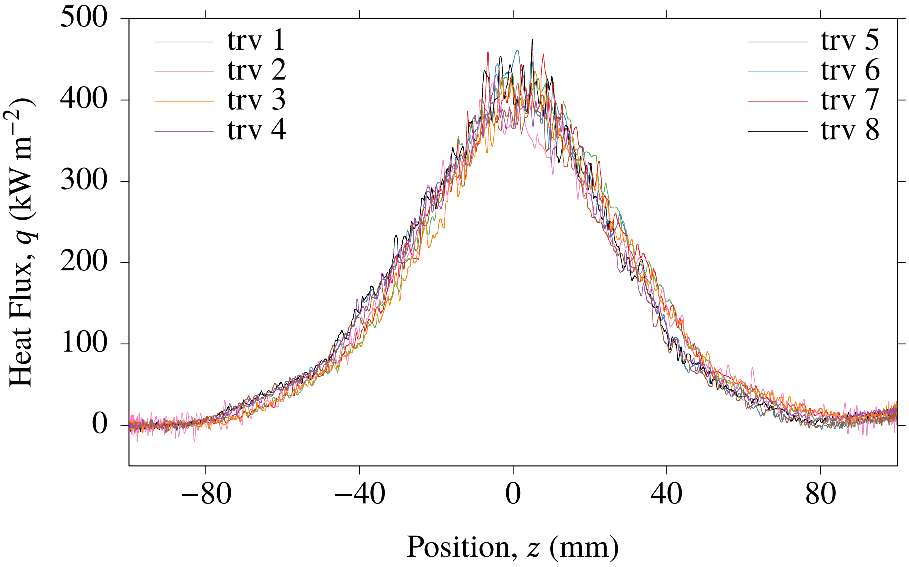

Figure 8.15: Spatially resolved heat flux across the plasma jet as measured for eight traverses.

8.7.2 Fluctuations and Variations of Heat Flux

The fast response heat flux gauge developed in this work facilitates the measurement of variations and fluctuations of heat flux. The raw temperature signal prior to a traverse of the jet was found to be very noisy, and consequently the amplified temperature signal was conditioned at the oscilloscope using an inbuilt pre-processing low-pass filter at 1 kHz. Therefore the maximum frequency of the fluctuations of heat flux that could be resolved was 1 kHz.

The temporally resolved heat flux signal was high-pass filtered at 4 Hz to isolate the fluctuations of heat flux (q') from the time-averaged heat flux level, and these data are presented in Fig. 8.16 for the four slower traverses. Large amplitude fluctuations of heat flux are apparent in all signals shown, and these fluctuations are significantly above the noise floor. Similar data were found for the traverses not shown, except for trv 1 where the baseline noise signal was higher because of the signal quantisation effects. With improved signal conditioning it is likely that the baseline noise signal can be further reduced, and

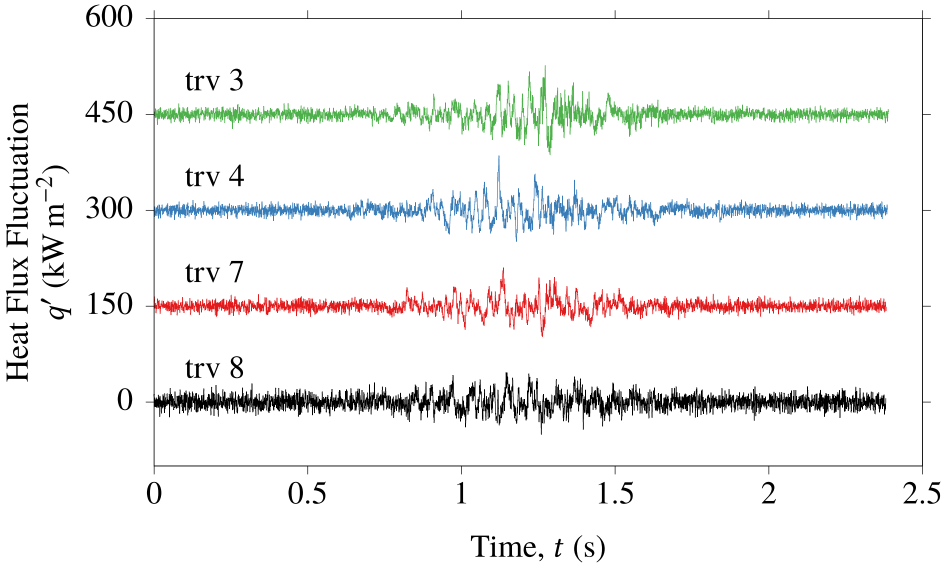

Figure 8.16: Temporally resolved fluctuations of heat flux for four traverses of the PWK4 jet.

frequencies above 1 kHz could then be resolved.

The temporally resolved fluctuations in heat flux were transformed to spatially resolved variations of heat flux. The spatially resolved variations of heat flux were smoothed over 100 points, and are presented in Fig. 8.17. The highest amplitude variations of heat flux are in the vicinity of $z = 0$ mm where the amplitude of heat flux is greatest. These variations were consistently observed throughout the duration of the testing (approximately 13 min to complete eight traverses).

The spatially resolved heat flux variations for traverses 2 – 8 are shown in Fig. 8.18. As was the case with the spatial distribution of heat flux, the magnitude of the fluctuations appears to be approximately symmetric about the jet centreline. High amplitude sudden changes of heat flux of up to ± 60 kW m^{-2} occur near $z = 0$ mm, and the amplitude of the variations of heat flux decrease with distance from the nozzle centreline.

Because of the large disagreement between the centreline heat flux measured using the fast response heat flux gauge and the calorimeter, the variations of heat flux are also expressed as a percentage of the centreline heat flux value. Additionally, expressing the fluctuations of heat flux as a percentage of the centreline heat flux allows simple comparison of results obtained using various gauges and geometries where the centreline heat flux may vary significantly (Löhle et al., 2016). The maximum variation of heat flux

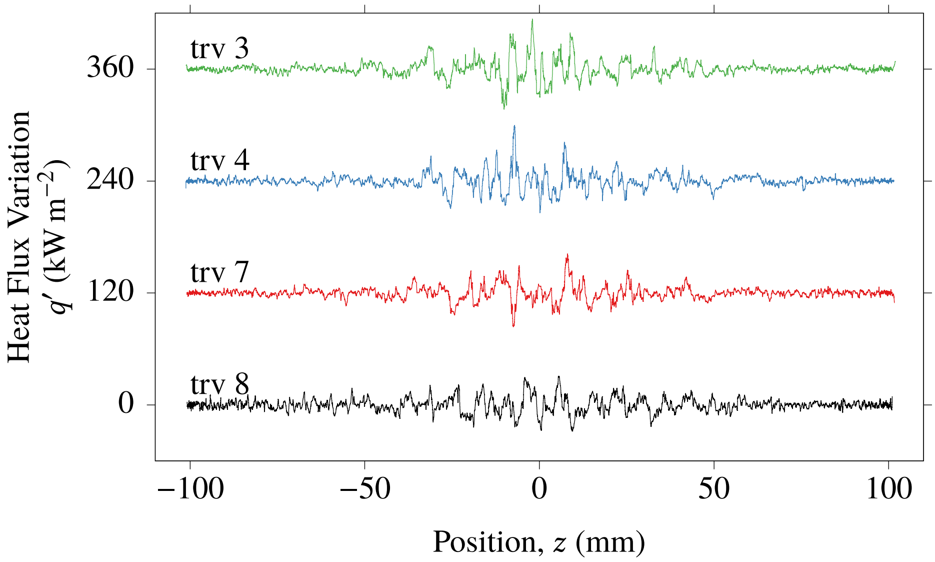

Figure 8.17: Spatially resolved variations of heat flux for four traverses of the PWK4 jet.

± 60 kW m^{-2} was measured near $z = 0$ mm, which equates to 15 % of the centreline heat flux ($q_{℄} = 404$ kW m^{-2}).

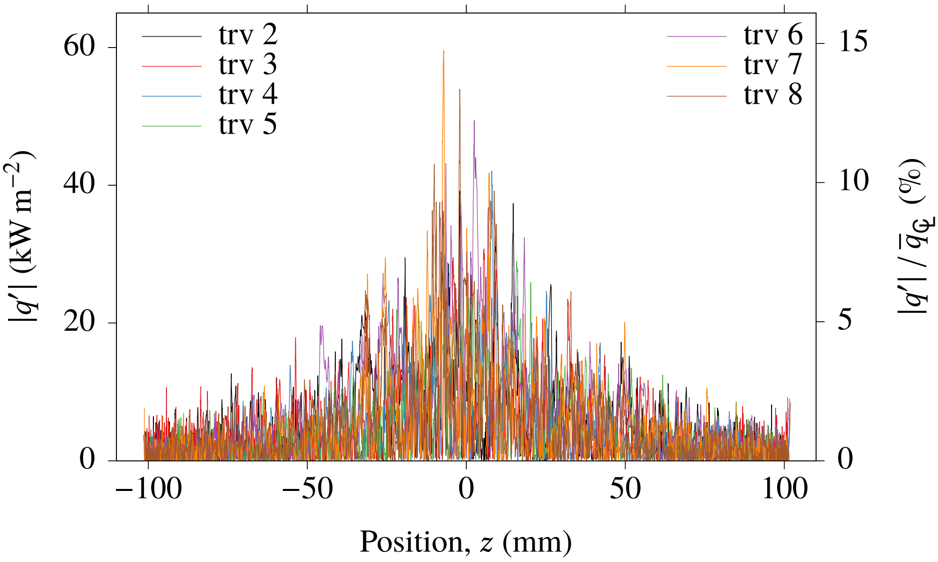

Figure 8.18: Amplitude of the fluctuations of heat flux for trv 2 – 8.

8.8 Conclusion

The stagnation region heat flux on a 50 mm diameter probe operated in a plasma wind tunnel (PWK4 at IRS) was determined using a new fast response heat flux gauge arrangement comprised of a surface junction thermocouple mounted behind a thin layer of PTFE.

The centreline heat flux measured by the fast response heat flux gauge was 404 kW m^{-2} ± 6 % across eight traverses of the plasma jet, which was significantly below the heat flux measured using the IRS calorimetric probe (929 kW m^{-2}). However, the fast response heat flux gauge was able to confirm a Gaussian-like distribution of heat flux across the plasma jet. This heat flux distribution was shown to be independent of the two different probe traverse speeds and traverse directions used.

Fluctuations of heat flux from 4 Hz to 1 kHz were measured, and these fluctuations used to determine heat flux variations of up to ± 60 kW m^{-2} exist near the vicinity of the nozzle centreline. Therefore, fluctuations of up to 15 % of the centreline heat flux exist in the plasma flow at the condition tested.

Chapter 9

Design of a Focused Laser Differential Interferometer

Contents

9.1 Introduction, Overview and Background

A focused laser differential interferometer was designed to measure the density fluctuations in the TUSQ freestream. This instrument is non-intrusive which allows direct measurement of the freestream disturbance environment, unlike the Pitot pressure (Chapter 5) and stagnation temperature (Chapter 7) measurements which measure the flow properties behind a normal shock. The focused laser differential interferometer is described in this chapter, which details the design, performance and design limitations for the measurement of density fluctuations in TUSQ.

9.2 Instrument Design

Two designs of FLDI instruments were initially considered: (1) the design used by Parziale et al. (2012); and (2) the design of Fulghum (2014). The major difference in the designs is the number of photodetectors used: one by Parziale et al. and two by Fulghum. The two detector design enables the analyst to identify frequency content largely free from electronic noise and stray light reflections. Additionally, Parziale et al. used a 200 mW polarised laser source compared to a 0.8 mW polarised source implemented by Fulghum. The demonstration of FLDI performance using a laser with power as low as 0.8 mW using the Fulghum design was attractive as procuring suitable lasers with power orders of magnitude greater than this was prohibitively expensive. Wollaston prisms were considered as the element for diverging the FLDI beams, however the adjustable beam divergence angle of Sanderson prisms was preferred. An instrument with spatial light modulators, as proposed by Kelly (2015), was considered but ultimately was prohibitively expensive to implement, especially for beams of the size used in this research.

The arrangement of the FLDI instrument is summarised as a general schematic in Fig. 9.1. The laser (i) provides a high quality (TEM_{00}) collimated laser beam that is linearly polarised at 45° relative to the axis of beam separation. This beam is expanded by the lens (ii), and the expanded beam is then spatially filtered at (iii) and (iv). When the beam reaches the first Sanderson prism at (v) it is split into two narrowly diverging orthogonally polarised beams. These two beams continue to diverge until the first field lens at (vi) which sets the beam separation and focuses the FLDI beams. In this research, the focus point is at the nozzle centreline The second field lens (vii) is used to refocus the two FLDI at the second Sanderson prism (viii) which is loaded in the same state as (v). The second Sanderson prism recombines the two beams to a single polarisation state where the original beams can interfere, and this beam is collimated at (ix). There is a small difference in optical path length for the two beams when they pass through the Sanderson prisms due to the difference in extra-ordinary and ordinary refractive indices for the prism material. This change in optical path length is compensated by a phase shift using a Berek compensator (x). The beam is split again at (xi) and the intensity of two subsequent beams measured at detectors (xii). These two beams represent the two beams that propagate between the two Sanderson prisms, and their intensity as measured by the photodetectors is identical but 180° out of phase.

The design of the FLDI instrument regularly refers to three axes: (1) the axis of beam

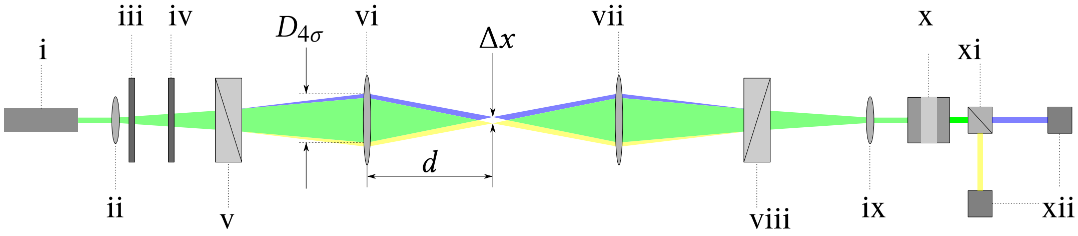

Figure 9.1: Layout of FLDI. i- Laser; ii- Diverging Lens; iii- Pinhole; iv- Variable Iris; v- Sanderson Prism 1; vi- Field Lens 1; vii- Field Lens 2; viii- Sanderson Prism 2; ix- Collimating Lens; x- Berek Compensator; xi- Polarising Beam Splitting Cube; xii- Photodetectors.

propagation; (2) the axis of beam separation; and (3) the axis of flow. These are illustrated in Fig. 9.2. The configuration used in this research places the axis of beam propagation perpendicular to the axis of the flow; and both of these axes perpendicular to the axis of beam separation. Setting the axis of beam separation perpendicular to the axis of the flow was found to produce the optimum frequency response (Fulghum, 2014).

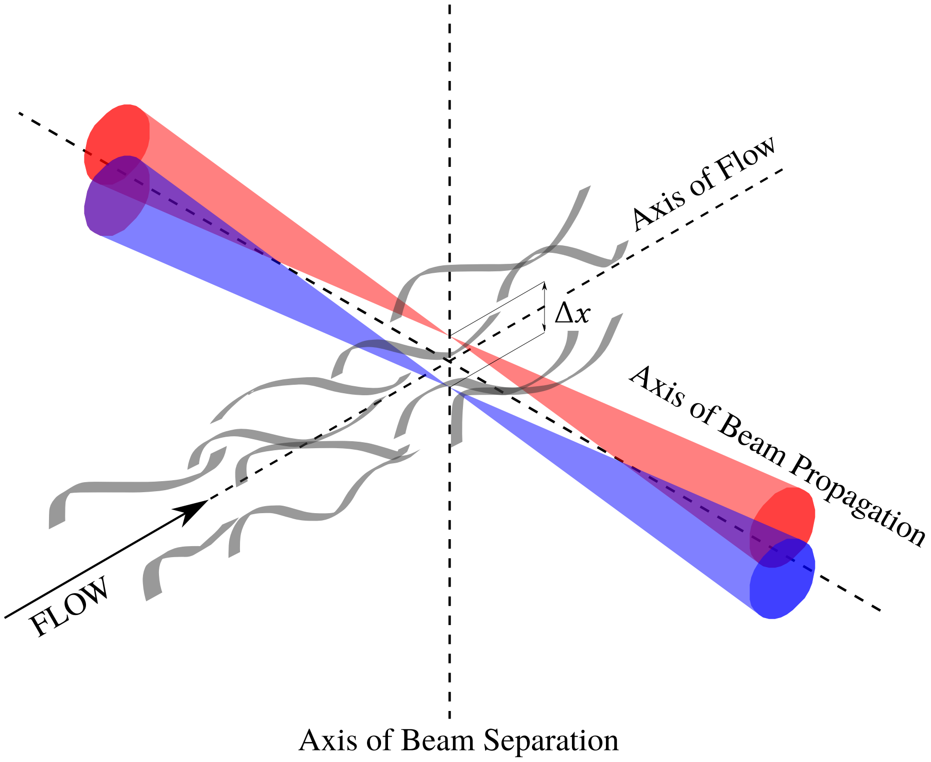

Figure 9.2: Definition of the axes used for focused laser differential interferometry.

All optical components of the FLDI instrument were isolated from the facility such that the optics were not subject to vibrations caused by movement of the facility. Therefore all components of the FLDI system were placed outside the test section, and mounted independent of the facility and its framework. By not connecting the optics to the test section, the capability to open and close the test section was maintained which is beneficial for future projects where models require mounting in the test section, and for measurement of the beam location. The TUSQ test section is a generic one-size-fits-all component common to all available nozzles and experiment types (free flight, fixed and heated models). Consequently the test section is not optimally designed for implementation of FLDI. Figure 9.3 shows that the test section windows are 1028 mm apart, compared to an exit diameter of 217.5 mm for the Mach 6 nozzle. This geometry reduces the effective focusing ability of FLDI. Safety features of the facility that increase this distance were omitted from Fig. 9.3. Best practice in FLDI is to place the field lenses as close to the flow field as possible, but the availability of only discrete focal lengths of commercial lenses further constrain the design.

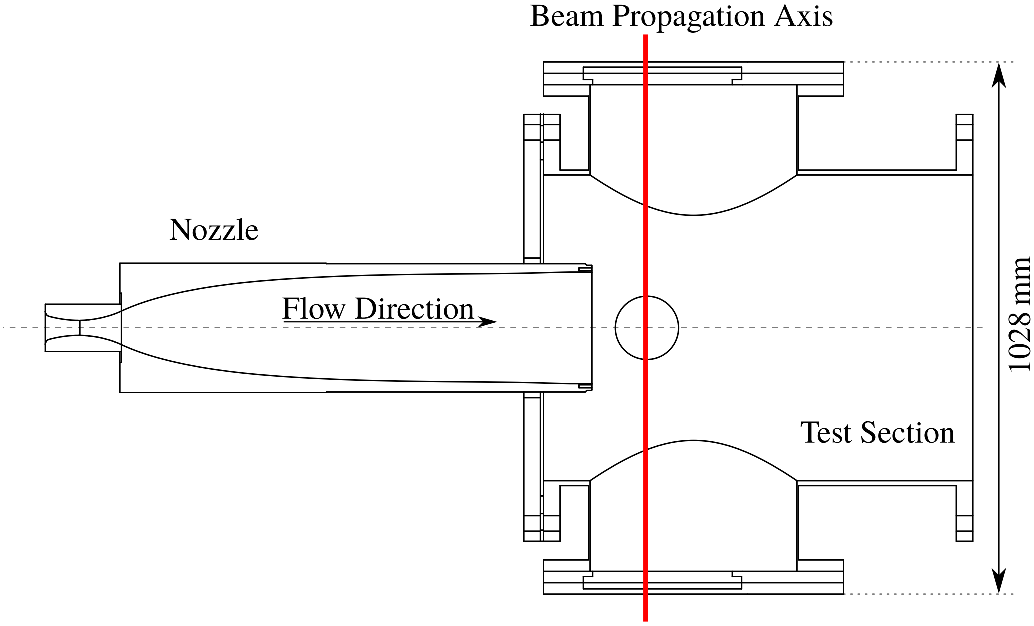

Figure 9.3: Facility geometry constraints for the implementation of FLDI. The figure illustrates a simplified horizontal slice through the nozzle centreline. The nozzle can be translated axially into the test section for probing of different downstream positions.

The maximum angle of rays entering a Sanderson prism was loosely defined by Fulghum (2014) as ‘shallow’ before refractive effects need to be considered; and no numeric limits were defined in that work. A linearly polarised 2 mW 632.8 nm Helium-Neon laser (Thorlabs HNL020L-EC) was selected for the laser source of the instrument. Expansion of the collimated laser beam of diameter 0.63 mm was desired to fill, as much as possible, the useful area of a 50.8 mm diameter field lens. The thin lens equation

$$\frac{1}{f_F} = \frac{1}{d_1} + \frac{1}{f_{FLDI}} \tag{9.1}$$

can be used to calculate the beam path as described in Fig. 9.4 for selection and positioning of all lenses in the FLDI instrument.

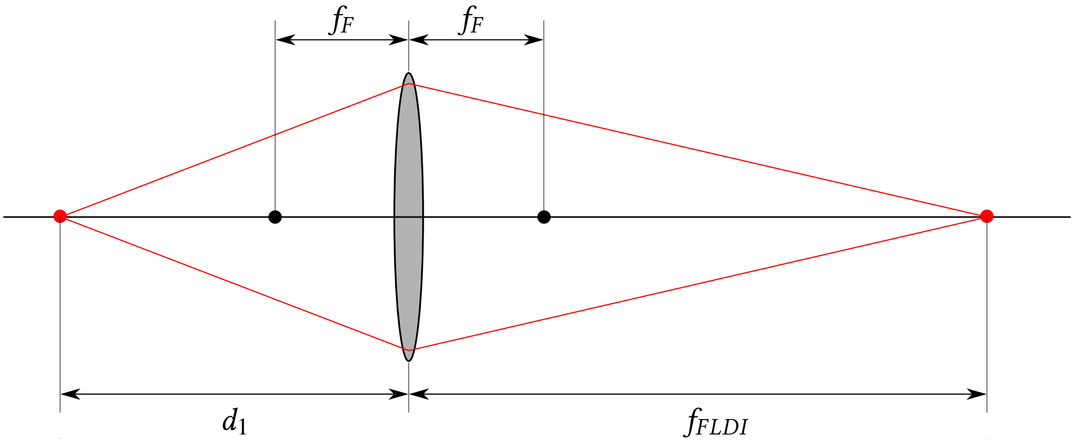

Figure 9.4: Thin lens schematic. f_F is the focal length of the field lens, f_{FLDI} the distance from the field lens to the measuring point and d_1 the distance between the field lens and the focal point used for expanding the beam.

By creating a matrix of available focal length lenses f_{FLDI} was solved and a pair of lenses suited to the limitations of the facility geometry and desired diameter at the field lens evaluated. Multiple functional pairs were found but to maximise the spatial resolution of the interferometer the pair with the highest $D_{4\sigma} : f_{FLDI}$ (f-number) was selected. After the lenses and laser source were selected other optical components were easily selected, summarised in Table 9.1 with the properties of the instrument in Table 9.2.

Figure 9.5 displays the transmitting optics (laser to first field lens) including the dial gauge for monitoring the deflection of the Sanderson prism and thus the beam separation. The variable iris slit was an addition to the Fulghum (2014) design. It is used to block the stray rings of the Airy disc caused by passing the beam through the 20 µm diameter pinhole. Figure 9.6 displays the receiving optics (excluding the second field lens). Note that: (1) the Sanderson prisms are identical in geometry and orientation; (2) the polarising beam splitting cube is rotated 45° to align with the initial polarisation output by the laser; and (3) a micrometer head was added for fine adjustment of the Berek compensator angle.

Item	Part Number	Specification
i	Thorlabs HNL020L-EC	632.8 nm Polarised Laser
ii	Thorlabs A375-A	Ashperic Lens, $f = 7.50$mm
iii	Thorlabs P20S	20 µm Pinhole
iv	Thorlabs ID15/M	Variable Iris
v, viii	-	Custom Sanderson Prism
vi, vii	Thorlabs LA1256-A	Plano-Convex Lens, $\varnothing$50.8 mm, $f = 300.0$mm
ix	-	Camera Lens $f = 28 - 50$mm
x	Newport 5540M	Berek Compensator
xi	Thorlabs PBS201	20 mm Polarising Beam Splitter
xii	Thorlabs DET100A2	Battery Biased Photodetector

Table 9.1: FLDI Instrument Components.

Description	Symbol	Value	Unit
Illumination Wavelength	λ	632.8	nm
Collimated Beam Diameter $(1/e^2)$	d_i	0.63	mm
Laser Power (TEM_{00})	-	2	mW
Laser Minimum Polarisation Ratio	-	500 : 1	
Field Lens Focal Length	f_F	300.0	mm
Maximum Diameter of Beam (95%) Intensity	$D_{4\sigma}$	43.6	mm
f-number	$f/$	$f/16.3$	-
FLDI focal length	f_{FLDI}	710	mm
Beam Waist Radius	w_0	6.55	µm

Table 9.2: Summary of FLDI Instrument Properties.

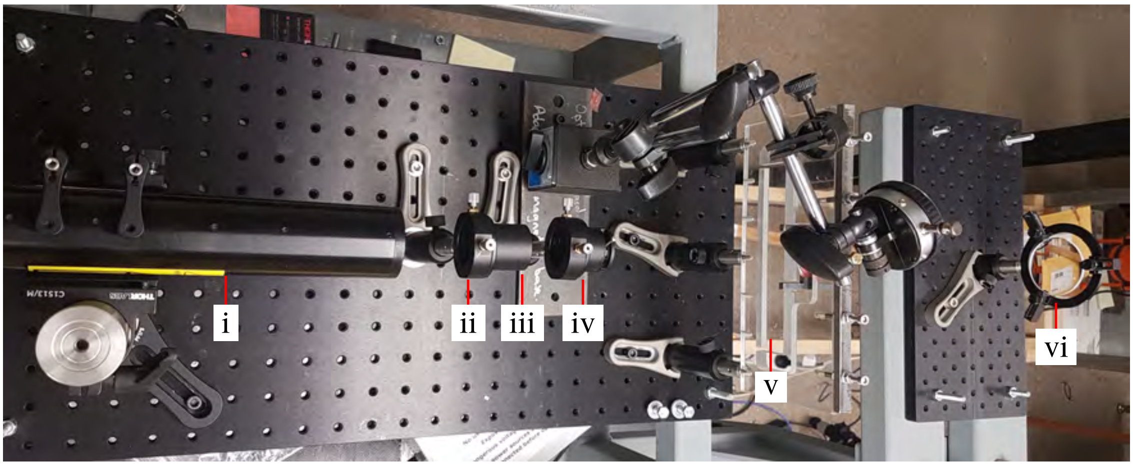

Figure 9.5: FLDI transmitting optics.

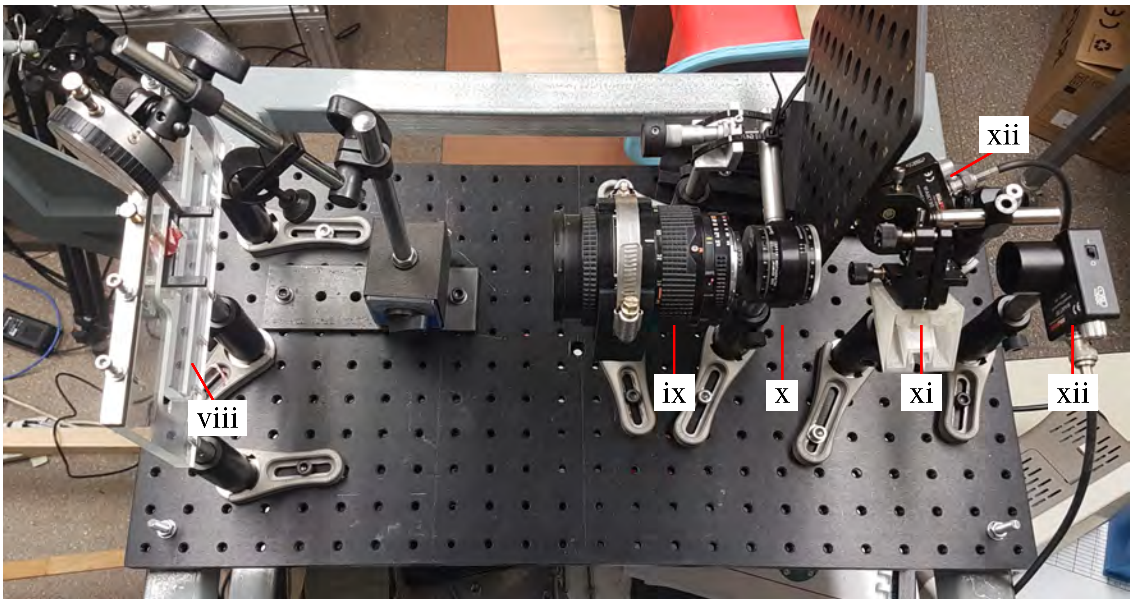

Figure 9.6: FLDI receiving optics.

9.3 Performance of FLDI Instrument

The spatial resolution and bandwidth of the focused laser differential interferometer require discussion for meaningful results to be presented. Fulghum (2014) and Schmidt and Shepherd (2015) present analysis of the performance of FLDI instruments. Before proceeding with the performance analysis it is useful to discuss how the RMS density fluctuations are calculated from the signals measured by the two photodetectors. First the photodetector difference signal is calculated and normalised using Eq. 9.2 where signals measured by the two photodetectors are arbitrarily designated A and B. The normalisation accounts for contrast effects. Conversion to a phase shift is achieved using Eq. 9.3 where the maximum and minimum are found by rotating the Berek compensator through its full range of indicator settings.

$$F_{AB} = \frac{A - B}{A + B} \tag{9.2}$$

$$\Delta\varphi_A - \Delta\varphi_B = \sin^{-1}\left[2\left(\frac{F_{AB} - F_{AB,MIN}}{F_{AB,MAX} - F_{AB,MIN}}\right) - 1\right] \tag{9.3}$$

The phase difference signal calculated using Eq. 9.3 is used in Eq. 9.4 to calculate the time-varying density fluctuations:

$$\rho'(t) = \frac{\lambda}{2\pi K_{GD}\Delta x}\mathcal{F}^{-1}\left\{\frac{\mathcal{F}\{\Delta\varphi_A - \Delta\varphi_B\}}{H_{\Delta x}(k)H_z(k)}\right\} \tag{9.4}$$

where K_{GD} is the Gladstone-Dale constant for the medium being probed, $H_{\Delta x}(k)$ the transfer function due to finite beam separation and $H_z(k)$ the transfer function due to path integrated spatial filtering from beam and turbulence profiles. $H_{\Delta x}(k)$ is a function of the flow direction relative to the axis of beam separation and defined as

$$H_{\Delta x}(k) = \left(\sqrt{1 + \left(\frac{k}{k_c}\right)^2}\right)^{-1} \tag{9.5}$$

where k is the wavenumber of the disturbance, which is a function of the frequency (f) and convective velocity (u_c),

$$k = \frac{2\pi f}{u_c} \tag{9.6}$$

and k_c is the cutoff wavenumber, which for the configuration of this instrument is $k_c = \frac{1.10}{\Delta x}$.

$H_z(k)$ is calculated by integrating the contribution of disturbance of a given wavenumber to the mean wave-front phase at each point along the beam between the limits of $\pm L$ where $0 < L \leq f_{FLDI}$. This transfer function is dependent on the flow field geometry, and for investigation of a freestream flow is defined by Fulghum (2014) and Schmidt and Shepherd (2015) as

$$H_z(k) = \int_{-L}^{L} \exp\left(\frac{-w_0^2 k^2}{8}\left(1 + \left[\frac{\lambda z}{\pi w_0^2}\right]\right)\right) \mathrm{d}z \tag{9.7}$$

Fulghum (2014) and Schmidt and Shepherd (2015) present different expressions for this integral.

Fulghum (2014) used an RMS analysis giving

$$H_{z,Fulghum}(k) = \sqrt{\left[\int_{-L}^{L} \exp\left(\frac{-w_0^2 k^2}{8}\left(1 + \left[\frac{\lambda z}{\pi w_0^2}\right]\right)\right) \mathrm{d}z\right]^2} \tag{9.8}$$

but incorrectly gives the result as

$$H_{z,Fulghum}(k) = \sqrt{2\pi^{3/2}\frac{w_0}{\lambda k}\,\mathrm{erf}\left(\frac{L\lambda k}{2\pi w_0}\right)\exp\left(-\frac{w_0^2 k^2}{4}\right)} \tag{9.9}$$

The correct simplification of Eq. 9.8 is

$$H_{z,Fulghum,corrected}(k) = \frac{2\sqrt{2}\pi^{3/2}w_0}{\lambda k} \operatorname{erf}\left(\frac{L\lambda k}{2\sqrt{2}\pi w_0}\right) \exp\left(-\frac{w_0^2 k^2}{8}\right) \tag{9.10}$$

where the full analysis in support of this correction is presented as Appendix G.

Schmidt and Shepherd (2015) use a normalised transfer function

$$H_{z,Schmidt}(k) = \frac{1}{2L}\int_{-L}^{L} \exp\left(\frac{-w_0^2 k^2}{8}\left(1 + \left[\frac{\lambda z}{\pi w_0^2}\right]^2\right)\right) \mathrm{d}z \tag{9.11}$$

and correctly give the result as

$$H_{z,Schmidt}(k) = \frac{\pi w_0 \sqrt{2\pi}}{kL\lambda} \operatorname{erf}\left(\frac{L\lambda k}{2\sqrt{2}\pi w_0}\right) \exp\left(-\frac{w_0^2 k^2}{8}\right) \tag{9.12}$$

No normalisation of H_z was communicated by Fulghum (2014), however the scaled and unscaled spectra presented in the Fulghum document as Fig. 5.44 – 5.48 are inconsistent with the transfer function of Fig. 3.24 in the same document, as there is no increase in power spectral density at low wavenumbers. However, the normalisation implemented by Schmidt and Shepherd (2015) is consistent with the results of Fulghum (2014). Therefore, the transfer function $H_z(k)$ implemented in this research is the same as proposed by Schmidt and Shepherd (2015) (Eq. 9.12).

Focused laser differential interferometry is known to have a wavenumber dependent spatial resolution along the beam propagation axis. This can be defined by calculating the distance from best focus that a disturbance of wavenumber k will no longer contribute to the overall signal (Schmidt & Shepherd, 2015) by analysing when $H_z(k)$ reduces to a small scalar (n) of its value at best focus. The distance from best focus, z_n, at which a disturbance of a given wavenumber will not significantly contribute to the overall signal is given by

$$z_n = \frac{\pi w_0^2}{\lambda}\sqrt{\frac{8\ln\left(\frac{1}{n}\right)}{k^2 w_0^2} - 1} \tag{9.13}$$

Beam waist radius (w_0) is a function of the f-number of the interferometer and this property provides a convenient way to compare instruments. z_n can be plotted for the FLDI instrument designed for this research in Fig. 9.7 for $n = 0.1$ attenuation and compared to other focused laser differential interferometers in literature. This analysis demonstrates that the FLDI instrument designed at USQ has similar rejection of low wavenumber effects away from the best focus when compared to the instruments used by Fulghum, and superior to that used by Parziale et al. (2014). However, the maximum resolvable wavenumber for the USQ instrument is less than the PSUSWT (Fulghum, 2014) and Parziale et al. (2014) instruments.

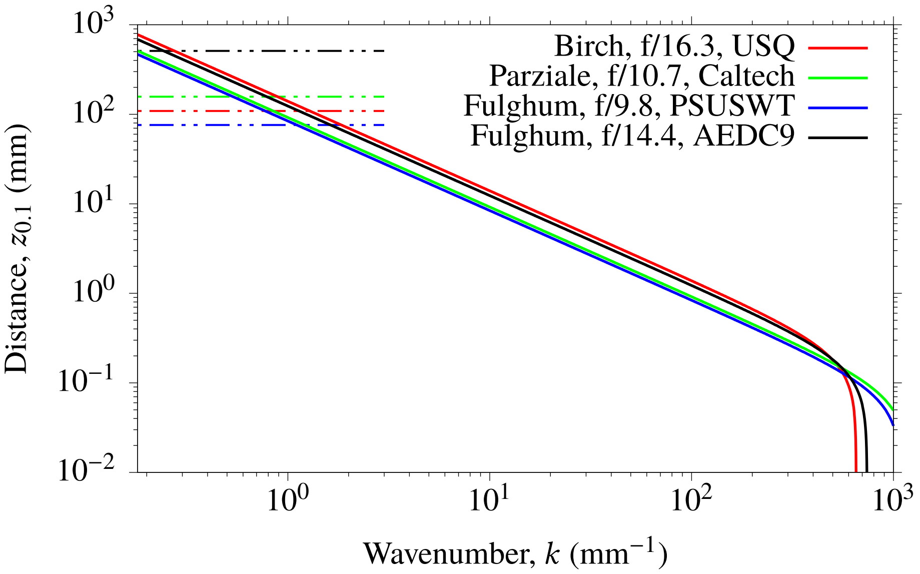

Figure 9.7: FLDI instrument spatial resolution along the axis of beam propagation. FLDI instruments found in literature are included and represented by their f-number. Dashed lines of the same colour represent the nozzle exit radius of the facilities where the instruments were applied.

The Parziale et al. (2014) instrument was used to measure freestream perturbations in the T5* reflected shock tunnel ($f/10.7$); while Fulghum investigated the density fluctuations of a Mach 3 PSUSWT† ($f/9.8$) flow condition and a Mach 10 condition at AEDC Tunnel 9‡ ($f/14.4$). Wavenumbers greater than 10 mm^{-1} will not contribute to the overall signal from more than a few millimetres from the best focus; while those less than, and in the order of, 1 mm^{-1} will be contaminated with significant signal from the turbulent shear layer (TSL). Therefore, for wavenumbers in the order of 1 mm^{-1} or less a significant contribution from the TSL of the TUSQ Mach 6 flow can be expected.

---

[*] California Institute of Technology T5 Hypervelocity Shock Tunnel

[†] Pennsylvania State University Supersonic Wind Tunnel

[‡] Arnold Engineering Development Complex Hypervelocity Wind Tunnel 9

9.4 Berek Compensator Calibration

A calibration curve for the Berek compensator is supplied by Newport, however Fulghum (2014) found this to be a poor match 'for unknown reasons' and it is therefore necessary to check the calibration supplied by Newport. The calibration supplied by Newport Optics for the Berek compensator is

$$\theta_R = \frac{\pi}{4} - \sin^{-1}\left(\frac{50.22 - I}{71}\right) \tag{9.14}$$

where θ_R is the tilt angle and I is the indicator setting of the compensator. The tilt angle is used to calculate the phase retardance (R);

$$R = \frac{2000}{\lambda_{\mu\text{m}}}\sqrt{n_0^2 - \sin^2(\theta_R)}\left[\sqrt{\frac{1 - n_e^{-2}\sin^2(\theta_R)}{1 - n_o^{-2}\sin^2(\theta_R)}} - 1\right] \tag{9.15}$$

The refractive indices n_o and n_e are found using the Sellmeier equation using the values for MgF_2 presented in Table 9.3.

$$n^2 - 1 = \frac{B_1\lambda_{\mu\text{m}}^2}{\lambda_{\mu\text{m}}^2 - C_1} + \frac{B_2\lambda_{\mu\text{m}}^2}{\lambda_{\mu\text{m}}^2 - C_2} + \frac{B_3\lambda_{\mu\text{m}}^2}{\lambda_{\mu\text{m}}^2 - C_3} \tag{9.16}$$

	Extraordinary Ray (e)	**Ordinary Ray (o)**
B_1 (μm^2)	0.41344023	0.48755108
B_2 (μm^2)	0.50497499	0.39875031
B_3 (μm^2)	2.4904862	2.3120353
C_1 (μm^2)	0.03684262	0.04338408
C_2 (μm^2)	0.09076162	0.09461442
C_3 (μm^2)	23.771995	23.793604

Table 9.3: Sellmeier Coefficients for MgF_2 (0.2 – 7.0μm) (Dodge, 1984).

To ensure the grid calibration technique was implemented correctly, the Berek compensator used in this research was calibrated prior to the prisms. An additional goal when performing these calibrations was determining why Fulghum (2014) required the use of different constants for Eq. 9.14 than supplied by the manufacturer.

A collimated polarised laser beam was passed through the Berek compensator with the resulting output beam split by a polarising beam splitting cube with the power of the two subsequent beams monitored using two photodetectors. Keeping the orientation setting of the compensator set to zero, the retardance was changed through the full range of I $(0-17)$ with recordings made at every 0.1 increment. Initial calibrations, like Fulghum (2014), did not match the supplied calibration. Repetition of the calibration could not successfully produce consistent results, and consequently, the change of constants was determined to be an alignment issue. An optical post was fitted to the second post mounting hole of the Berek compensator and a micrometer head used for precision adjustment of the incident angle as defined in Fig. 9.8.

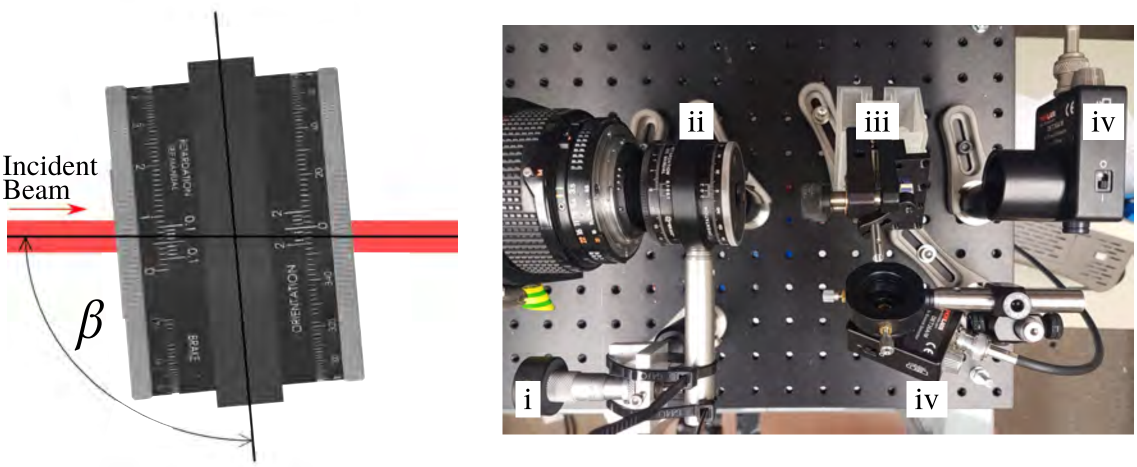

(a) (b)

Figure 9.8: Berek Compensator Alignment: (a) Schematic defining the incident angle β; (b) Image of the receiving optics showing the- (i) Micrometer head; (ii) Berek Compensator; (iii) Polarising beam splitting cube rotated to be aligned with the initial polarisation state of the incident beam; (iv) Photodetectors.

The ideal alignment can be found by setting the incident beam to a 45° polarisation state and setting the Berek compensator indicator and orientation to zero. While monitoring the difference between the signals measured by the two detectors, the micrometer head can be used to adjust β until the difference signal is maximised. At this point the Berek compensator is properly aligned. Figure 9.9 compares the Newport calibration to calibrations for aligned and slightly misaligned compensators. Despite the misalignment of the Berek compensator used by Fulghum (2014), it is possible that the results were unaffected if the calibration of the Sanderson Prisms was conducted at the same incident angle. Alternatively, with enough points used when grid sampling for Sanderson prism calibration, it is possible to perform an in-situ calibration of the Berek compensator during a calibration of the Sanderson prisms.

The Berek compensator is also very sensitive to incident beam collimation. Poor col-

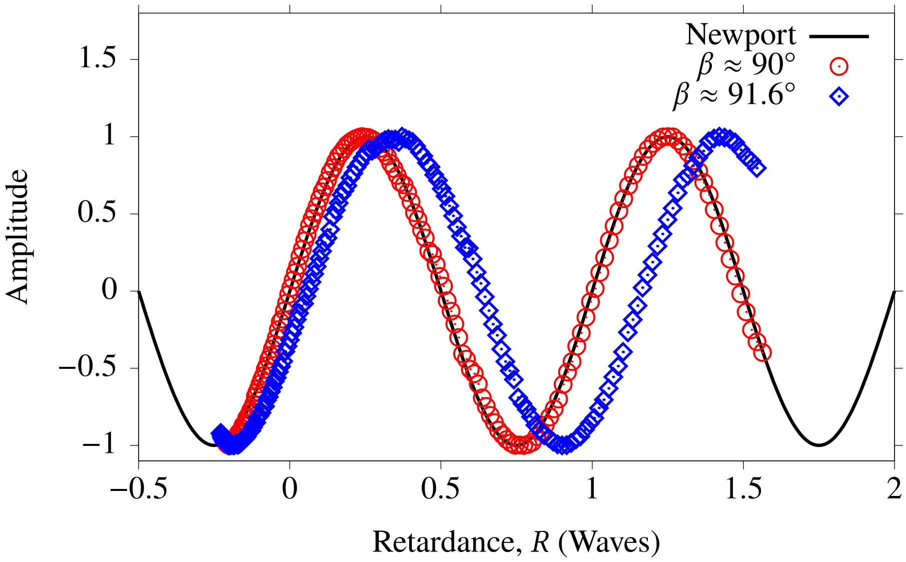

Figure 9.9: Calibration of Berek compensator demonstrating that proper alignment is required to match the calibration provided by Newport.

limation results in non-uniform retardation of the beam. Collimation of the beam can be conveniently checked using the Berek compensator when the collimating lens is an adjustable focal length lens. Using an iterative approach the collimating lens is first placed approximately and the Berek compensator set to zero orientation and retardance.

By monitoring the output voltage of each photodetector as the Berek compensator is rotated through its full range of indicator settings, the operator can view the approximately 1.5 waves of retardance. Over this range one detector output will have two maxima and the other detector output two minima. Considering just the detector output with two maxima, when the beam is not collimated the two maxima will not be of equal amplitude. The focal length of the collimating lens can be changed and the process repeated until the maxima are equal indicating a perfectly collimated beam.

9.5 Sanderson Prisms

9.5.1 Design of a Sanderson Prism

Two Sanderson prisms were used as adjustable inexpensive beam splitting and beam polarising elements as an alternative to an expensive pair of fixed small divergence angle Wollaston prisms. When a stress birefringent prismatic bar is loaded in four point bending (Fig. 9.10) it polarises and diverges the incident beam, providing a first order approximation of the Wollaston prism (Sanderson, 2005). The material used to create the prisms in this research is Makrolon; a polycarbonate also marketed as Hyzod, Lexan and Tuffak. The material properties of Makrolon relevant to the prism design are presented in Table 9.4, along with the geometry of the prisms designed for this research.

Symbol	Value	Description
b	9.525 mm	Prism Thickness
L	70.0 mm	See Fig. 9.10
Y	52.0 mm	See Fig. 9.10
E	2300–2400 MPa	Modulus of Elasticity
n_o	1.5816	Refractive Index
q_{11}	$-4.6 \times 10^{-12}\,\mathrm{Pa}^{-1}$	Stress Optic Coefficient
q_{12}	$24.6 \times 10^{-12}\,\mathrm{Pa}^{-1}$	Stress Optic Coefficient

Table 9.4: Properties of the Sanderson Prisms.

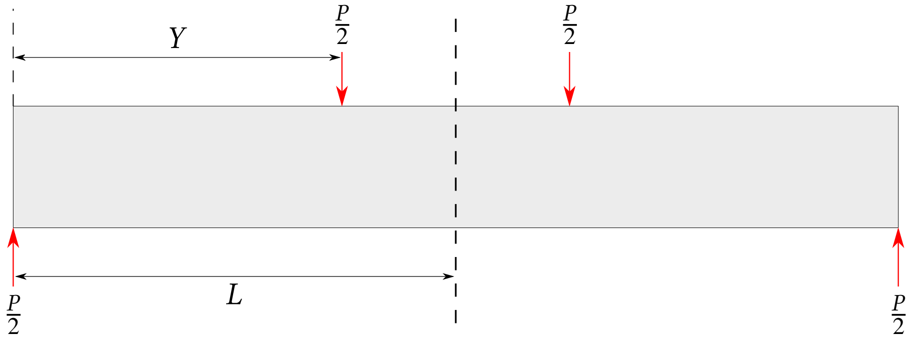

Figure 9.10: Sanderson prism geometry. $L = 70.0$ mm and $Y = 52.0$ mm.

The beam divergence ($\Delta\theta$) is approximated by:

$$\Delta\theta \approx \left| \frac{-n_0^3}{2} \left[q_{11} - q_{12} \right] \frac{3bEX}{\left(3L^2 - Y^2\right)} \right| \tag{9.17}$$

where X is the midspan deflection of the prism and all other values are defined in Table 9.4. For a given beam divergence $\Delta\theta$ the beam separation (Δx) is fixed by the field lens, and through simple trigonometry,

$$\Delta x = 2\, f_F\, \tan\left(\frac{\Delta\theta}{2}\right) \tag{9.18}$$

Note that the dial gauge (Mitutoyo NO. 2052F) does not monitor the midspan deflection of the prism (X) in contrast to previous implementations (Biss, Settles, Staymates & Sanderson, 2008; Fulghum, 2014; Sanderson, 2005) but the deflection of the loading bar (X_L). This configuration was selected as it offered a reliable and more convenient location for the dial gauge and added versatility for any future applications by not restricting the position of the relatively large dial gauge.

The Sanderson prism can be calibrated using the grid sampling technique described by Fulghum (2014). A long focal length positive meniscus lens is used as a reference refraction. By traversing the meniscus lens along the axis of beam separation, the beam separation can be calculated using Eq. 9.19.

$$\Delta x = \frac{k\lambda f_F f_M^2}{z\,(f_F + f_L - z)} \tag{9.19}$$

where λ is the illumination wavelength, k is the spatial frequency of the resulting sinusoid and all other values are defined in Fig. 9.11.

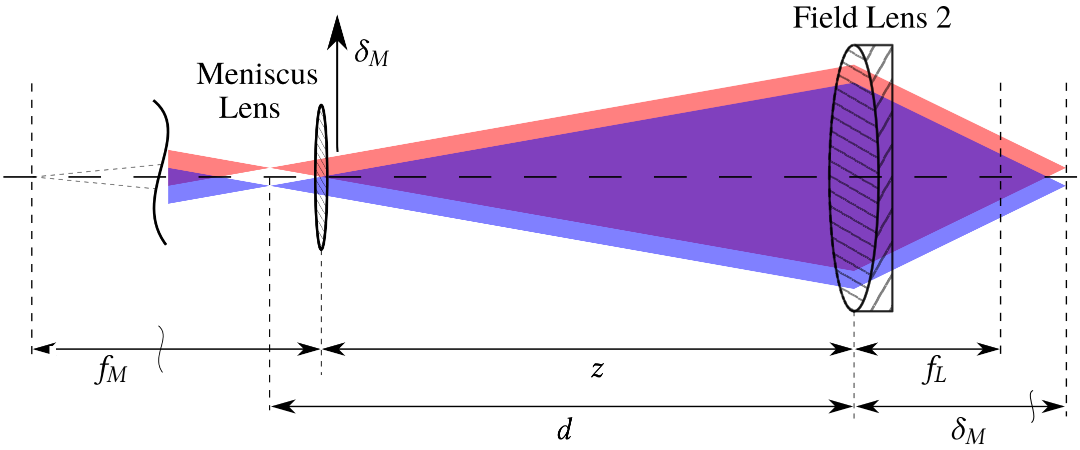

Figure 9.11: Calibration optics for the measurement of beam separation.

A single traverse of the meniscus lens may not produce a full sinusoidal wave resulting in an ambiguous result for k. The Berek compensator can be used to perform a grid sampling calibration over a range of phase retardance and meniscus lens positions. By operating the Berek compensator over a range of indicator settings, the meniscus lens can be traversed for a grid sampling method. The resulting data can be fitted to the equation

$$F_n = \sin(2\pi R + 2\,\pi\,k\,\delta_M + c) \tag{9.20}$$

where F_n is the normalised response, R is the phase retardance provided by the Berek Compensator (Eq. 9.14 & 9.15), k is the spatial frequency of the sinusoid along the lens offset axis, δ_M is the offset of the meniscus lens and c is a constant to completely align the phases of the sinusoids.

9.5.2 Calibration of a Sanderson Prism

Figure 9.12 displays the result of calibration for the case of $X_L = 210\,\mu\text{m}$ with only the data at 4 mm increments of δ_M shown for clarity. The resulting fit is $\sin(2\pi R - 120.1\delta_M + 4.97)$ indicating a beam separation of 23 µm. An added benefit of the grid sampling technique is that the Berek compensator can be calibrated in-situ rather than in a separate procedure.

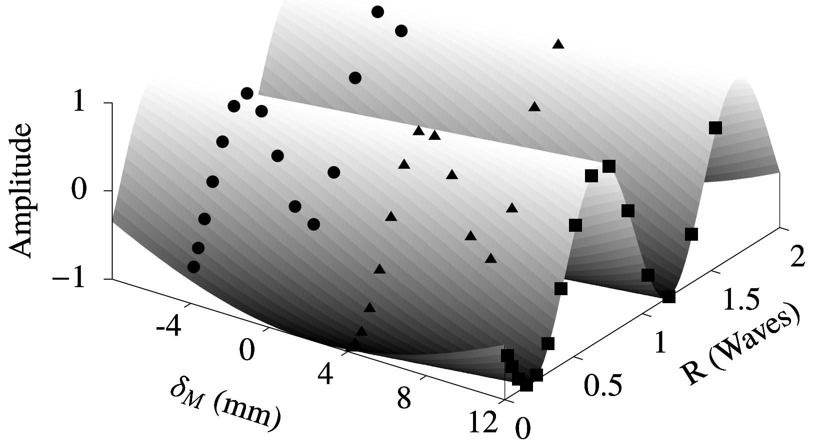

Figure 9.12: Grid calibration sample result. Data were taken at each indicator setting from 2 to 16 in increments of 1; and at lens offsets in increments of 4 mm from −8 mm to 12 mm. Samples of only three lens positions have been presented for clarity.

To compare the results of the calibration to theory, X_L must be related to X to use Eq. 9.15. Assuming an infinitely stiff loading bar the ratio of deflections can be expressed as

$$\frac{X}{X_L} = \frac{1}{4Y}\left(\frac{6L^2 - 2Y^2}{3L - 2Y}\right) \approx 1.09 \tag{9.21}$$

This forms an upper bound for the ratio of deflections, while a minimum bound can be assumed as $X = X_L$. Variability in the modulus of elasticity for the prism material (Table 9.4) also effects the theoretical performance of the prism. Thus the bounds for theoretical comparison can be set as

$$\Delta x_{min} = 2 f_F \tan\left(\frac{1}{2}\left|\frac{-n_0^3}{2}\left[q_{11} - q_{12}\right]\frac{3bE_{min}X_L}{\left(3L^2 - Y^2\right)}\right|\right) \tag{9.22}$$

$$\Delta x_{max} = 2 f_F \tan\left(\frac{1}{2}\left|\frac{-n_0^3}{2}\left[q_{11} - q_{12}\right]\frac{3bE_{max}\left(1.09X_L\right)}{\left(3L^2 - Y^2\right)}\right|\right) \tag{9.23}$$

Results of the Sanderson prism grid calibration as displayed in Fig. 9.13 demonstrate agreement with the estimated theoretical bounds when an offset is introduced to account for non-zero beam divergence resulting from residual stresses in the prism.

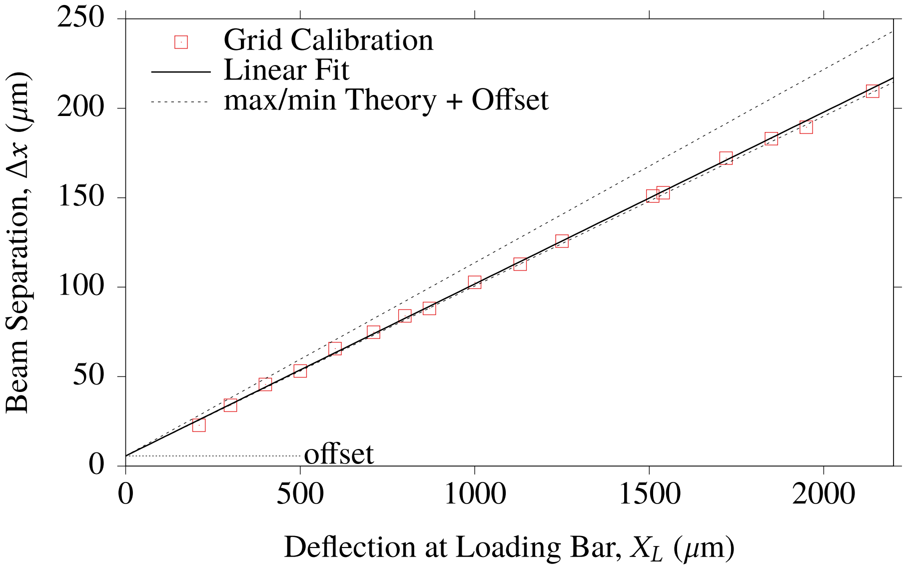

Figure 9.13: Calibration of Sanderson Prism with the theoretical results offset to the zero load beam displacement due to pre-strain in the prism.

9.6 Identification of Photodetector Transfer Function

The two photodetectors used in the focused laser differential interferometer designed for the TUSQ facility are Thorlabs DET100A2 battery biased photodiodes. When light is absorbed by the Silicon photodiode, a photocurrent proportional to the input optical power ($\approx$0.315 A W^{-1} at 632.8 nm) is generated. To convert the current to a voltage, an external terminating resistor of resistance R_T is used. For maximum bandwidth response of the photodetectors, $R_T = 50\,\Omega$ where a matching 50 Ω coaxial cable is used to carry the signal. However, at the small signal levels in this research, the signal may be lower than, or close to, the electronic noise floor. A higher resistance terminating resistor can be used, but this has a detrimental effect on the frequency response of the photodetector. Additionally, when $R_T \neq 50\,\Omega$ the length of the coaxial cable must be minimised to mitigate the effects of signal reflections. Therefore, the need to boost the signal to a sufficiently high voltage using higher resistance terminations must be balanced with the need to preserve the high frequency capability of FLDI.

The DET100A2 manual (*DET100A2 Large Area Si Biased Detector User Guide Rev A*,

2017) states the bandwidth (f_{BW}) at any R_T can be calculated by

$$f_{BW} = \left[2\pi R_T C_j\right]^{-1} \tag{9.24}$$

where C_j is the junction capacitance, given as 150 pF by the supplier. Substituting the typical value for junction capacitance, $f_{BW} \approx 21.2\,\text{MHz}$ at $R_T = 50\,\Omega$. However, this value is significantly different to the bandwidth listed on the specification sheet, $f_{BW} = 8\,\text{MHz}$ at $R_T = 50\,\Omega$ which suggests $C_j \approx 400\,\text{pF}$. This discrepancy in bandwidth means the manufacturer specified data cannot be reasonably relied upon for determination of the photodetector frequency response.

The frequency response of each photodiode can be determined experimentally at any termination resistance by exposing the photodiode to repeated nominally square pulses of light provided by an LED. In theory, for an infinite bandwidth photodetector the output will perfectly match the applied optical input. As the bandwidth reduces, the reduced frequency response is visible as rounded corners on the photodiode output signal. This reduced frequency response can be quantified by taking the Fourier transform of the photodetector output signal. The Fourier transform of a sequence of nominally square pulses is an infinite series of odd multiples of the square wave fundamental frequency. As the bandwidth of the photodetector reduces, the amplitude of high frequency harmonics reduces. By determining the ratio of the input and output amplitude at each harmonic, a transfer function can be identified for each termination resistance.

The effect of termination load resistance on the bandwidth of each detector was determined using the square pulse calibration technique. A 10.5 µs duration pulse of light was supplied by a HARDsoft IL-106G LED illuminator at a repetition rate of 1 kHz for 250 ms with the output of each photodetector recorded at $4\,\text{MS s}^{-1}$. Testing was conducted using resistors in the range $50\,\Omega \leq R_T \leq 38.4\,\text{k}\Omega$. The effect of reduced bandwidth as R_T increases is shown in Fig. 9.14.

The ratio of the Fourier transform of the input and output signals at odd multiples of the fundamental frequency (1 kHz) can be modelled by a first order lowpass filter:

$$H_{PD}(f) = \left[1 + \left(\frac{f}{f_c}\right)^2\right]^{-0.5} \tag{9.25}$$

to identify the transform function for photodetector response $H_{PD}(f)$.

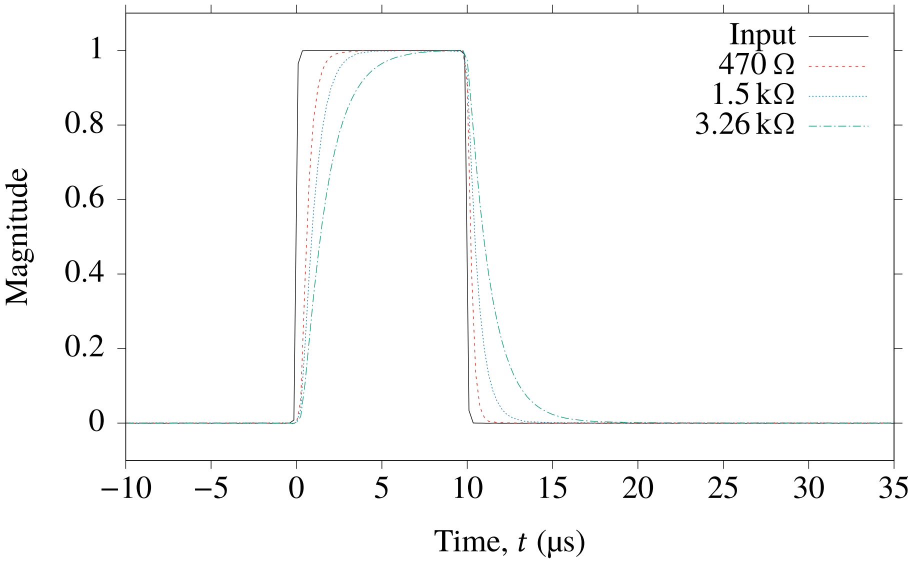

Figure 9.14: Photodetector response to a square wave input pulse at different termination resistances.

The reduced bandwidth response at high termination resistance can be compensated for by processing the raw data by the inverse of Eq. 9.25 which is defined as the transfer function for photodetector frequency response $H_{PD}(f)$. Since the required termination resistance is difficult to determine accurately and changes to the termination resistance between runs of TUSQ may be required, the transfer function for photodetector frequency response effects was determined for $50\,\Omega \leq R_T \leq 38.4\,\mathrm{k}\Omega$. Figure 9.15 shows that the two detectors have slightly different frequency response characteristics, but for R_T <200 Ω the photodetector frequency response is flat to frequencies above what can be resolved from data recorded at 4 MS s^{-1}. The experimental results are in excellent agreement with the theoretical bandwidth when $C_j = 400\,\mathrm{pF}$, suggesting the specified $C_j = 150\,\mathrm{pF}$ to be erroneous.

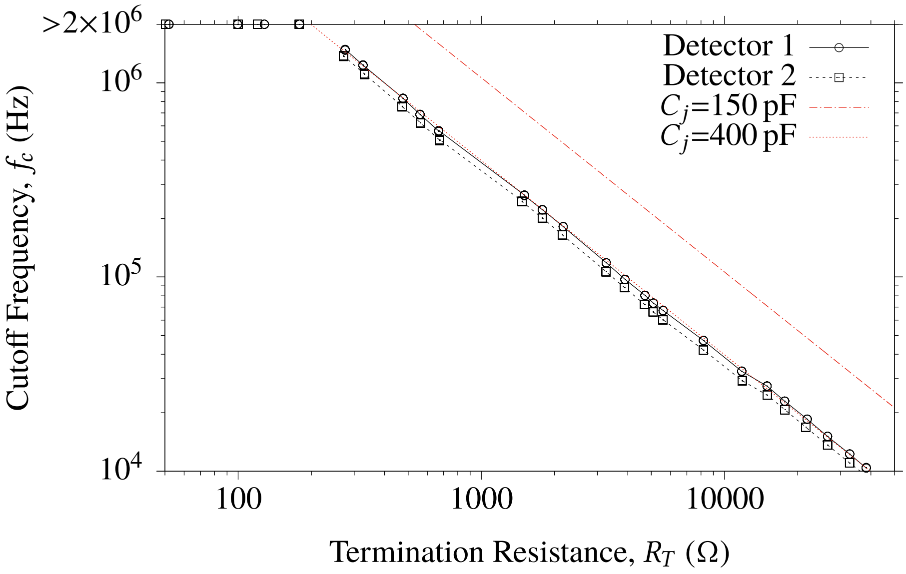

Figure 9.15: Determination of photodetector cutoff frequency as a function of termination resistance.

Chapter 10

Density Fluctuations in TUSQ

Contents

10.1 Introduction

The focused laser differential interferometer described in Chapter 9 was used to investigate the density fluctuations of the TUSQ freestream. This chapter describes the post-processing of the raw photodetector signals required to identify the RMS density fluctuations. Time-resolved density fluctuations are presented, and when the density fluctuations are presented in the wavenumber domain the data can be analysed with reference to models for the energy spectrum of turbulence. A capability demonstration for FLDI measurements in boundary layers in TUSQ was performed, and preliminary data from this experimentation are presented in Section 10.7.

10.2 Illustrative Time-Resolved FLDI Signals

Raw barrel pressure and photodetector data from Run 829 where $\Delta x = 169\,\mu\text{m}$ and $R_T = 660\,\Omega$ are shown in Fig. 10.1. For clarity the signals have been offset, and data arranged such that flow initiation occurs at $t = 0$ ms.

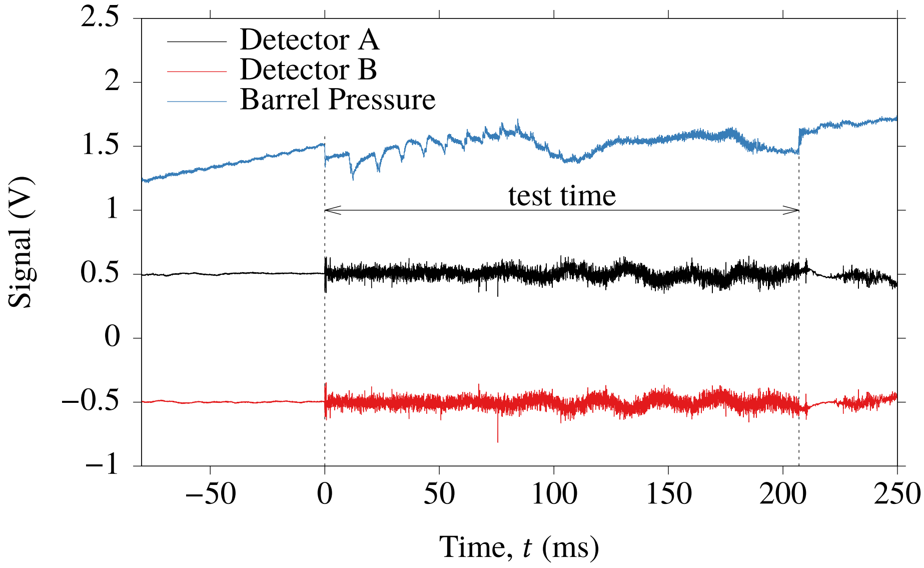

Figure 10.1: Raw FLDI photodetector voltage data for Run 829 with $\Delta x = 169\,\mu\text{m}$. Data offset for clarity.

In Fig. 10.1 a high signal-to-noise ratio (SNR) for the photodetector signals is evident during the test time, and the property of the two-detector FLDI arrangement where the two detectors output identical signals that are 180° out of phase is also clear. The barrel pressure transducer shows that the nozzle flow terminates at approximately 210 ms, and at this time the amplitude of the fluctuations measured by each detector reduces to the pre-flow levels. If the optics were not well isolated from the facility, the signal would slowly dampen. Therefore, because of the signal fluctuations of the photodetector signals reducing to pre-flow levels immediately upon nozzle flow termination, it was concluded that the optics were well isolated from the facility, and the signal dominated by density fluctuations. At $t \approx 220$ ms the results show that the photodetectors measured significant density fluctuations, and this is because the gas is subjected to pressure wave disturbances as the test section pressure equilibrates with the dump tank pressure on nozzle flow termination.

The amplitude and frequency response of the FLDI instrument are a function of the beam separation and photodetector terminating resistor, and the combination of these two parameters directly impacts the SNR. The amplitude of the density fluctuations measured by the FLDI instrument are determined using

$$\rho'_{\infty}(t) = \frac{\lambda}{2\pi K_{GD} \Delta x} \mathcal{F}^{-1} \left\{ \frac{\mathcal{F}\{\Delta\varphi_A - \Delta\varphi_B\}}{H_{\Delta x}(k) H_z(k)} \right\} \tag{10.1}$$

which was introduced in Section 9.3. For comparison of the effect that varying the beam separation and termination resistance has on the amplitude of the fluctuations measured, it is useful to analyse Eq. 10.1 further. The same laser was used for all testing, and the same test gas was used. Therefore, $\frac{\lambda}{2\pi K_{GD}}$ has a constant value throughout all tests. The transfer function $H_{\Delta x}$ is approximately unity for $k < 3\,\mathrm{mm}^{-1}$ for the beam separations possible with the instrument, and the eddies greater than this size were found to dominate the turbulent energy spectrum. Therefore for comparison of the time-resolved density fluctuations at different beam separations, the assumption $H_{\Delta x} \approx 1$ can be made. The transfer function $H_z(k)$ is unaffected by changes to the beam separation and termination resistance and is therefore constant for all tests, assuming that the radius of the flow-field, beam waist radius, and convective velocity can be treated as constant across all runs. The termination resistance affects H_{PD}, but similar to $H_{\Delta x}$, it is unity for the energy containing eddies.

Therefore Eq. 10.1 can be reduced to

$$\rho'_{\infty}(t) \underset{\sim}{\propto} \frac{\Delta\varphi_A - \Delta\varphi_B}{\Delta x} \tag{10.2}$$

where the normalisation of phase difference signal by beam separation $\left(\frac{\Delta\varphi_A - \Delta\varphi_B}{\Delta x}\right)$ is convenient for comparison of raw phase difference data in the time, frequency and wavenumber domains.

Normalised phase difference data for two beam separations and four termination resistances are shown in Fig. 10.2. At $\Delta x = 170\,\mu\mathrm{m}$ there is a small, but visually apparent difference in the amplitude of the normalised phase difference signal for the two termination resistances shown, and this is because of the low-pass filter effect of the terminating resistor. The bandwidth of the photodetectors is 320 kHz and 1.6 MHz for $R_T = 3.3\,\mathrm{k\Omega}$ and $R_T = 660\,\Omega$ respectively.

The amplitude of the normalised phase difference signal during nozzle flow is similar for $R_T = 180 - 660\ \Omega$ and $\Delta x = 85 - 170\ \mu\mathrm{m}$. However as the terminating resistance decreases

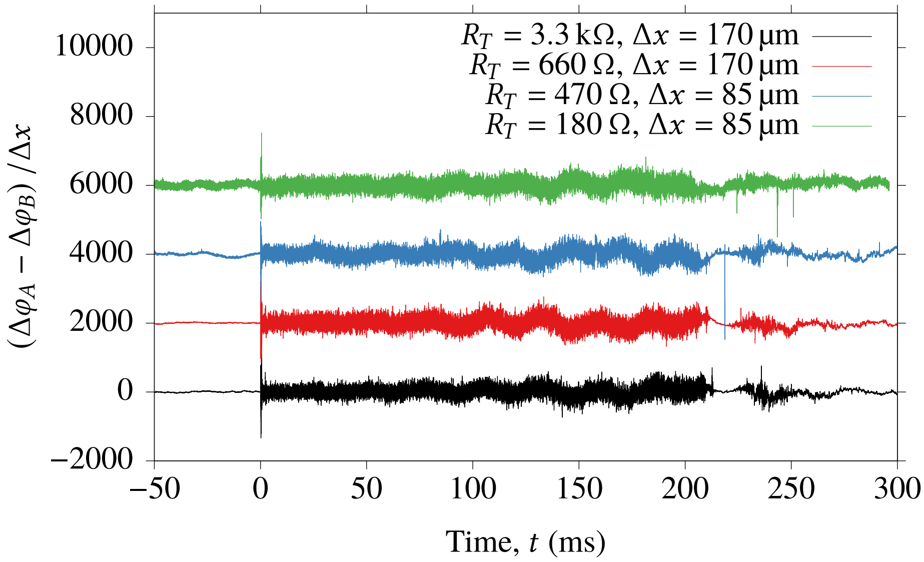

Figure 10.2: Phase difference signal normalised by beam separation distance Δx. Data offset for clarity.

the SNR also decreases. The maximum sample rate of the data acquisition system is $4\,\mathrm{MS\,s^{-1}}$ and therefore, there is no benefit in using terminating resistors that result in a bandwidth $> 2\,\mathrm{MHz}$, which occurs for $R_T < 530\,\Omega$. Consequently termination resistors of $R_T = 470\,\Omega$ and $R_T = 660\,\Omega$ were used for most runs.

10.3 Transfer Functions for FLDI Instrument

Four transfer functions are used to transform the FLDI phase difference signal and account for the attenuation of high frequency content:

1. $H_{\Delta x}(k)$, spatial filtering due to finite beam separation;
2. $H_z(k)$, path integrated spatial filtering due to beam size and turbulence profile;
3. $H_{PD}(f)$, attenuation of high frequency content due to termination resistance R_T; and
4. $H_{Amp}(f)$, attenuation of high frequency content due to the amplifier performance.

These transfer functions are presented in Fig. 10.3 for a typical configuration of the FLDI instrument. The convective velocity was assumed to be independent of wavenumber, and set to the freestream velocity, consistent with the work of Fulghum (2014) in AEDC9 and PSUSWT. The average freestream velocity over the full run duration in the TUSQ facility is approximately $980\,\mathrm{m\,s^{-1}}$.

The frequency response of the instrument is dominated by the path integrated spatial

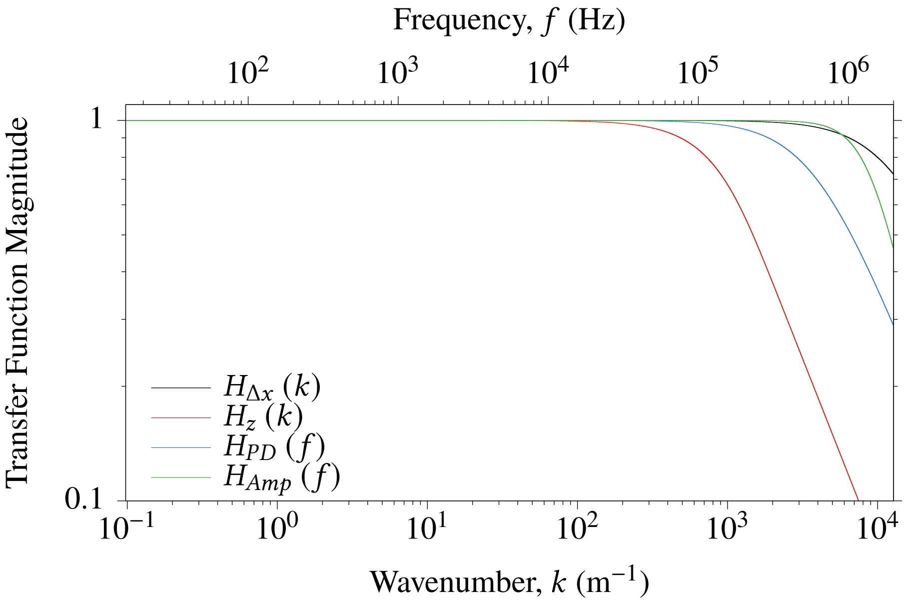

Figure 10.3: Magnitude of transfer functions for $\Delta x = 83\,\mu\mathrm{m}$, $L = 109\,\mathrm{mm}$, $R_T = 660\,\Omega$, and $u_c = 980\,\mathrm{m\,s^{-1}}$.

filtering due to beam size and turbulence profile which is independent of Δx and R_T. The attenuation of the photodetector output is dependent on the termination resistance, but for $R_T = 660\,\Omega$ the transfer function H_{PD} is approximately unity for $f \lesssim 100\,\mathrm{kHz}$, and the bandwidth as defined by Eq. 9.24 is 1.6 MHz. The amplifier transfer function was identified in Appendix F and is approximately unity for $f < 1\,\mathrm{MHz}$. The filtering due to finite beam separation is dependent on the beam separation set for each test, however $H_{\Delta_x}(k)$ always has a lesser impact on the frequency content than $H_z(k)$.

10.4 Analysis of Spectra

10.4.1 Introduction and Raw Spectra

The FLDI signal in the time domain must be transformed into the frequency domain to apply the transfer functions $H_A(f)$ and $H_{PD}(f)$, and into the wavenumber domain to apply the transfer functions $H_{\Delta x}(k)$ and $H_z k$. Although the SNR was found to be high in the time domain, in the wavenumber domain the SNR of the FLDI signal is wavenumber dependent, and therefore an important step is to assess the noise baseline across the wavenumber range. Immediately prior to a run a baseline measurement of the photodetector voltages is recorded, and these can be used to calculate the baseline phase difference signal. Using a power spectral density (PSD) estimate of this signal, the baseline noise in the frequency and wavenumber domains is shown in Fig. 10.4, and compared to the spectral content for 1 – 200 ms after flow initialisation. The PSDs presented in Fig. 10.4 were calculated using Welch's method with symmetric Blackman windows of width 2^{15} points and 90 % overlap for 2^{18} fft points.

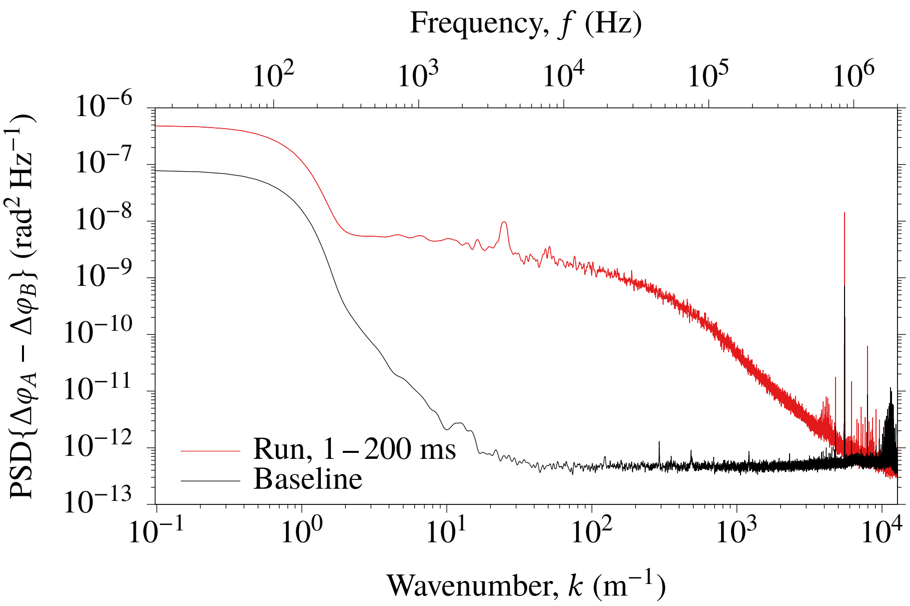

Figure 10.4: Raw FLDI spectra for Run 837, $\Delta x = 83\,\mu\text{m}$, $u_c = 980\,\text{m}\,\text{s}^{-1}$.

Relatively high amplitude, low frequency noise is present in the baseline signal which can result from 50 Hz electrical line noise, variations in laser power intensity and slow convective currents in the laboratory environment passing across the beam. For $300\,\text{Hz} \lesssim f \lesssim 700\,\text{kHz}$ the measured phase difference during a run is significantly above the baseline noise level, while for frequency content in the order of 1 MHz there is little-to-no useful flow information. The baseline and run spectra both exhibit many strong narrowband peaks bound between 600 kHz and 2 MHz which is interference from local AM and amateur radio stations.

The FLDI spectra of a TUSQ run, like the Pitot pressure and stagnation temperature surveys, exhibits a peak in content at 3 – 4 kHz. By analysing data for smaller time periods within the overall flow duration the temporal development of this frequency content can be better analysed. The spectrum of each photodetector signal can be compared to identify portions of the FLDI spectrum dominated by flow features and generally free from electronic, electromagnetic and stray light noise.

10.4.2 Signal Coherence

By using the two photodetector FLDI system the turbulence signal can be discriminated from background noise by analysing the magnitude squared coherence, $C_{AB}(f)$, of the photodetector output signals (Fulghum, 2014) using Eq. 10.3.

$$C_{AB}(f) = \frac{|P_{AB}(f)|^2}{P_{AA}(f)\, P_{BB}(f)} \tag{10.3}$$

Here $P_{AB}(f)$ is the cross-spectral density of the voltage output signals from photodetectors A and B, and $P_{AA}(f)$ and $P_{BB}(f)$ are the autocorrelations of signals A and B respectively. The magnitude squared coherence is bound in the range $0 \leq C_{AB}(f) \leq 1$, where 1 indicates a perfectly coherent signal and 0 that the signals are unrelated.

Segments of the spectra dominated by the density fluctuations present in the TUSQ flow have a high coherence. These segments can be consistently identified by setting a minimum coherence cutoff value. A study of the coherence of the two photodetector signals was performed by Fulghum (2014), but the coherence cutoff inconsistently applied. For a free-space turbulent jet a threshold of $C_{AB}(f) > 0.9$ was implemented, but for measurements in a Mach 3 atmospheric blow down facility (PSUSWT) the threshold used was $C_{AB}(f) > 0.85$ or $C_{AB}(f) > 0.75$. No justification was provided for these thresholds, but it is likely that it is a judgement made by the experimenters in each application of the instrument.

10.4.3 von Kármán Spectrum

Turbulence is a complicated broadband phenomenon, however by discussing turbulence spectra models the turbulent density spectra measured by the focused laser differential interferometer can be better understood. Kolmogorov (1941) proposed that the kinetic energy in large spatial scale motions of turbulent flow is transferred to smaller scale motions, and assumed that the small scale turbulent motions are homogeneous and isotropic. The turbulent kinetic energy is transferred from large eddies to smaller eddies such that the three dimensional energy spectrum, $E(k)$, is proportional to $k^{-5/3}$. This region is known as the inertial subrange, which is illustrated in Fig. 10.5.

Considering the spectrum model of Fig. 10.5, the Kolmogorov turbulence model can be split into three regions:

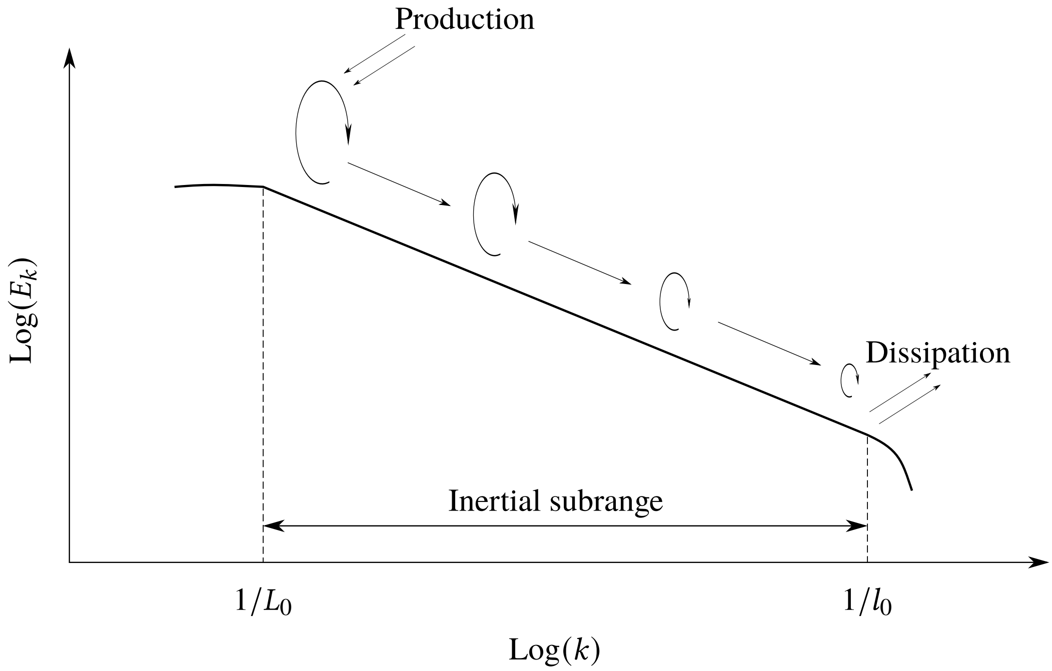

Figure 10.5: Schematic of the energy production, cascade and dissipation in the energy spectrum of turbulence.

1. $k < 2\pi/L_0$ containing the large eddies;
2. $k > 2\pi/l_0$, which is smaller than the smallest turbulent eddies; and
3. $2\pi/L_o \leq k \leq 2\pi/l_0$, the inertial subrange.

The Kolmogorov turbulence model can only be used to model the inertial subrange.

In FLDI, the turbulent density fluctuations are inferred from the measurement of the fluctuating refractive index of the test gas. The index of refraction of the test gas $\left(n\left(\overrightarrow{r}, t\right)\right)$ can be modelled as the sum of a mean refractive index $(\overline{n})$ and a fluctuating term $\left(n'\left(\overrightarrow{r}, t\right)\right)$ by:

$$n\left(\overrightarrow{r}, t\right) = \overline{n} + n'\left(\overrightarrow{r}, t\right) \tag{10.4}$$

where $\overrightarrow{r}$ is a three dimensional vector position (Roggemann & Welsh, 1996). The statistical size and number of the turbulent eddies can be characterised by the PSD of $n'\left(\overrightarrow{r}, t\right)$ which can be assigned as $\Phi_n\left(\overrightarrow{k}\right)$. Assuming homogeneous, isotropic turbulence as required for the Kolmogorov model, $\overrightarrow{k}$ can be replaced by the scalar wavenumber k.

Following vector decomposition of the turbulent energy, the Kolmogorov spectrum can be written as

$$\Phi_n^K(k) = 0.033\, C_n^2\, k^{-11/3} \tag{10.5}$$

where C_n is known as the structure constant of the index of refraction fluctuations (Roggemann & Welsh, 1996).

The von Kármán spectrum can be used to predict the turbulence spectrum for the inertial subrange, small and large wavenumbers, and is defined as:

$$\Phi_n^V(k) = \frac{0.033\,C_n^2}{\left(k^2 - k_0^2\right)^{11/6}} \exp\left(-\frac{k^2}{k_m^2}\right) \tag{10.6}$$

where $k_0 = 2\pi/L_0$ and $k_m = 5.92/l_0$ and the form for $k < 2\pi/L_0$ is considered approximate. The exponential term of Eq. 10.6 has the effect of rapidly rolling off the spectrum for $k > k_m$, and for a spectral fit to the data can be neglected without introducing significant error. Therefore, Eq. 10.6 can be approximated as:

$$\Phi_n^V(k) \approx \frac{A^2}{\left(k^2 + k_0^2\right)^{-B/2}} \tag{10.7}$$

where A and B are constants representing the amplitude and slope of the energy decay respectively. Recognising that the indices applied to the wavenumber term of Eq. 10.6 $(-11/6)$ is half of the corresponding index of Eq. 10.5 $(-11/3)$, the index $-B/2$ was introduced so not to constrain the spectrum fit to the von Kármán models. In the case of $B = -5/3$, the fit is identical to the von Kármán spectrum of turbulence.

To demonstrate the measured density fluctuation spectrum and how it compares to a von Kármán model, experimentally measured spectra are presented for five runs during the period 5 – 25 ms using different instrument parameters in Fig. 10.6. Note that the energy spectrum is calculated as a power spectral density (PSD), not by fast Fourier transform (FFT). The PSD and FFT are related by:

$$\mathrm{PSD}(x) = |\mathrm{FFT}(x)|^2 \tag{10.8}$$

The amplitudes of the spectra for $k < 5\,\mathrm{m}^{-1}$ varied significantly, and there was no region of uniform intensity fluctuations which is predicted by the von Kármán turbulence model. Consequently, the von Kármán spectrum line is an example of the shape of spectra expected and not a fit to the data. The deviation from ideal shape at low wavenumbers is a result of signal contamination, predominantly from the turbulent shear layer (TSL) originating from the boundary layer on the nozzle wall. Despite the difficulty fitting a von Kármán spectrum to the experimental data because of the impact of the TSL at low wavenumbers, a $-5/3$ rolloff is apparent at higher wavenumbers. However, because of the significant signal from the TSL present in the spectra shown in Fig. 10.6, the spatial filtering of the present FLDI instrument is not sufficient to accurately investigate the amplitude of freestream density fluctuations. Therefore, to extract meaningful measurements of the density fluctuations in TUSQ, the rejection of the TSL had to be improved.

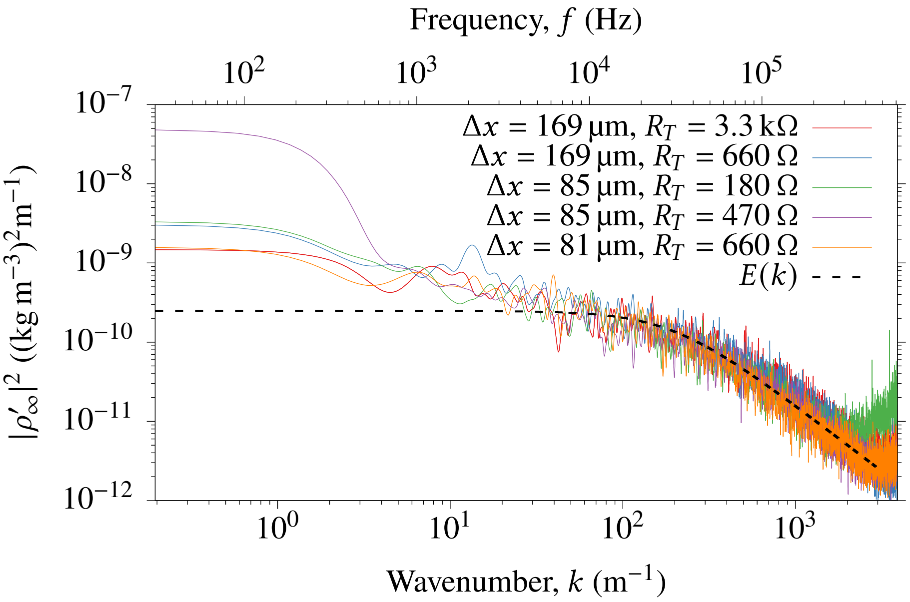

Figure 10.6: Density fluctuation spectra for $t = 5 - 25$ ms with a sample von Kármán spectrum.

10.5 Improved Rejection of the Turbulent Shear Layer

Because of the rather gradual focusing that could be achieved due to geometric limitations, ‘beam shrouds’ were positioned on either side of the flow to allow the FLDI beams to pass unperturbed through the turbulent shear layer from the nozzle wall. These beam shrouds are a mechanical method of improving the wavenumber-dependent optical filtering of FLDI implemented to improve the rejection of lower-wavenumber disturbances far from the best focus of the instrument. One of the beam shroud devices is represented schematically in Fig. 10.7. Once the boundary layer is ejected from the nozzle it is no longer attached to a body, and is termed a free shear layer. Two diametrically opposed beam shrouds were fixed to the nozzle at the exit plane, with the sharpened leading edge positioned 35 mm upstream of the nozzle exit plane. These devices forced the boundary layer on the nozzle wall and the turbulent free shear layer to pass around the path of the FLDI beams, which could then pass through the cylindrical passage unperturbed by the TSL.

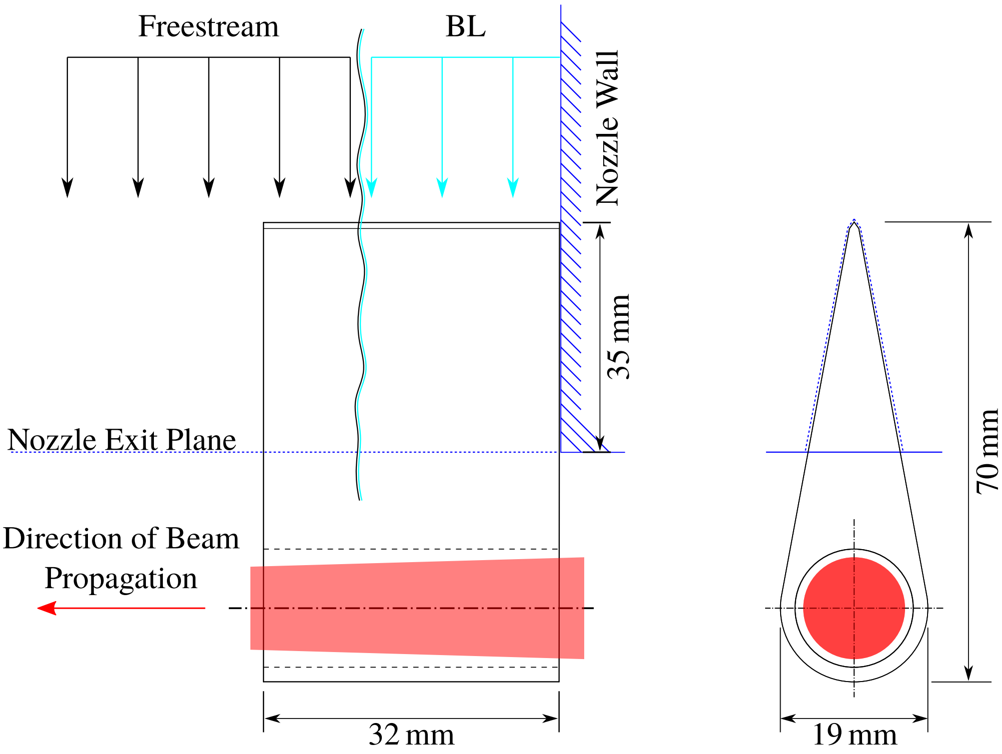

Figure 10.7: Schematic of a beam shroud which allows the FLDI beams to pass through the turbulent shear layer (TSL) unperturbed.

A detrimental effect of the beam shrouds is that they with the flow. Consequently the flow across the FLDI beam in the vicinity of the beam shroud is not a true representation of the freestream conditions. The freestream density fluctuations were measured using FLDI with and without the beam shrouds installed, and comparative results shown in Fig. 10.8. When the beam shrouds are installed, the distance from FLDI focus to the extremity of flow (L) is reduced to 77 mm from 109 mm when the beam shrouds are not installed. Therefore, to demonstrate only the effect of the beam shroud on the measurement of phase difference, Fig. 10.8 presents the phase difference normalised by beam separation. The spectra for Run 837 and Run 843 exhibit significant differences for $k \lesssim 1000\,\mathrm{m}^{-1}$, where the improved rejection of the TSL is evident in the Run 843 spectrum.

The beam shrouds have no influence on the baseline noise spectrum, and this demonstrates that the FLDI beams were not clipped by the beam shrouds, nor were any stray reflections significant. The beam shrouds removed the signal contamination caused by the TSL, and this enables improved fitting of the von Kármán spectrum to the experimental data. Additionally, because the FLDI beams did not pass through the TSL, the content at 3 –

4 kHz is more evident, and a possible harmonic that was not detected by the intrusive Pitot pressure and total temperature surveys at about 7 – 8 kHz is also apparent.

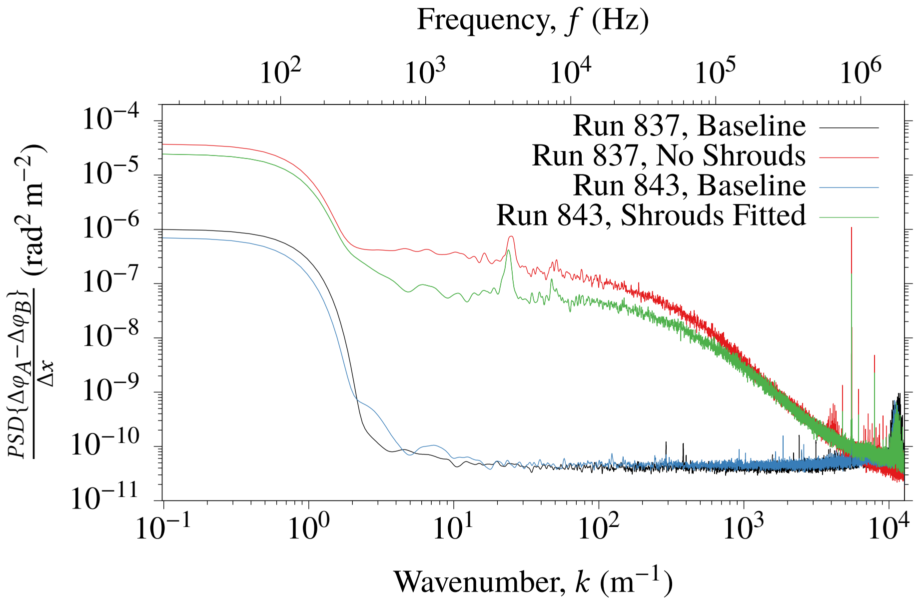

Figure 10.8: Comparison of normalised phase difference spectra for runs with and without the beam shrouds installed.

10.6 Density Based Turbulence Intensity

Using FLDI measurements from runs where the beam shrouds were installed, a von Kármán turbulence spectrum can be fitted to the experimental data. Recalling that the coherence spectrum of the two photodetector signals can be used to identify the regions dominated by the density fluctuations close to the FLDI best focus, the spectral fit is only to this region of data. The coherence spectrum was found to be a function of the duration of time examined, too long a window tended to result in reduced coherence, especially at higher wavenumbers. Shorter windows by definition use less temporal data and therefore less data can be transformed into the frequency domain. This reduction in the available data results in a ‘noisier’ power spectrum, but this data tends to be more coherent than for longer windows. Windows of 20 ms duration were found to produce smooth spectra while preserving a high signal coherence for data analysis.

A power spectral density analysis of Run 843 for $t = 10 - 30$ ms after diaphragm rupture is presented in Fig. 10.9. The power spectral density for the run and baseline were found using Blackman windows of 2^{14} points wide with 90 % overlap, and the signal coherence and SNR found for every frequency examined. Hamming and rectangular windows were considered, however using these windows resulted in a reduced SNR for $k < 100\,\mathrm{m}^{-1}$.

The overlapping and window lengths were selected such that the presented spectra were clear but maintained the flow features. The SNR was defined as:

$$\mathrm{SNR} = \frac{\mathrm{PSD}\left\{(\Delta\varphi_A - \Delta\varphi_B)_{run}\right\}}{\mathrm{PSD}\left\{(\Delta\varphi_A - \Delta\varphi_B)_{baseline}\right\}} \tag{10.9}$$

such that the signal-noise-ratio considered the raw data, and not that processed by FLDI transfer functions.

The power spectral density of the turbulent density fluctuations ($|\rho'_\infty|^2$) is well above the baseline noise level for $4\,\mathrm{m}^{-1} \lesssim k \lesssim 2000\,\mathrm{m}^{-1}$ (Fig. 10.9b). For $k \gtrsim 3000\,\mathrm{m}^{-1}$, the SNR is low and this is manifested in the PSD of density fluctuations. Because the intensity of density fluctuations is of the order of, or less than, the baseline noise level, the turbulent density fluctuations cannot be determined for $k > 3000\,\mathrm{m}^{-1}$. At these high wavenumber this results in the transfer functions modulating a small signal embedded in the baseline noise resulting in the increase of $|\rho'_\infty|^2$ for $k \gtrsim 3000\,\mathrm{m}^{-1}$ in Fig. 10.9a which is a non-physical behaviour.

The coherence spectrum is very noisy at high wavenumbers, and a low coherence is observed at low wavenumbers. The noise at high wavenumbers is at least in part attributable to differences in sensitivity of the photodetectors at high wavenumbers, but this region was found to have a SNR of approximately unity. Due to the reduced coherence spectrum and low SNR, results for $k > 2000\,\mathrm{m}^{-1}$ were excluded from the von Kármán spectrum fit. Similarly wavenumbers of $k < 10\,\mathrm{m}^{-1}$ were also excluded. Therefore the von Kármán spectrum was fit to $10\,\mathrm{m}^{-1} \leq k \leq 2000\,\mathrm{m}^{-1}$ for the case of Fig. 10.9. For the wavenumber range $10\,\mathrm{m}^{-1} \leq k \leq 2000\,\mathrm{m}^{-1}$ the coherence was greater than 80%, and therefore a coherence threshold of $C_{AB} > 0.8$ was implemented for all data.

Two von Kármán spectrum fits are shown on Fig. 10.9a, one where the constants A, B and C of Eq. 10.7 are all determined from the fitting process, and a second fixing $B = -5/3$ corresponding to the Kolmogorov spectrum rolloff. The free fit and the $B = -5/3$ fit are in strong agreement with the experimental spectrum for the fit region $4\,\mathrm{m}^{-1} \lesssim k \lesssim 2000\,\mathrm{m}^{-1}$. At higher wavenumbers the SNR was approximately one which causes the experimental spectrum, when processed by the transfer functions, to increase which is a non-physical result. Consequently the dissipation scale could not be resolved, which appears in the exponential term of the general von Kármán spectrum model (Eq. 10.6). Therefore, the approximate von Kármán spectrum fit (Eq. 10.7) was used for the analysis of all spectra.

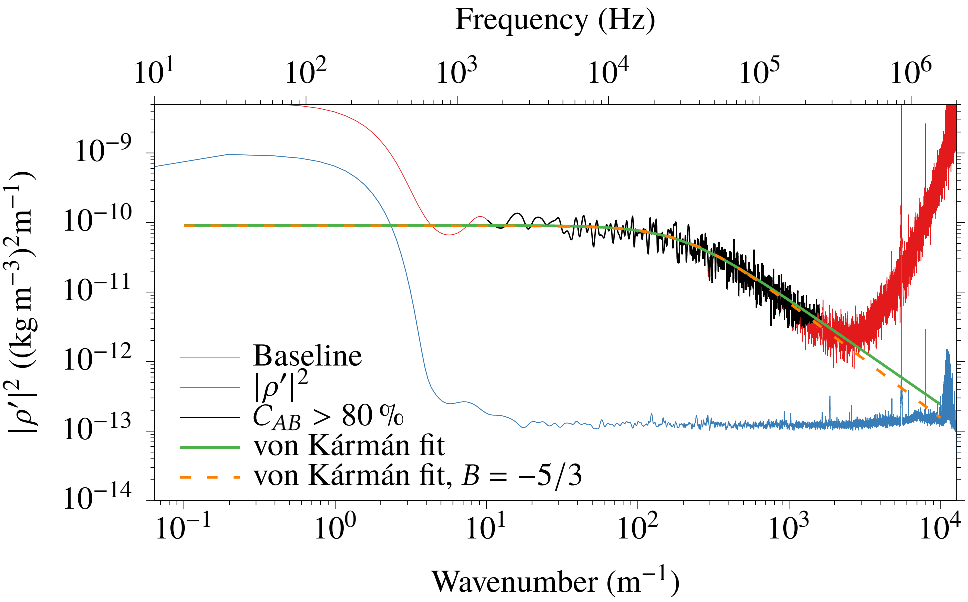

(a) Power spectral density of density fluctuations.

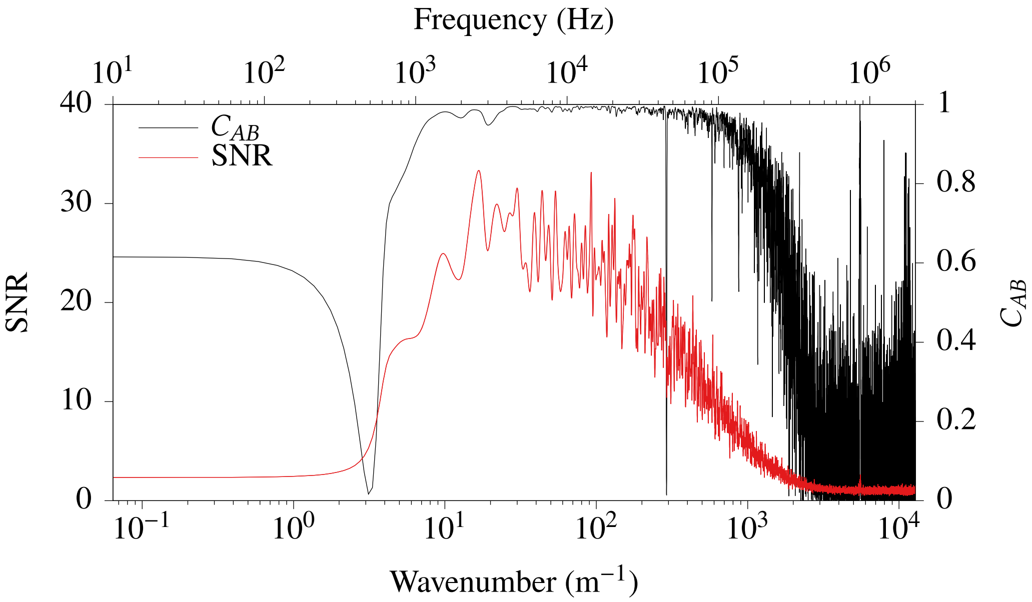

(b) Coherence and signal-to-noise ratio.

Figure 10.9: Spectrum of density fluctuations for Run 843, $t = 10-30$ ms with a von Kármán spectrum fit to the coherent portion of the experimental spectrum.

Close agreement between the free and $B = -5/3$ von Kármán spectrum fits was found, and as a result all further fitting routines were fixed to $B = -5/3$.

Power spectral density estimates using Welch's method for three selected 20 ms segments of flow data from Run 843 are presented in Fig. 10.10. These PSDs were created using Blackman windows of 2^{14} points wide with 90 % overlap and 2^{17} fft points. The von Kármán spectrum model was fitted to experimental data where the coherence was greater than 80 %.

In Fig. 10.10a the coherent segment of the spectra closely follows the von Kármán spectrum and no peaks in energy are observed. For the spectra presented in Fig. 10.10b and Fig. 10.10c, a strong peak is observed between 3 – 4 kHz, and a first harmonic of this content is also visible in Fig. 10.10b. Because the peaks have a significant impact on the von Kármán fit, the peaks were excluded from the fitting routine. The amplitude of the von Kármán spectra fit is higher for Fig. 10.10b and Fig. 10.10c than in Fig. 10.10a which indicates an increase in density perturbations at later flow times.

The integral scale of turbulence was identified as $L_0 = 28 - 29$ mm from the von Kármán spectrum fit and using $L_0 = 2\pi/k_0$. The transfer of energy from the energetic eddies ($L > L_0$) to successively smaller scales followed the classic $-5/3$ energy cascade, however signal intensity at high wavenumbers was not sufficient to identify the dissipative scales of turbulence.

The spectral content of the turbulent density fluctuations was found to change over time (Fig. 10.10), and therefore a spectrogram analysis was performed, the results of which are presented in Fig. 10.11. The spectrogram was created using Blackman windows of 5 ms width using 90 % overlap evaluated every 5 ms and windowed to the wavenumber range where greater than 80 % coherence was observed. Since this is plotted in the wavenumber domain, not the frequency domain, the 3 – 4 kHz content appears at 20 – 25 m^{-1}. This narrowband content begins at approximately 60 ms and is superimposed on a consistent background of broadband noise. A weak first harmonic of this fundamental is sometimes visible when viewed using a PSD such as in Fig. 10.10b, however the first harmonic is not always clear on the spectrogram.

Because there is a change in the intensity and frequency content of turbulent density

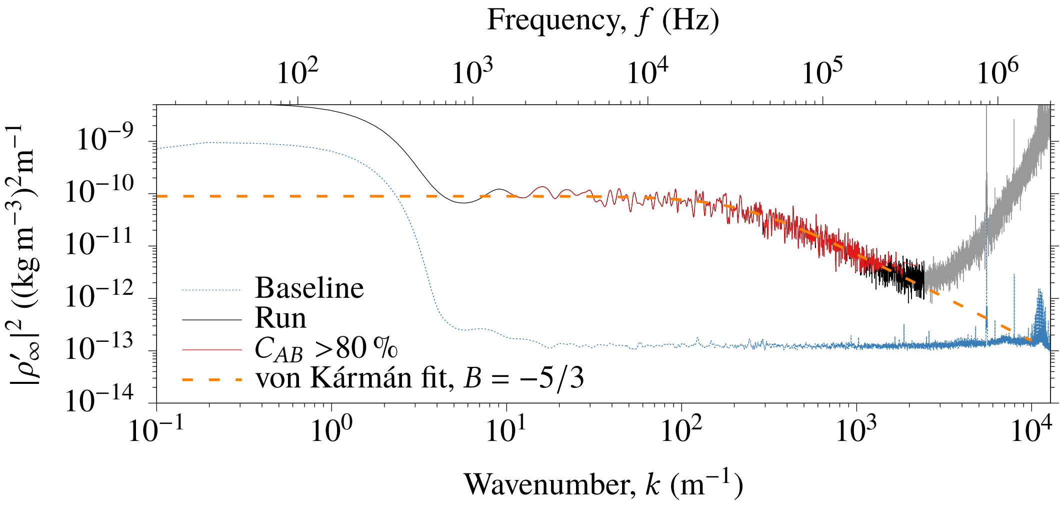

(a) $t = 10 - 30$ ms, $k_0 = 220.6\,\mathrm{m}^{-1}$, $L_0 = 28.5$ mm

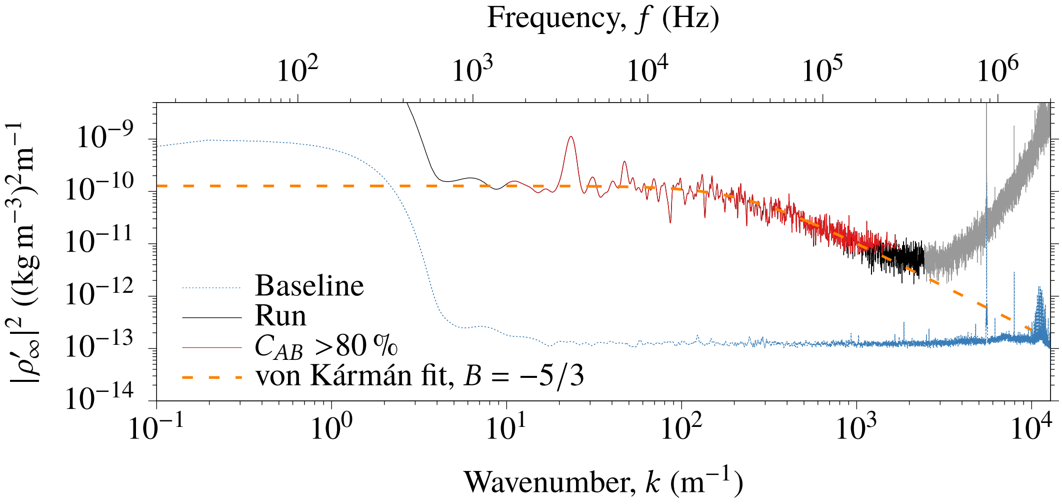

(b) $t = 100 - 120$ ms, $k_0 = 223.3\,\mathrm{m}^{-1}$, $L_0 = 28.1$ mm

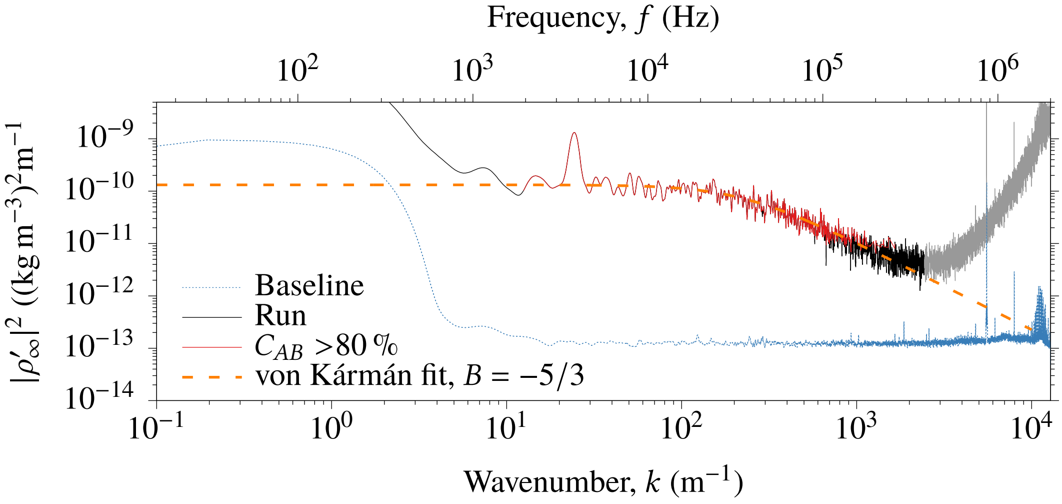

(c) $t = 160 - 180$ ms, $k_0 = 218.4\,\mathrm{m}^{-1}$, $L_0 = 28.8$ mm

Figure 10.10: Power spectral density plots of the density fluctuations for three periods of flow.

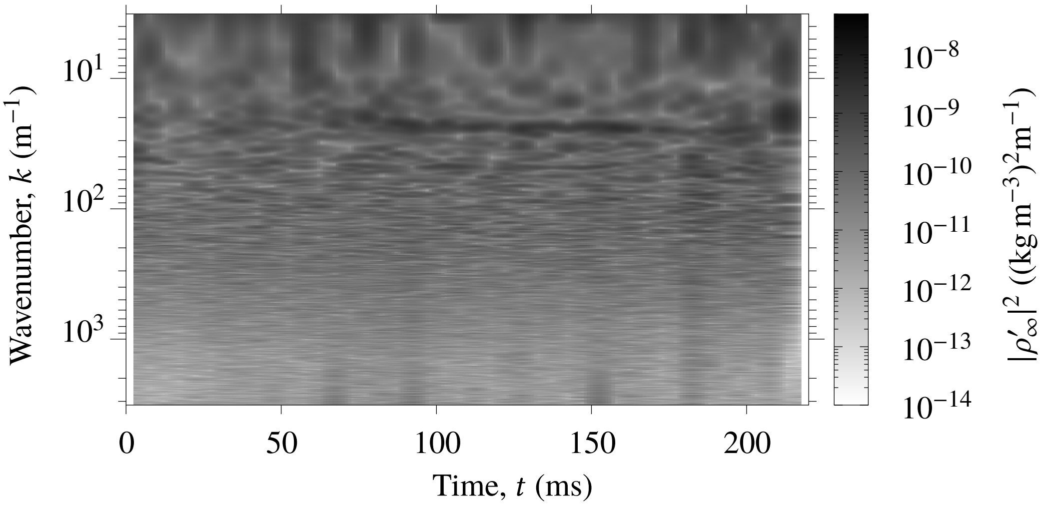

Figure 10.11: Spectrogram of density fluctuations showing how the turbulence changes throughout the flow.

fluctuations with time, and because the data is coherent in only a portion of the energy spectrum, defining the root-mean-square turbulent density fluctuations such that they can be identified from a frequency analysis is useful. The density-based turbulence intensity is calculable from a frequency analysis using (Fulghum, 2014):

$$TI_{\rho_\infty}\,(\%) = \frac{\langle \rho'_\infty \rangle}{\overline{\rho_\infty}} = \frac{1}{\overline{\rho_\infty}} \sqrt{\frac{1}{N^2} \sum_N \left| \frac{\lambda}{2\pi K_{GD} \Delta x} \frac{\mathcal{F}\left\{\Delta\varphi_A - \Delta\varphi_B\right\}}{H_{\Delta x}(k) H_z(k)} \right|^2} \times 100\% \tag{10.10}$$

Evaluating Eq. 10.10 in the range $1 \leq f \leq 250$ kHz for 5 ms periods every 5 ms, the root-mean-square turbulent density fluctuations can be shown to change over the run duration as shown by Fig. 10.12a. The RMS density fluctuations were repeatable across each run and all followed the same trends over time. Bandpass filtering the turbulent density fluctuations in the time domain to 1 – 250 kHz, the time-resolved density fluctuations are shown in Fig. 10.12b for Run 841. The change in intensity of ρ' at $t = 0$ on Fig. 10.12b shows the high SNR of the FLDI instrument for the measurement of density fluctuations in the low density ($\approx 34\,\mathrm{g\,m^{-3}}$) freestream flow. At $t = 180$ ms there is a sudden increase of the RMS density fluctuations in Fig. 10.12a which is also visible in the time-resolved signal of Fig. 10.12b.

Comparing Fig. 10.12a and Fig. 10.12b to the barrel pressure and temperature displayed in Fig. 10.12c, the density fluctuations can be viewed relative to the barrel pressure and stagnation temperature signals. The sudden increase of the turbulent density fluctuation amplitude at $t \approx 180\,\mathrm{ms}$ is visible as a sudden increase of ρ' in Fig. 10.10b, and the timing of this change is consistent with the colder gas in the barrel being expelled through the nozzle, and with the reflected expansion wave arriving at the nozzle inlet for the second time. However, because no similar sudden increase of density fluctuations occurred when the reflected expansion wave arrives at the nozzle inlet for the first time, it is concluded that the sudden increase in density fluctuations was actually due to the cold vortices being expelled through the nozzle. Note that the rate of temperature drop of an individual run is significantly more rapid than shown in Fig. 10.12c, which was calculated from the average of eight runs.

A high amplitude density fluctuation is apparent at $t = 0\,\mathrm{s}$ due to the nozzle starting effects. Following the start of the flow, $\langle \rho'_\infty \rangle / \overline{\rho_\infty}$ increases with time to $t \approx 60\,\mathrm{ms}$ and remains relatively constant until $t \approx 180\,\mathrm{ms}$ where a sudden increase in the amplitude of the turbulent density fluctuations is observed.

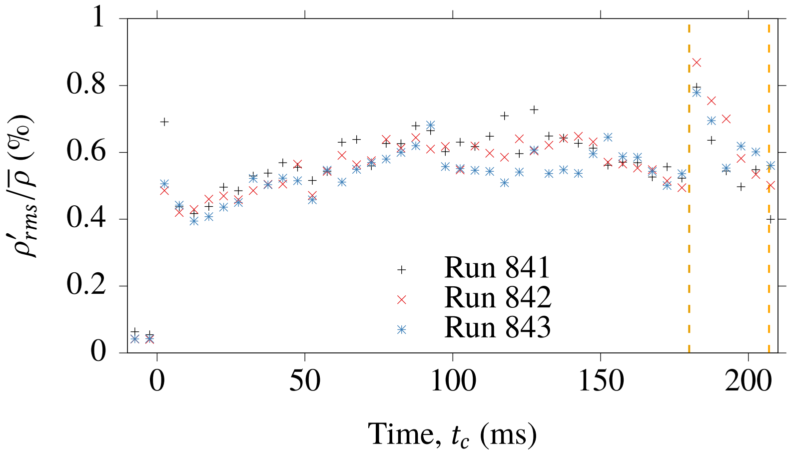

(a) Root-mean-square density fluctuations evaluated for 5 ms windows centred at t_c.

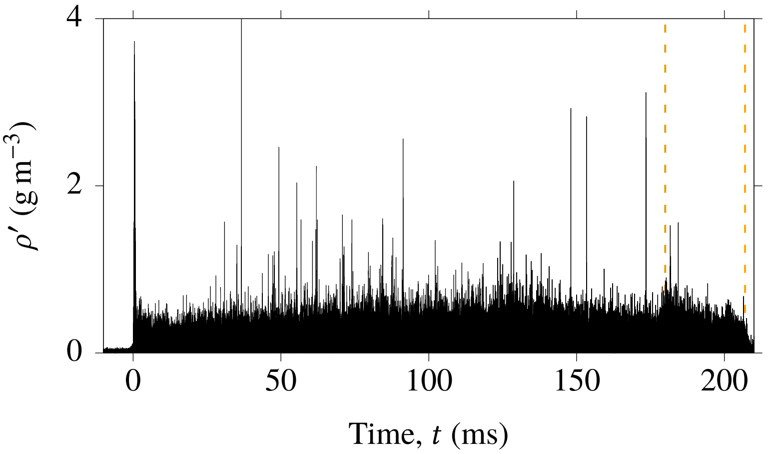

(b) Time-resolved density fluctuations for Run 841.

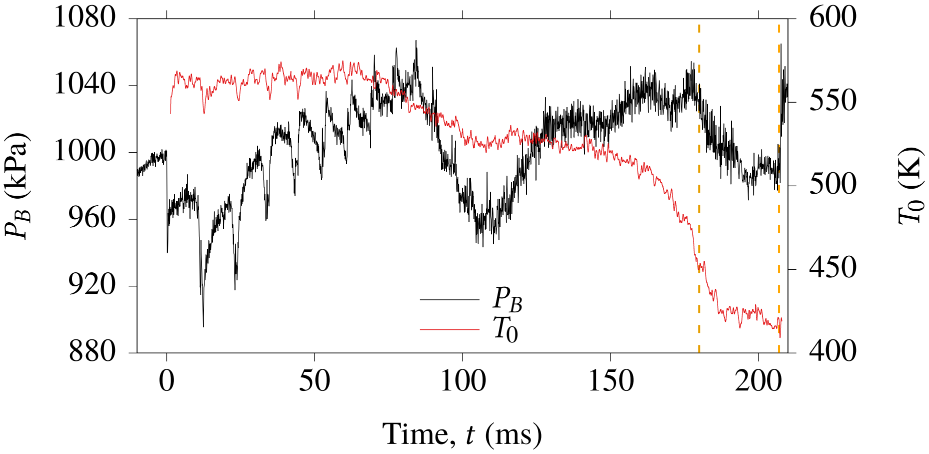

(c) Barrel pressure for Run 841, and the mean time-resolved total temperature identified in Chapter 7.

Figure 10.12: Comparison of density fluctuations, barrel pressure and total temperature.

10.7 Preliminary Measurements of a Boundary Layer on an Axisymmetric Body

10.7.1 Experiment Design

Following the investigation of the freestream disturbances using the FLDI instrument, the boundary layer on a cylindrical body (Fig. 10.13) was investigated as a demonstration of the capability of the instrument for future work in the TUSQ facility. A cylinder with a sharp conical nose with a half angle $\theta \approx 6.9°$, illustrated in Fig. 10.13, was manufactured to investigate laminar, transitional and turbulent boundary layer flows. For this capability demonstration, the FLDI beam and TUSQ nozzle were fixed in position and the model traversed axially. The focus of the FLDI beam was at the nozzle centreline, 25 mm downstream of the nozzle exit.

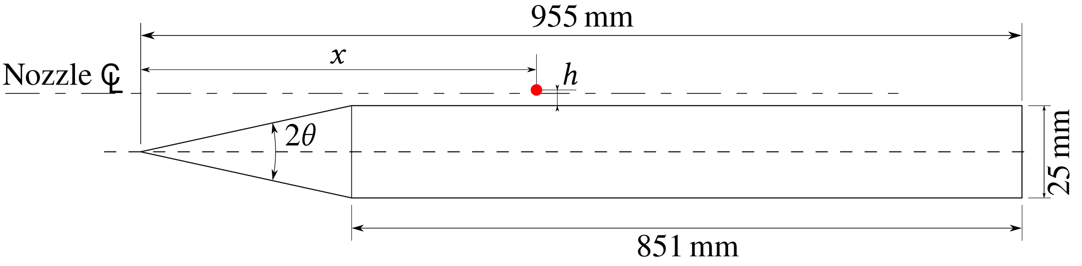

Figure 10.13: Schematic of model geometry.

The axis of the cylindrical model was positioned below the nozzle centreline axis such that the focus of the FLDI system was $h = 2.8$ mm above the model surface. The position of the nose of the cylindrical model varied from $x = 125 - 451$ mm ahead of the FLDI beam focus.

The eight locations listed in Table 10.1 were interrogated using the FLDI instrument. The thickness of a laminar boundary layer was calculated at each probe location for Mach 5.9 flow with a $Re_u = 7.16 \times 10^6\,\mathrm{m}^{-1}$. The model geometry was assumed to be better approximated by a flat plate model than a cone model, and therefore the thickness of the boundary layer calculated using (Van Driest, 1952)

$$\frac{y}{x}\sqrt{Re_x} = 13 \tag{10.11}$$

where Re_x is $Re_u \times x$.

The nozzle flow at the tip of the model nose was confirmed from CFD nozzle flow simulations (Chapter 4, Section 4.2) to be very similar for all locations interrogated (Fig. 10.14).

Location	x_n (mm)	x (mm)	Re_x	y (mm)
1	-100	125	896×10^3	1.7
2	-200	225	1.61×10^6	2.3
3	-222	247	1.77×10^6	2.4
4	-246	271	1.94×10^6	2.5
5	-274	299	2.14×10^6	2.7
6	-299	324	2.32×10^6	2.8
7	-352	377	2.70×10^6	3.0
8	-426	451	3.23×10^6	3.3

Table 10.1: Model locations and the estimated laminar boundary layer thickness at each location.

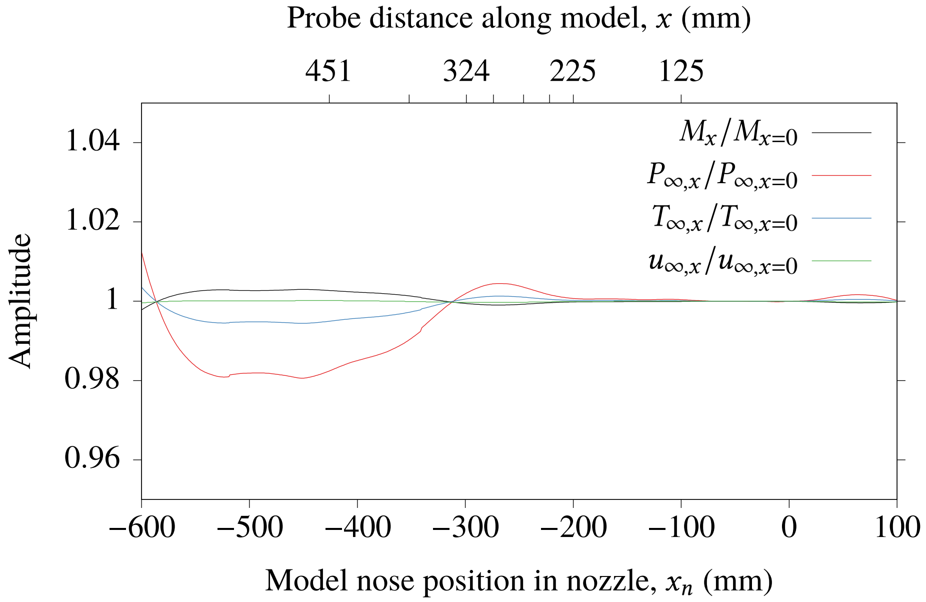

Figure 10.14: Computed flow conditions at the model nose, normalised by the value at the nozzle exit for $r = 15.3$ mm. The nozzle exit is at $x_n = 0$ mm.

10.7.2 Measurements of Phase Difference

For the preliminary study of the boundary layer on the sharp cylinder model, the transfer function $H_z(k)$ is different from that which was used for investigation of the freestream disturbances. A new $H_z(k)$ must be developed using the method proposed by Schmidt and Shepherd (2015), in combination with CFD. The convective velocity of the disturbances in the boundary layer has to be identified for calculation of k and therefore, for the purposes of the capability demonstration and presentation of preliminary data, the results are expressed without the transfer functions $H_z(k)$ and $H_{\Delta x}(k)$. The phase difference signal normalised by beam separation is:

$$\xi' = \frac{\mathrm{PSD}\{\Delta\varphi_A - \Delta\varphi_B\}}{\Delta x \cdot H_A(f) \cdot H_{PD}(f)} \tag{10.12}$$

Normalised phase difference data are presented for the eight positions along the boundary layer for three separate 20 ms periods within the flow duration in Fig. 10.15. The three periods were chosen because the stagnation conditions in the barrel are known to have different properties at these times. The three regions presented are:

1. $t = 5-25$ ms, where the stagnation temperature in the barrel is approximately the isentropic value and the fluctuations of temperature and pressure are broadband in nature (Fig. 10.15a);
2. $t = 80-100$ ms, where the stagnation temperature in the barrel is significantly less than the isentropic value, and a $3-4$ kHz narrowband peak of pressure, temperature and density fluctuation is embedded within a broadband noise environment (Fig. 10.15b); and
3. $t = 180-200$ ms, where the cold vortices propagating ahead of the piston are expelled through the nozzle (Fig. 10.15c).

Data where the SNR was approximately one were excluded from Fig. 10.15. When the boundary layer was identified as fully turbulent, the coherence of the two FLDI signals was over 80 % for frequencies up to 1.2 MHz.

At $x = 125$ mm and $h = 2.8$ mm the spectra were consistent with the freestream spectra. The laminar boundary layer thickness was calculated as 1.7 mm (Table 10.1). Therefore the FLDI probe location was concluded to be outside the boundary layer and data at $x = 125$ mm omitted from Fig. 10.15.

In Fig. 10.15a for $247 \leq x \leq 377$ mm, there is a growth and decay of a feature in the $100-200$ kHz frequency band. This feature is the second mode instability (also known as the Mack mode). The second mode instabilities drive the transition process (Wagner et al., 2018), increasing in amplitude before breaking down into turbulence (Parziale et al., 2015). These instabilities are focused on using inset (ii) of Fig. 10.15.

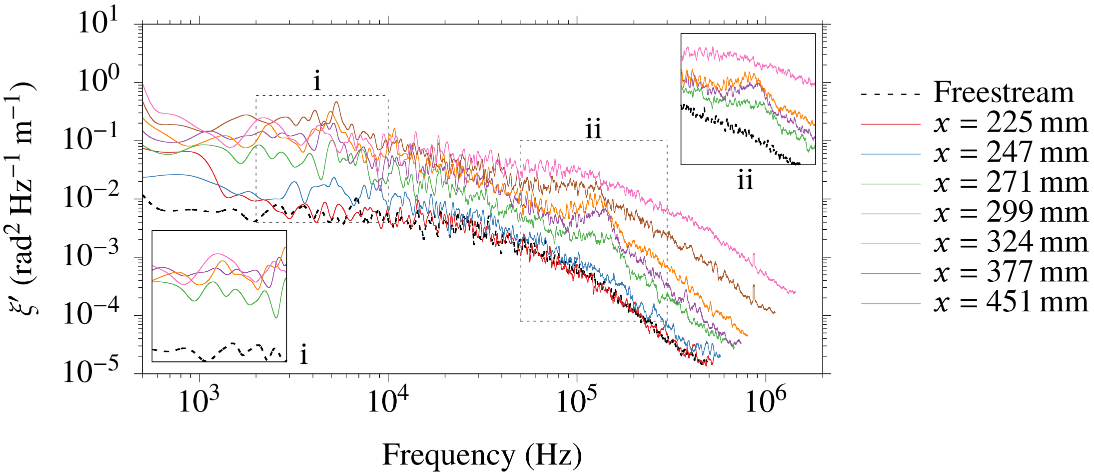

(a) $t = 5 - 25$ ms

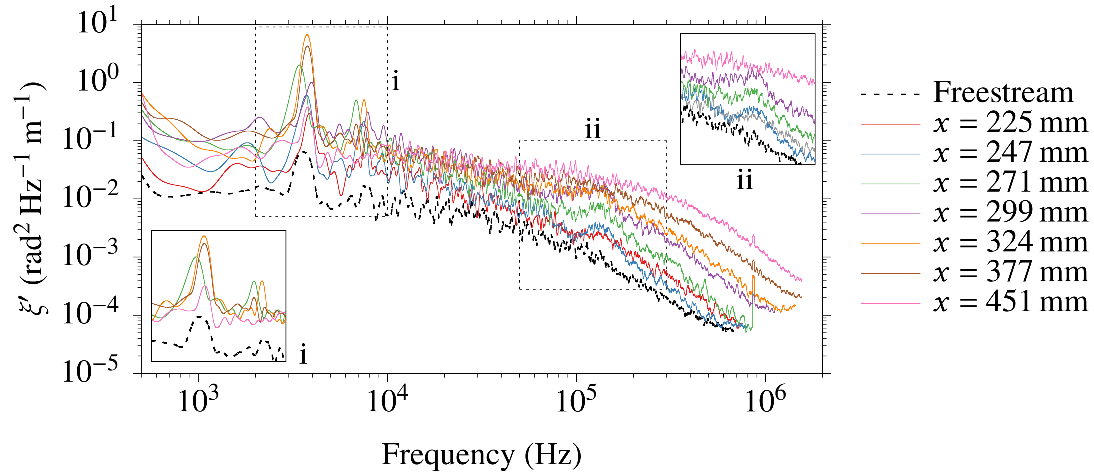

(b) $t = 80 - 100$ ms

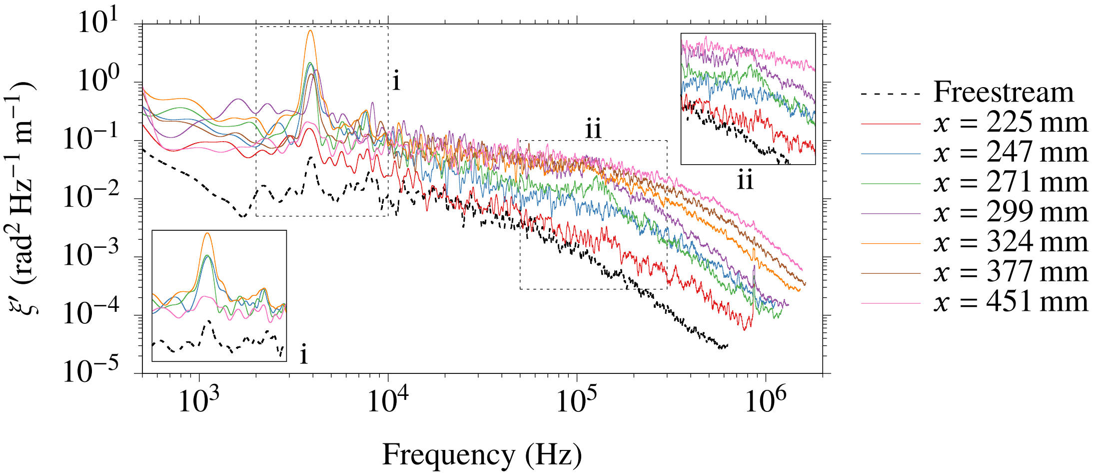

(c) $t = 180 - 200$ ms

Figure 10.15: Normalised phase difference fluctuations for boundary layer measurements on the axisymmetric body illustrated in Fig. 10.13. Insets of selected data- (i) focused on the 3 – 4 kHz disturbance region, and (ii) focused on the second mode instabilities.

The frequency of second mode instabilities (f^*) can be found analytically using

$$f^* = \frac{CU_e}{2\delta_{99}} \tag{10.13}$$

where C is a constant in the range of $0.4 < C < 1$, U_e is the flow velocity at the edge of the boundary layer, and δ_{99} is the thickness of the boundary layer (Bitter & Shepherd, 2015). Equation 10.13 shows that f^* is inversely proportional to the boundary layer thickness. Therefore, by estimating δ_{99} to be the thickness of the laminar boundary layer at each interrogated position (Table 10.1), the maximum value of f^* can be calculated. The theoretical frequency of the second mode instabilities at the experimentally interrogated locations are shown in Table 10.2 for the locations where these second mode instabilities were identified experimentally.

Location	2	3	4	5	6	7
x (mm)	225	247	271	299	324	377
y (mm)	2.3	2.4	2.5	2.9	2.8	3.0
f^* (kHz)	87–219	84–210	80–201	75–186	72–180	67–168

Table 10.2: Most unstable frequency of the second mode disturbances based on the laminar boundary layer thickness for the range $0.4 < C < 1$.

The transitional boundary layer (where the second mode was identified experimentally) is thicker than the laminar boundary layer, and therefore the f^* values are the maximum possible unstable frequencies. Since there is significant uncertainty for C, the upper bound for f^* is a reasonable maxima for the maximum unstable frequency in a transitional boundary layer. The frequency of the second mode instabilities measured in TUSQ on a sharpened cylinder model (Fig. 10.15) decrease with increasing boundary layer thickness, and the peak of the measured frequencies are in qualitative agreement with the predictions of f^* which are shown in Table 10.2. Because the second mode instabilities grow in a transitional boundary layer and decay to turbulence, these instabilities were used to identify if the FLDI beams were focused on a laminar, transitional or turbulent boundary layer.

For $t = 5-25$ ms, the boundary layer was transitional for $x = 247-377$ mm and fully turbulent at $x = 451$ mm. For $t = 80-100$ ms (Fig. 10.15b), the boundary layer was found to transition earlier than for $t = 5-25$ ms, with transition first measured at $x = 225$ mm. This earlier onset of transition led to a fully turbulent boundary layer being measured at $x = 377$ mm. For $t = 180-200$ ms (Fig. 10.15c), the boundary layer appears to be transitional at $x = 271$ mm and fully turbulent at $x = 324$ mm.

In Fig. 10.15a, there was no 3 – 4 kHz feature in the freestream measurement and therefore the feature does not appear in the boundary layer measurements. The 3 – 4 kHz feature is present in the freestream measurements for Fig. 10.15b and Fig. 10.15c, and this feature is shown more clearly using inset (i) for selected data. This feature is strongly amplified in the transitional boundary layer. When the boundary layer is turbulent (*i.e.*, at $x = 451$ mm), the 3 – 4 kHz feature is still present but at a much lower amplitude than for the transitional boundary layer. The first harmonic of the 3 – 4 kHz feature is clear in Fig. 10.15b and Fig. 10.15c, and the second harmonic can be observed in inset (i) of these figures.

An illustration of the changes in the PSD for the boundary layer flow over the full run duration is shown in Fig. 10.16 for $x = 324$ mm. The power spectral density estimates are for 20 ms periods of flow centred at t_c. A fundamental in the 3 – 4 kHz band is clear for $t_c \geq 50$ ms, and the second harmonic can be identified in some spectra. The regions of each spectra where Mack mode instabilities are evident have also been identified. For $t_c = 10 - 70$ ms and $t_c = 170$ ms there appears to be a small hump in the spectrum at about 300 kHz which is likely the first harmonic of the second mode instabilities, but this feature is weak and difficult to clearly identify. Because there were no second mode instabilities present for $t_c = 110$ ms and $t_c = 130$ ms, the boundary layer was identified as turbulent for these periods, demonstrating a degree of intermittent turbulence. The spectrum at $t_c = 190$ ms indicates a turbulent boundary layer was probed, and that this point in the boundary layer had more energy than the other spectra at high frequencies. This is suggested to be a function of the substantially colder nozzle flow for $t = 180$ ms – 200 ms, which may result in the earlier onset of transition than for the periods earlier in the test flow duration.

The 3 – 4 kHz feature was found to be strongly amplified in a transitional boundary layer, and this amplification is shown in Fig. 10.17 by tracing the peak amplitude of this feature for all runs. The amplitude of the peak was consistent for repeated runs at the same probe location. Second mode instabilities were detected for $247 \leq x \leq 377$ mm, and in this region the 3 – 4 kHz feature is strongly amplified. At $x = 451$ mm the boundary layer is turbulent, and the amplification of the 3 – 4 kHz is much less than for the measurements in the transitional boundary layer.

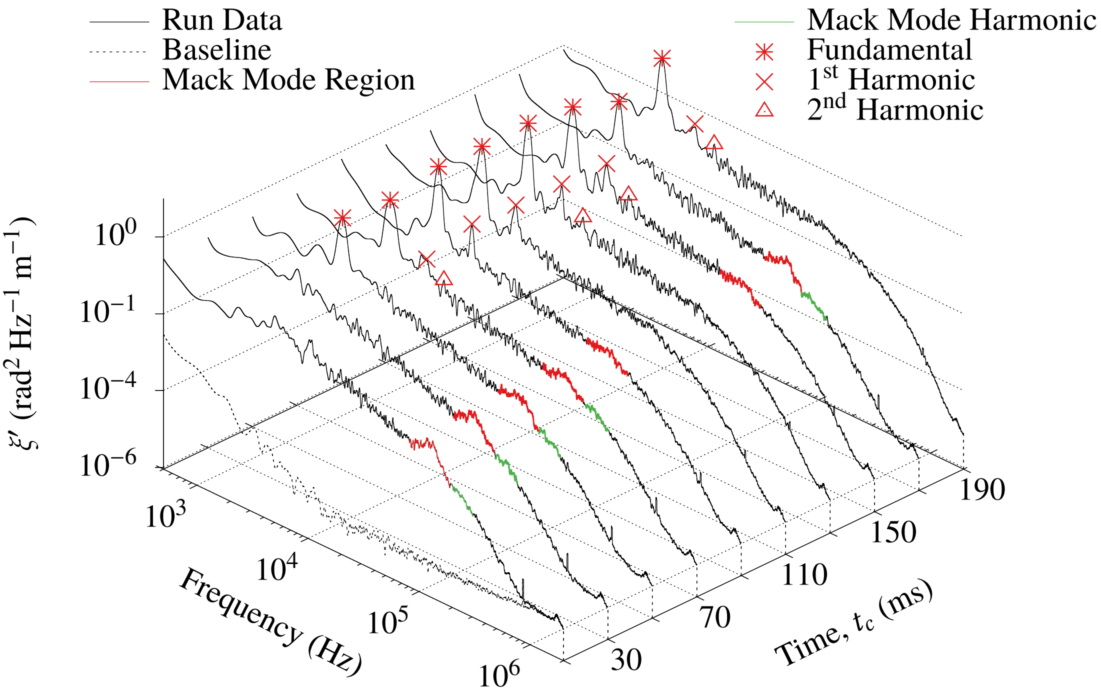

Figure 10.16: Array of phase difference spectra for Run 851, $x = 324$ mm. Spectra are for 20 ms duration centred at t_c and determined using Welch's power spectral density estimate.

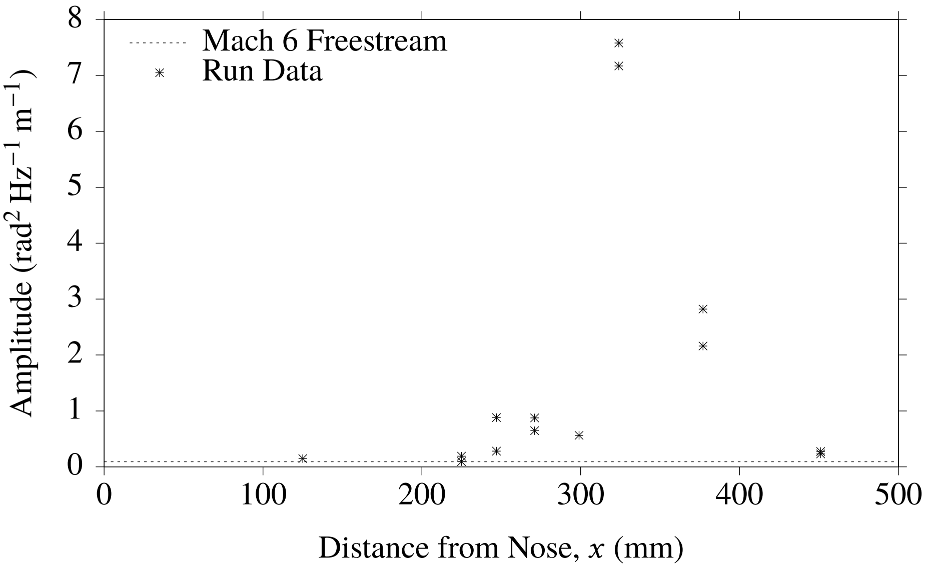

Figure 10.17: Peak amplitude of the PSD density fluctuations in the range of 3 – 4 kHz at positions along the model for $t = 120 – 140$ ms.

10.7.3 Future Work

The data presented for the sharp cylinder model were in terms of a fluctuating phase difference signal, not density fluctuations. This was because transfer functions for the path integration spatial filtering ($H_z(k)$) of the FLDI instrument were not implemented. Fulghum (2014) presented a $H_z(k)$ for a Gaussian profile disturbance which may be applicable here, however the geometry of the disturbance field will require investigation with CFD, and will need to consider the effects of the freestream disturbance field. The results of the CFD analysis would then be used with the tool proposed by Schmidt and Shepherd (2015) to develop the appropriate transfer function.

Complementary simultaneous high speed schlieren imaging of the boundary layer for qualitative comparison of the FLDI results is desirable. TUSQ has a high speed schlieren system, however it was obstructed by the FLDI instrument. Both instruments required their beams to pass horizontally through the test section. Reconfiguring the schlieren or the FLDI instrument such that the path of one of the diagnostics passes vertically through the test section would allow simultaneous measurements on axisymmetric models.

10.7.4 Conclusions

Preliminary measurements of a boundary layer on a sharp cylinder model demonstrated that second mode instabilities could be identified using FLDI in TUSQ. The 3 – 4 kHz disturbance present in the freestream from after $t \approx 65\,\mathrm{ms}$ was found to be strongly amplified in transitional boundary layers. The FLDI instrument at TUSQ was found to be able to resolve disturbances of greater than 1 MHz. Additionally, the analysis presented here provided insight into the results of the freestream FLDI measurements.

Chapter 11

Conclusion

Contents

11.1 Characterisation of TUSQ Flow

11.1.1 Overview

To determine time-averaged and fluctuating components of fundamental flow properties, the Mach 6 Ludwieg tube with free piston compression heating at the University of Southern Queensland was characterised using measurements of:

1. the pressure in the barrel;
2. the Pitot pressure in the freestream;
3. the stagnation temperature in the freestream; and
4. the density fluctuations in the freestream.

The operation of the facility was also numerically investigated using computational tools to validate experimental measurements and support the analysis of the experimental data.

11.1.2 Time-Averaged Flow

A core flow diameter in excess of 160 mm for the full hypersonic flow duration of approximately 200 ms was identified at the nozzle exit plane. At 50 mm downstream of the nozzle exit plane, the core flow diameter is greater than 160 mm for $t < 180$ ms. Run-to-run Pitot pressure variations are small; the standard deviation at the nozzle exit plane is less than 2 % for the full run duration, and at $x = 50$ mm the run-to-run changes are less than 3.5 % while the probe is measuring the core flow.

The Mach number was found to decrease over the flow duration from 5.95 to 5.85. Therefore, the Mach number over a full run can be specified as 5.90 ± 1% for a core flow diameter of at least 160 mm at the nozzle exit plane.

The time-averaged stagnation temperature was calculated using measurements of stagnation point heat flux, and was compared to calculations using two computational tools: (1) a quasi one dimensional flow solver (L1d3); and (2) an in-house TUSQ code based on the pressure history with an empirical correlation for the barrel heat transfer. As shown in Fig. 11.1, the L1d3 simulation showed excellent agreement with the experimental data for $t = 0 - 50$ ms and $t = 100 - 160$ ms. The results of the TUSQ code are within 2 % of the experimental data for $t = 0 - 150$ ms, increasing to 5 % at $t = 170$ ms. For $t > 170$ ms, cold vortices that propagate ahead of the piston which are not modelled in the TUSQ code increase the error of the simulation to 20 %.

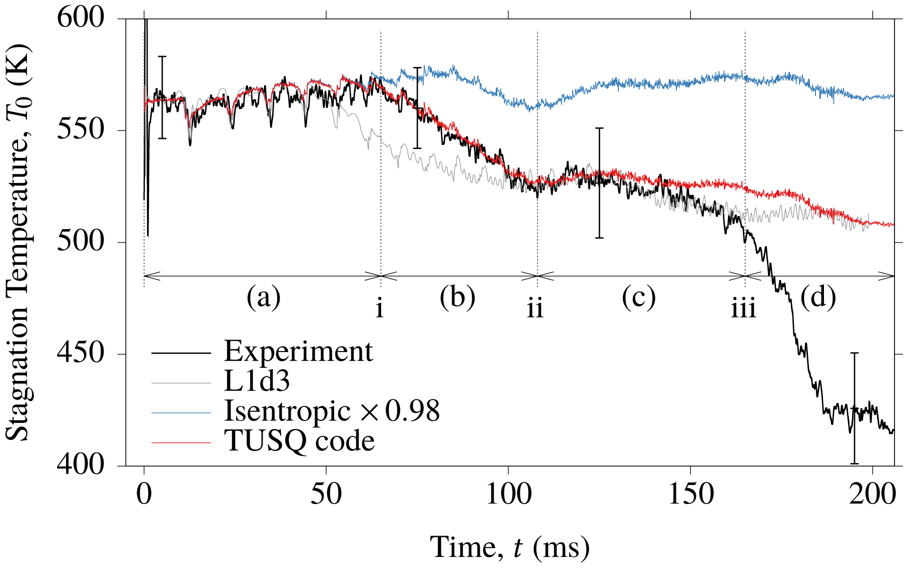

Figure 11.1: Time-averaged stagnation temperature.

Three events that cause large changes of the stagnation temperature were identified (Fig. 11.1):

i) a reduction in stagnation temperature, the onset of which is associated with the barrel boundary layer transitioning according to the flat plate heat loss model;
ii) a point where the heat lost to the barrel can be modelled using a turbulent flat plate correlation; and
iii) a time when cold vortical flow propagating ahead of the piston is expelled through the nozzle.

The experimental data was compared to the temperature calculated from the measured barrel pressure using isentropic flow relations, and four periods of flow were identified:

a) for $t = 0$ ms to feature (i), where T_0 is approximately 98 % of the isentropic stagnation temperature;
b) from feature (i) to (ii), where T_0 reduces at a rate of approximately 1100 K s^{-1};
c) from feature (ii) to (iii), where T_0 reduces slowly; and
d) from feature (iii) to the end of nozzle flow, where the cold vortices propagating ahead of the piston are expelled through the nozzle causing a large and sudden drop of stagnation temperature.

11.1.3 Fluctuations

In addition to the time-averaged Pitot pressure and stagnation temperature, the fluctuating components of these flow properties, and the fluctuating freestream density were measured. For all measurements, a 3 – 4 kHz disturbance which originates in the barrel was measured, initiated at approximately 65 ms after diaphragm rupture. The 3 – 4 kHz disturbance first appears at feature (i) in Fig. 11.1, and it is therefore concluded that the 3 – 4 kHz disturbance is likely related to the transitional and turbulent flow in the barrel which is expelled through the nozzle.

Pitot pressure fluctuations are a common measurement for characterisation of hypersonic facilities, and this measurement offers an insight into the acoustic noise environment. Because the characteristics of the flow changed during the run, it is appropriate to quote two RMS Pitot pressure fluctuation magnitudes in the 300 Hz to 25 kHz bandwidth:

1. $\langle P'_{pt} \rangle / \overline{P}_{pt} = 2.52\,\%$ for the period $t = 5 – 65$ ms, prior to the arrival of the narrowband 3 – 4 kHz content; and
2. $\langle P'_{pt} \rangle / \overline{P}_{pt} = 2.86\,\%$ for the period $t = 65 – 200$ ms, after the arrival of the narrowband 3 – 4 kHz content.

Period 1 is dominated by broadband noise, indicative of acoustic noise that is radiated from the turbulent boundary layer on the nozzle wall into the freestream. Period 2 is also dominated by broadband noise, but has a significant contribution from the 3 – 4 kHz disturbance that originates in the barrel.

Root-mean-square stagnation temperature fluctuations were evaluated for $f = 4\,\text{Hz} - 5\,\text{kHz}$. The onset of the 3 – 4 kHz disturbance was consistent with the onset identified by the Pitot pressure fluctuations. RMS fluctuations of stagnation temperature, $\langle T_0' \rangle / \overline{T}_0$, were observed to increase throughout the flow period, from approximately 1.5 % at the start of a run to 2.4 % at the end of a run. However, because there was a large amount of scatter (approximately ±0.5 %) in the stagnation temperature fluctuation results, there remains significant uncertainty in these magnitudes.

The fluctuating components of the freestream density were measured using a focused laser differential interferometer. Even in the low density environment ($\approx 34\,\text{g}\,\text{m}^{-3}$), a frequency dependent signal-to-noise ratio of up to 30 was possible.

The freestream density fluctuations were resolvable up to $f = 400\,\text{kHz}$, or $k \approx 1300\,\text{m}^{-1}$. This was sufficient for fitting a von Kármán spectrum to the data, and to demonstrate a $-5/3$ rolloff consistent with the Kolmogorov spectrum rolloff in the inertial subrange. Using the von Kármán spectrum fit, the integral scale of turbulence was found to be approximately 28 mm.

The RMS density fluctuations were evaluated for $f = 1 - 250$ kHz. In this range, the RMS density fluctuations increased with run time from $\langle \rho_\infty' \rangle / \overline{\rho}_\infty = 0.4\,\%$ at the start of the run to $\langle \rho_\infty' \rangle / \overline{\rho}_\infty = 0.6\,\%$ towards the end of a run.

The FLDI measurements resolved the 3 – 4 kHz disturbance without the presence of a normal shock, demonstrating that it is not a function of the geometry of the intrusive diagnostics. The presence and behaviour of this disturbance in the boundary layer on a sharp cylindrical body was investigated using FLDI. Laminar, transitional and turbulent boundary layers were measured and identified, and the 3 – 4 kHz freestream disturbance found to be strongly amplified in the transitional boundary layer. Second mode instabilities were also identified in the transitional boundary layer on the sharp cylindrical body.

11.2 PWK4 Characterisation

The stagnation region heat flux on a 50 mm diameter flat faced probe operated in a plasma wind tunnel (PWK4 at IRS) was determined using a new fast response heat flux gauge arrangement comprised of a surface junction thermocouple mounted behind a thin layer of PTFE.

The centreline heat flux measured by the fast response heat flux gauge was 404 kW m^{-2} ± 6 % across eight traverses of the plasma jet, which was significantly below the heat flux measured using the IRS calorimetric probe (929 kW m^{-2}). The fast response heat flux gauge was able to confirm a Gaussian-like distribution of heat flux across the plasma jet. This heat flux distribution was shown to be independent of the two different probe traverse speeds and traverse directions used.

Fluctuations of heat flux at frequencies from 4 Hz to 1 kHz were measured, and these fluctuations used to determine that heat flux variations of up to ± 60 kW m^{-2} exist near the vicinity of the nozzle centreline. Therefore, fluctuations of up to ± 15 % of the centreline heat flux exist in the plasma flow at the condition tested.

11.3 Diagnostics

11.3.1 Computational Tools

A method for modifying the initial condition of an L1d3 simulation to facilitate the implementation of gas slugs with non-uniform thermodynamic properties was developed. These L1d3 simulation efforts were moderately successful: there were regions of strong agreement with experimental barrel pressure and stagnation temperature measurements, however an expansion wave appeared in the simulation which corrupted the agreement between the experimental measurements and the simulation.

The existing in-house code for determining the flow stagnation temperature from the barrel pressure measurements was modified and extended. The extension was to pair the experimental barrel pressure measurements during nozzle flow with the total temperature predicted by the flat plate heat transfer model. This pairing identified that the critical Reynolds number had to be changed from 0.2×10^6 to 1×10^6 to better represent the transition process in the barrel. Computational results were within 2 % of the experimentally determined stagnation temperature for the first 150 ms of nozzle flow.

11.3.2 Pressure Measurements

A method for temporal alignment of the barrel pressure measurement and measurements of pressure in the hypersonic flow using the first reflected expansion wave was proposed. This method is an improvement on using the sudden drop in barrel pressure at diaphragm rupture and the first pressure increase registered in the test section. Similar methods of signal alignment can be used for other diagnostics used in TUSQ, and other similar piston-driven facilities.

11.3.3 Coaxial Surface Junction Thermocouples

Coaxial surface junction thermocouples were developed and used as the sensing element in the heat flux gauges used in TUSQ and PWK4. These thermocouples were made from a tapered pin and matching taper annulus, insulated by a thin oxide layer. The matching taper design theoretically allows the thermocouple to be resurfaced until the annulus is completely worn, as long as the gauge can be analysed as a semi-infinite solid. This extends the life well past what can be achieved by other designs identified in literature. The oxide insulating layer allows the thermocouple body to be heated to elevated temperatures well above what is possible with the common epoxy insulating and bonding method. The enhanced preheating capacity of the thermocouples used in TUSQ allowed the convective heat transfer coefficient to be determined experimentally. The grit size used to form the junctions was not found to be a reliable indicator of thermocouple response time, which was in the order of microseconds.

For use in PWK4, the thermocouples were electrically insulated from the plasma by a thin layer of PTFE. The heat flux gauge formed thereby was calibrated using a laser technique. The thermocouple was able to respond sufficiently fast to identify an overshoot of laser power which has not been previously accommodated in calibration work at IRS which was for much slower response time heat flux gauges.

A method of extrapolating the experimentally measured temperature to times longer than a calibration pulse was developed. This facilitates the experimental identification of a impulse response which is valid for a duration longer than the duration of the calibration experiment. Here, the impulse response for a heat flux gauge which was identified using a 50 ms calibration pulse was able to be extended, and used for test durations of up to 1.4 s. The extrapolation of the experimental calibration data is particularly useful for irradiative calibration methods where a high intensity heat flux may only be applied for a limited time.

11.3.4 Focused Laser Differential Interferometry

Fulghum (2014) showed that the Berek compensator in the FLDI instrument required calibration, because in their work the compensator performance was significantly different from the manufacturer supplied calibration. The Berek compensator was calibrated in this research, and this was found to match the manufacturer calibration when the compensator is properly aligned. A similar change in the performance of the Berek compensator from the standard manufacturer calibration to that reported by Fulghum (2014) was achieved by deliberately misaligning the Berek compensator.

The coherence spectrum for the two photodetector signals is improved by considering shorter periods of flow data, rather than the full run. The higher coherence increased the maximum resolvable wavenumber of the instrument.

Beam shrouds that deflect the turbulent shear layer (TSL) around the FLDI beams were implemented and found to significantly improve the measurements. These were a very important addition to the FLDI instrument at TUSQ, and allowed investigation of lower wavenumbers that would not normally be accessible to the FLDI instrument due to the effects of the TSL. The implementation of beam shrouds for the rejection of lower-wavenumber content away from the best focus of a focused laser differential interferometer is particularly useful for facilities where the f-number of the FLDI instrument is constrained by the geometry of the facility.

A preliminary study of the boundary layer on a sharp cylinder using FLDI was performed. Laminar, transitional and turbulent boundary layers were identified at different locations along the model, and at different times during the flow. The second mode instability was able to be identified in the transitional boundary layer, and in some cases a weak resonance of this instability was observed. The 3 – 4 kHz freestream disturbance was found to be strongly amplified in transitional boundary layer flows. The FLDI instrument designed was able to resolve density fluctuations in the boundary layer flow of up to 1 MHz.

11.4 Relevance of Characterisation Results for Other Research in TUSQ

The findings of the characterisation of the TUSQ freestream environment are relevant for a broad range of experiments, and particular highlights and implications are:

1. the ability to accurately reconstruct the flow stagnation temperature from the measured barrel pressure, which can be used for CFD and better simulations of experiments:
    - previously only time-varying pressure from experimental measurements and a calculated time-varying temperature based on the isentropic flow assumption have been used (Currao et al., 2016).
2. the fluctuations of Pitot pressure, stagnation temperature and freestream density can be used:
    - in CFD, such as direct numerical simulations (DNS), to better understand the impact of the freestream disturbance environment on experimental results;
    - for comparison to results from research in other facilities; and
    - to understand and justify any early onset transition on an experimental model when compared to numerical simulation and flight test results.
3. the discovery of the 3 – 4 kHz disturbance that originates in the barrel, which is particularly relevant to:
    - transition experiments, as evidenced by the strong amplification of this disturbance in the transitional boundary layer on a sharp cylinder model; and
    - fluid-structure interaction (FSI) studies, where Casper et al. (2018) demonstrated that in noisy flows, if a narrowband disturbance is matched to a modal frequency of a structure, the amplitude of the response can be an order of magnitude higher than when the narrowband disturbance is not present.

When transition or FSI experiments are performed in TUSQ, the experiment must be carefully designed to avoid structural modes in this bandwidth or, if this is unavoidable, recognise that only the results for the first 65 ms of flow are useful.

11.5 Future Research Directions

The numerical analysis of the TUSQ barrel compression process presented in Chapter 4, while being an insightful exercise in understanding the facility operation and for validation of experimental data, was limited by the current capabilities of the L1d3 code and computational resources. The capabilities of the `Eilmer4` code are currently being extended by researchers at the University of Queensland and the University of Southern Queensland, and collaborators from other institutions, with the goal of full facility simulations from the instant a run is triggered, through the compression processes and to the termination of the flow. The time between a run being triggered and the run conclusion is an order of magnitude longer in TUSQ than complementary high enthalpy facilities at UQ (T4 and X2). However, unlike the high enthalpy facilities, the cold flows of the TUSQ facility do not require resource intensive non-equilibrium gas state calculations and therefore require a computationally less intensive simulation. The time-resolved measurements of stagnation pressure, Pitot pressure and total temperature presented in this thesis offer an abundance of data critical for the validation of future simulations.

Higher bandwidth Pitot pressure fluctuation measurements can be performed. This could be achieved using PCB piezoelectric pressure transducers, or Kulite pressure transducers without the protective screens which then could then be used up to their resonance frequency at approximately 240 kHz. In the unscreened case, a wedge probe similar to that proposed by Wagner et al. (2018) would need to be used to protect the pressure transducer. However, the non-intrusive FLDI measurements did not identify narrowband density fluctuations for $f > 25$ kHz, and these measurements were used to identify turbulent length scales. Since lower frequencies dominate the RMS calculation, perhaps a better use of improved bandwidth pressure transducers would be surface pressure measurements for the identification of transitional boundary layers on cones and flat plates.

Methods for improving the signal-to-noise ratio for the coaxial surface junction thermocouples are a clear path for further research. Currently the thermocouple acts as an antenna and the output emf therefore contains a large amount of interference from sources such as AM radio stations and fluorescent light switching.

The effective thermal effusivity of the type E thermocouples was found to vary as junctions were lost, and as new junctions were formed. Reflected shock tube calibration requires a significant expenditure of time, and requires the thermocouple to be removed from a model. Developing a reliable, fast, convenient and portable method for in situ thermocouple calibration before and after a run is seen as a major, valuable contribution.

The coaxial surface junction thermocouples were well suited to measurement of stagnation point heat flux in TUSQ, and this suitability could be improved with further thermocouple and probe head miniaturisation to increase the signal since the stagnation heat flux at a surface increases as the effective head radius decreases. Implementing these thermocouples in physical models is a natural step which would facilitate improvements in heat flux measurements. With appropriate amplification and signal conditioning, small amplitude heat flux does not appear to be a barrier for this diagnostic.

The capability of the TUSQ facility is in the process of being extended by implementing a heated barrel configuration where temperature gradients in the barrel are to be used to maintain a constant flow total temperature, achieve higher enthalpy conditions and longer run times. This will require a large amount of data to tune and validate the stagnation temperature, and the rugged, fast response heat flux gauges developed are ideal for this purpose, especially when the heat flux gauges are preheated to near the flow total temperature.

Promising results were obtained in PWK4 for the measurement of heat flux fluctuations in a plasma jet, however the signal conditioning used limited the measurement of heat flux to frequencies less than 1 kHz. This work could be revisited with improved signal conditioning and data acquisition. Prior to repeating the PWK4 experiments, investigation of thin, electrically insulating but thermally conductive materials as an alternative to PTFE would be a valuable contribution, especially if the thickness of such materials could be ascertained in a non-destructive manner.

With a focused laser differential interferometer now amongst the diagnostic tools available at TUSQ the possibilities for future research are numerous. In the current configuration where the focusing ability of the instrument is somewhat limited by the test section geometry, the beam shrouds should be implemented to mechanically deflect the turbulent shear layer around the FLDI beams. Settles and Fulghum (2016) state that a multiplexed FLDI system could be used to determine true convective velocities, while a crossed beam arrangement could further improve the rejection of signals away from the best focus. However, there is significant room for improvement of, and research with, the single FLDI arrangement. Boundary layer instability measurements were made in this research and this instrument can be applied to the investigation of boundary layers on a variety of model geometries. It is here, rather than freestream measurements, where the current TUSQ FLDI system can be of most value due to the increased signal-to-noise ratio.

A diagnostic that was not widely used in this research was high speed schlieren imaging, and this was because of the limited capability of the LED light source currently used in the schlieren setup at TUSQ. The current LED system reaches a limit at a 10 μs exposure and 2500 Hz repetition rate; smaller exposure times or faster repetition rates are unable to emit enough light. However, the USQ Hypersonics Research Group has recently acquired a Cavitar Cavilux Smart UHS System which has yet to be commissioned. This illumination source will greatly improve the quality of the schlieren system for all experiments. Specific to the theme of this thesis, the schlieren system can be used to "freeze" the flow and investigate transitional boundary layers, such as on the sharp cone model investigated with FLDI. Global schlieren images will allow a researcher to quickly identify the location of transition, and track its movement over the flow duration. This information can be used to position the FLDI instrument, or validate the measurements. With a focused schlieren arrangement implemented in TUSQ, it would be an interesting test to see if the 3 – 4 kHz freestream disturbance can be imaged, either before or after a shock, or in a boundary layer flow.

References

Agarwal, S., Sahoo, N., Irimpan, K., Menezes, V. & Desai, S. (2017). Comparative Performance Assessments of Surface Junction Probes for Stagnation Heat Flux Estimation in a Hypersonic Shock Tunnel. *International Journal of Heat and Mass Transfer*, *114*, 748–757. doi:10.1016/j.ijheatmasstransfer.2017.06.109

Ali, S. R. C., Wu, J., Radespiel, R., Schilden, T. & Schroeder, W. (2014). High-Frequency Measurements of Acoustic and Entropy Disturbances in a Hypersonic Wind Tunnel. In *44th AIAA Fluid Dynamics Conference*. doi:10.2514/6.2014-2644

Auweter-Kurtz, M., Kurtz, H. & Laure, S. (1996). Plasma Generators for Re-entry Simulation. *Journal of Propulsion and Power*, *12*(6), 1053–1061. doi:10.2514/3.24143

Beckwith, I. E. (1975). Development of a High Reynolds Number Quiet Tunnel for Transition Research. *AIAA Journal*, *13*(3), 300–306. doi:10.2514/3.49695

Birch, B., Buttsworth, D., Choudhury, R. & Stern, N. (2018). Characterization of a Ludwieg Tube with Free Piston Compression Heating in Mach 6 Configuration. In *22nd AIAA International Space Planes and Hypersonics Systems and Technologies Conference*. doi:10.2514/6.2018-5266

Birch, T., Prince, S., Ludlow, D. & Qin, N. (2001). The Application of a Parabolized Navier-Stokes Solver to Some Hypersonic Flow Problems. In *International Space Planes and Hypersonic Systems and Technologies Conferences* (Vol. 1753, p. 2001). doi:10.2514/6.2001-1753

Biss, M. M., Settles, G. S., Staymates, M. E. & Sanderson, S. R. (2008). Differential Schlieren-Interferometry with a Simple Adjustable Wollaston-Like Prism. *Applied Optics*, *47*(3), 328. doi:10.1364/ao.47.000328

Bitter, N. P. & Shepherd, J. E. (2015). Stability of Highly Cooled Hypervelocity Boundary Layers. *Journal of Fluid Mechanics*, *778*, 586–620. doi:10.1017/jfm.2015.358

Blanchard, A. E., Lachowicz, J. T. & Wilkinson, S. P. (1997). NASA Langley Mach 6 Quiet Wind-Tunnel Performance. *AIAA Journal*, *35*(1), 23–28. doi:10.2514/2.82

Bounitch, A., Lewis, D. & Lafferty, J. (2011). Improved Measurements of "Tunnel Noise" Pressure Fluctuations in the AEDC Hypervelocity Wind Tunnel No. 9. In *49th AIAA Aerospace Sciences Meeting Including the New Horizons Forum and Aerospace Exposition*. doi:10.2514/6.2011-1200

Buttsworth, D. R. & Jones, T. V. (1998). A Fast-Response Total Temperature Probe For Unsteady Compressible Flows. *Journal of Engineering for Gas Turbines and Power*, *120*(4), 694. doi:10.1115/1.2818456

Buttsworth, D. R. (2001). Assessment of Effective Thermal Product of Surface Junction Thermocouples on Millisecond and Microsecond Time Scales. *Experimental Thermal and Fluid Science*, *25*(6), 409–420. doi:10.1016/s0894-1777(01)00093-0

Buttsworth, D. R. (2010). Ludwieg Tunnel Facility with Free Piston Compression Heating for Supersonic and Hypersonic Testing. In *Proceedings of the 9th Australian Space Science Conference* (pp. 153–162). National Space Society of Australia Ltd.

Buttsworth, D. R., Stern, N. & Choudhury, R. (2017). A Demonstration of Hypersonic Pitching Control in the TUSQ Hypersonic Wind Tunnel. In *55th AIAA Aerospace Sciences Meeting*. doi:10.2514/6.2017-0261

Buttsworth, D. R. & Jacobs, P. A. (2000). Measurement of Fluctuations in a Mach 4 Shock Tunnel Nozzle Flow. In *Proceedings of 7th Australasian Heat & Mass Transfer Conference* (pp. 53–59). James Cook University, Townsville.

Buttsworth, D. R. & Jacobs, P. A. (1998). Total Temperature Measurements in a Shock Tunnel Facility. In *13th Australian Fluid Mechanics Conference* (pp. 51–54).

Buttsworth, D. R. & Jones, T. V. (2003). High Bandwidth Stagnation Temperature Measurements in a Mach 6 Gun Tunnel Flow. *Experimental Thermal and Fluid Science*, *27*(2), 177–186. doi:10.1016/s0894-1777(02)00281-9

Buttsworth, D. R. & Smart, M. K. (2010). Development of a Ludwieg Tube with Free Piston Compression Heating for Scramjet Inlet Starting Experiments. In *48th AIAA Aerospace Sciences Meeting Including the New Horizons Forum and Aerospace Exposition, Aerospace Sciences Meetings*. doi:10.2514/6.2010-588

Casper, K. M., Beresh, S. J., Henfling, J. F., Spillers, R. W., Pruett, B. O. M. & Schneider, S. P. (2016). Hypersonic Wind-Tunnel Measurements of Boundary-Layer Transition on a Slender Cone. *AIAA Journal*, *54*(4), 1250–1263. doi:10.2514/1.j054033

Casper, K. M., Beresh, S. J., Henfling, J., Spillers, R., Hunter, P. & Spitzer, S. (2018). Hypersonic Fluid-Structure Interactions on a Slender Cone. In *2018 AIAA Aerospace Sciences Meeting*. doi:10.2514/6.2018-1825

Casper, K., Beresh, S., Henfling, J., Spillers, R., Pruett, B. & Schneider, S. (2009). Hypersonic Wind-Tunnel Measurements of Boundary-Layer Pressure Fluctuations. In *39th AIAA Fluid Dynamics Conference*. doi:10.2514/6.2009-4054

Cengel, Y. A. & Boles, M. A. (2007). *Thermodynamics: An Engineering Approach Sixth Edition (SI Units)*. McGraw Hill Higher Education.

Chaudhry, R. S. & Candler, G. V. (2016). Recovery of Freestream Acoustic Disturbances from Stagnation Pressure Spectrum in Hypersonic Flow. In *54th AIAA Aerospace Sciences Meeting*. doi:10.2514/6.2016-2059

Clutter, D. W. & Smith, A. M. O. (1965). Machine Calculation of Compressible Laminar Boundary Layers. *AIAA Journal*, *3*(4), 639–647. doi:10.2514/3.2940

Currao, G., Neely, A. J., Buttsworth, D. R. & Choudhury, R. (2016). Measurement and Simulation of Hypersonic Fluid-Structural Interaction on a Cantilevered Plate in a Mach 6 Flow. In *15th Dynamics Specialists Conference*. American Institute of Aeronautics and Astronautics. doi:10.2514/6.2016-1088

Davis, H. J. & Curchack, H. D. (1969). *Shock Tube Techniques and Instrumentation* (tech. rep. No. TR-1429). Harry Diamond Laboratories.

DET100A2 Large Area Si Biased Detector User Guide Rev A. (2017). Thorlabs.

Dodge, M. J. (1984). Refractive Properties of Magnesium Fluoride. *Applied Optics*, *23*(12), 1980–1985. doi:10.1364/ao.23.001980

Doolabh, A. (2016). *A Concept Study for a Piston Driven CO_2 Turbine Test Facility* (Bachelor's Thesis, University of Queensland).

Doorly, J. & Oldfield, M. (1987). The Theory of Advanced Multilayer Thin Film Heat Transfer Gauges. *International Journal of Heat and Mass Transfer*, *30*(6), 1159–1168. doi:10.1016/0017-9310(87)90045-7

Duan, L., Choudhari, M. M., Chou, A., Munoz, F., Radespiel, R., Schilden, T., ... Schneider, S. P. (2019). Characterization of Freestream Disturbances in Conventional Hypersonic Wind Tunnels. *Journal of Spacecraft and Rockets*, *56*(2), 357–368. doi:10.2514/1.a34290

East, R. & Qasrawi, A. (1978). *A Long Stroke Isentropic Free Piston Hypersonic Wind Tunnel*. Aeronautical Research Council, Reports and Memoranda, R & M No. 3844. H.M. Stationery Office.

Eremenko, P., Mouton, C. & Hornung, H. (2003). The Wave Drag of Blunted Cones in Axisymmetric Supersonic Flow. In *41st Aerospace Sciences Meeting and Exhibit*. American Institute of Aeronautics and Astronautics. doi:10.2514/6.2003-1269

Estorf, M., Wolf, T. & Radespiel, R. (2005). Experimental and Numerical Investigations on the Operation of the Hypersonic Ludwieg Tube Braunschweig, In *Fifth European Symposium on Aerothermodynamics for Space Vehicles* (Vol. 563, pp. 579–586).

Fay, J. A. & Kemp, N. H. (1965). Theory of Heat Transfer to a Shock-Tube End-Wall from an Ionized Monatomic Gas. *Journal of Fluid Mechanics*, *21*(4), 659–672. doi:10.1017/s002211206500040x

Fulghum, M. R. (2014). *Turbulence Measurements in High-Speed Wind Tunnels Using Focused Laser Differential Interferometry* (Doctoral dissertation, Pennsylvania State University).

Gatowski, J. A., Smith, M. K. & Alkidas, A. C. (1989). An Experimental Investigation of Surface Thermometry and Heat Flux. *Experimental Thermal and Fluid Science*, *2*(3), 280–292. doi:10.1016/0894-1777(89)90017-4

Gollan, R. & Jacobs, P. (2013). About the Formulation, Verification and Validation of the Hypersonic Flow Solver Eilmer. *International Journal for Numerical Methods in Fluids*, *73*(1), 19–57. doi:10.1002/fld.3790

Greenwood, R. T. (2014). *Measurements of Entropy-Layer Instabilities Over Cone-Ogive-Cylinders at Mach 6* (Doctoral dissertation, Purdue University).

Grossir, G., Masutti, D. & Chazot, O. (2015). Flow Characterization and Boundary Layer Transition Studies in VKI Hypersonic Facilities. In *53rd AIAA Aerospace Sciences Meeting*. doi:10.2514/6.2015-0578

Harris, F. (1978). On the Use of Windows for Harmonic Analysis with the Discrete Fourier Transform. *Proceedings of the IEEE*, *66*(1), 51–83. doi:10.1109/proc.1978.10837

Heitmann, D., Röediger, T., Kähler, C., Knauss, H., Radespiel, R. & Krämer, E. (2008). Disturbance-Level and Transition Measurements in a Conical Boundary Layer at Mach 6. In *6th AIAA Aerodynamic Measurement Technology and Ground Testing Conference* (Vol. 3951). doi:10.2514/6.2008-3951

Herdrich, G., Löhle, S., Petkow, D. & Fasoulas, S. (2010). Ground Testing Facilities and Modeling Tools: Research Examples. In *Fluid Dynamics and Co-located Conferences*. American Institute of Aeronautics and Astronautics. doi:10.2514/6.2010-4339

Hirsch, C. (2007). *Numerical Computation of Internal and External Flows: The Fundamentals of Computational Fluid Dynamics*. Butterworth-Heinemann.

Hufgard, F., Loehle, S., von Wolfersdorf, J., Fasoulas, S., Rocher, M. E., Hermann, T. A., . . . Steelant, J. (2019). Surface Heat Flux Measurement in Transpiration-Cooled Porous Materials using Plenum Pressure Data. In *AIAA SciTech 2019 Forum*. doi:10.2514/6.2019-2062

Ito, T., Randall, L. A. & Schneider, S. P. (2001). Effect of Noise on Roughness-Induced Boundary-Layer Transition for Scramjet Inlet. *Journal of Spacecraft and Rockets*, *38*(5), 692–698. doi:10.2514/2.3754

Jacobs, P. (1998). *Shock Tube Modelling with L1d* (No. 13/98). University of Queensland.

Jacobs, P. (2005). *Using l_script to Define L1d Simulations* (No. 2005-09). University of Queensland.

Jacobs, P. & Gollan, R. (2016). Implementation of a Compressible-Flow Simulation Code in the D Programming Language. *Applied Mechanics and Materials*, *846*, 54–60. doi:10.4028/www.scientific.net/amm.846.54

James, C. M., Birch, B. J. C., Smith, D. R., Cullen, T. G., Millard, T., Vella, S., . . . Buttsworth, D. R. (2019). Testing of Ultra Fast Response, Durable Co-axial Thermocouples for High Enthalpy Impulse Facilities. In *2019 AIAA Aviation and Aeronautics Forum and Exposition*. doi:10.2514/6.2019-3007

Jones, T., Schultz, D. & Hendley, A. (1973). *On the Flow in an Isentropic Light Piston Tunnel*. Aeronautical Research Council, Reports and Memoranda, R & M No. 3731.

Karel, J. (2009). *A Wavelet Approach to Cardiac Signal Processing for Low-Power Hardware Applications* (Doctoral dissertation, Maastricht University, Netherlands).

Kegerise, M. A. & Rufer, S. J. (2016). Unsteady Heat-Flux Measurements of Second-Mode Instability Waves in a Hypersonic Boundary Layer. In *AIAA SciTech Forum* (Vol. 57, p. 130). doi:10.2514/6.2016-0357

Kelly, R. (2015). *Differential Interferometry of Hypersonic Flow* (Bachelor's Thesis, University of Queensland).

Kemp, N., Rose, P. & Detra, R. (1959). Laminar Heat Transfer Around Blunt Bodies in Dissociated Air. *Journal of the Aerospace Sciences*, *26*(7), 421–430. doi:10.2514/8.8128

Kennell, C., Neely, A. J., Buttsworth, D. R., Choudhury, R. & Tahtali, M. (2016). Free Flight Testing in Hypersonic Flows: HEXAFLY-INT EFTV. In *54th AIAA Aerospace Sciences Meeting*. doi:10.2514/6.2016-1152

Kimmel, R. L., Borg, M. P., Jewell, J. S., Lam, K.-Y., Bowersox, R. D., Srinivasan, R., . . . Mooney, T. (2017). AFRL Ludwieg Tube Initial Performance. In *55th AIAA Aerospace Sciences Meeting*. doi:10.2514/6.2017-0102

Kimmel, R. L. & Poggie, J. (2000). Effect of Total Temperature on Boundary-Layer Stability at Mach 6. *AIAA Journal*, *38*(9), 1754–1755. doi:10.2514/2.1164

Kolmogorov, A. N. (1941). The Local Structure of Turbulence in Incompressible Viscous Fluid for Very Large Reynolds Numbers. *C. R. Acad. Sci. URSS*, *30*, 301–305.

Kovásznay, L. S. (1953). Turbulence in Supersonic Flow. *Journal of the Aeronautical Sciences*, *20*(10), 657–674. doi:10.2514/8.2793

Kraetzig, B., Buttsworth, D. R., Zander, F. & Löhle, S. (2015). Temperature and Heat Flux Measurement on Hot Models in Short-Duration Facilities. *Journal of Thermophysics and Heat Transfer*, *29*(1), 37–46. doi:10.2514/1.t4309

Laderman, A. J. (1977). Review of Wind-Tunnel Freestream Pressure Fluctuations. *AIAA Journal*, *15*(4), 605–608. doi:10.2514/3.7353

Lafferty, J. & Norris, J. (2007). Measurements of Fluctuating Pitot Pressure, "Tunnel Noise," in the AEDC Hypervelocity Wind Tunnel No. 9. In *2007 U.S. Air Force T&E Days*. doi:10.2514/6.2007-1678

Laufer, J. (1961). Aerodynamic Noise in Supersonic Wind Tunnels. *Journal of the Aerospace Sciences*, *28*(9), 685–692. doi:10.2514/8.9150

Laufer, J. (1954). Factors Affecting Transition Reynolds Numbers on Models in Supersonic Wind Tunnels. *Journal of the Aeronautical Sciences*, *21*(7), 497–498. doi:10.2514/8.3095

Laure, S. (1998). *Experimentelle Simulation der Staupunktströmung wiedereintretender Raumflugkörper und deren Charakterisierung mittels mechanischer Sonden* (Dissertation, Universität Stuttgart, Institut für Raumfahrtsysteme).

Lein, S. (2016). *Entwicklung eines auf Emissionsspektroskopie basierenden Sensorsystems zum Einsatz auf Wiedereintrittsplattformen* (Doctoral dissertation, Universität Stuttgart).

Leslie, J. D. & Marren, D. E. (2009). Hypersonic Test Capabilities Overview. In *U.S. Air Force T&E Days*. doi:10.2514/6.2009-1702

Liebert, C. H. & Hibbard, R. R. (1970). *Spectral Emittance of Soot*. NASA.

Logan, P. (1988). Modal Analysis of Hot-Wire Measurements in Supersonic Turbulence. In *26th Aerospace Sciences Meeting*. American Institute of Aeronautics and Astronautics. doi:10.2514/6.1988-423

Löhle, S. (2006). *Untersuchung von Wiedereintrittsplasmen mit Hilfe laserinduzierter Fluoreszenzmessungen* (Dissertation, Universität Stuttgart, Institut für Raumfahrsysteme).

Löhle, S. & Fuchs, U. (2012). Radial Heat Flux Profile Measurements in High Enthalpy Plasma Flows using Calibrated Miniaturized Sensors. In *43rd AIAA Thermophysics Conference* (p. 3103). doi:10.2514/6.2012-3103

Löhle, S., Nawaz, A., Herdrich, G., Fasoulas, S., Martinez, E. & Raiche, G. (2016). Comparison of Heat Flux Gages for High Enthalpy Flows - NASA Ames and IRS. In *46th AIAA Thermophysics Conference, AIAA Aviation Forum*. doi:10.2514/6.2016-4422

Lu, F. K. & Marren, D. E. (2002). Hypersonic Ground Test Requirements. In *Advanced Hypersonic Test Facilities* (pp. 1–15). doi:10.2514/5.9781600866678.0001.0015

Ma, Y. & Zhong, X. (2005). Receptivity of a Supersonic Boundary Layer Over a Flat Plate. Part 3. Effects of Different Types of Free-Stream Disturbances. *Journal of Fluid Mechanics*, *532*, 63–109. doi:10.1017/s0022112005003836

Mack, L. M. (1986). *Boundary-Layer Stability Analysis for Sharp Cones at Zero Angle-of-Attack*. California Institute of Technology Pasadena Jet Propulsion Laboratory.

Mack, L. M. (1987). Stability of Axisymmetric Boundary Layers on Sharp Cones at Hypersonic Mach Numbers. In *19th AIAA, Fluid Dynamics, Plasma Dynamics, and Lasers Conference*. doi:10.2514/6.1987-1413

Mahrle, A. & Beyer, E. (2009). Theoretical Aspects of Fibre Laser Cutting. *Journal of Physics D: Applied Physics*, *42*(17), 175507. doi:10.1088/0022-3727/42/17/175507

Mai, C. L. N. (2014). *Near-Region Modification of Total Pressure Fluctuations by a Normal Shock Wave in a Low-Density Hypersonic Wind Tunnel* (Doctoral dissertation, Texas A & M University).

Maicke, B., Barber, T. & Majdalani, J. (2010). Evaluation of CFD Codes for Hypersonic Flow Modeling. In *46th AIAA/ASME/SAE/ASEE Joint Propulsion Conference & Exhibit*. doi:10.2514/6.2010-7184

Marineau, E. & Hornung, H. (2009). Modeling and Calibration of Fast-Response Coaxial Heat Flux Gages. In *47th AIAA Aerospace Sciences Meeting including The New Horizons Forum and Aerospace Exposition, Aerospace Sciences Meetings*. doi:10.2514/6.2009-737

Marineau, E., Lewis, D., Smith, M., Lafferty, J., White, M. & Amar, A. (2013). Investigation of Hypersonic Laminar Heating Augmentation in the Stagnation Region. In *51st AIAA Aerospace Sciences Meeting including the New Horizons Forum and Aerospace Exposition*. doi:10.2514/6.2013-308

Masutti, D., Spinosa, E., Chazot, O. & Carbonaro, M. (2012). Disturbance Level Characterization of a Hypersonic Blowdown Facility. *AIAA Journal*, *50*(12), 2720–2730. doi:10.2514/1.j051502

McKenzie, J. F. & Westphal, K. O. (1968). Interaction of Linear Waves with Oblique Shock Waves. *Physics of Fluids*, *11*(11), 2350. doi:10.1063/1.1691825

Mohammed, H., Salleh, H. & Yusoff, M. Z. (2009). An Experimental Method for Effusivity Determination of Different Scratched Temperature Sensors. In *2009 3rd International Conference on Energy and Environment (ICEE)* (pp. 240–250). doi:10.1109/ICEENVIRON.2009.5398639

Morkovin, M. V. (1959). On Supersonic Wind Tunnels with Low Free-Stream Disturbances. *Journal of Applied Mechanics*, *26*(3), 319–323.

Morkovin, M. V. (1957). On Transition Experiments at Moderate Supersonic Speeds. *Journal of the Aeronautical Sciences*, *24*(7), 480–486. doi:10.2514/8.3887

Nawaz, A., Loehle, S., Herdrich, G. & Martinez, E. R. (2013). Comparison of Calorimetric Sensors - NASA Ames and IRS. In *44th AIAA Thermophysics Conference*. American Institute of Aeronautics and Astronautics. doi:10.2514/6.2013-3018

Oldfield, M. L. G. (2008). Impulse Response Processing of Transient Heat Transfer Gauge Signals. *Journal of Turbomachinery*, *130*(2), 021023. doi:10.1115/1.2752188

Panda, J. & Seasholtz, R. (2002). Experimental Investigation of Density Fluctuations in High-Speed Jets and Correlation with Generated Noise. *Journal of Fluid Mechanics*, *450*, 97–130. doi:10.1017/s002211200100622x

Parziale, N., Shepherd, J. & Hornung, H. (2013). Differential Interferometric Measurement of Instability in a Hypervelocity Boundary Layer. *AIAA Journal*, *51*(3), 750–754. doi:10.2514/1.j052013

Parziale, N., Shepherd, J. & Hornung, H. (2014). Free-Stream Density Perturbations in a Reflected-Shock Tunnel. *Experiments in Fluids*, *55*(2), 1662. doi:10.1007/s00348-014-1665-0

Parziale, N., Shepherd, J. & Hornung, H. (2015). Observations of Hypervelocity Boundary-Layer Instability. *Journal of Fluid Mechanics*, *781*, 87–112. doi:10.1017/jfm.2015.489

Parziale, N. J. (2013). *Slender-Body Hypervelocity Boundary-Layer Instability* (Doctoral dissertation, California Institute of Technology).

Parziale, N., Shepherd, J. & Hornung, H. (2012). Reflected Shock Tunnel Noise Measurement by Focused Differential Interferometry. In *42nd AIAA Fluid Dynamics Conference and Exhibit*. doi:10.2514/6.2012-3261

Pate, S. (1978). *Dominance of Radiated Aerodynamic Noise on Boundary-Layer Transition in Supersonic-Hypersonic Wind Tunnels. Theory and Application* (tech. rep. No. AEDC-TR-77-107). Arnold Engineering Development Center.

Paull, A. & Stalker, R. (1992). Test Flow Disturbances in an Expansion Tube. *Journal of Fluid Mechanics*, *245*(1), 493–521. doi:10.1017/s0022112092000569

Penty Geraets, R. T., McGilvray, M., Loehle, S. & Hufgard, F. (2019). Stagnation Point Heat Flux Measurements in a Plasma Wind Tunnel Using a Diamond Heat Transfer Gauge. In *2019 AIAA SciTech Forum*. doi:10.2514/6.2019-0535

Physical Properties of Thermoelement Materials. (n.d.). OMEGA Engineering.

Practical Temperature Measurements. (n.d.). OMEGA Engineering.

Reda, D. C. (1979). Boundary-Layer Transition Experiments on Sharp, Slender Cones in Supersonic Free Flight. *AIAA Journal*, *17*(8), 803–810. doi:10.2514/3.61231

Roediger, T., Knauss, H., Smorodsky, B. V., Estorf, M. & Schneider, S. P. (2009). Hypersonic Instability Waves Measured Using Fast-Response Heat-Flux Gauges. *Journal of Spacecraft and Rockets*, *46*(2), 266–273. doi:10.2514/1.37026

Roggemann, M. C. & Welsh, B. M. (1996). *Imaging Through Turbulence (Laser & Optical Science & Technology)*. CRC Press.

Ross, R. (1973). Influence of Total Temperature on Transition in Supersonic Flow. *AIAA Journal*, *11*(4), 563–565. doi:10.2514/3.6796

Sanderson, S. (2005). Simple, Adjustable Beam Splitting Element for Differential Interferometer Based on Photoelastic Birefringence of a Prismatic Bar. *Review of Scientific Instruments*, *76*(11), 113703. doi:10.1063/1.2132271

Sanderson, S. & Sturtevant, B. (2002). Transient Heat Flux Measurement Using a Surface Junction Thermocouple. *Review of Scientific Instruments*, *73*(7), 2781–2787. doi:10.1063/1.1484255

Schilden, T., Schröder, W., Ali, S. R. C., Schreyer, A.-M., Wu, J. & Radespiel, R. (2016). Analysis of Acoustic and Entropy Disturbances in a Hypersonic Wind Tunnel. *Physics of Fluids*, *28*(5), 056104. doi:10.1063/1.4948435

Schmidt, B. E. & Shepherd, J. E. (2015). Analysis of Focused Laser Differential Interferometry. *Applied Optics*, *54*(28), 8459–8472. doi:10.1364/ao.54.008459

Schneider, S. P. (2008). Development of Hypersonic Quiet Tunnels. *Journal of Spacecraft and Rockets*, *45*(4), 641–664. doi:10.2514/1.34489

Schneider, S. P. (2001). Effects of High-Speed Tunnel Noise on Laminar-Turbulent Transition. *Journal of Spacecraft and Rockets*, *38*(3), 323–333. doi:10.2514/2.3705

Settles, G. S. & Fulghum, M. R. (2016). The Focusing Laser Differential Interferometer, an Instrument for Localized Turbulence Measurements in Refractive Flows. *Journal of Fluids Engineering*, *138*(10), 101402. doi:10.1115/1.4033960

Smeets, G. (1977). Flow Diagnostics by Laser Interferometry. *IEEE Transactions on Aerospace and Electronic Systems*, *13*(2), 82–90. doi:10.1109/taes.1977.308441

Smeets, G. (1972). Laser Interferometer for High Sensitivity Measurements on Transient Phase Objects. *IEEE Transactions on Aerospace and Electronic Systems*, *2*(AES-8), 186–190. doi:10.1109/taes.1972.309488

Smeets, G. & George, A. (1973). *Andwendungen des Laser-Differentialinterferometers in der Gasdynamik* (tech. rep. No. 28/73). Institut Saint-Louis Report.

Smith, D. M., Felderman, E. J., Shope, F. L. & Balboni, J. A. (2002). Arc-Heated Facilities. In F. K. Lu (Ed.). D. E. Marren (Ed.), *Advanced Hypersonic Test Facilities* (Vol. 198, pp. 279–314). doi:10.2514/5.9781600866678.0279.0314

Smith, D. R. & Smits, A. J. (1993). Simultaneous Measurement of Velocity and Temperature Fluctuations in the Boundary Layer of a Supersonic Flow. *Experimental Thermal and Fluid Science*, *7*(3), 221–229. doi:10.1016/0894-1777(93)90005-4

Smits, A. J., Hayakawa, K. & Muck, K. C. (1983). Constant Temperature Hot-Wire Anemometer Practice in Supersonic Flows. *Experiments in Fluids*, *1*(2), 83–92. doi:10.1007/bf00266260

Sprinks, T. (1963). On the Calibration of Calorimeter Heat-Transfer Gages. *AIAA Journal*, *1*(2), 464–464. doi:10.2514/3.54837

Stainback, P. & Wagner, R. (1972). A Comparison of Disturbance Levels Measured in Hypersonic Tunnels Using a Hot-Wire Anemometer and a Pitot Pressure Probe. In *7th Aerodynamic Testing Conference*. American Institute of Aeronautics and Astronautics. doi:10.2514/6.1972-1003

Steen, L. (2010). *Characterization and Development of Nozzles for a Hypersonic Quiet Wind Tunnel* (Master's thesis, Purdue University).

Stern, N., Buttsworth, D., Birch, B. & Choudhury, R. (2018). Hypersonic Pitching Control Model Development. In *22nd AIAA International Space Planes and Hypersonics Systems and Technologies Conference*. doi:10.2514/6.2018-5267

Tsai, B. K. A., Hanssen, D. W., Wilthan, L. M. & Boris Zeng, J. (2008). A Comparison of Optical Properties Between Solid PTFE (Teflon) and (Low Density) Sintered PTFE. *Reflection, Scattering, and Diffraction from Surfaces*, International Society for Optics and Photonics, *7065*, 70650Y.

Van Driest, E. R. (1952). *Investigation of Laminar Boundary Layer in compressive Fluids Using the Crocco Method* (tech. rep. No. NACA-TN-2597). National Advisory Committee for Aeronautics; Washington, DC, United States.

Vennik, J., Neely, A. J., Tuttle, S., Choudhury, R. & Buttsworth, D. R. (2017). Reproducing Non-Uniform Surface Temperature Profiles on Hypersonic Cruise Vehicles in Impulsive Wind Tunnels. In *21st AIAA International Space Planes and Hypersonics Technologies Conference*. doi:10.2514/6.2017-2194

Wagner, A., Schülein, E., Petervari, R., Hannemann, K., Ali, S. R. C., Cerminara, A. & Sandham, N. D. (2018). Combined Free-Stream Disturbance Measurements and Receptivity Studies in Hypersonic Wind Tunnels by Means of a Slender Wedge Probe and Direct Numerical Simulation. *Journal of Fluid Mechanics*, *842*. doi:10.1017/jfm.2018.132

Wang, Y. (1995). Jump and Sharp Cusp Detection by Wavelets. *Biometrika*, *82*(2), 385–397. doi:10.1093/biomet/82.2.385

Weiss, J. (2002). *Experimental Determination of the Freestream Disturbance Field in the Short Duration Supersonic Wind Tunnel of Stuttgart University* (Doctoral dissertation, Stuttgart University).

Weiss, J., Knauss, H. & Wagner, S. (2003). Experimental Determination of the Free-Stream Disturbance Field in a Short-Duration Supersonic Wind Tunnel. *Experiments in Fluids*, *35*(4), 291–302. doi:10.1007/s00348-003-0623-z

Wendt, J. F. (1997). External Hypersonic Aerodynamics: State-of-the-Art and Future Perspective. In *Future Aerospace Technology in the Service of the Alliance: AGARD*

Conference Proceedings 600 (Vol. 3: Sustained Hypersonic Flight, pp. C10.1–C10.7).

White, F. M. (2005). *Viscous Fluid Flow*. McGraw-Hill Education.

Widodo, A. S. (2012). *Temperature Variations in a Free Piston Compression Wind Tunnel* (Doctoral dissertation, University of Southern Queensland).

Widodo, A. & Buttsworth, D. (2013). Stagnation Temperature in a Cold Hypersonic Flow Produced by a Light Free Piston Compression Facility. *Experiments in Fluids*, *54*(4). doi:10.1007/s00348-013-1486-6

Zander, F., Hermann, T. & Loehle, S. (2016). Plasma Wind Tunnel Flow Analysis with High Speed Imaging. In *46th AIAA Thermophysics Conference*. doi:10.2514/6.2016-3202

Zoby, E. & Sullivan, E. (1966). Effects of Corner Radius on Stagnation-Point Velocity Gradients on Blunt Axisymmetric Bodies. *Journal of Spacecraft and Rockets*, *3*(10), 1567–1567. doi:10.2514/3.59538

Appendix A

L1d3 Non-Uniform Initial Conditions

The properties of the gas slugs along the facility were determined using the procedure described in Section 4.3.3, but L1d3 does not have a method for implementing non-uniform gas slugs. To identify where the gas slugs can be modified to a non-uniform state it is useful to examine the workflow for setting up and running a simulation in L1d3, and this workflow is shown in Fig. A.1.

A Python (*job*.py) file is created by the user which contains all the facility geometry and feature information, and definitions of the uniform gas slugs. In step 1 this file is processed using `l_script.py` and the output file *job*.Lp created. The *job*.Lp contains the job controls and the information for creating the job mesh and the gas slugs. However, the gas slug definition here is limited to a scalar value of pressure, velocity, temperature and mass fraction, as shown by the excerpt of *job*.Lp in Fig. A.2, and is therefore unsuitable for modification.

At step 2 *job*.Lp is processed by `l_prep.exe` to create the initial solution at $t = 0$ s which is written to two files: (1) *job*.La containing only the geometry definition, and (2) *job*.L0 which contains the first flow solution. The three files created in the first two steps are then used as inputs to `l1d.exe`. Therefore, *job*.L0 was identified as a file that can be edited to modify the initial flow solution and achieve a non-uniform distribution of properties within individual slugs.

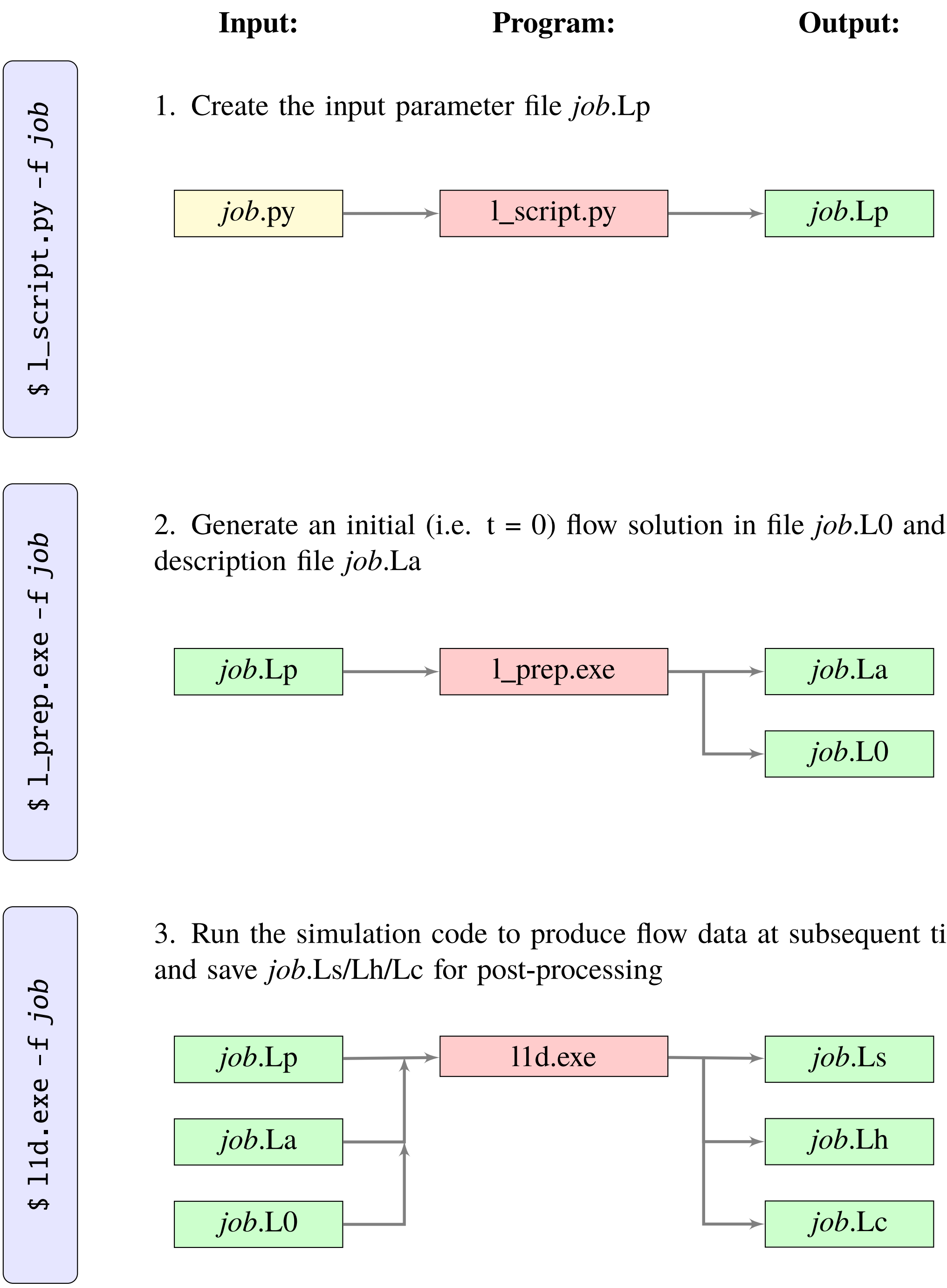

```
$ l_script.py -f job
```

1. Create the input parameter file *job*.Lp

```
$ l_prep.exe -f job
```

2. Generate an initial (i.e. t = 0) flow solution in file *job*.L0 and tube description file *job*.La

```
$ l1d.exe -f job
```

3. Run the simulation code to produce flow data at subsequent times and save *job*.Ls/Lh/Lc for post-processing

Figure A.1: L1d3 Workflow.

```
initial_p = 6.000000e+02    % initial pressure, Pa
initial_u = 0.000000e+00    % initial velocity, m/s
initial_T = 2.930000e+02    % initial temperature, K
massf = 1.000000e+00        % air mass fraction
```

Figure A.2: Excerpt of *job*.Lp showing how the properties of the gas slugs are defined.

The *job*.L0 structure has n header lines with the piston, valve and diaphragm information, if these are present in the simulation. Following this each gas slug is defined. First the cell midpoint x coordinate and cross sectional area at that position, one line for each cell in each slug. Next the flow properties of the slug are defined for each cell of the slug. These properties are in thirteen columns, consistent with the layout of Table 4.3. The values in these columns are replaced by those determined using the procedure described in Section 4.3.3.

This modification process was implemented using a MATLAB script (`Modify_L0.m`), and the new process flowchart presented in Fig. A.3. The first two steps are unchanged from Fig. A.1. A flow state is determined for the instant in time that the simulation starts using the method described in Section 4.3.3, and this flow state and the *job*.L0 file input to `Modify_L0.m`.

`Modify_L0.m` uses linear interpolation to fit the flow state to the cell centres of *job*.L0. The initial *job*.L0 is preserved for reference as *job*_OLD.L0 and the updated *job*.L0 file with non-uniform gas slug properties saved. The simulation is run using Step 4, which is identical to Step 3 of Fig. A.1, and output files for post-processing created.

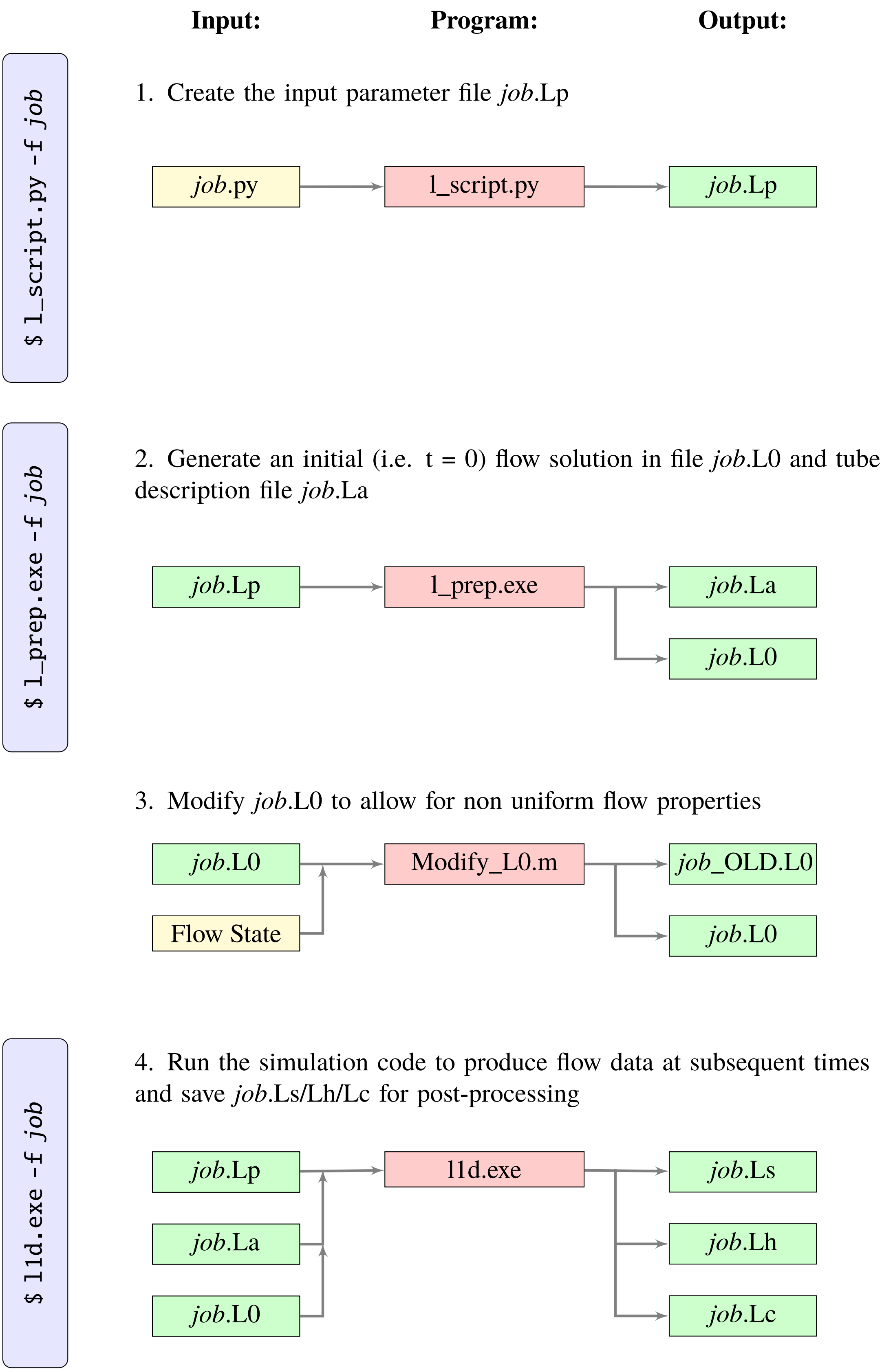

```
$ l_script.py -f job
```

1. Create the input parameter file *job*.Lp

```
$ l_prep.exe -f job
```

2. Generate an initial (i.e. t = 0) flow solution in file *job*.L0 and tube description file *job*.La

3. Modify *job*.L0 to allow for non uniform flow properties

```
$ l1d.exe -f job
```

4. Run the simulation code to produce flow data at subsequent times and save *job*.Ls/Lh/Lc for post-processing

Figure A.3: Modified L1d3 Workflow

Appendix B

Thermocouple Geometry

The dimensions of the type E and type K surface junction thermocouples developed for the TUSQ experiments and the PWK4 experiments respectively are illustrated on the following page.

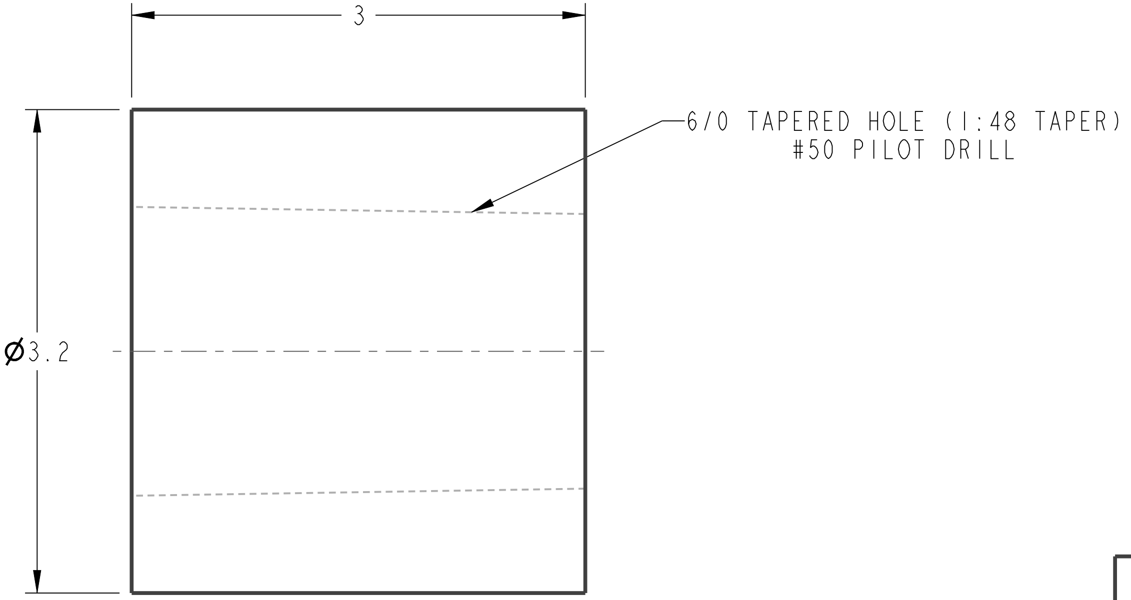

ANNULUS- CHROMEL

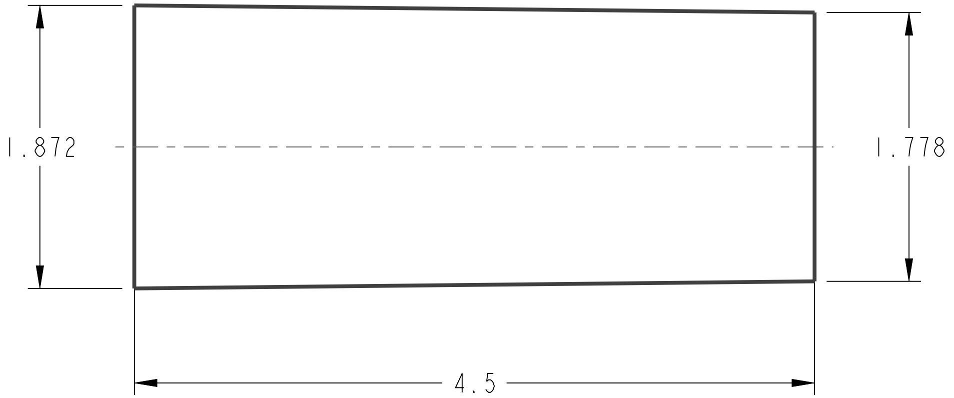

PIN
TYPE E- CONSTANTAN
TYPE K- ALUMEL

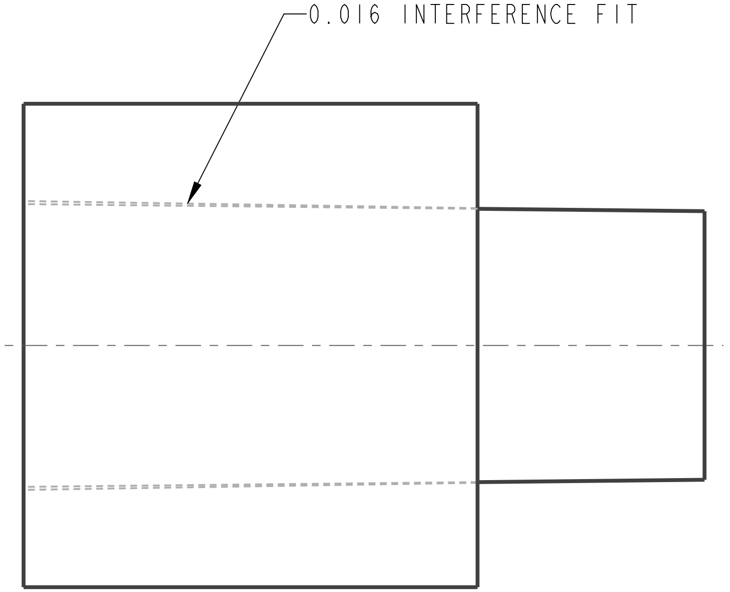

THERMOCOUPLE ASSEMBLY

ALL DIMENSIONS mm	UNIVERSITY OF SOUTHERN QUEENSLAND		
	TITLE THERMOCOUPLE		
DRAWN: BYRENN BIRCH	SCALE 20:1	DRG.NO	A4
DATE: 11/06/2019			

Appendix C

Reflected Shock Tube Calculations

The calculations presented here were used to populate Table 6.1 where the driver (State 4) and driven (State 1) gases are ideal air. The pressure and temperature of State 1 are known a priori, as is the temperature of State 4. The wave speed, w, is measured from the signals from PT1, PT2 and the thermocouple being calibrated.

The incident shock Mach number, M_{s1} is defined as

$$M_{s1} = \frac{w}{\sqrt{\gamma_1 R T_1}} \tag{C.1}$$

The speed of sound at State i was calculated using

$$a_i = \sqrt{\gamma_i R T_i} \tag{C.2}$$

and the density calculated using the ideal gas law

$$\rho_i = \frac{P_i}{R T_i} \tag{C.3}$$

The pressure at State 2, P_2, was calculated using

$$P_2 = P_1 \left[1 + 2\frac{\gamma_1}{\gamma_1 + 1}\left(M_{s1}^2 - 1\right)\right] \tag{C.4}$$

and T_2 calculated by

$$T_2 = T_1 \frac{P_2}{P_1}\left[\frac{\frac{\gamma_1+1}{\gamma_1-1} + \frac{P_2}{P_1}}{1 + \frac{P_2}{P_1}\frac{\gamma_1+1}{\gamma_1-1}}\right] \tag{C.5}$$

and the velocity, u_2, by

$$u_2 = \frac{a_1}{\gamma_1}\left(\frac{P_2}{P_1} - 1\right)\left(\frac{\frac{2\gamma_1}{\gamma_1+1}}{\frac{P_2}{P_1} + \frac{\gamma-1}{\gamma+1}}\right)^{0.5} \tag{C.6}$$

At State 4, the temperature was known a priori, and the pressure calculated using

$$P_4 = P_2\left[1 + \frac{\frac{\gamma_4-1}{a_4/a_1}\left(\frac{P_2}{P_1} - 1\right)}{\sqrt{2\gamma_1\left(2\gamma_1 + (\gamma_1 + 1)\left(\frac{P_2}{P_1} - 1\right)\right)}}\right]^{(-2\gamma_4)/(\gamma_4-1)} \tag{C.7}$$

The temperature of the gas behind the reflected shock, T_5, can be found using

$$T_5 = T_1\left[\frac{\left(2\left(\gamma_1 - 1\right)M_{s1}^2 + 3 - \gamma_1\right)\left(\left(3\gamma_1 - 1\right)M_{s1}^2 - 2\left(\gamma_1 - 1\right)\right)}{\left(\gamma_1 + 1\right)^2 M_{s1}^2}\right] \tag{C.8}$$

and P_5 calculated using

$$P_5 = P_2\left[\frac{\left(3\gamma_1 - 1\right)\frac{P_2}{P_1} - \left(\gamma_1 - 1\right)}{\left(\gamma_1 - 1\right)\frac{P_2}{P_1} + \left(\gamma_1 + 1\right)}\right] \tag{C.9}$$

Appendix D

Stationary Wavelet Filtering

The ungrounded thermocouple junction was found to sense a large amount of electromagnetic interference over a large number of narrowband frequency bands as shown in Fig. D.1. The sources of this noise included other laboratory equipment and lighting, while the high amplitude content at $f > 700\,\mathrm{kHz}$ was found to be local AM radio broadcasts. Preliminary facility runs identified that there was no discernible signal above the baseline noise level for frequencies in the order of tens of kilohertz, and this was also the case when testing with a different amplifier (AMETEK Model 5113). Consequently the 40 kHz first order low-pass filter of stage 2 was implemented which reduced the noise level significantly. However the DC stage 1 was not fitted with a low-pass filter, and consequently the electromagnetic interference had a larger impact on the measurement than for stage 2.

Despite the presence of the low-pass filter on stage 2, significant baseline noise was still present and had to be removed digitally. Simple low-pass and bandstop Butterworth filters were found to be inadequate to attenuate the environmental noise to a reasonable level.

To determine the mean flow temperature a wavelet denoising technique was implemented, and the data presented for mean flow analysis section has been filtered in this way. The wavelet denoising method is an application of the stationary wavelet transform (SWT) and is used to reconstruct a signal from a noisy one. When compared to traditional Fourier domain filtering, such as a Butterworth filter, a SWT is localised in time and

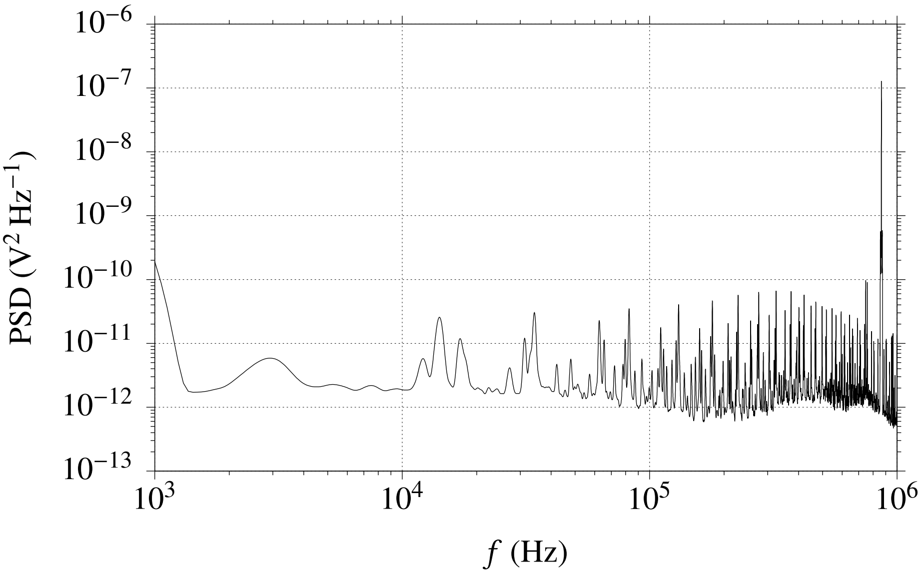

Figure D.1: Spectrum of the electromagnetic interference detected by the thermocouple.

frequency while the Fourier techniques are localised in frequency only (Karel, 2009). A SWT better resolves sharp signal changes than Fourier techniques without broadening or erasing information like kernel methods for noise reduction (Wang, 1995).

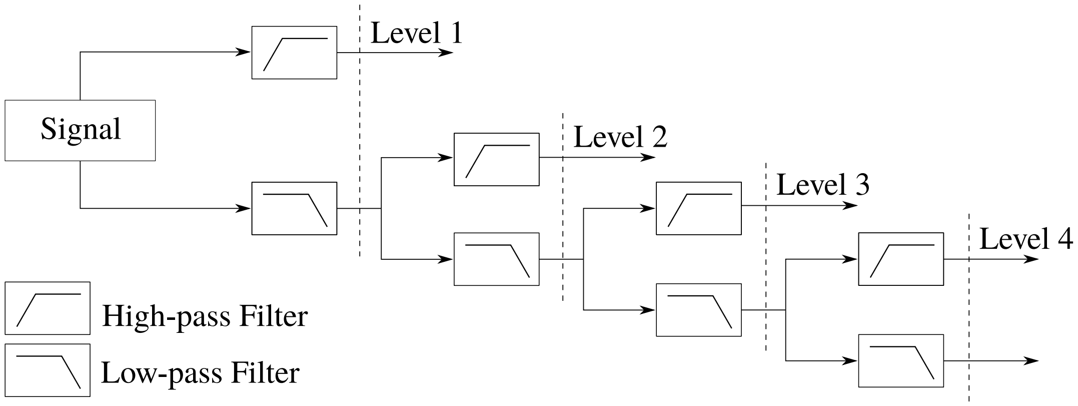

Figure D.2: Four level stationary wavelet transform (SWT) filter bank.

The SWT can be considered a bank of high and low-pass filters of various cut-off frequencies as illustrated in Fig. D.2. The thermocouple data for DC coupled and reconstructed AC coupled signals were SWT filtered using a second order level 6 Symlet wavelet, and an example of the results of this filtering is shown in Fig. 7.4. The Symlet wavelet family is suitable for detection of closely spaced features, and the SWT filtering used hard thresholding of unscaled white noise for improved edge preservation. Symlet wavelets are orthogonal, and this is an important feature of the selected wavelet because it preserves the energy of the signal.

Appendix E

ESA Standard Probe Geometry

The 50 mm flat faced probe head geometry used for mounting the fast response thermocouple probe for the research in PWK4 is shown on the following page.

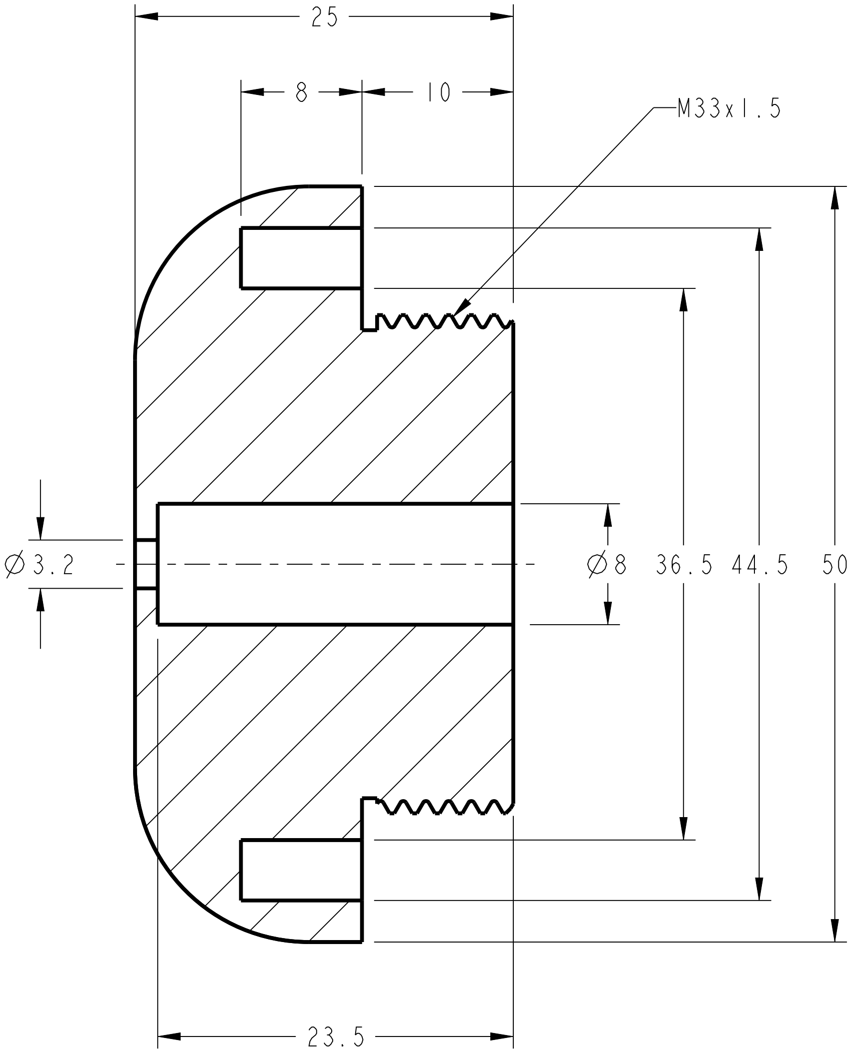

UNIVERSITY OF SOUTHERN QUEENSLAND

TITLE ESA 50mm FF PROBE

DRAWN: BYRENN BIRCH
DATE: 24-08-2017
SCALE 2:1
REV 1
A4

Appendix F

Amplifier Repair and Characterisation

One of the two nominally identical AMETEK Model 5113 pre-amplifiers was found to not amplify the photodetector signal, but output a constant voltage regardless of the input signal level. This was common to the operation of this amplifier in both AC and DC coupled modes and independent of the gain setting. By measuring the continuity of the two amplifiers, the faulty amplifier was found to lack a connection from the negative side of the BNC input to the amplifier shield. The amplifier shield is readily accessible at the bolts connecting the housing to the chassis, while the negative side of the BNC input are common for inputs A and B. As shown by Fig. F.1, the negative side of the BNC for input B was connected to the amplifier shield using an alligator cable via a 47 Ω resistor in series.

Using a function generator to provide a known amplitude sinusoidal input, the performance of the repaired amplifier was compared to the functional amplifier. The gain of the two amplifiers was consistent and, as shown in Fig. F.2, the frequency response was independent of the gain setting selected for $10 \leq G \leq 250$ with flat amplification to 1 MHz demonstrated. A transfer function representing the frequency response of the amplifier (H_{Amp}) was fitted to the data of Fig. F.2 using an equation of the form

$$H_{Amp}\left(f\right) = \left[1 + \left(\frac{f}{f_c}\right)^{2n}\right]^{-0.5} \tag{F.1}$$

Figure F.1: Modification of AMETEK Model 5113 pre-amplifier to repair the amplifier.

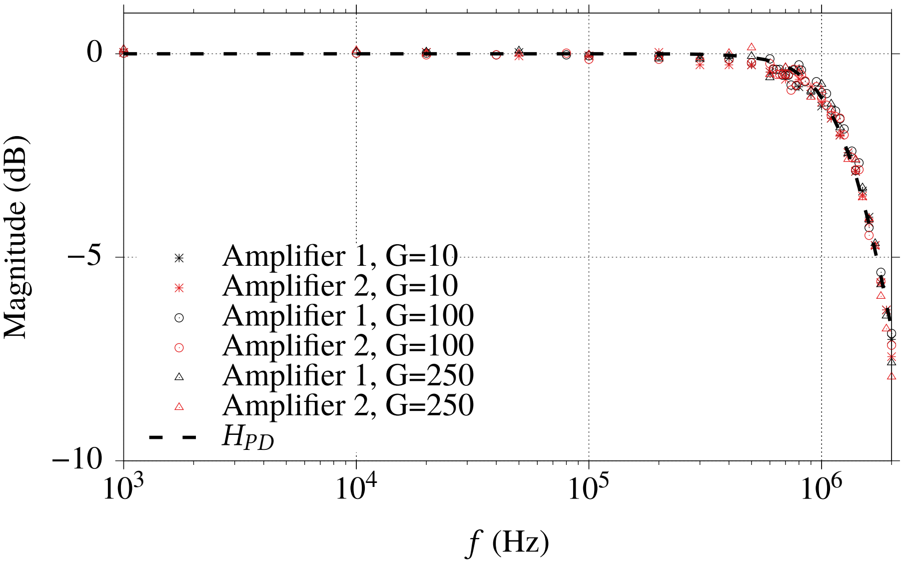

Figure F.2: Normalised frequency response of the both the functioning and corrected amplifiers.

Appendix G

Calculation of FLDI Path Integration Spatial Filter

The FLDI transfer function due to the path integrated spatial filtering from the beam and turbulence profile (H_z) was given by Fulghum (2014) as Eq. G.1. For a uniform disturbance field of width $2L$, two different simplifications of Eq. G.1 were identified in literature Fulghum (2014) and Schmidt and Shepherd (2015). This appendix shows how Eq. G.1 can be simplified for this disturbance field, and shows that the solution proposed by Schmidt and Shepherd (2015) is correct.

$$H_z(k) = \int_{-L}^{L} \exp\left(-\frac{w_0^2 k^2}{8}\left(1 + \left[\frac{\lambda z}{\pi w_0^2}\right]^2\right)\right) \mathrm{d}z \tag{G.1}$$

Expand the brackets

$$H_z(k) = \int_{-L}^{L} \exp\left(-\frac{w_0^2 k^2}{8} + \frac{-w_0^2 k^2 \lambda^2 z^2}{8\pi^2 w_0^4}\right) \mathrm{d}z \tag{G.2}$$

Move the constant outside of the integral

$$H_z(k) = \exp\left(\frac{-w_0^2 k^2}{8}\right) \int_{-L}^{L} \exp\left(\left[\frac{-k^2 \lambda^2}{8\pi^2 w_0^2}\right] z^2\right) \mathrm{d}z \tag{G.3}$$

The equation is now of the form $\int \exp\left(-cx^2\right) \mathrm{d}x = \sqrt{\frac{\pi}{4c}} \operatorname{erf}\left(\sqrt{c}x\right)$. Therefore

$$H_z(k) = \exp\left(\frac{-w_0^2 k^2}{8}\right) \frac{\sqrt{2}\pi\sqrt{\pi}w_0}{k\lambda} \times \left(\operatorname{erf}\left(\frac{k\lambda}{2\sqrt{2}\pi w_0} L\right) - \operatorname{erf}\left(\frac{k\lambda}{2\sqrt{2}\pi w_0}(-L)\right)\right). \tag{G.4}$$

Since erf(x) is an odd function (erf$(-x) = -$erf(x)),

$$H_z(k) = \exp\left(\frac{-w_0^2 k^2}{8}\right) \frac{\sqrt{2}\pi\sqrt{\pi}w_0}{k\lambda} \times 2 \times \operatorname{erf}\left(\frac{k\lambda}{2\sqrt{2}\pi w_0} L\right) \tag{G.5}$$

which can be rearranged to,

$$H_z(k) = \frac{2\sqrt{2}\pi\sqrt{\pi}w_0}{k\lambda} \exp\left(\frac{-w_0^2 k^2}{8}\right) \operatorname{erf}\left(\frac{kL\lambda}{2\sqrt{2}\pi w_0}\right). \tag{G.6}$$

This result demonstrates the error made by Fulghum (2014) and produces a result consistent with Schmidt and Shepherd (2015).

$$\tag{G.7}$$